# Study of the interaction between hydrogen and ultradispersed metals for heterogeneous catalysis

Wang Liu

Thesis to obtain the degree of **Doctor of Philosophy**
from the Université de Paris-Est Créteil

Degree in **Chemistry**
Institut de Chimie et des Matériaux de Paris-Est, UMR 7182, CNRS

# Study of the interaction between hydrogen and ultradispersed metals for heterogeneous catalysis

Submitted by: **Wang LIU**
Thesis defended on December 6th, 2021

## Jury:

| | | |
|---|---|---|
| Dr. Petra de Jongh | Utrecht University, Netherlands | Reviewer |
| Dr. Philippe Serp | LCC,ENSIACET, CNRS, France | Reviewer |
| Dr. Valérie Paul-Boncour | ICMPE, CNRS, France | Examiner |
| Dr. Camille La Fontaine | Synchrotron SOLEIL, France | Examiner |
| Dr. Ovidiu Ersen | IPCMS, CNRS, France | Invited |
| Dr. Franck Morfin | IRCELYON, CNRS, France | Invited |
| Dr. Claudia Zlotea | ICMPE, CNRS, France | PhD. supervisor |

# Acknowledgements

I would like to express my most sincere acknowledgments to my supervisor Dr. **Claudia Zlotea**. You have been the best mentor and scientific guide that I could ever have. Thank you for your patience, for your guidance, and your help that greatly helped me in all the time of the research work and the redaction of this thesis.

I would like to thank my jury members, Prof. **Petra de Jongh**, Prof. **Philippe Serp**, Dr. **Valérie Paul-Boncour**, Dr. **Camille La Fontaine**, Prof. **Ovidiu Ersen** and Dr. **Franck Morfin** for their willingness to read and judge this thesis.

I would like to thank my collaborators at IRCELYON: Dr. **Laurent Piccolo**, Dr. **Franck Morfin**, Dr. **Thomas Len** and Dr. **Noémie Perret** for their kind reception when I was at IRCELYON and for their help during the experiment at Soleil Synchrotron. Special thanks to **Franck**, **Franck** helped me a lot during my thesis, ex: the experiment of hydrogenation of butadiene, ICP, XPS, TGA-MS, Fluo-X, CHNS and BET. I would also like to thank my collaborators at IPCMS: Prof. **Ovidiu Ersen**, Dr. **Mounib Bahri** and Dr. **Walid Baaziz** for their characterization of HAADF-STEM.

I would like to thank my colleagues at ICPME where I worked for 3 years. I would like to thank **Michel Latroche** and **Fermin Cuevas** for their kindness and help as my office colleagues. I am very much thankful to **Julie Bourgon** for the numerous TEM measurements. Thanks to **Valérie Lalanne**, **Benjamin Villeroy**, **Fabrice Couturas**, and **Olivier Rouleau** for their technical supports. Thanks to **Karine Provost** for the help in the treatment of XAS data. Thanks to **Mohamed Guerrouache** for Raman analysis, **Pierre Dubot** for XPS analysis and **Rémy Pires Brazuna** for SEM analysis. Thanks to **Dominique Alain**, **Gladys Bernari**, **Hélène Barrès** and **Amina Hocini** (Délégation-Villejuif) for the administrative works.

I would like to thank staffs at Soleil Synchrotron for the reception during my 3 experiments there, special thanks to the team in line Rock: **Stéphanie Belin**, **Camille La Fontaine**, **Laurent Barthe** and **Valerie Briois**.

I would like to express my happiness for having friends with PhD students: **Abdelmalek Malouche**, **Jorge Montero**, **Anna Celeste**, **Bruno Hessel Silva**, **Anis Bouzidi**, **Nayely Pineda-Romero**, **Maxime Dottor** and **Abou Diack-Rasselio**.

I would like to thank the new friends I have made during 3 years of PhD: **Yanlong Zhou** and his wife **Jun Tang**, **Liqin Wang**, **Hao Shen**, **Guanyu Cai** and his wife **Yingqi Bi**, **Xiaoyu Yan** and his husband **Xin Guo**, **Lv Fu** and his wife **Qi Shi**. I would like to thank **Marie Réveillaud** for her kindness as friend.

I would like to thank all the professors I have met in France during my study in French learning in Dufos (Le Mans), Licence 3 Chimie (Le Mans) and Master Green Chemistry (Strasbourg), they helped me a lot.

I would like to thank my family: my parents, my sister and my niece, for your support throughout the past 7 years since I live in France. I would like to thank my uncle, my aunt, my cousin and his girlfriend, for their support and guidance during my life in France. I would like to thank my host family in Le Mans: **Marie** and **Bruno**, **Orianne** and **Christophe**, for their kind reception during my life in Le Mans.

I would like to thank my girlfriend **Jingyi** for your love, company and full support during my PhD works, and our two little cats: **Niangao** and **Lyon**.

**Wang Liu**

# Table of contents

**SUMMARY**

# List of figures

## List of tables

Heterogeneous catalysis is one of the pillars of the chemical industry as it is involved in a wide range of applications, from the production of fuels, chemicals and manufactured commodities to environmental protection and sustainable chemical technologies. However, the design of catalysts with high efficiency, selectivity and stability remains a major challenge. As a matter of fact, the heterogeneous catalysis occurs usually at the surface of metal catalysts, therefore the downscaling of metal particles to the ultra-small size range, which increases the metal surface area and thus enhances the number of the metallic active sites, has become an important strategy for the design of new and efficient materials. Moreover, nanometric and subnanometric downsizing gives rise to a dramatic change in the electronic properties of metals, which in turn leads to promising catalytic performances (Figure 1.1).[1,2]

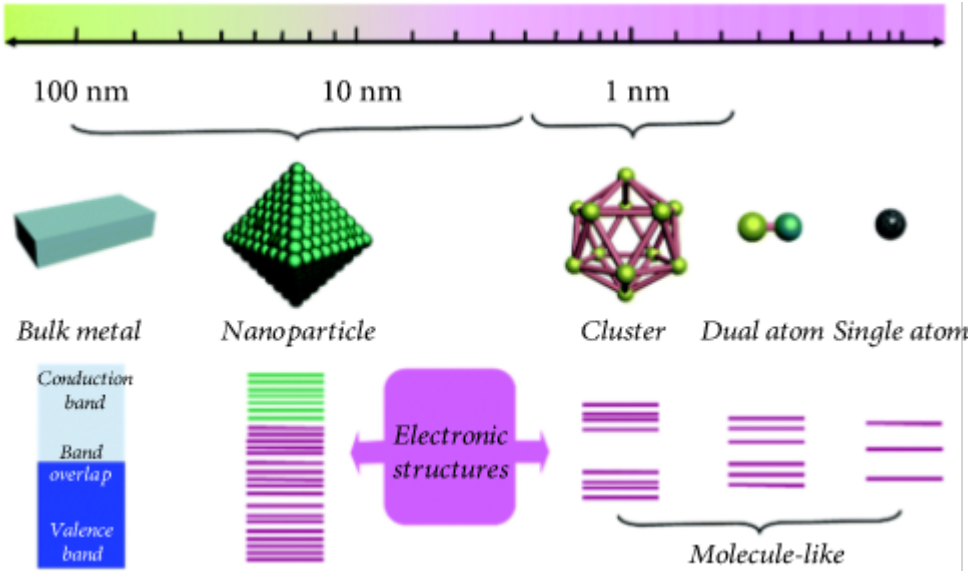


*Figure 1. 1: Illustration of the downsizing metal sizes, and evolution of the electronic structures.*[3]

On the other side, in the field of catalysis, hydrogen is involved in many industrially relevant reactions and it is known that hydrogen interaction with metal-based catalyst has important effects on the catalytic performance.[4,5] The understanding of the interaction between the metal-based catalyst and hydrogen is paramount for the design of efficient catalysts. Many nanosize effects in hydrogen interaction are observed in metals. For example, it has been shown that Pd particles of a few nanometres absorb less hydrogen per Pd atom than bulk Pd,[6] and that nanoparticles of non-absorbing elements such as Rh and Ir do absorb hydrogen and can even form a stable hydride at atmospheric temperature and pressure.[7,8] Moreover, the formed Rh hydride showed better catalytic performance than its metal

counterpart in the hydrogenation of butadiene.[8] These behaviours are due to the important thermodynamic changes introduced by nanosizing. For particles with subnanometric dimensions, the thermodynamics of hydrogen absorption (and hydride formation) are expected to change due to increased surface/interface energy and kinetics as improved because of short diffusion paths and large number of surface active sites for dissociation and recombination. However, due to the experimental difficulties in elaborating and characterizing ultradispersed supported metals, the hydrogen sorption properties of such materials are very scarcely reported.

In this context, the National Research Agency (ANR) is financing the UltraCat project, based on a collaboration between the Institut de Recherches sur la Catalyse et l'Environnement de Lyon (IRCELYON), the Institut de Chimie et des Matériaux Paris-Est (ICMPE) and Institut de Physique et Chimie des Matériaux de Strasbourg (IPCMS). The UltraCat project aims at the design and investigation of new catalysts based on ultradispersed metals in the form of nanometric particles down to isolated atoms, supported on mesoporous materials for reactions with high interest for clean-energy-production processes involving hydrogen.

Within this context, this PhD project has three interrelated goals:

- The design and synthesis of novel catalytic materials with controlled metal dispersion by tuning the metal particle dimension from nanoscale to atomic state through favourable interaction with carbon-based porous supports;
- The evaluation of the performances of these new catalysts in selective hydrogenations: hydrogenation of butadiene and hydrogenation of levulinic acid;
- The characterization of the interaction between hydrogen and these materials (hydrogen absorption/desorption), dependence on the metal cluster size and structure, and its interplay with catalysis.

The structure of this manuscript consisted of 5 following chapters:

**Chapter 1** begins with a brief description of hydrogen generalities and applications, then hydrogen interaction with metals is discussed along with the nanosize effects in hydrogen-metal interaction. The synthesis methods and uses of ultradispersed metals in catalytic reactions are also described.

**Chapter 2** describes the methodologies used for the preparation of the metal nanoparticles and single atom catalysts supported on carbon-based materials, and the characterization techniques used for the determination of their physicochemical properties, their interaction with hydrogen and the protocol of the catalytic experiments.

**Chapter 3** extensively discusses the interaction between hydrogen and Pd bulk, Pd nanoparticles with different sizes and Pd single atoms samples.

**Chapter 4** presents the characterization of Ir single atom catalyst and Ir nanoparticles as well as their performance in catalytic reaction of hydrogenation of butadiene and hydrogenation of levulinic acid.

**Chapter 5** describes the Co, Cu, Ni, Mo, Pd, Ir and Pt single atom catalysts with different metal loadings and their catalytic tests in the reaction of hydrogenation of butadiene and hydrogenation of levulinic acid.

Lastly, the manuscript will end with a general conclusion of the most significant results obtained during this PhD work and we propose some research perspectives.

# CHAPTER I: INTRODUCTION

## 1.1 Hydrogen: generalities, and current uses

Hydrogen atom is composed of one electron and one proton, making it the lightest element. It is also the most abundant element in the universe, accounting for more than 75 wt.% of the universe. At standard temperature and pressure conditions (STP), hydrogen is a diatomic gas with molecular formula $H_2$ possessing the following features: colourless, non-toxic, and highly flammable. Since hydrogen readily forms covalent bonds with most non-metallic elements, most of the hydrogen on Earth exists in molecular forms such as water or organic compounds.

In the context of energy insecurity, global climate change and protection of environment, hydrogen is identified as a critical and indispensable element of a decarbonised sustainable energy system to provide secure, cost-effective and non-polluting energy.[9] Today, energy leaders see hydrogen as the lowest impact molecule in the global energy system.[10] In this context, hydrogen can be seen as an energy carrier or a means of energy storage.

Hydrogen has multiple industrial applications, mainly for the chemical and refining activities. As shown in Figure 1.2, about 55% of the total consumption of hydrogen is in ammonia production, an important part of fertilizers used in agricultural industries around the world. The second most important use is in petroleum refining process where hydrogen is commonly used in hydrocracking to create petroleum product, including gasoline and diesel or to remove contaminants like sulphur. Around 10% of hydrogen is employed to create methanol ($CH_3OH$). The remaining 10% applications are categorized in miscellaneous uses such as, food industry, metalworking, welding or medical applications. Recently, hydrogen has been used more and more to produce synthetic fuels and in energy sector, as an alternative combustible fuel.[11]

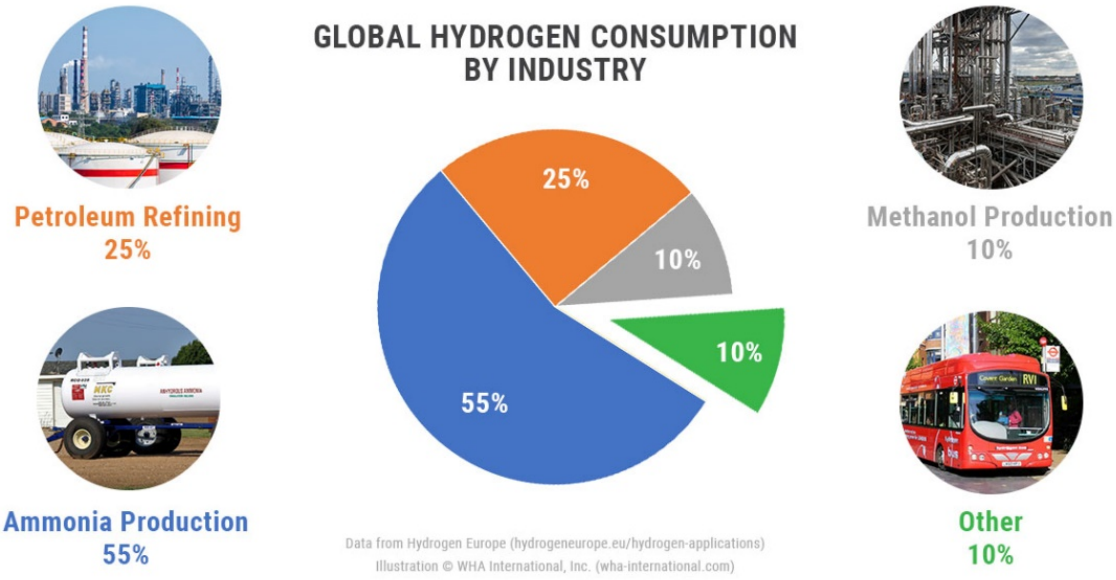


*Figure 1. 2: Hydrogen applications in industry.*

The chemical industry use of hydrogen often involves a chemical process: the hydrogenation. Hydrogenation is a chemical reaction involving the molecular hydrogen ($H_2$) which is added to an unsaturated moiety (Figure 1.3). For example, hydrogenation is used to saturate alkenes and aromatics from petrochemical refineries, making them less toxic and reactive. Moreover, in food industry, vegetable oils derived from polyunsaturated fatty acids can also be processed to improve their flavour stability and melting behaviour by hydrogenation reactions.[12]

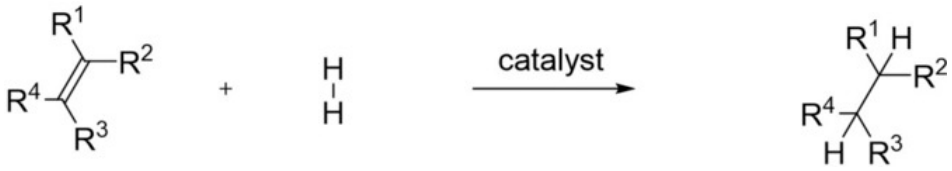


*Figure 1. 3: Schematic representation of hydrogenation.*[13]

However, molecular hydrogen is rather unreactive at STP conditions and consequently, the hydrogenation reactions often require the use of catalysts, in particular transition metal-based catalysts which can bind and therefore activate the hydrogen. The molecular $H_2$ can thus be transformed into $H^-$ (hydride), $H\cdot$ (hydrogen radical) or $H^+$ (proton) after being in contact with the metal catalysts. Subsequently, these forms of hydrogen are transferred to the substrate and prompt to bind with the reactants in order to produce the desired final product.[14] As a major constituent in catalysis, the heterogeneous catalysis where the phase

of catalysts differs from that of the reactants or products, is involved in about 80% of industrial processes.[15]

In heterogeneous catalysis, hydrogenation reaction is happened usually at the surface of metal catalyst, and the key step of the reaction mechanism is the dissociation of strong H-H bond into two weak metal-H bonds with the metal atoms at the surface. However, the hydrogen metal interaction below the surface can also affect the catalytic activity. For example, by using Density Functional Theory (DFT) calculations, Aleksandrov *et al*.[5] reported that the reaction rate of hydrogenation of ethyl was found to increase with increasing the content of hydrogen in the subsurface of Pd et Pt metal particles. In fact, hydrogen in subsurface of Pd et Pt metal particles could significantly decrease the bond energy of the adsorbed hydrogen atoms at the surface, *i.e.*, the destabilisation of hydrogen at the surface accelerates the reaction. Morfin *et al*.[8] demonstrated that the hydride form of 1 nm Rh nanoparticles was more active in hydrogenation of butadiene compared to Rh metal counterpart. The strong polar character of Rh-H bonds in Rh hydride leads to an increased positive charge of surface metal atoms which could attract hydrogen more strongly. Consequently, the strengthening of the Rh-H bond at the surface facilitates the hydrogen dissociative chemisorption and increases the catalytic activity. Therefore, it is necessary to understand the hydrogen interaction with metals below the surface in the domain of catalytic hydrogenation reaction, and this will be discussed in detail in the next paragraph.

### 1.2 Hydrogen interaction with metals

The dominant role of hydrogen in heterogeneous catalysis has become evident during the past few decades.[16] Moreover, hydrogen absorption in metals/alloys/intermetallic compounds is considered as an attractive, high energy density and safe route to store hydrogen for further use as combustion fuel. Consequently, hydrogen interaction with metals, in particular transition metals, as frequently used in catalysis,[17–19] has been extensively studied.[5,20–23]

The hydrogen sorption process in metals, which consists of several steps (Figure 1.4 a) involves different energy barriers that can be described by the Lennard-Jones potential diagram,[24] as shown in Figure 1.4 b.

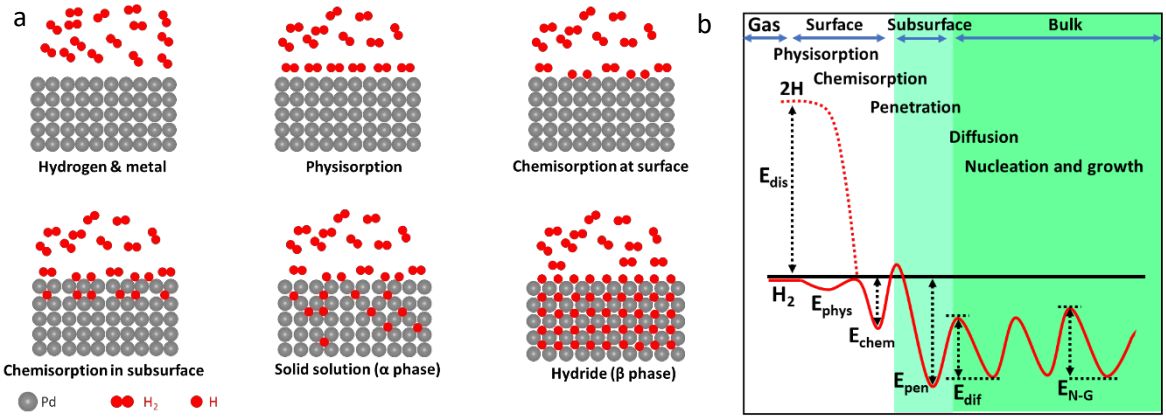


*Figure 1. 4: a) Schematic representation of the interaction of hydrogen in metals, and b) Lennard-Jones potential diagram corresponding to the successive energy barriers encountered by hydrogen during absorption/desorption in a metal. $E_{phys}$: energy for hydrogen physisorption, $E_{chem}$: energy for hydrogen chemisorption, $E_{pen}$: energy for hydrogen penetration in the subsurface, $E_{dif}$: energy for hydrogen diffusion in the bulk, and $E_{N-G}$: energy for the nucleation and growth of the hydride phase.*[24]

Away from the metal surface, the potential of $H_2$ molecule and that of two hydrogen atoms are separated by the dissociation energy ( $1/2H_2 \rightarrow H$ , $E_D$ = 218 kJ·mol$^{-1}$ H). Approaching the metal surface, the $H_2$ molecule undergoes an attractive interaction *via* weak van der Waals forces leading to the physisorption with small energy ($E_{Phys}$ ≈ −5 kJ·mol$^{-1}$ H) at an approximate distance of one $H_2$ molecule radius (≈ 0.2 nm) from the metal surface. Closer to the surface, the $H_2$ molecule must overcome an activation barrier for dissociation into two hydrogen atoms and formation of a chemical bond between H and metal atoms at surface. The activation barrier strongly depends on the nature of surface elements. This chemisorption step is characterised by the hydrogen atoms sharing their electron with the metal atoms at the surface and involves larger energy ($E_{Chem}$ ≈ −50 kJ·mol$^{-1}$ H) than in the case of physisorption. In the next step, the chemisorbed hydrogen atom can jump into the subsurface layer and finally diffuse in the available interstitial sites throughout the bulk metal lattice. The hydrogen atoms contribute with their unique electron to the conduction band of the metal. Once occupying the interstitial sites of the metal subsurface, hydrogen atoms can diffuse from one interstitial site to another to form firstly a solid solution ($\alpha$ phase) characterized by random hydrogen distribution within the interstitial sites. The absorption of the hydrogen atoms inside of the metal lattice and the formation of solid solutions with hydrogen causes the expansion of lattice parameters. Afterwards, as the hydrogen concentration increases in

the metal lattice, the hydrogen atoms begin to occupy interstitial sites in an ordered arrangement and subsequently the solid solution ($\alpha$ phase) transforms progressively to the metal hydride ($\beta$ phase). Generally, the crystalline structure of the metal hydride phase is different from the solid solution.

This hydrogen metal interaction process can be expressed by the chemical equation:

$$M_{(s)} + \frac{x}{2} H_{2\,(g)} \leftrightarrow MH_{x\,(s)} \qquad \text{Equation (1.1)}$$

The interaction process between hydrogen and metal can be described by pressure-concentration-isotherms (PCI), as shown in Figure 1.5 a.

At low gas pressure, random solid solutions ($\alpha$) with hydrogen are formed, as described above, with the hydrogen concentration increasing linearly with the applied pressure. At a certain maximum hydrogen solubility, a new phase is formed, *i.e.*, the metal hydride ($\beta$) with ordered hydrogen occupation. This is evidenced in the PCI curves by the existence of a plateau at fixed pressure at a given temperature. This plateau represents the miscibility gap of the $\alpha$ and $\beta$ phases.

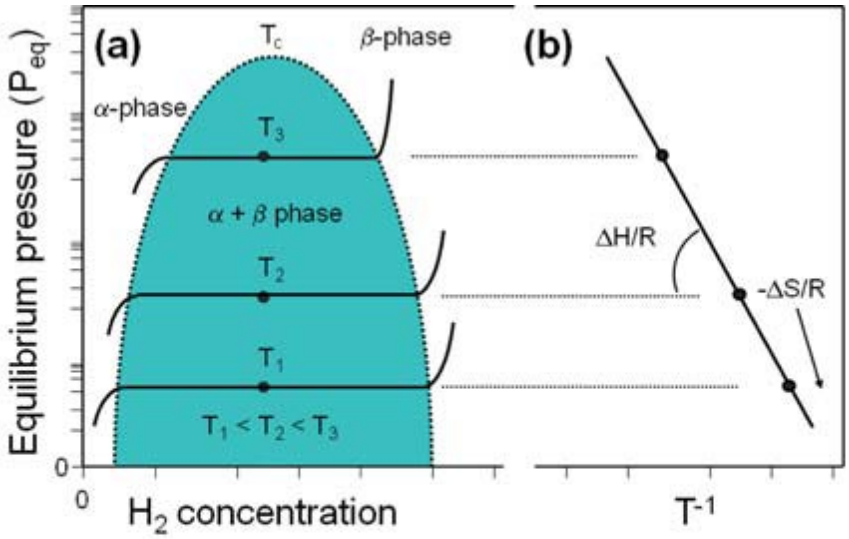


*Figure 1. 5: a) Pressure–concentration–isotherms plots and b) a van't Hoff curve (logarithm of the equilibrium or plateau pressure against the reciprocal temperature).*[24]

The increase of temperature is accompanied by the raise of plateau pressure and the reduction of the plateau width. The narrowing of the plateau width continues with the increase of temperature up to a critical temperature $T_c$, the plateau disappears totally and $\alpha$

phase converts to $\beta$ phase continuously. The relationship between plateau pressure ($P_{eq}$) and the temperature can be described by van't Hoff equation (Figure 1.5 b)

$$lnP_{eq} = \frac{\Delta H}{RT} - \frac{\Delta S}{R} \qquad \text{Equation 1.2}$$

where $\Delta H$ and $\Delta S$ are the enthalpy and entropy change for the phase transition from the $\alpha$ to the $\beta$ phase, $R$ is the ideal gas constant (8.314 $m^3 \cdot mol^{-1} \cdot K^{-1}$) and $T$ is the absolute temperature (K).

### 1.3 Hydrogen interaction with nanosized and ultradispersed metals

In heterogeneous catalysis, the design of atom-efficient catalysts, *i.e.*, with improved performance (activity, selectivity, stability) and minimized amount of rare and expensive materials, remains a major challenge.[26,27] The downscaling of metal particles to the ultra-small size range has become an important strategy for the design of new materials in this field.

As shown in Figure 1.6, the surface free energy increases with the decrease of metal particle size. The ratio of surface/volume atoms, *i.e.*, the number of low-coordinated metal atoms, which often play as active sites, increases as the metal size decreases. Therefore, downsizing of metal particle catalysts increases the atom utilization and consequently, this might boost the catalytic performance. The metal catalyst in the ideal form of a series of single and discrete atoms may maximize the atom utilization to 100% and increase the specific catalytic activity. Furthermore, size reduction also affects the electronic properties of metals. For example, a continuous energy level is characteristic of bulk metal. The decrease of metal size (<2 nm) leads to a more discrete energy level distribution and a widening of the HOMO-LUMO gap in the case of clusters of several atoms. HOMO and LUMO are types of molecular orbitals, which stand for highest occupied molecular orbital and lowest unoccupied molecular orbital, respectively. Single atoms show discrete electronic levels.

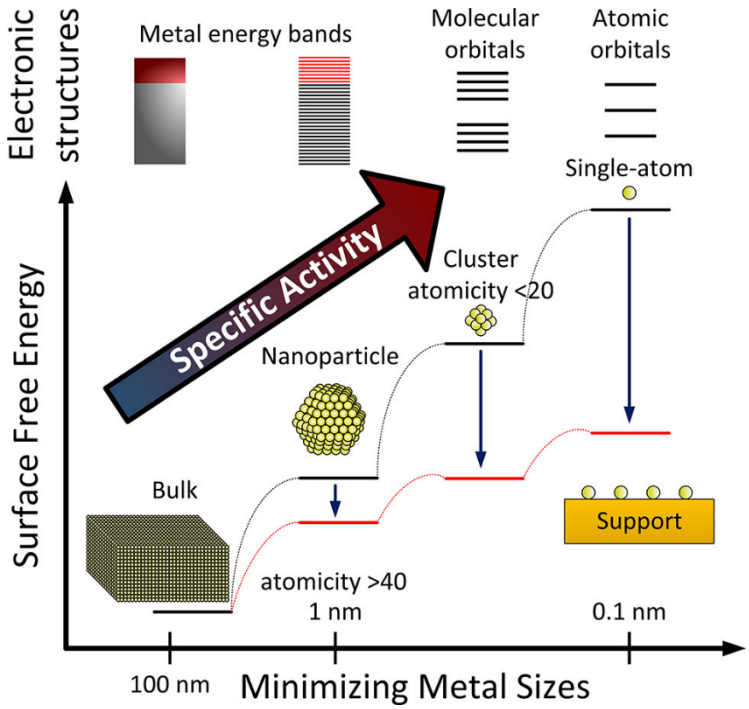


*Figure 1. 6: Illustration of the downsizing metal sizes and evolution of the geometric configuration, electronic structure and surface free energy as the size of metal particles decreases.*[28]

However, these nano- and sub-nanometric objects can easily agglomerate and create larger nanoparticles to decrease their free surface energy. Consequently, the surface area decreases, which leads to a loss of activity. Therefore, the metal catalysts are usually stabilized on support, although sintering occurs in most supported catalysts at high temperature. In the presence of supports, the catalytic selectivity, activity, and stability of nanocatalysts might be influenced by the mutual interaction between the metal and supports.

Thus, it is obvious that the most important step is the control of the catalyst size distribution and shape as well as their dispersion on the support. Subsequently, the synthetic efforts to control and stabilize both metal nanoparticles and single atoms catalysts on a support are paramount for the catalyst design and further comprehension of reactive mechanisms. These aspects will be addressed in the next paragraph.

### 1.3.1 Metal nanoparticles

#### 1.3.1.1 Synthesis of Metal nanoparticles

The synthesis of metal nanoparticles is based on two types of methods: *top-down* and *bottom-up* (Figure 1.7). The *top-down* approach refers to the breaking of a solid to smaller

particles by chemical etching, mechanical ball milling, sputtering, etc. While the *bottom-up* approach consists in the preparation of nanoparticles by assembling elementary units into larger structures. The *bottom-up* approach is widely used due to a better control of size and shape of the nanoparticles.[29] Furthermore, in order to hinder sintering, a promising strategy is the confinement of particles within a porous inert matrix such as, porous carbon materials.[30] As the synthesis of nanoparticles is well documented in literature, we will not discuss in detail all synthetic methods for nanoparticles preparation but just focus on our *bottom-up* approach.

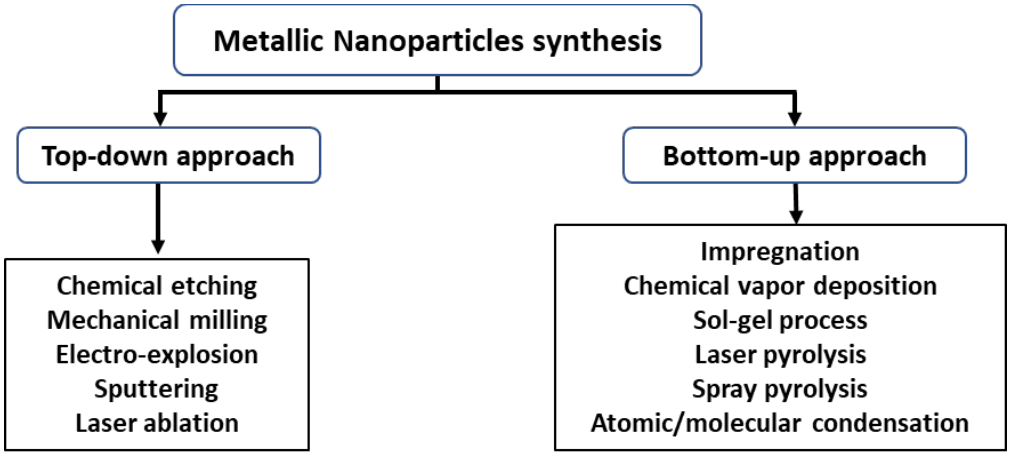


*Figure 1. 7: Different synthesis approaches available for the preparation of metal nanoparticles.*[31]

In our laboratory, the synthesis of metal nanoparticles is achieved by a liquid impregnation method (*bottom-up* approach), it consists of three steps: dispersion of the metal precursor onto porous support by liquid impregnation, the reduction of metal ions by chemical reducers (*ex*: $H_2$), the nucleation and growth of metal nanoparticles within the pores of the support. The size of the metal nanoparticles may be controlled essentially by varying the synthesis parameters: precursor type, reduction temperature and support. Normally, the metal nanoparticles size increases with the increase of reduction temperature. For example, Bastide *et al*.[32] obtained different sizes of Pd nanoparticles supported on a high surface area graphite (HSAG: 500 $m^2/g$) by varying the reduction temperature. Pd nanoparticles with average size of 2, 6 and 18 nm were obtained at reduction temperatures of 300, 500 and 800 °C, respectively. Furthermore, changing the support with different porosities and specific surface areas (SSA) is also a practical method to control the metal particle size. By using the

MIL-101(Cr) which has higher SSA (3000 $m^2/g$) as HSAG, Malouche *et al*.[33] successfully synthesized a 1 nm Pd nanoparticles at the reduction temperature 300 °C.

Once the synthesis of supported nanoparticles is controlled, the next paragraph will highlight the specific interaction between nanoparticles and hydrogen since size effects are often encountered and are known to change the physicochemical properties of metal nanoparticles. Thus, the metal-hydrogen interaction, as described in paragraph 1.2, might also be affected by nanometric size effect.

#### 1.3.1.2 Hydrogen interaction with Metal Nanoparticles

Reducing the size of metal particles to several nanometres leads to a dramatic change in the physicochemical properties. For example: the melting point of Au nanoparticles was found to be much lower than the melting point of Au bulk owing to the large surface-to-volume ratio.[34] Moreover, the thermal conductivity of silver nanoparticles was found smaller compared to metal bulk and it decreased with decreasing particle size.[35] Therefore, the nanosize effect is also expected to change the hydrogen-metal interaction properties, *e.g.*, the thermodynamics, the kinetics of reaction with hydrogen and eventually, showing trapping effects.

Pd is the only element in noble metals that absorbs hydrogen at ambient temperature and pressure forming an interstitial metallic hydride $PdH_{0.7}$. For this reason, bulk Pd is the most studied element for hydrogen storage and is one of the best understood metal-hydrogen system. Therefore, nanosized Pd has become the model material to study the nanosize effect on metal–hydrogen interaction. Thus, the Pd-H system is used to discuss the size effect in this chapiter and this is also the object of our first experimental study in **Chapter III**.

The size effect is obviously observed in the Pressure-Composition Isotherms (PCI) in Figure 1.8. Overall, the hydrogen absorption capacity diminishes with decreasing the Pd size. The hydrogen solubility and solubility limit ($\alpha_{max}$) in the $\alpha$ phase increase with decreasing the Pd size and the hydrogen solubility and solubility limit ($\beta_{min}$) in the $\beta$ phase decrease with reducing the Pd size. Consequently, the width of the plateau narrows and the critical temperature decreases with decreasing the Pd size. Furthermore, the slope of the pressure plateau becomes steeper with decreasing the particle size.

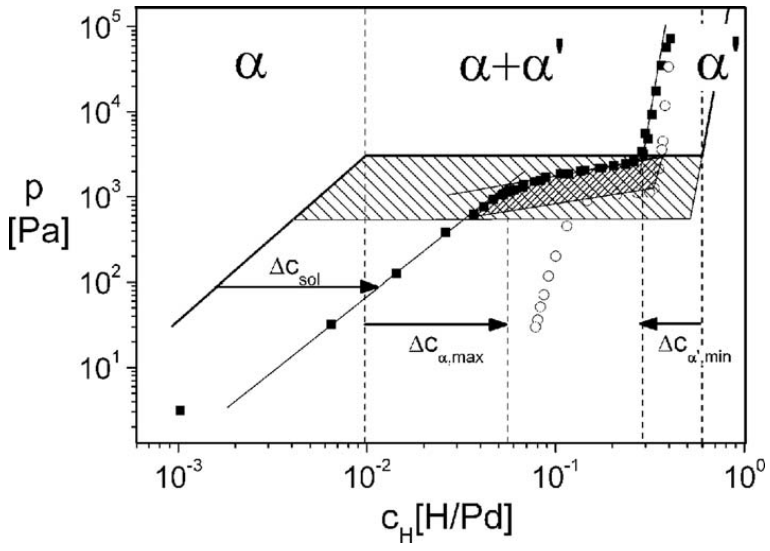


*Figure 1. 8: Pressure-composition-isotherms for Pd bulk (straight lines) and clusters (full squares indicate absorption and empty circles correspond to desorption). The $\alpha$ phase corresponds to a solid solution and the $\alpha'$ (or $\beta$) is the hydride phase.*[36]

This change of hydrogen solubility has been explained by a core/shell model: a subsurface shell in which interstitial sites are less favourable for hydrogen atoms and a bulk-like inner core that more easily absorb hydrogen to form a bulk-like hydride. Thus, the number of interstitial sites available for hydrogen and the volume that will transform into the hydride phase reduce with decreasing the size.[30] This behaviour can be also explained by the thermodynamic changes of nanosized Pd-H system. The $-\Delta H$ and $-\Delta S$ of the $\alpha \rightarrow \beta$ transition has been found to reduce with the decrease of Pd size (Figure 1.9).[37] On the other hand, the tilt of the slope makes the determination of the plateau pressure difficult and perhaps inaccurate, which could cause false diminution of the values of enthalpy and entropy change.[38] The hydrogen absorption capacity diminishes as well with the decrease in Pd particle size. This is directly related to the narrowing of the miscibility plateau of Pd nanoparticles hydrogen phase diagram.

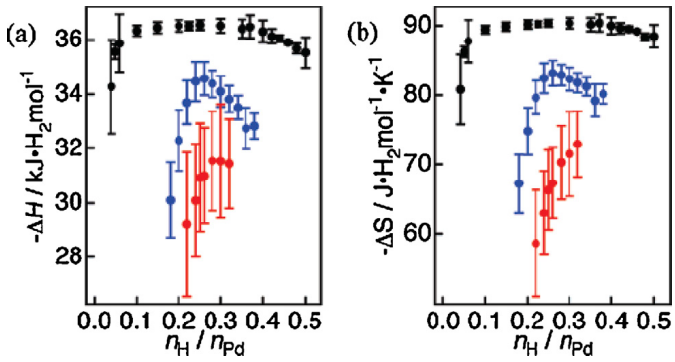


*Figure 1. 9: Hydrogen concentration dependence of a) the heat of formation ($-\Delta H$) and b) the standard entropy ($-\Delta S$) for the phase transition $\alpha \rightarrow \beta$: bulk Pd (black), 7 nm (blue) and 2.6 nm (red) Pd nanoparticles confined into PVP polymer.*[37]

Nanosize effect is also reflected on the kinetic properties during the hydriding/dehydriding process. The absorption and desorption kinetics improve due to the decrease of the hydrogen diffusion pathways and the increase of the specific surface area of metal nanoparticles. Langhammer *et al.*[39,40] demonstrated by Monte Carlo simulations that the kinetics of the formation of the hydride phase increase with the decrease of Pd size. By using an indirect nanoplasmonic sensing method, they confirmed that the absorption and desorption kinetics enhance with decreasing the Pd size for 5.35, 2.47 and 1.81 nm Pd, as shown in Figure 1.10. Furthermore, Narayan *et al.*[41] visualized the hydrogen absorption dynamics for Pd nanoparticles of different sizes by STEM-EELS techniques, the absorption kinetics were also shown to increase by decreasing the Pd size.

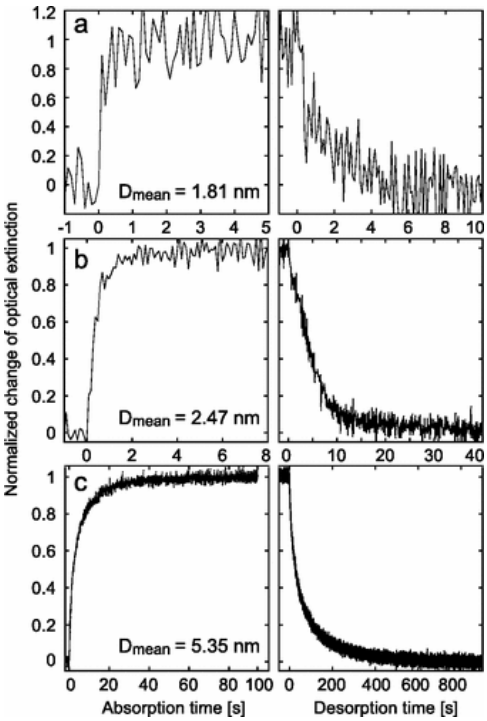


*Figure 1. 10: Experimental hydrogen absorption (left column) and desorption (right column) kinetics for three mean diameters: a) 1.81 , b) 2.47, and c) 5.35 nm of Pd nanoparticles.*[40]

It has been reported that in PCI curves at room temperature, the desorption of hydrogen is partially irreversible: the desorption is not complete for Pd nanoparticles, while it is completely reversible for Pd bulk. As shown in Figure 1.11, the PCI curve for Pd bulk is fully reversible at low pressure, nevertheless the 7.0 and 2.6 nm Pd PCI curves show incomplete recovery between the absorption and desorption branches at low pressure.[42] Kobayashi *et al.*[43] demonstrated that this irreversible part of hydrogen atoms was strongly trapped in the metal lattice of a 6.1 nm Pd nanoparticles by *in situ* XRD and solid-state $^{2}H$ NMR measurement. Using a Gibbs approach for the construction of the absorption isotherm for 3.6 nm Pd nanoparticles, Ren *et al.*[44] suggested that the responsible sites for H trapping are located within a surface shell of around 0.4 nm. Moreover, another study claims an irreversible trapping of H atoms inside 2.5 nm Pd nanoparticles and the desorption is uncomplete even at temperatures as high as 140 °C.[45]

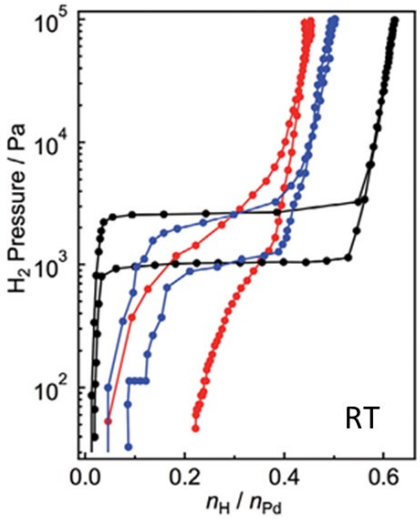


*Figure 1. 11: Pressure-Composition-Isotherms curves at room temperature for Pd bulk (black) and Pd nanoparticles of size 7.0 ± 0.4 nm (blue) and 2.6 ± 0.4 nm (red).*[42]

In addition, obvious size effects are also observed for the hydrogen desorption by Thermal-Desorption-Spectroscopy (TDS). Malouche *et al.*[33] reported remarkable difference in the TDS spectra between 1.0 nm Pd and Pd bulk (Figure 1.12 a). The hydrogen desorption from bulk Pd undergoes two main steps: first, the small hydrogen quantity soluble in the $\beta$ phase (hydride) is desorbed at low temperature followed by the desorption that accompanies the $\beta \rightarrow \alpha$ phase transition (main desorption peak) at higher temperature. The typical two-peak desorption from Pd hydride occurs at lower temperatures in 1 nm Pd than the bulk counterpart. A significant reduction of the activation energy of desorption was found for 1 nm Pd (0.27 eV) compared to Pd bulk (0.51 eV) by Kissinger plots (Figure 1.12 b). This indicates that the thermal stability of Pd hydride decreases with decreasing the Pd size.

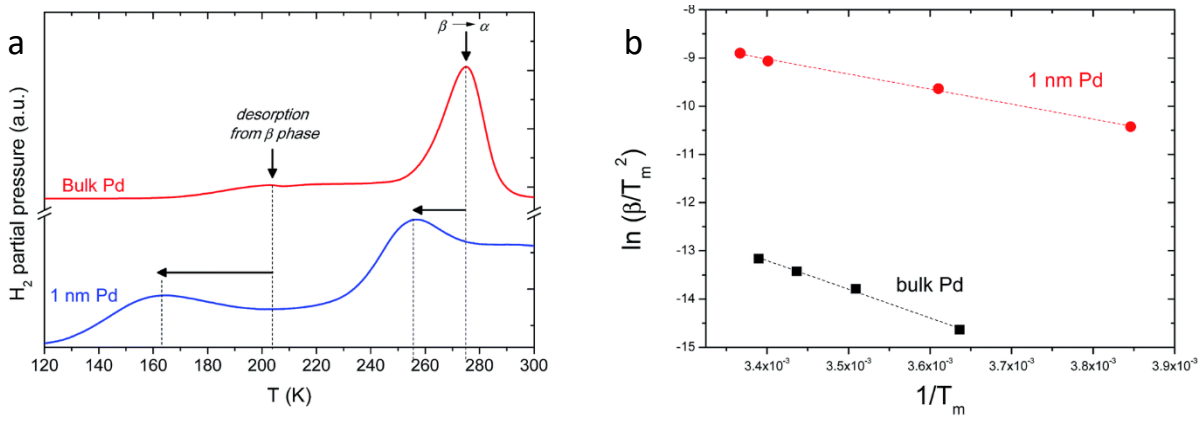


*Figure 1. 12: a)Thermo-desorption spectra of the bulk and 1 nm Pd with a heating rate of 2 K/min and b) The Kissinger plots for bulk and 1 nm Pd.*[33]

In conclusion, important changes in the thermodynamics and kinetics of reactions with hydrogen have been reported with the downsizing of Pd nanoparticles. Moreover, a hydrogen trapping effect was evidenced for hydrogen desorption in Pd nanoparticles.

### 1.3.2 Single atom catalysts (SACs)

Nanosize effects of metal-hydrogen interaction have been discussed in the previous section for metal nanoparticles (essentially for Pd nanoparticles) and compared to bulk. Consequently, one may wonder why not reducing the size of metal to an even smaller scale, *i.e.*, single atom state. Indeed, recently the single atom catalysts (SACs), defined as catalysts in which all of active metal atoms exist as isolated single atoms stabilized on a support, have been introduced and gained considerable attention due to their maximized atomic utilization and unique electronic properties.[2,46–48] Because of the changes in the active-site structure in comparison with metal nanoparticles, SACs are expected to have distinct behaviors in catalysis such as, high selectivity and stability.[49–51] Since the first practical report of SACs ($Pt/FeO_x$) by Qiao *et al.*[52] in 2011, significant progress has been made in this field.[53–56] SACs have shown superior catalytic performance (activity and/or selectivity) for several industrial relevant reactions such as, CO oxidation, MeOH oxidation, and electrochemical $CO_2$ reduction.[52,53,57]

There are different types of SACs depending on the chemical interaction between the isolated metal atom and supports, including metal surfaces,[58,59] metal oxides,[60,61] metal-organic frameworks (MOFs)[62] as well as carbon-based materials.[63,64] In this project, we will focus on the preparation SACs supported on carbon-based materials. The preparation of SACs on other supports is summarized in several recent review articles.[51,65,66]

Carbon materials are presently chosen because of their high thermal and chemical stability, in acid or basic condition, together with their high surface area, porosity and their tuneable surface chemistry. Moreover, they have high conductivity while being cost effective. For these many reasons, carbons are often use as supports in heterogenous catalysis. The preparation of single metal atom supported on carbon-based materials is remaining rather challenging due to the high surface energy of isolated metal atoms which easily causes the aggregation into clusters. Up to now, great advances have been made in overcoming these difficulties. Among them, the strategy of nitrogen (N) doping on carbon support has been particularly studied. Actually, four different kinds of nitrogen can be observed on a nitrogen-

doped carbon (Figure 1.13): pyridinic N, graphitic N, pyrrolic N or oxidized N, with increasing binding energies from 398.2, 399.4, 400.8 to 402.7 eV, respectively.[67] Pyridinic-N and pyrrolic-N are the nitrogen species at the edges or in the vacancies of the graphitic host. The pyridinic–N bonds with two C atoms and contributes one *p* electron to the $\pi$ system. Pyrrolic–N refers to N atoms incorporated in pentagonal ring and contributes two *p* electrons to the $\pi$ system. Graphitic–N refers to N atoms that substitute C atoms in the hexagonal ring.

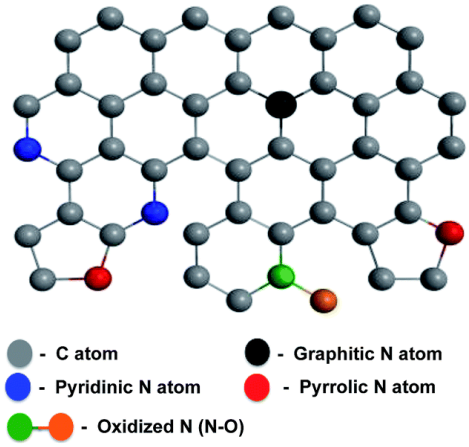


*Figure 1. 13: Schematic representation of different types of N atoms (graphitic, pyridinic, pyrrolic and oxidized N) in nitrogen-doped carbon.*[68]

If a metal is dispersed on such N doped carbon support, it is expected that there is more charge transfer between the metal atoms and the N atoms as N is more electronegative than C. Therefore, metal atoms may form stronger chemical bonds with the N-doped supports thus preventing aggregation. In fact, Yang *et al.*[69] demonstrated by DFT calculation that the adsorption energy for transition metals (Si, Ti, V, Cr Mn, Fe, Co and Ni) on nitrogen-dopped graphene was stronger than pristine graphene and the transitional metals moieties as $N_4V_2$ (N: nitrogen et V: vacancy) forming a 4-N centred structure showed the strongest binding energies (formation energy < -7 eV) (Figure 1.14). Similarly, through DFT calculation study, Cheng *et al.*[70] demonstrated that Pt single atoms form stronger bond with nitrogen-doped graphene than pristine graphene. A charge transfer (about 0.25 $e^-$) from Pt atom to the support occurs on the nitrogen-doped graphene for the single Pt atom case, while almost no charge transfer exists between the Pt atom and the pristine graphene. Moreover, nitrogen doping could cause defects, like vacancies, as well as developing edges of carbons, which provide additional anchor sites for the metal atoms.[64,71]

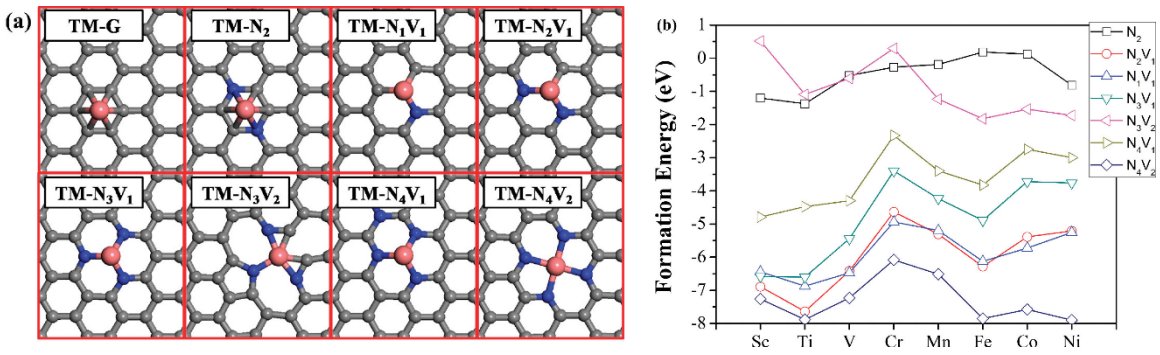


*Figure 1. 14: a) Optimized structures and b) formation energies for N-doped graphene.*[69]

SACs are interesting for catalysis for the above-mentioned reasons, but their synthesis is complex, the main challenge is to avoid agglomeration and formation of clusters/nanoparticles. These aspects will be developed in the next section.

### 1.3.2.1 Synthesis of SACs

A variety of experimental techniques have been reported in recent literature for the preparation of carbon-based SACs, such as atomic layer deposition, wet chemistry synthesis, pyrolysis of Metal-Organic Frameworks (MOFs) or organometallic complexes, as well as ball milling. Certainly, the synthesis methods discussed in this section are not exhaustive, and many reviews can be found in literature.[48,72,73]

**Atomic layer deposition**: Atomic layer deposition (ALD) is a thin film deposition technique where chemical precursors are sequentially introduced to the surface of a substrate where they chemically react directly with the surface to form sub-monolayers of film. The ALD generally consists of four steps described in Figure 1.15:

(1) Introduction of the first precursor in the reactor chamber to form a layer on the substrate,

(2) Purge of the excess first precursor and by-products,

(3) Introduction of the second precursor,

(4) Purge or evacuation of the excess second precursor and by-products.

In this technique, the key factor is the self-limiting reaction cycles, which makes it possible to precisely control the dispersion of metal atoms onto the deposited materials. For example, by controlling the ALD cycle numbers, Huang *et al.*[74] obtained Pd single atoms supported on $C_3N_4$ (0.5 wt.% Pd/$C_3N_4$) after one ALD cycle while nanoparticles of average size 6.0 nm (3.5 wt.% Pd/$C_3N_4$) were formed after ten Pd ALD cycles. Furthermore, by using

dimethyl ((3,4-η) N,N-dimethyl-3-butene-1-amine-N) platinum ($C_8H_{19}NPt$) and $O_2$ as precursors, Pt single atoms and very small Pt clusters were dispersed on the nitrogen-doped carbon cloth (NC-CC) for 10 cycles ALD, and increasing the number of ALD cycles resulted in a decrease in the fraction of single atoms and an increase of nanoparticles formation.[75] It should be noted that although ALD shows great advantages in tailoring metal particle size and metal loadings by simply varying the number of ALD cycles or other parameters (ex: deposition temperature), the high cost of this technique restricts the industrial scalability.[76]

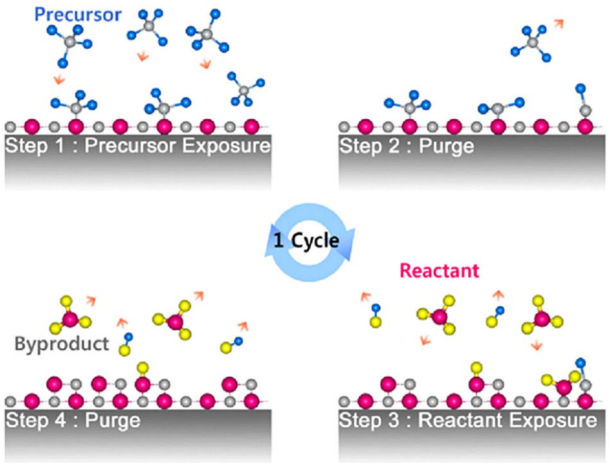


*Figure 1. 15: Schematics showing the different steps of the ALD process for SAC preparation.*[77]

**Wet chemistry synthesis**: SACs have also been prepared by wet chemistry routes. The most common method is the impregnation method, in which the metal precursors are dispersed on the carbon-based supports or incorporated during the synthesis of carbon hosts. The typical steps of the process are as follows: 1) introduction of the metal precursor on the carbon support by liquid impregnation along with a chelating agent and/or nitrogen source, 2) drying step, 3) calcination under an inert gas or $NH_3$ and /or reduction step, and 4) possibly, a post-treatment such as acid leaching to eliminate the formed metal nanoparticles. The incorporation process is a one-pot synthesis in which the metal precursor is mixed with a carbon and nitrogen source by impregnation accompanied by a calcination and/or reduction step and also a post-treatment step. It should be noted that for SACs of metal content less than 1 wt.%, adding the chelating agent is not always necessary. Hu *et al.*[78] reported that 0.18 wt.% Pd dispersed on graphitic carbon nitride was synthesized by a simple impregnation reduction approach without any chelating agent and post-treatment. However, the chelating

agent is widely used for higher loading SACs. For example, by using this impregnation method, Zhao *et al.*[79] successfully synthesized high loading single atomic metals supported on nitrogen-doped carbon material (Figure 1.16). They chose the glucose as the chelating agent which efficiently sequestered metal ions and bound to carbon support during the process. The addition of glucose was in great excess compared to the quantity of metal added. The excessive glucoses also played a role to physically isolate glucose-metal complexes. Thus, the chelating agent together with the $CN_x$ species originating from the decomposition of melamine at high temperature can prevent the coalescence of the metal atoms during the pyrolysis. Melamine is employed here as a nitrogen resource added just after the drying step and before the pyrolysis step. Besides, the choice of carbon substrate played a key factor in the synthesis. They found that O-rich surface with high surface area carbon support was necessary to achieve uniform dispersion of glucose-metal complex and physically isolate metal centres on substrate.

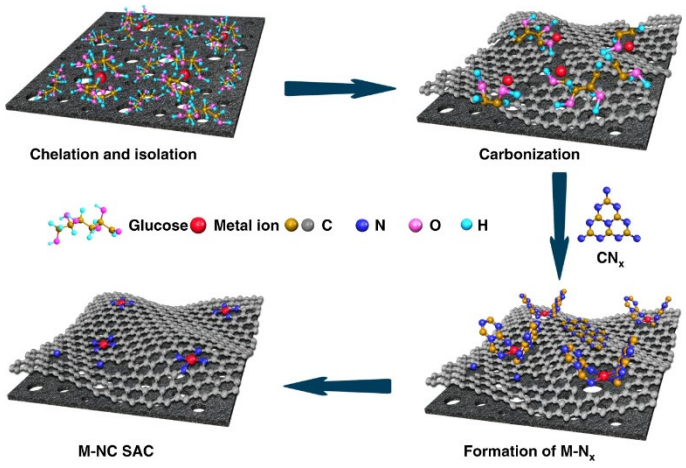


*Figure 1. 16: Synthesis of M-NC SACs dispersed on carbon based support.*[79]

On the other hand, a low loading of 0.17 wt.% Mn SACs was prepared through one pot impregnation of Mn acetate, carbon nanotube and dicyandiamide, accompanied by a calcination under $N_2$ at 600 °C and hydrochloric acid washing.[80] In addition, high loading SACs can be prepared by this method as well. For example, Liu *et al.*[81] reported that high loading of Pt (9.26 wt.%) metal single atoms were synthesized by a one-pot method by mixing metal salt solution with glucose and dicyandiamide (DICY) followed thermal pyrolysis at 900 °C under Ar atmosphere. In fact, during the pyrolysis at low temperature (550 – 750 °C), DICY was first assembled to form layered graphitic carbon nitride (g-$C_3N_4$), which can serve as a template to isolate Pt metal atoms in its frameworks at higher temperature (Figure 1.17). The

incorporation of nitrogen atoms in carbon frameworks is essential to form high loading metal SACs. Li *et al.*[82] studied the effect of pyrolysis temperature on the metal dispersion in the range of 700 – 1000 °C. They found that the overall nitrogen loading in carbon nitride decreased from 26.53 wt.% to 5.17 wt.% with increasing the pyrolysis temperature from 700 °C to 1000 °C. Consequently, the metal particles size increases with increasing the pyrolysis temperature due to the loss of nitrogen preventing them against aggregation.

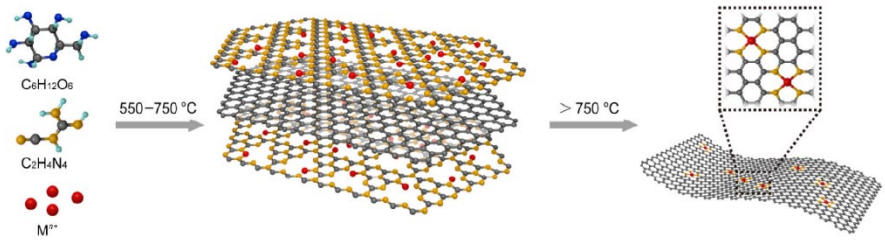


*Figure 1. 17: Synthesis of M-NC SACs via one pot synthesis.*[81]

**Pyrolysis of MOFs or organometallic complexes**: First of all, it should be noted that Metal-organic frameworks (MOFs) can be directly used as supports for the immobilisation of metal single atoms owing to well-defined porous structures, good designability and ultrahigh surface area.[83] MOFs are composed of metal-containing nodes and organic linkers, and metal ions in MOFs are typically characterized as atomically dispersed metal sites. With this characteristic, the direct pyrolysis of MOFs serves as an ideal route for preparing various metal SACs.[84] As a classical Zn-based MOF, Zeolitic Imidazolate Frameworks (ZIFs), has been widely used for preparing N-doped porous carbons owing to the high N content ligands. For example, Yin *et al.*[85] reported that a 4 wt.% Co SACs on nitrogen-doped porous carbon was prepared using a pyrolysis processes of a bimetallic Zn/Co ZIFs. Here, Zn in the ZIFs played a vital role in the formation of Co single atoms. In the first hand, Co metal atoms were more dispersed spatially with the addition of Zn atoms. Secondly, Zn species can be removed by the self-evaporation during the pyrolysis at high temperature (melting point: 419 °C; boiling point: 907 °C). Thus, free N sites can be formed, which favour the stabilization of Co single atoms. In the contrary, Co nanoparticles were formed without the protection of Zn after the pyrolysis of a pure Co-containing ZIFs, as shown in Figure 1.18. Besides, Wei *et al.*[86] reported that surprisingly Pd nanoparticles supported on ZIF-8 were transformed to thermally stable atoms via a top-down route above 900 °C in an inert atmosphere. Using density functional theory (DFT) calculation, they concluded that the formation of Pd single atoms was driven by the

formation of more thermodynamically stable $PdN_4$ structure (two pyrrolic N and two pyridinic N) as mobile Pd atoms are preferentially sequestered on defects of nitrogen-doped carbon instead of metal aggregation. Furthermore, the pyrolysis temperature plays an important role as well. Wang *et al.*[87] observed that during the pyrolysis of Co/Zn ZIFs, the coordination number of Co-N decreased from 4 to 2 with increasing the pyrolysis temperatures, the following structures $Co\text{-}N_4$, $Co\text{-}N_3$ and $Co\text{-}N_2$ were obtained at 800 °C, 900 and 1000 °C, respectively. As discussed previously, N is lost during the pyrolysis at high temperature.

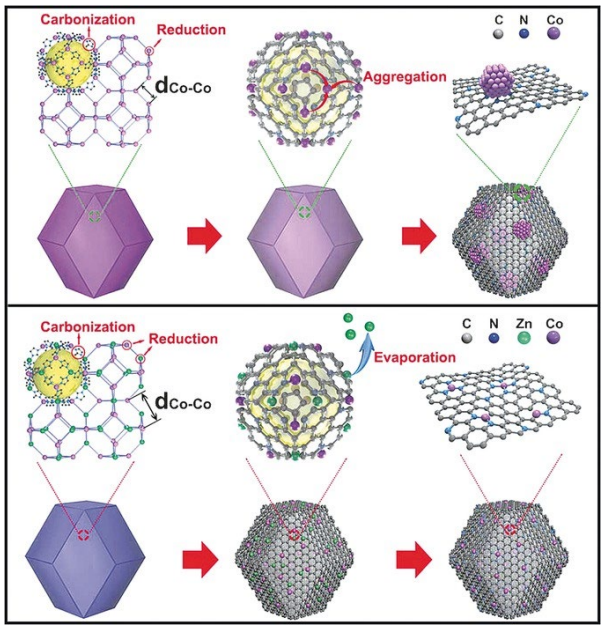


*Figure 1. 18: The formation of Co Nanoparticles/N-C (top) and Co Single-atoms/N-C (bottom).*[85]

**Ball milling approach**: SACs can be also synthesized by ball-milling approach as it is a powerful method to cut and/or reconstruct chemical bonds. It was initially developed in Bao's group as shown in Figure 1.19.[88] In fact, the graphite was first ball-milled to crush and exfoliate into graphene with some defects under Ar atmosphere. Afterwards, metal phthalocyanines (*M*Pc) were ball-milled with the obtained graphene under Ar atmosphere. The structure of *M*Pc was destroyed during the mechanical process to form $MN_4$ centres. The latter could be embedded into the graphene defects to form metal single atoms. 4 wt.% Fe single atoms on nitrogen-doped carbon was first prepared by this method. $MnN_4$, $FeN_4$, $CoN_4$, $NiN_4$ and $CuN_4$ SACs have been also successfully synthesized.[89]

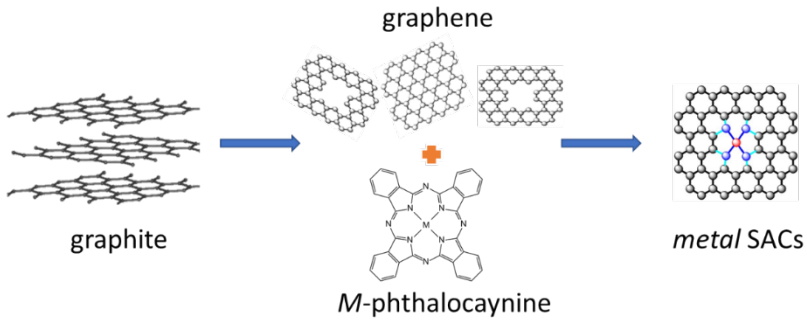


*Figure 1. 19: Scheme of a proposed mechanism for synthesis of metal SACs via ball milling method.*[88]

As discussed previously, important effects of physicochemical properties can be seen by reducing metal size into nanoscale. In comparison, the metal single atoms are expected to have "atomic size" effects on metal-hydrogen interaction properties compared to metal bulk or metal nanoparticles. The "atomic size" effects will be discussed in the next paragraph.

### 1.3.2.2 Hydrogen interaction with SACs

The downsizing of metal nanoparticles to metal single atoms causes dramatic changes in metal electronic properties and geometric structure. Consequently, the interaction between hydrogen and metals as nanoparticles and single atoms should have distinct behaviours. Unlike the hydrogen-bulk metal or hydrogen-metal nanoparticles systems, the hydrogen metal single atoms system has not been thoroughly studied so far. Szilágyi *et al.*[90] reported a Pd SACs supported on a metal-organic framework [$NH_2$-MIL-101(Cr)]. Using a combination of DFT calculations, *in-situ* Raman spectroscopy and temperature-desorption spectroscopy, Pd($H_2$) complexes (Figure 1.20) were proved to form on single Pd atoms. In addition, hydrogen was strongly bound in the Pd($H_2$) complex with an elongated H-H bond by over 15%. This elongation signified that there was an activation or destabilisation of the H–H bonds, which could have very important consequences in hydrogenation reactions.

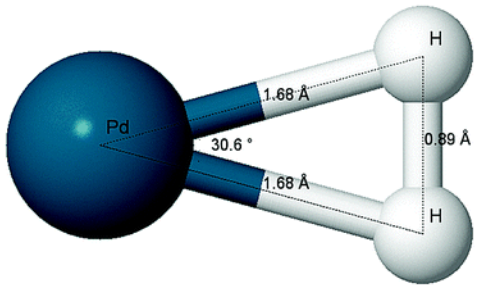


*Figure 1. 20: Structure of the Pd($H_2$) complex as calculated by DFT, indicating bond lengths and angles.*[90]

On the other hand, Hossain *et al.*[91] calculated hydrogen adsorption energy (Gibbs free energy: $\Delta G_H$) of transition metals during the reaction pathway of hydrogen evolution reaction (HER) by using a model where the transition metal coordinated with four nitrogen atoms forming strong covalent bonds are embedded on the graphene structure, as shown in Figure 1.21. They found that Ni and Pd single atoms interacted weakly with hydrogen ($\Delta G_H$ = 1.62 and 1.86 eV, respectively), while Re, Mo, Ti, W and Ta bound strongly with hydrogen as they have large negative $\Delta G_H$ (-0.92, -0.93, -0.94, -1.44 and -1.64 eV, respectively). The Co SACs which have a near zero value of $\Delta G_H$ was predicted to have high HER activity according to Sabatier principle,[92] and it has been confirmed by experimental results. Similar results were also obtained by Fung's group.[93]

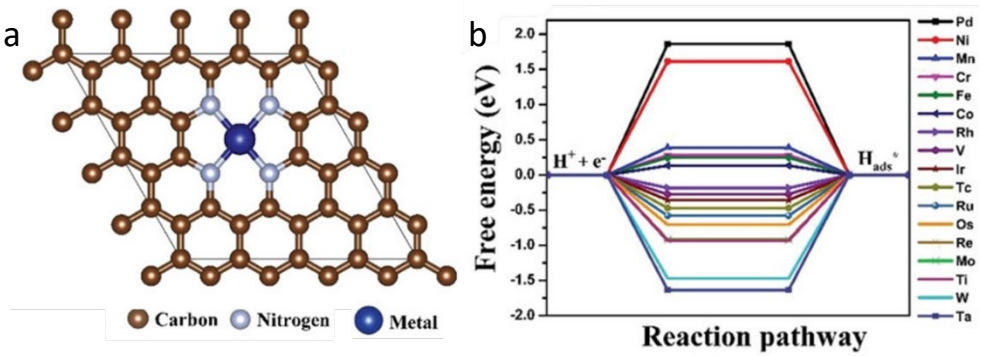


*Figure 1. 21: a) Metal coordinated with four nitrogen atoms in graphene sheet. d) Gibbs free energy ($\Delta G_H$) diagram for hydrogen adsorption reaction (Volmer reaction) toward a series of transition metals used as single atom catalysts.*[91]

### 1.4 Hydrogenation reactions with ultra-dispersed metal catalysts

As discussed previously, the hydrogenation is an important process in industries. There are many kinds of hydrogenation reactions: alkyne ($C \equiv C$), alkene ($C = C$), oxygen-

nitrogen double bond ($O = N$), carbon-nitrogen double bond ($C = N$) and carbon-oxygen double bond ($C = O$) hydrogenations are common hydrogenation reactions, for example: hydrogenation of acetylene, hydrogenation of 1-3-butadiene, hydrogenation of $CO_2$. The dominant catalysts for hydrogenation are metal nanoparticles owing to their high catalytically metal active sites originated from the high dispersion of nanoparticles on a support. However, it has been shown that the single atom catalysts are also reactive for this reaction, sometimes performing better in hydrogenation than the nanoparticles. For example, Hu *et al.*[78] synthesized a Pd SACs supported on a graphitic carbon nitride. The Pd SACs catalyst was compared with a Pd nanoparticles sample embedded on the same support for the hydrogenation of styrene to ethylbenzene (Figure 1.22 a). Pd SACs catalyst was found to attain higher TOF value of 834 $h^{-1}$ and yielded 98% conversion to ethylbenzene within 1.5h, while the TOF was 476 $h^{-1}$ for Pd nanoparticles and the conversion was less than 55% in the same conditions. Wang *et al.*[94] compared a Ru SACs on nitrogen-doped porous carbon with a Ru nanoparticles used in the hydrogenation of quinoline (Figure 1.22 b). The two catalysts showed 100% conversion of quinoline. However, the Ru SACs had a nearly 100% selectivity for the desired product to 1,2,3,4-tetrahydroquinolin (py-THQ) (2a), whereas the by-product 5,6,7,8-tetrahydroquinoline (21%) (bz-THQ, 2b) was found for Ru nanoparticles. Moreover, the Ru SACs catalyst was very stable, it did not deactivate (same activity and selectivity) after 5 cycles of reactions and its atomic dispersion remained unchanged. Shao *et al.*[95] fabricated a stable atomically dispersed Ir catalyst supported on a porous organic polymer. The Ir SACs exhibited excellent catalytic activity during the liquid phase hydrogenation of $CO_2$ to formate (Figure 1.22 c). In fact, the Ir SACs gave a turnover number (TON) as high as 6784 while the Ir nanocatalysts showed only several hundred TON value. The recycling tests indicated that there was no decrease in the catalytic activity after four uses.

a

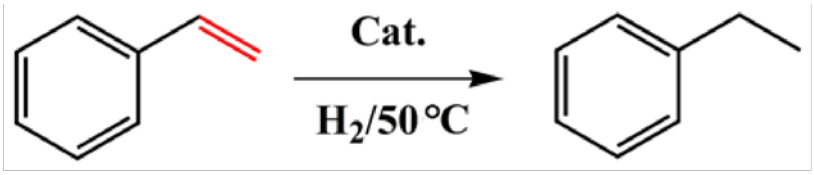


b

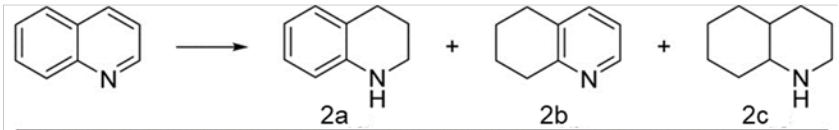


| Entry | Catalysts | Conv. (%) | Selec. (%) | | |
|---|---|---|---|---|---|
| | | | 1a | 1b | 1c |
| 1 | Ru SAs/N-C | > 99 | > 99 | < 1 | 0 |
| 2 | Ru NCs/C | > 99 | 79 | 21 | 0 |

c

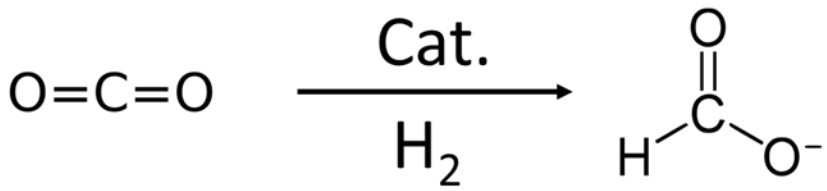


*Figure 1. 22: a) Hydrogenation of styrene,[78] b) Hydrogenation of quinoline and Catalytic performance of Ru SACs and Nanoparticles catalysts,[94] and c) Hydrogenation of $CO_2$ to formate.*

In this PhD project, different kinds of metal single atom catalysts supported on carbon-based materials were synthesized and tested in two hydrogenation reactions: gas-phase hydrogenation of butadiene and liquid-phase hydrogenation of levulinic acid. Therefore, a short overview of these reactions will be discussed briefly below.

### 1.4.1 Hydrogenation of Butadiene

Steam cracking is an industrial process that takes place at high temperature (about 800 °C) and it is used for producing light olefins including ethylene, propylene, 1-butene, butadiene, isoprene, benzene.[96] Among them, $C_4$ cuts products, 1-butene and 2-butene, are intermediates widely used in industry for the polymerization process.[96,97] However, the presence of 1-3-butadiene (0.3% to 6%) in $C_4$ species is considered as a poison which causes unwanted side reactions and deactivates the catalysts.[98] Consequently, the removal of butadiene is essential and it is normally reached by the heterogeneous catalytic hydrogenation reaction (Figure 1.23). Commonly, nanocatalysts based on Pd and Pt are widely used in the industrial process due to their high activity.[99–103] However the over-

hydrogenation to undesirable product butane remains a major issue at high butadiene conversion for these catalysts.[104]

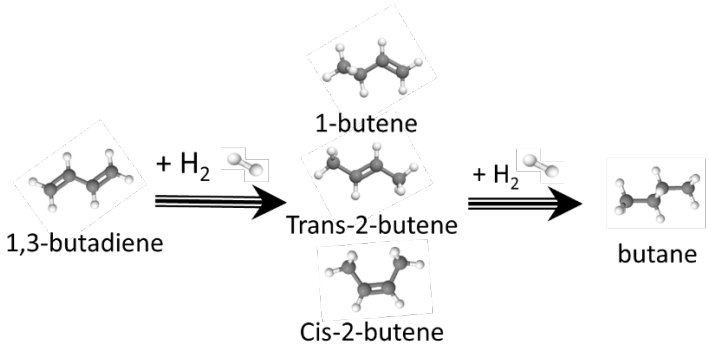


*Figure 1. 23: Schema of hydrogenation of butadiene to butenes (1-butene, Trans-2-butene and Cis-2-butene) and butane.*

Over the last few years, researchers have reported the selective hydrogenation of 1,3-butadiene with SACs which showed promising catalytic performances. For example, Lucci *et al.*[105] reported that low concentration of Pt SACs dispersed on Cu surface showed 90% selectivity to butenes at full conversion and the catalyst remained stable over 2 days at 160 °C. Through DFT study, *Lv et al.*[58] showed that Pt single atoms embedded on Cu surface [$Pt_1$/Cu(1 1 1)] had a higher selectivity toward 1-butene than high Pt content catalyst [$Pt_{4\text{-line}}$/Cu(1 1 1), *i.e.*, four Pt atoms in a linear type]. Yan *et al*.[106] compared an atomically dispersed $Pd_1$/graphene catalyst prepared by ALD method with 3 different Pd nanoparticles supported on carbon catalysts and they found that the SAC showed an excellent reactivity by remaining 100% butenes selective up to 95% conversion while the selectivity of Pd nanoparticle catalysts dropped sharply at high 1,3-butadiene conversion. Furthermore, Zhang *et al*.[107] found that very small concentration (0.08 %) of isolated $Au^{3+}$ on a $ZrO_2$ support were highly selective in the hydrogenation of 1,3-butadiene to butene isomers.

### 1.4.2 Hydrogenation of Levulinic Acid

Recognized as one of the “top 10” most promising biomass-derived platform molecules by the U.S. Department of Energy,[108] levulinic acid (LA) is used as a precursor to produce fuels, plasticizers, pharmaceuticals and other chemicals.[109] Among these products, selective hydrogenation of LA to γ-valerolactone (GVL) (Figure 1.24) has received extensive attention due to its unique properties and various applications, such as a solvent, food additives and fuels.[110,111]

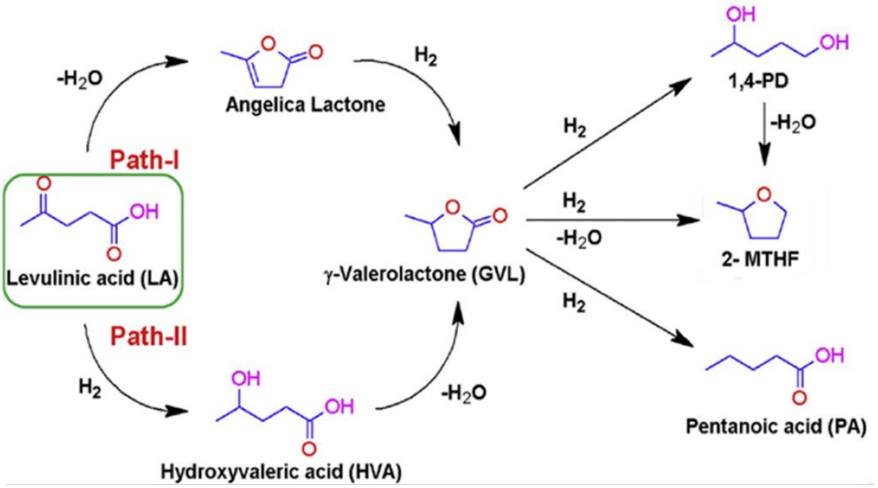


*Figure 1. 24: Hydrogenation of levulinic acid.*[112]

The hydrogenation of LA is mainly operated in liquid phase in a batch reactor system by using metal-based heterogeneous catalysts, such as Cu, Fe, Ni, Ru, Ir and Pd.[113–117] However, as the reaction medium is generally at reaction temperature between 130 and 220 °C and hydrogen up to 55 bar,[115] catalysts tend to suffer deactivation due to metal leaching and sintering. For example, Shyam *et al.*[118] reported that a significant decrease of reactivity was observed when the Cu/Ni hydrotalcite-derived catalyst was used for successive catalytic runs at 140 °C and 30 bar $H_2$ without reactivation. Furthermore, Yan *et al.*[119] reported that part of Ru was lost because of leaching during reaction process over a Ru/C catalyst at 130 °C and 12 bar $H_2$ pressure and its catalytic performance dropped after several recycle uses. Due to its high stability as compared to metal nanoparticle catalyst, single atom catalyst has been used recently in hydrogenation of LA to GVL. Cao *et al.*[120] synthesized an Ir@$ZrO_2$@C SAC which showed an excellent stability and selectivity in the hydrogenation of LA to GVL in acidic aqueous solution at 180 °C. In addition, Zhang *et al.*[121] designed a Ru/$TiO_2$@CN SAC, with 100% conversion of LA and a GVL selectivity of 100% at room temperature.

## 1.5 References


(1) Strizhak, P. E. Nanosize Effects in Heterogeneous Catalysis. *Theor Exp Chem* **2013**, *49* (1), 2–21. https://doi.org/10.1007/s11237-013-9297-7.

(2) Yang, X.-F.; Wang, A.; Qiao, B.; Li, J.; Liu, J.; Zhang, T. Single-Atom Catalysts: A New Frontier in Heterogeneous Catalysis. *Acc. Chem. Res.* **2013**, *46* (8), 1740–1748. https://doi.org/10.1021/ar300361m.

(3) Han, J.; Bian, J.; Sun, C. Recent Advances in Single-Atom Electrocatalysts for Oxygen Reduction Reaction. *Research* **2020**, *2020*. https://doi.org/10.34133/2020/9512763.

(4) Valcarcel, A.; Morfin, F.; Piccolo, L. Alkene Hydrogenation on Metal Surfaces: Why and When Are Pd Overlayers More Efficient Catalysts than Bulk Pd? *Journal of Catalysis* **2009**, *263* (2), 315–320. https://doi.org/10.1016/j.jcat.2009.02.023.

(5) Aleksandrov, H. A.; Kozlov, S. M.; Schauermann, S.; Vayssilov, G. N.; Neyman, K. M. How Absorbed Hydrogen Affects the Catalytic Activity of Transition Metals. *Angewandte Chemie International Edition* **2014**, *53* (49), 13371–13375. https://doi.org/10.1002/anie.201405738.

(6) Zlotea, C.; Cuevas, F.; Paul-Boncour, V.; Leroy, E.; Dibandjo, P.; Gadiou, R.; Vix-Guterl, C.; Latroche, M. Size-Dependent Hydrogen Sorption in Ultrasmall Pd Clusters Embedded in a Mesoporous Carbon Template. *J. Am. Chem. Soc.* **2010**, *132* (22), 7720–7729. https://doi.org/10.1021/ja101795g.

(7) Kobayashi, H.; Yamauchi, M.; Kitagawa, H. Finding Hydrogen-Storage Capability in Iridium Induced by the Nanosize Effect. *J. Am. Chem. Soc.* **2012**, *134* (16), 6893–6895. https://doi.org/10.1021/ja302021d.

(8) Morfin, F.; Blondeau, L.; Provost, K.; Malouche, A.; Piccolo, L.; Zlotea, C. Absorbed Hydrogen Enhances the Catalytic Hydrogenation Activity of Rh-Based Nanocatalysts. *Catalysis Science & Technology* **2018**, *8* (10), 2707–2715. https://doi.org/10.1039/C8CY00522B.

(9) National Renewable Energy Lab., Golden, CO (United States). *The Green Hydrogen Report. The 1995 Progress Report of the Secretary of Energy`s Hydrogen Technical Advisory Panel*; DOE/GO--10095-179, 81032; 1995; p DOE/GO--10095-179, 81032. https://doi.org/10.2172/81032.

(10) World Energy Issues Monitor | 2017: Exposing the new energy realities https://www.worldenergy.org/publications/entry/world-energy-issues-monitor-2017-exposing-the-new-energy-realities (accessed 2021 -06 -04).

(11) Staffell, I.; Scamman, D.; Abad, A. V.; Balcombe, P.; Dodds, P. E.; Ekins, P.; Shah, N.; Ward, K. R. The Role of Hydrogen and Fuel Cells in the Global Energy System. *Energy Environ. Sci.* **2019**, *12* (2), 463–491. https://doi.org/10.1039/C8EE01157E.

(12) Veldsink, J. W.; Bouma, M. J.; Schöön, N. H.; Beenackers, A. A. C. M. Heterogeneous Hydrogenation of Vegetable Oils: A Literature Review. *Catalysis Reviews* **1997**, *39* (3), 253–318. https://doi.org/10.1080/01614949709353778.

(13) Stoffels, M. A.; Klauck, F. J. R.; Hamadi, T.; Glorius, F.; Leker, J. Technology Trends of Catalysts in Hydrogenation Reactions: A Patent Landscape Analysis. *Advanced Synthesis & Catalysis* **2020**, *362* (6), 1258–1274. https://doi.org/10.1002/adsc.201901292.

(14) Pettinari, C.; Marchetti, F.; Martini, D. Metal Complexes as Hydrogenation Catalysts. In *Comprehensive Coordination Chemistry II*; McCleverty, J. A., Meyer, T. J., Eds.; Pergamon: Oxford, 2003; pp 75–139. https://doi.org/10.1016/B0-08-043748-6/09125-8.

(15) Li, J.; Stephanopoulos, M. F.; Xia, Y. Introduction: Heterogeneous Single-Atom Catalysis. *Chem. Rev.* **2020**, *120* (21), 11699–11702. https://doi.org/10.1021/acs.chemrev.0c01097.

(16) Paál, Z. Hydrogen Effects in Catalysis; Fundamentals and Practical Applications. 774.

(17) Takaya, J. Catalysis Using Transition Metal Complexes Featuring Main Group Metal and Metalloid Compounds as Supporting Ligands. *Chemical Science* **2021**, *12* (6), 1964–1981. https://doi.org/10.1039/D0SC04238B.

(18) Twilton, J.; Le, C. (Chip); Zhang, P.; Shaw, M. H.; Evans, R. W.; MacMillan, D. W. C. The Merger of Transition Metal and Photocatalysis. *Nat Rev Chem* **2017**, *1* (7), 1–19. https://doi.org/10.1038/s41570-017-0052.

(19) Trowbridge, A.; Walton, S. M.; Gaunt, M. J. New Strategies for the Transition-Metal Catalyzed Synthesis of Aliphatic Amines. *Chem. Rev.* **2020**, *120* (5), 2613–2692. https://doi.org/10.1021/acs.chemrev.9b00462.

(20) McLellan, R. B.; Harkins, C. G. Hydrogen Interactions with Metals. *Materials Science and Engineering* **1975**, *18* (1), 5–35. https://doi.org/10.1016/0025-5416(75)90069-5.

(21) Kiriyama, T.; Tanabe, T. Interaction of Hydrogen Atoms with Metals. *Journal of Nuclear Materials* **1995**, *220–222*, 873–877. https://doi.org/10.1016/0022-3115(94)00601-6.

(22) Bhatia, S. Fundamental Studies of Hydrogen Interaction with Supported Metal and Bimetallic Catalysts, 1993.

(23) Goyhenex, C.; Piccolo, L. How the Hydrogen Sorption Properties of Palladium Are Modified through Interaction with Iridium. *Phys. Chem. Chem. Phys.* **2017**, *19* (48), 32451–32458. https://doi.org/10.1039/C7CP07155H.

(24) Aguey-Zinsou, K.-F.; Ares-Fernández, J.-R. Hydrogen in Magnesium: New Perspectives toward Functional Stores. *Energy Environ. Sci.* **2010**, *3* (5), 526–543. https://doi.org/10.1039/B921645F.

(25) Li, Z.; Ji, S.; Liu, Y.; Cao, X.; Tian, S.; Chen, Y.; Niu, Z.; Li, Y. Well-Defined Materials for Heterogeneous Catalysis: From Nanoparticles to Isolated Single-Atom Sites. *Chem. Rev.* **2020**, *120* (2), 623–682. https://doi.org/10.1021/acs.chemrev.9b00311.

(26) Friend, C. M.; Xu, B. Heterogeneous Catalysis: A Central Science for a Sustainable Future. *Acc. Chem. Res.* **2017**, *50* (3), 517–521. https://doi.org/10.1021/acs.accounts.6b00510.

(27) Fonseca, J.; Lu, J. Single-Atom Catalysts Designed and Prepared by the Atomic Layer Deposition Technique. *ACS Catal.* **2021**, 7018–7059. https://doi.org/10.1021/acscatal.1c01200.

(28) *Sustainable Preparation of Metal Nanoparticles: Methods and Applications*; Luque, R., Varma, R. S., Eds.; Green Chemistry Series; Royal Society of Chemistry: Cambridge, 2012. https://doi.org/10.1039/9781849735469.

(29) Zlotea, C.; Latroche, M. Role of Nanoconfinement on Hydrogen Sorption Properties of Metal Nanoparticles Hybrids. *Colloids and Surfaces A: Physicochemical and Engineering Aspects* **2013**, *439*, 117–130. https://doi.org/10.1016/j.colsurfa.2012.11.043.

(30) Singh, J.; Dutta, T.; Kim, K.-H.; Rawat, M.; Samddar, P.; Kumar, P. 'Green' Synthesis of Metals and Their Oxide Nanoparticles: Applications for Environmental Remediation. *Journal of Nanobiotechnology* **2018**, *16* (1), 84. https://doi.org/10.1186/s12951-018-0408-4.

(31) Bastide, S.; Zlotea, C.; Laurent, M.; Latroche, M.; Cachet-Vivier, C. Direct Assessment from Cyclic Voltammetry of Size Effect on the Hydrogen Sorption Properties of Pd Nanoparticle/Carbon Hybrids. *Journal of Electroanalytical Chemistry* **2013**, *706*, 33–39. https://doi.org/10.1016/j.jelechem.2013.07.036.

(32) Malouche, A.; Blanita, G.; Lupu, D.; Bourgon, J.; Nelayah, J.; Zlotea, C. Hydrogen Absorption in 1 Nm Pd Clusters Confined in MIL-101(Cr). *Journal of Materials Chemistry A* **2017**, *5* (44), 23043–23052. https://doi.org/10.1039/C7TA07159K.

(33) Semaltianos, N. G. Nanoparticles by Laser Ablation of Bulk Target Materials in Liquids. In *Handbook of Nanoparticles*; Aliofkhazraei, M., Ed.; Springer International Publishing: Cham, 2016; pp 67–92. https://doi.org/10.1007/978-3-319-15338-4_1.

(34) Warrier, P.; Teja, A. Effect of Particle Size on the Thermal Conductivity of Nanofluids Containing Metallic Nanoparticles. *Nanoscale Res Lett* **2011**, *6* (1), 247. https://doi.org/10.1186/1556-276X-6-247.

(35) Pundt, A.; Kirchheim, R. HYDROGEN IN METALS: Microstructural Aspects. *Annu. Rev. Mater. Res.* **2006**, *36* (1), 555–608. https://doi.org/10.1146/annurev.matsci.36.090804.094451.

(36) Yamauchi, M.; Ikeda, R.; Kitagawa, H.; Takata, M. Nanosize Effects on Hydrogen Storage in Palladium. *J. Phys. Chem. C* **2008**, *112* (9), 3294–3299. https://doi.org/10.1021/jp710447j.

(37) Griessen, R.; Strohfeldt, N.; Giessen, H. Thermodynamics of the Hybrid Interaction of Hydrogen with Palladium Nanoparticles. *Nature Mater* **2016**, *15* (3), 311–317. https://doi.org/10.1038/nmat4480.

(38) Zhdanov, V. P.; Kasemo, B. Kinetics of the Formation of a New Phase in Nanoparticles. *Chemical Physics Letters* **2008**, *460* (1), 158–161. https://doi.org/10.1016/j.cplett.2008.05.067.

(39) Zhdanov, V. P.; Zorić, I.; Kasemo, B.; Langhammer, C. Size-Dependent Kinetics of Hydriding and Dehydriding of Pd Nanoparticles. *Phys. Rev. Lett.* **2010**, *104* (13), 135502. https://doi.org/10.1103/PhysRevLett.104.135502.

(40) Narayan, T. C.; Hayee, F.; Baldi, A.; Leen Koh, A.; Sinclair, R.; Dionne, J. A. Direct Visualization of Hydrogen Absorption Dynamics in Individual Palladium Nanoparticles. *Nat Commun* **2017**, *8* (1), 14020. https://doi.org/10.1038/ncomms14020.

(41) Yamauchi, M.; Kobayashi, H.; Kitagawa, H. Hydrogen Storage Mediated by Pd and Pt Nanoparticles. *ChemPhysChem* **2009**, *10* (15), 2566–2576. https://doi.org/10.1002/cphc.200900289.

(42) Kobayashi, H.; Yamauchi, M.; Kitagawa, H.; Kubota, Y.; Kato, K.; Takata, M. On the Nature of Strong Hydrogen Atom Trapping Inside Pd Nanoparticles. *J. Am. Chem. Soc.* **2008**, *130* (6), 1828–1829. https://doi.org/10.1021/ja7102372.

(43) Ren, H.; Zhang, T.-Y. H Concentrations and Stresses in Pd Nanoparticles. *Materials Letters* **2014**, *130*, 176–179. https://doi.org/10.1016/j.matlet.2014.05.104.

(44) Jose, D.; Jagirdar, B. R. Nature of Hydrogen Atom Trapped inside Palladium Lattice. *International Journal of Hydrogen Energy* **2010**, *35* (13), 6804–6811. https://doi.org/10.1016/j.ijhydene.2010.03.117.

(45) Li, X.; Yang, X.; Zhang, J.; Huang, Y.; Liu, B. In Situ/Operando Techniques for Characterization of Single-Atom Catalysts. *ACS Catal.* **2019**, *9* (3), 2521–2531. https://doi.org/10.1021/acscatal.8b04937.

(46) Liu, J. Catalysis by Supported Single Metal Atoms. *ACS Catal.* **2017**, *7* (1), 34–59. https://doi.org/10.1021/acscatal.6b01534.

(47) Rivera-Cárcamo, C.; Serp, P. Single Atom Catalysts on Carbon-Based Materials. *ChemCatChem* **2018**, *10* (22), 5058–5091. https://doi.org/10.1002/cctc.201801174.

(48) Liu, J. Single-Atom Catalysis for a Sustainable and Greener Future. *Current Opinion in Green and Sustainable Chemistry* **2020**, *22*, 54–64. https://doi.org/10.1016/j.cogsc.2020.01.004.

(49) Mitchell, S.; Vorobyeva, E.; Pérez-Ramírez, J. The Multifaceted Reactivity of Single-Atom Heterogeneous Catalysts. *Angewandte Chemie International Edition* **2018**, *57* (47), 15316–15329. https://doi.org/10.1002/anie.201806936.

(50) Cheng, N.; Zhang, L.; Doyle-Davis, K.; Sun, X. Single-Atom Catalysts: From Design to Application. *Electrochem. Energ. Rev.* **2019**, *2* (4), 539–573. https://doi.org/10.1007/s41918-019-00050-6.

(51) Qiao, B.; Wang, A.; Yang, X.; Allard, L. F.; Jiang, Z.; Cui, Y.; Liu, J.; Li, J.; Zhang, T. Single-Atom Catalysis of CO Oxidation Using $Pt_1/FeO_x$. *Nature Chemistry* **2011**, *3* (8), 634–641. https://doi.org/10.1038/nchem.1095.

(52) Yang, H. B.; Hung, S.-F.; Liu, S.; Yuan, K.; Miao, S.; Zhang, L.; Huang, X.; Wang, H.-Y.; Cai, W.; Chen, R.; Gao, J.; Yang, X.; Chen, W.; Huang, Y.; Chen, H. M.; Li, C. M.; Zhang, T.; Liu, B. Atomically Dispersed Ni(i) as the Active Site for Electrochemical CO2 Reduction. *Nat Energy* **2018**, *3* (2), 140–147. https://doi.org/10.1038/s41560-017-0078-8.

(53) Millet, M.-M.; Algara-Siller, G.; Wrabetz, S.; Mazheika, A.; Girgsdies, F.; Teschner, D.; Seitz, F.; Tarasov, A.; Levchenko, S. V.; Schlögl, R.; Frei, E. Ni Single Atom Catalysts for CO2 Activation. *J. Am. Chem. Soc.* **2019**, *141* (6), 2451–2461. https://doi.org/10.1021/jacs.8b11729.

(54) Song, P.; Luo, M.; Liu, X.; Xing, W.; Xu, W.; Jiang, Z.; Gu, L. Zn Single Atom Catalyst for Highly Efficient Oxygen Reduction Reaction. *Advanced Functional Materials* **2017**, *27* (28), 1700802. https://doi.org/10.1002/adfm.201700802.

(55) Gu, J.; Hsu, C.-S.; Bai, L.; Chen, H. M.; Hu, X. Atomically Dispersed Fe $^{3+}$ Sites Catalyze Efficient CO $_2$ Electroreduction to CO. *Science* **2019**, *364* (6445), 1091–1094. https://doi.org/10.1126/science.aaw7515.

(56) Sun, S.; Zhang, G.; Gauquelin, N.; Chen, N.; Zhou, J.; Yang, S.; Chen, W.; Meng, X.; Geng, D.; Banis, M. N.; Li, R.; Ye, S.; Knights, S.; Botton, G. A.; Sham, T.-K.; Sun, X. Single-Atom Catalysis Using Pt/Graphene Achieved through Atomic Layer Deposition. *Sci Rep* **2013**, *3* (1), 1775. https://doi.org/10.1038/srep01775.

(57) Lv, C.-Q.; Liu, J.-H.; Guo, Y.; Wang, G.-C. Selective Hydrogenation of 1,3-Butadiene over Single Pt1/Cu(1 1 1) Model Catalysts: A DFT Study. *Applied Surface Science* **2019**, *466*, 946–955. https://doi.org/10.1016/j.apsusc.2018.10.084.

(58) Hannagan, R. T.; Giannakakis, G.; Flytzani-Stephanopoulos, M.; Sykes, E. C. H. Single-Atom Alloy Catalysis. *Chem. Rev.* **2020**, *120* (21), 12044–12088. https://doi.org/10.1021/acs.chemrev.0c00078.

(59) Dessal, C.; Sangnier, A.; Chizallet, C.; Dujardin, C.; Morfin, F.; Rousset, J.-L.; Aouine, M.; Bugnet, M.; Afanasiev, P.; Piccolo, L. Atmosphere-Dependent Stability and Mobility of Catalytic Pt Single Atoms and Clusters on γ-Al2O3. *Nanoscale* **2019**, *11* (14), 6897–6904. https://doi.org/10.1039/C9NR01641D.

(60) Zhou, J.; Xu, Z.; Xu, M.; Zhou, X.; Wu, K. A Perspective on Oxide-Supported Single-Atom Catalysts. *Nanoscale Adv.* **2020**, *2* (9), 3624–3631. https://doi.org/10.1039/D0NA00393J.

(61) He, T.; Chen, S.; Ni, B.; Gong, Y.; Wu, Z.; Song, L.; Gu, L.; Hu, W.; Wang, X. Zirconium–Porphyrin-Based Metal–Organic Framework Hollow Nanotubes for Immobilization of Noble-Metal Single Atoms. *Angewandte Chemie International Edition* **2018**, *57* (13), 3493–3498. https://doi.org/10.1002/anie.201800817.

(62) Fei, H.; Dong, J.; Arellano-Jiménez, M. J.; Ye, G.; Dong Kim, N.; Samuel, E. L. G.; Peng, Z.; Zhu, Z.; Qin, F.; Bao, J.; Yacaman, M. J.; Ajayan, P. M.; Chen, D.; Tour, J. M. Atomic Cobalt

on Nitrogen-Doped Graphene for Hydrogen Generation. *Nat Commun* **2015**, *6* (1), 8668. https://doi.org/10.1038/ncomms9668.

(63) Guo, J.; Huo, J.; Liu, Y.; Wu, W.; Wang, Y.; Wu, M.; Liu, H.; Wang, G. Nitrogen-Doped Porous Carbon Supported Nonprecious Metal Single-Atom Electrocatalysts: From Synthesis to Application. *Small Methods* **2019**, 1900159. https://doi.org/10.1002/smtd.201900159.

(64) Wang, A.; Li, J.; Zhang, T. Heterogeneous Single-Atom Catalysis. *Nat Rev Chem* **2018**, *2* (6), 65–81. https://doi.org/10.1038/s41570-018-0010-1.

(65) Zang, W.; Kou, Z.; Pennycook, S. J.; Wang, J. Heterogeneous Single Atom Electrocatalysis, Where "Singles" Are "Married." *Adv. Energy Mater.* **2020**, 1903181. https://doi.org/10.1002/aenm.201903181.

(66) Zhou, N.; Wang, N.; Wu, Z.; Li, L. Probing Active Sites on Metal-Free, Nitrogen-Doped Carbons for Oxygen Electroreduction: A Review. *Catalysts* **2018**, *8* (11), 509. https://doi.org/10.3390/catal8110509.

(67) Faisal, S. N.; Haque, E.; Noorbehesht, N.; Zhang, W.; Harris, A. T.; Church, T. L.; Minett, A. I. Pyridinic and Graphitic Nitrogen-Rich Graphene for High-Performance Supercapacitors and Metal-Free Bifunctional Electrocatalysts for ORR and OER. *RSC Adv.* **2017**, *7* (29), 17950–17958. https://doi.org/10.1039/C7RA01355H.

(68) Yang, M.; Wang, L.; Li, M.; Hou, T.; Li, Y. Structural Stability and O2 Dissociation on Nitrogen-Doped Graphene with Transition Metal Atoms Embedded: A First-Principles Study. *AIP Advances* **2015**, *5* (6), 067136. https://doi.org/10.1063/1.4922841.

(69) Cheng, N.; Stambula, S.; Wang, D.; Banis, M. N.; Liu, J.; Riese, A.; Xiao, B.; Li, R.; Sham, T.-K.; Liu, L.-M.; Botton, G. A.; Sun, X. Platinum Single-Atom and Cluster Catalysis of the Hydrogen Evolution Reaction. *Nat Commun* **2016**, *7* (1), 13638. https://doi.org/10.1038/ncomms13638.

(70) Li, X.-F.; Lian, K.-Y.; Liu, L.; Wu, Y.; Qiu, Q.; Jiang, J.; Deng, M.; Luo, Y. Unraveling the Formation Mechanism of Graphitic Nitrogen-Doping in Thermally Treated Graphene with Ammonia. *Sci Rep* **2016**, *6* (1), 23495. https://doi.org/10.1038/srep23495.

(71) Wang, Y.; Mao, J.; Meng, X.; Yu, L.; Deng, D.; Bao, X. Catalysis with Two-Dimensional Materials Confining Single Atoms: Concept, Design, and Applications. *Chem. Rev.* **2019**, *119* (3), 1806–1854. https://doi.org/10.1021/acs.chemrev.8b00501.

(72) Peng, Y.; Lu, B.; Chen, S. Carbon-Supported Single Atom Catalysts for Electrochemical Energy Conversion and Storage. *Advanced Materials* **2018**, *30* (48), 1801995. https://doi.org/10.1002/adma.201801995.

(73) Huang, X.; Xia, Y.; Cao, Y.; Zheng, X.; Pan, H.; Zhu, J.; Ma, C.; Wang, H.; Li, J.; You, R.; Wei, S.; Huang, W.; Lu, J. Enhancing Both Selectivity and Coking-Resistance of a Single-Atom Pd1/C3N4 Catalyst for Acetylene Hydrogenation. *Nano Res.* **2017**, *10* (4), 1302–1312. https://doi.org/10.1007/s12274-016-1416-z.

(74) Ramesh, R.; Han, S.; Nandi, D. K.; Sawant, S. Y.; Kim, D. H.; Cheon, T.; Cho, M. H.; Harada, R.; Shigetomi, T.; Suzuki, K.; Kim, S.-H. Ultralow Loading (Single-Atom and Clusters) of the Pt Catalyst by Atomic Layer Deposition Using Dimethyl ((3,4-η) N,N-Dimethyl-3-Butene-1-Amine-N) Platinum (DDAP) on the High-Surface-Area Substrate for Hydrogen Evolution Reaction. *Advanced Materials Interfaces* **2021**, *8* (3), 2001508. https://doi.org/10.1002/admi.202001508.

(75) Rong, H.; Ji, S.; Zhang, J.; Wang, D.; Li, Y. Synthetic Strategies of Supported Atomic Clusters for Heterogeneous Catalysis. *Nat Commun* **2020**, *11* (1), 5884. https://doi.org/10.1038/s41467-020-19571-6.

(76) Kim, H.; Lee, H.-B.-R.; Maeng, W.-J. Applications of Atomic Layer Deposition to Nanofabrication and Emerging Nanodevices. *Thin Solid Films* **2009**, *517* (8), 2563–2580. https://doi.org/10.1016/j.tsf.2008.09.007.

(77) Hu, F.; Leng, L.; Zhang, M.; Chen, W.; Yu, Y.; Wang, J.; Horton, J. H.; Li, Z. Direct Synthesis of Atomically Dispersed Palladium Atoms Supported on Graphitic Carbon Nitride for Efficient Selective Hydrogenation Reactions. *ACS Appl. Mater. Interfaces* **2020**, *12* (48), 54146–54154. https://doi.org/10.1021/acsami.0c13881.

(78) Zhao, L.; Zhang, Y.; Huang, L.-B.; Liu, X.-Z.; Zhang, Q.-H.; He, C.; Wu, Z.-Y.; Zhang, L.-J.; Wu, J.; Yang, W.; Gu, L.; Hu, J.-S.; Wan, L.-J. Cascade Anchoring Strategy for General Mass Production of High-Loading Single-Atomic Metal-Nitrogen Catalysts. *Nature Communications* **2019**, *10* (1). https://doi.org/10.1038/s41467-019-09290-y.

(79) Feng, J.; Gao, H.; Zheng, L.; Chen, Z.; Zeng, S.; Jiang, C.; Dong, H.; Liu, L.; Zhang, S.; Zhang, X. A Mn-N 3 Single-Atom Catalyst Embedded in Graphitic Carbon Nitride for Efficient CO 2 Electroreduction. *Nature Communications* **2020**, *11* (1), 4341. https://doi.org/10.1038/s41467-020-18143-y.

(80) Liu, D.; Wu, C.; Chen, S.; Ding, S.; Xie, Y.; Wang, C.; Wang, T.; Haleem, Y. A.; ur Rehman, Z.; Sang, Y.; Liu, Q.; Zheng, X.; Wang, Y.; Ge, B.; Xu, H.; Song, L. In Situ Trapped High-Density Single Metal Atoms within Graphene: Iron-Containing Hybrids as Representatives for Efficient Oxygen Reduction. *Nano Res.* **2018**, *11* (4), 2217–2228. https://doi.org/10.1007/s12274-017-1840-8.

(81) Li, T.; Lin, H.; Ouyang, X.; Qiu, X.; Wan, Z. In Situ Preparation of Ru@N-Doped Carbon Catalyst for the Hydrogenolysis of Lignin To Produce Aromatic Monomers. *ACS Catal.* **2019**, 5828–5836. https://doi.org/10.1021/acscatal.9b01452.

(82) Huang, H.; Shen, K.; Chen, F.; Li, Y. Metal–Organic Frameworks as a Good Platform for the Fabrication of Single-Atom Catalysts. *ACS Catal.* **2020**, *10* (12), 6579–6586. https://doi.org/10.1021/acscatal.0c01459.

(83) Zheng, Y.; Qiao, S.-Z. Metal-Organic Framework Assisted Synthesis of Single-Atom Catalysts for Energy Applications. *National Science Review* **2018**, *5* (5), 626–627. https://doi.org/10.1093/nsr/nwy010.

(84) Yin, P.; Yao, T.; Wu, Y.; Zheng, L.; Lin, Y.; Liu, W.; Ju, H.; Zhu, J.; Hong, X.; Deng, Z.; Zhou, G.; Wei, S.; Li, Y. Single Cobalt Atoms with Precise N-Coordination as Superior Oxygen Reduction Reaction Catalysts. *Angewandte Chemie International Edition* **2016**, *55* (36), 10800–10805. https://doi.org/10.1002/anie.201604802.

(85) Wei, S.; Li, A.; Liu, J.-C.; Li, Z.; Chen, W.; Gong, Y.; Zhang, Q.; Cheong, W.-C.; Wang, Y.; Zheng, L.; Xiao, H.; Chen, C.; Wang, D.; Peng, Q.; Gu, L.; Han, X.; Li, J.; Li, Y. Direct Observation of Noble Metal Nanoparticles Transforming to Thermally Stable Single Atoms. *Nature Nanotech* **2018**, *13* (9), 856–861. https://doi.org/10.1038/s41565-018-0197-9.

(86) Wang, X.; Chen, Z.; Zhao, X.; Yao, T.; Chen, W.; You, R.; Zhao, C.; Wu, G.; Wang, J.; Huang, W.; Yang, J.; Hong, X.; Wei, S.; Wu, Y.; Li, Y. Regulation of Coordination Number over Single Co Sites: Triggering the Efficient Electroreduction of CO2. *Angewandte Chemie International Edition* **2018**, *57* (7), 1944–1948. https://doi.org/10.1002/anie.201712451.

(87) Deng, D.; Chen, X.; Yu, L.; Wu, X.; Liu, Q.; Liu, Y.; Yang, H.; Tian, H.; Hu, Y.; Du, P.; Si, R.; Wang, J.; Cui, X.; Li, H.; Xiao, J.; Xu, T.; Deng, J.; Yang, F.; Duchesne, P. N.; Zhang, P.; Zhou, J.; Sun, L.; Li, J.; Pan, X.; Bao, X. A Single Iron Site Confined in a Graphene Matrix for the Catalytic Oxidation of Benzene at Room Temperature. *Sci Adv* **2015**, *1* (11), e1500462. https://doi.org/10.1126/sciadv.1500462.

(88) Cui, X.; Xiao, J.; Wu, Y.; Du, P.; Si, R.; Yang, H.; Tian, H.; Li, J.; Zhang, W.-H.; Deng, D.; Bao, X. A Graphene Composite Material with Single Cobalt Active Sites: A Highly Efficient Counter Electrode for Dye-Sensitized Solar Cells. *Angewandte Chemie International Edition* **2016**, *55* (23), 6708–6712. https://doi.org/10.1002/anie.201602097.

(89) Szilágyi, P. Á.; Rogers, D. M.; Zaiser, I.; Callini, E.; Turner, S.; Borgschulte, A.; Züttel, A.; Geerlings, H.; Hirscher, M.; Dam, B. Functionalised Metal–Organic Frameworks: A Novel Approach to Stabilising Single Metal Atoms. *J. Mater. Chem. A* **2017**, *5* (30), 15559–15566. https://doi.org/10.1039/C7TA03134C.

(90) Hossain, M. D.; Liu, Z.; Zhuang, M.; Yan, X.; Xu, G.-L.; Gadre, C. A.; Tyagi, A.; Abidi, I. H.; Sun, C.-J.; Wong, H.; Guda, A.; Hao, Y.; Pan, X.; Amine, K.; Luo, Z. Rational Design of Graphene-Supported Single Atom Catalysts for Hydrogen Evolution Reaction. *Advanced Energy Materials* **2019**, *9* (10), 1803689. https://doi.org/10.1002/aenm.201803689.

(91) Medford, A. J.; Vojvodic, A.; Hummelshøj, J. S.; Voss, J.; Abild-Pedersen, F.; Studt, F.; Bligaard, T.; Nilsson, A.; Nørskov, J. K. From the Sabatier Principle to a Predictive Theory of Transition-Metal Heterogeneous Catalysis. *Journal of Catalysis* **2015**, *328*, 36–42. https://doi.org/10.1016/j.jcat.2014.12.033.

(92) Fung, V.; Hu, G.; Wu, Z.; Jiang, D. Descriptors for Hydrogen Evolution on Single Atom Catalysts in Nitrogen-Doped Graphene. *J. Phys. Chem. C* **2020**, *124* (36), 19571–19578. https://doi.org/10.1021/acs.jpcc.0c04432.

(93) Wang, X.; Chen, W.; Zhang, L.; Yao, T.; Liu, W.; Lin, Y.; Ju, H.; Dong, J.; Zheng, L.; Yan, W.; Zheng, X.; Li, Z.; Wang, X.; Yang, J.; He, D.; Wang, Y.; Deng, Z.; Wu, Y.; Li, Y. Uncoordinated Amine Groups of Metal–Organic Frameworks to Anchor Single Ru Sites as Chemoselective Catalysts toward the Hydrogenation of Quinoline. *J. Am. Chem. Soc.* **2017**, *139* (28), 9419–9422. https://doi.org/10.1021/jacs.7b01686.

(94) Shao, X.; Yang, X.; Xu, J.; Liu, S.; Miao, S.; Liu, X.; Su, X.; Duan, H.; Huang, Y.; Zhang, T. Iridium Single-Atom Catalyst Performing a Quasi-Homogeneous Hydrogenation Transformation of CO2 to Formate. *Chem* **2019**, *5* (3), 693–705. https://doi.org/10.1016/j.chempr.2018.12.014.

(95) Derrien, M. L. Chapter 18 Selective Hydrogenation Applied to the Refining of Petrochemical Raw Materials Produced by Steam Cracking. In *Studies in Surface Science and Catalysis*; Cerveny, L., Ed.; Catalytic Hydrogenation; Elsevier, 1986; Vol. 27, pp 613–666. https://doi.org/10.1016/S0167-2991(08)65364-1.

(96) Yang, Q.; Qiu, R.; Ma, X.; Hou, R.; Sun, K. Surface Reconstruction and the Effect of Ni-Modification on the Selective Hydrogenation of 1,3-Butadiene over Mo $_2$ C-Based Catalysts. *Catal. Sci. Technol.* **2020**, *10* (11), 3670–3680. https://doi.org/10.1039/D0CY00402B.

(97) Méndez, F. J.; Piccolo, L.; Solano, R.; Aouine, M.; Villasana, Y.; Guerra, J.; Curbelo, S.; Olivera-Fuentes, C.; Brito, J. L. Promoting Effect of Ceria on the Performance of NiPd/CeO $_2$ –Al $_2$ O $_3$ Catalysts for the Selective Hydrogenation of 1,3-Butadiene in the Presence of 1-Butene. *New J. Chem.* **2018**, *42* (13), 11165–11173. https://doi.org/10.1039/C7NJ04558A.

(98) Ouchaib, T.; Massardier, J.; Renouprez, A. Competitive Hydrogenation of Butadiene and Butene on Palladium and Platinum Catalysts. *Journal of Catalysis* **1989**, *119* (2), 517–520. https://doi.org/10.1016/0021-9517(89)90180-2.

(99) Furlong, B. K.; Hightower, J. W.; Chan, T. Y.-L.; Sarkany, A.; Guczi, L. 1,3-Butadiene Selective Hydrogenation over Pd/Alumina and CuPd/Alumina Catalysts. *Applied Catalysis A: General* **1994**, *117* (1), 41–51. https://doi.org/10.1016/0926-860X(94)80157-6.

(100) Sarkany, A.; Zsoldos, Z.; Stefler, G.; Hightower, J. W.; Guczi, L. Promoter Effect of Pd in Hydrogenation of 1,3-Butadiene over Co-Pd Catalysts. *Journal of Catalysis* **1995**, *157* (1), 179–189. https://doi.org/10.1006/jcat.1995.1278.

(101) Goetz, J.; Volpe, M. A.; Gigola, C. E.; Touroude, R. Low-Loaded Pd–Pb/α-Al2O3 Catalysts: Effect of Alloying in the Hydrogenation of Buta-1,3-Diene and Hydrogenation and Isomerization of Butenes. *Journal of Catalysis* **2001**, *199* (2), 338–345. https://doi.org/10.1006/jcat.2001.3171.

(102) Molnár, Á.; Sárkány, A.; Varga, M. Hydrogenation of Carbon–Carbon Multiple Bonds: Chemo-, Regio- and Stereo-Selectivity. *Journal of Molecular Catalysis A: Chemical* **2001**, *173* (1), 185–221. https://doi.org/10.1016/S1381-1169(01)00150-9.

(103) Wang, Z. Selective Hydrogenation of Butadiene over Non-Noble Bimetallic Catalysts.

(104) Lucci, F. R.; Liu, J.; Marcinkowski, M. D.; Yang, M.; Allard, L. F.; Flytzani-Stephanopoulos, M.; Sykes, E. C. H. Selective Hydrogenation of 1,3-Butadiene on Platinum–Copper Alloys at the Single-Atom Limit. *Nature Communications* **2015**, *6* (1), 8550. https://doi.org/10.1038/ncomms9550.

(105) Yan, H.; Cheng, H.; Yi, H.; Lin, Y.; Yao, T.; Wang, C.; Li, J.; Wei, S.; Lu, J. Single-Atom Pd $_1$ /Graphene Catalyst Achieved by Atomic Layer Deposition: Remarkable Performance in Selective Hydrogenation of 1,3-Butadiene. *J. Am. Chem. Soc.* **2015**, *137* (33), 10484–10487. https://doi.org/10.1021/jacs.5b06485.

(106) Zhang, X.; Shi, H.; Xu, B.-Q. Catalysis by Gold: Isolated Surface Au3+ Ions Are Active Sites for Selective Hydrogenation of 1,3-Butadiene over Au/ZrO2 Catalysts. *Angew. Chem. Int. Ed.* **2005**, *44* (43), 7132–7135. https://doi.org/10.1002/anie.200502101.

(107) Bozell, J. J.; Petersen, G. R. Technology Development for the Production of Biobased Products from Biorefinery Carbohydrates—the US Department of Energy's "Top 10" Revisited. **2010**, 17.

(108) Hayes, G. C.; Becer, C. R. Levulinic Acid: A Sustainable Platform Chemical for Novel Polymer Architectures. *Polym. Chem.* **2020**, *11* (25), 4068–4077. https://doi.org/10.1039/D0PY00705F.

(109) Alonso, D. M.; Wettstein, S. G.; Dumesic, J. A. Gamma-Valerolactone, a Sustainable Platform Molecule Derived from Lignocellulosic Biomass. *Green Chem.* **2013**, *15* (3), 584–595. https://doi.org/10.1039/C3GC37065H.

(110) Heeres, H.; Handana, R.; Chunai, D.; Rasrendra, C. B.; Girisuta, B.; Heeres, H. J. Combined Dehydration/(Transfer)-Hydrogenation of C6-Sugars (D-Glucose and D-Fructose) to γ-Valerolactone Using Ruthenium Catalysts. *Green Chem.* **2009**, *11* (8), 1247–1255. https://doi.org/10.1039/B904693C.

(111) Kumaravel, S.; Thiripuranthagan, S.; Erusappan, E.; Durai, M.; Vembuli, T.; Durai, M. Catalytic Conversion of Levulinic Acid under Noncorrosive Conditions Using Ru/Zr/Al-SBA-15 Catalysts. *Microporous and Mesoporous Materials* **2020**, *305*, 110298. https://doi.org/10.1016/j.micromeso.2020.110298.

(112) Yan, K.; Liao, J.; Wu, X.; Xie, X. A Noble-Metal Free Cu-Catalyst Derived from Hydrotalcite for Highly Efficient Hydrogenation of Biomass-Derived Furfural and Levulinic Acid. *RSC Adv.* **2013**, *3* (12), 3853–3856. https://doi.org/10.1039/C3RA22158J.

(113) Upare, P. P.; Lee, J.-M.; Hwang, D. W.; Halligudi, S. B.; Hwang, Y. K.; Chang, J.-S. Selective Hydrogenation of Levulinic Acid to γ-Valerolactone over Carbon-Supported Noble Metal Catalysts. *Journal of Industrial and Engineering Chemistry* **2011**, *17* (2), 287–292. https://doi.org/10.1016/j.jiec.2011.02.025.

(114) Hengst, K.; Schubert, M.; Carvalho, H. W. P.; Lu, C.; Kleist, W.; Grunwaldt, J.-D. Synthesis of γ-Valerolactone by Hydrogenation of Levulinic Acid over Supported Nickel Catalysts. *Applied Catalysis A: General* **2015**, *502*, 18–26. https://doi.org/10.1016/j.apcata.2015.05.007.

(115) Galletti, A. M. R.; Antonetti, C.; Luise, V. D.; Martinelli, M. A Sustainable Process for the Production of γ-Valerolactone by Hydrogenation of Biomass-Derived Levulinic Acid. *Green Chem.* **2012**, *14* (3), 688–694. https://doi.org/10.1039/C2GC15872H.

(116) Luo, W.; Sankar, M.; Beale, A. M.; He, Q.; Kiely, C. J.; Bruijnincx, P. C. A.; Weckhuysen, B. M. High Performing and Stable Supported Nano-Alloys for the Catalytic Hydrogenation of Levulinic Acid to g-Valerolactone. *NATURE COMMUNICATIONS* **2015**, 10.

(117) Gupta, S. S. R.; Kantam, M. L. Selective Hydrogenation of Levulinic Acid into γ-Valerolactone over Cu/Ni Hydrotalcite-Derived Catalyst. *Catalysis Today* **2018**, *309*, 189–194. https://doi.org/10.1016/j.cattod.2017.08.007.

(118) Yan, Z.; Lin, L.; Liu, S. Synthesis of γ-Valerolactone by Hydrogenation of Biomass-Derived Levulinic Acid over Ru/C Catalyst. *Energy Fuels* **2009**, *23* (8), 3853–3858. https://doi.org/10.1021/ef900259h.

(119) Cao, W.; Lin, L.; Qi, H.; He, Q.; Wu, Z.; Wang, A.; Luo, W.; Zhang, T. In-Situ Synthesis of Single-Atom Ir by Utilizing Metal-Organic Frameworks: An Acid-Resistant Catalyst for Hydrogenation of Levulinic Acid to γ-Valerolactone. *Journal of Catalysis* **2019**, *373*, 161–172. https://doi.org/10.1016/j.jcat.2019.03.035.

(120) Zhang, K.; Meng, Q.; Wu, H.; Yuan, T.; Han, S.; Zhai, J.; Zheng, B.; Xu, C.; Wu, W.; He, M.; Han, B. Levulinic Acid Hydrogenation to γ-Valerolactone over Single Ru Atoms on a TiO2@nitrogen Doped Carbon Support. *Green Chem.* **2021**, *23* (4), 1621–1627. https://doi.org/10.1039/D0GC04108D.

# CHAPTER II: MATERIALS AND METHODS

## 2.1 Synthesis

### 2.1.1 Materials

The purpose of this project is to synthesize ultra-dispersed metals in the forms of nanoparticles and single atoms supported on porous carbon hosts. Two types of commercial carbons have been used: a High Surface Area Graphite (HSAG with specific surface area of 500 $m^2/g$) from Imerys & Carbon and an Activated Carbon (AC with specific surface area of 1400 $m^2/g$) from STREM Chemicals. The AC was washed with 2 mol/L $HNO_3$ during 24 h for the purpose of eliminating the impurities in the material and increasing the hydrophilicity of the AC. Afterwards, the AC was filtered and washed with distilled water until neutral pH was reached. In the end, the treated AC was dried at 120 °C for 24 hours to remove water. The treated AC instead of the initial AC was subsequently used in the synthesis of materials.

The other chemical products used for the preparation of ultra-dispersed metals on porous carbons are listed below:

Palladium chloride ($PdCl_2$, 99.9%), copper nitrate hydrate ($Cu(NO_3)_2{\cdot}3H_2O$, > 98.0%), rhodium chloride hydrate ($RhCl_3{\cdot}xH_2O$, 99.99%), platinum chloride ($PtCl_4$, > 99.99%), and iridium chloride hydrate ($IrCl_3{\cdot}xH_2O$, 99.8%) were bought from Alfa Aesar. Nickel nitrate hexahydrate ($Ni(NO_3)_2{\cdot}6H_2O$, 99.99%), sodium molybdate dihydrate ($Na_2MoO_4{\cdot}2H_2O$, > 99%), ethylenediaminetetraacetic acid (EDTA, $[CH_2N(CH_2CO_2H)_2]_2$, > 99.0%), and melamine ($C_3H_6N_6$, 99%) were obtained from Sigma-Aldrich. Cobalt nitrate hexahydrate ($Co(NO_3)_2{\cdot}6H_2O$), ammonia solution ($NH_3{\cdot}H_2O$, 28%), concentrated nitric acid ($HNO_3$, 65%), concentrated chlorohydric acid (HCl, 37%) were purchased from VWR Chemicals. The deionized water used in all experiments was obtained through ion-exchange and filtration. All the chemicals were analytical grade and used without further purification.

### 2.1.2 Metal nanoparticles supported on carbon materials

The metal nanoparticles have been synthesized with a simple liquid-phase impregnation method adapted from a previous method.[1] First, the porous carbon host was mixed with metal precursor solution in 10 mL aqueous solution under continuous magnetic stirring in a beaker. The solution was stirred (500 rpm) at room temperature for 2 h to completely disperse the carbon support and the metal precursor. Afterwards, the solution was dried under stirring at 60 °C until the total evaporation of water (about 3 h). Subsequently,

the recovered powder was dried at 70 °C overnight. The dried solid was finally reduced under 5% $H_2$/Ar flow (500 mL/min) at high temperature (300 - 800 °C) with a ramp of 10 °C/min. The metal nanoparticles supported on carbon were obtained after the reduction step. The schematic description of synthesis is shown in Figure 2.1.

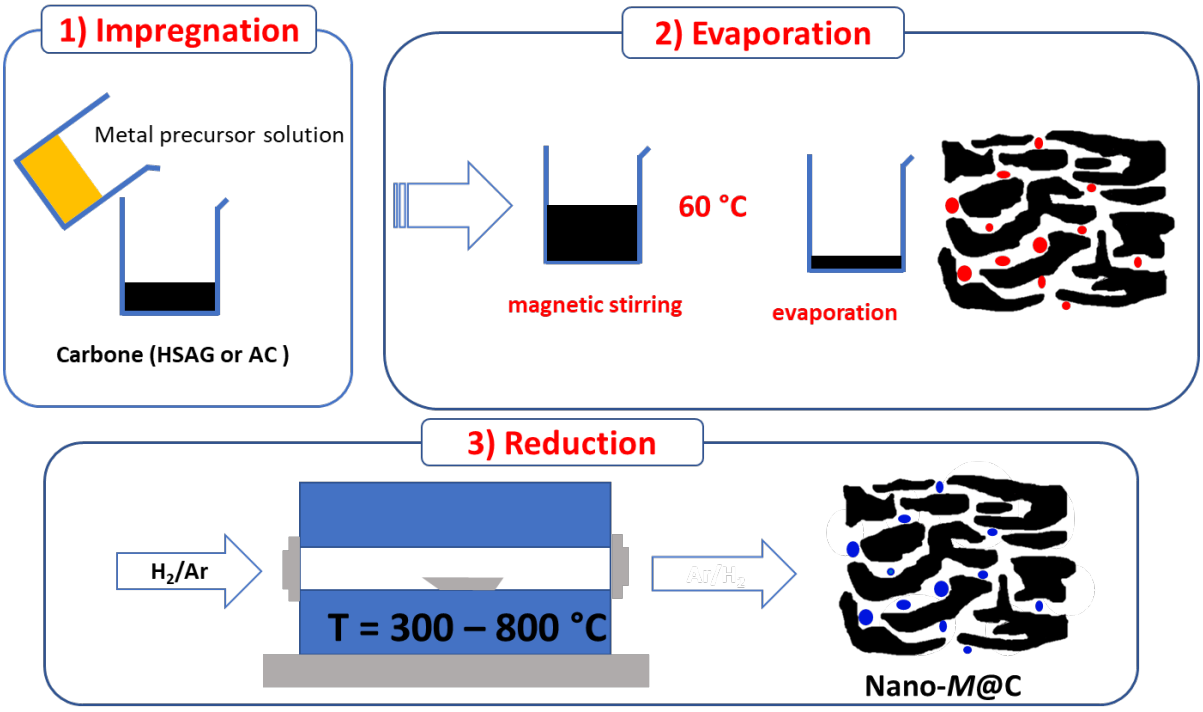


*Figure 2. 1: Schematic illustration of the synthesis of metal nanoparticles supported on porous carbon materials.*

The metal precursor solution was prepared by dissolving the metal salt in distilled water with the final concentration 0.1 mol/L with one exception for palladium precursor solution that was obtained by dissolving the $PdCl_2$ in 10% HCl solution with the final concentration 0.1 mol/L $PdCl_2$.

The metal nanoparticles were supported on two different carbon materials (HSAG and AC) to tune the metal nanoparticles size distribution.

As the reactivity of metal precursors is different, the reduction conditions, temperature and time, have to be adapted for each metal precursor. For Pd samples, two reduction temperatures (300 or 500 °C) were used to control the nanoparticles size. The metal content over the entire sample mass was between 1 and 10 wt.% for different metals. The samples are named *x-M@Y-z*, where *x* ( wt.%) is the metal content over the entire sample mass, *M* is the metal, *Y* (HSAG or AC) stands for the carbon support and *z* (300 - 800 °C)

represents the reduction temperature. High loading (10 wt.%) Pd nanoparticles supported on carbon hosts were synthesized for the study of the interaction between Pd and hydrogen while low metal loadings (1 - 4 wt.%) were used as catalysts in hydrogenation of butadiene. More detail of synthesis information is assembled in table 2.1.

| sample | Metal precursor | Metal content (wt.%) | Carbon support | Reduction temperature (°C) | Reduction time (min) | Utilization |
|---|---|---|---|---|---|---|
| 10-Pd@HSAG-300 | $PdCl_2$ | 10 | HSAG | 300 | 15 | Hydrogen interaction |
| 10-Pd@HSAG-500 | $PdCl_2$ | 10 | HSAG | 500 | 15 | |
| 10-Pd@AC-300 | $PdCl_2$ | 10 | AC | 300 | 15 | |
| 2-Co@AC-400 | $Co(NO_3)_2{\cdot}6H_2O$ | 2 | AC | 400 | 120 | Hydrogenation of butadiene |
| 2-Ni@AC-400 | $Ni(NO_3)_2{\cdot}6H_2O$ | 2 | AC | 400 | 120 | |
| 2-Cu@AC-250 | $Cu(NO_3)_2{\cdot}3H_2O$ | 2 | AC | 250 | 60 | |
| 2-Mo@AC-800 | $Na_2MoO_4{\cdot}2H_2O$ | 2 | AC | 800 | 60 | |
| 1-Pd@AC-300 | $PdCl_2$ | 1 | AC | 300 | 15 | |
| 3.7-Ir@AC-700 | $IrCl_3{\cdot}xH_2O$ | 3.7 | AC | 700 | 120 | |
| 1-Pt@AC-300 | $PtCl_4$ | 1 | AC | 300 | 60 | |

*Table 2. 1: List of metal nanoparticle samples, synthesis details and utilization.*

### 2.1.3 Metal single atom catalysts supported on carbon materials

The synthesis of metal single atom catalysts supported on carbon materials consists of 4 main steps as described in Figure 2.2. The sample 1 wt.% Ir SAC supported on AC was taken as an example:

(1) **Impregnation**: 200 mg of EDTA (ethylenediaminetetraacetic acid) was dispersed in 10 ml distilled water in a beaker under vigorous stirring, several drops of $NH_3{\cdot}H_2O$ were added to the solution to completely dissolve the EDTA. 3.8 mg of metal salt $IrCl_3{\cdot}xH_2O$ was then added to the solution. After the total dissolution of metal salt and the formation of a stable complex (the solution color is stable after about 6 h), 100 mg of the carbon host (AC or HSAG) was added.

(2) **Evaporation**: The solution was stirred (500 rpm) at room temperature for 2 h to completely disperse the carbon support and the metal complex. Afterwards, the solution was drying under stirring at 60 °C until the total evaporation of water (about 3 h). The recovered powder was dried at 70 °C in an oven overnight.

(3) **Grinding**: The dried solid was mixed with 500 mg of melamine and hand milled during 15 min.

(4) **Calcination**: The mixture was calcined at 800 °C under Ar flow (200 mL/min) for 2 h with a ramp of 3 °C/min. The 1 wt.% Ir SAC sample was obtained after calcination.

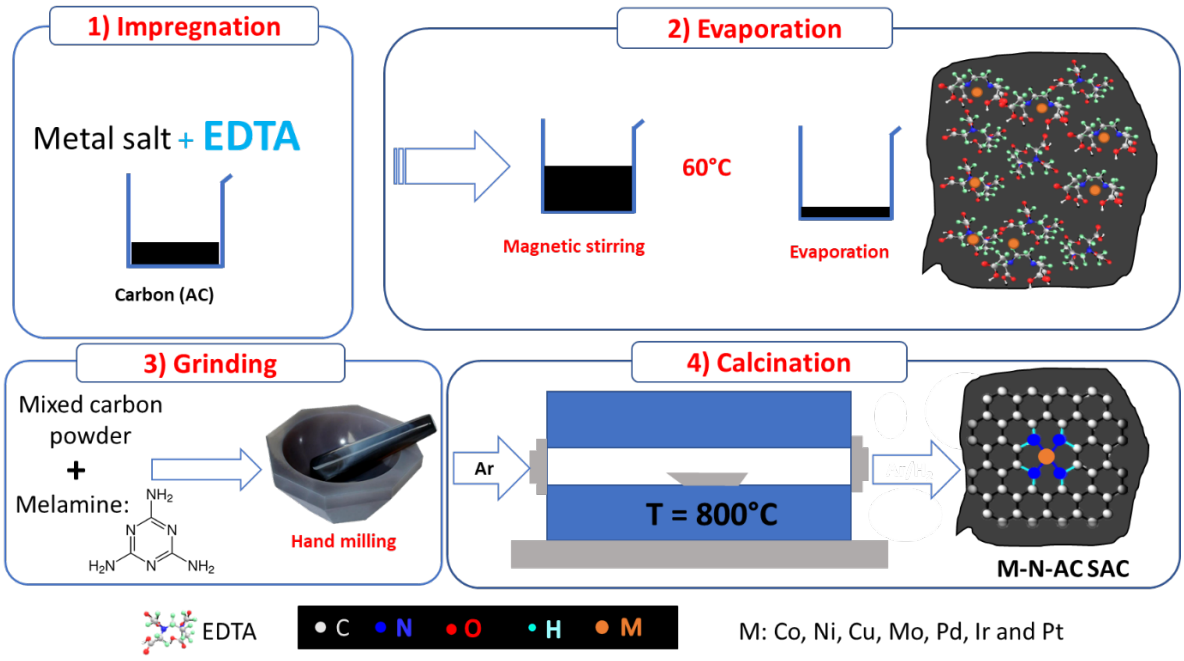


*Figure 2. 2: Schematic illustration of the synthesis of metal SACs supported on porous carbon materials.*

An additional step of acid leaching was needed for certain samples: the obtained sample was washed with 10 mL diluted aqua regia (4 mL $H_2O$, 6 mL 37% HCl, 2 mL 65% $HNO_3$) for 6 h to eliminate the possibly formed metal nanoparticles during the calcination step.

Here, EDTA serves as chelating agent to sequester and isolate precursor metal ions. The amount of EDTA added is in excess to physically isolate metal complexes and avoid coalescence. The quantity of EDTA used in the synthesis depends on the nature and content of metal precursor. The melamine, together with EDTA, serves as a nitrogen source for the formation of M-N moieties. The acid treated AC is chosen as the carbon support because of its high specific surface area (1400 $m^2/g$).

The samples are named *x-M-Y*, where *x* stands for the metal content over the entire sample mass, *M* is the metal and *Y* stands for carbon support. For the purpose of comparison with the initial carbon supports and metal SACs in the study of hydrogen sorption properties and catalysis, a nitrogen doped carbon sample ($CN_x$) was also prepared with same method without the addition of metal precursor. More detail of synthesis information is assembled in Table 2.2.

| sample | Metal precursor | Metal content (wt.%) | Carbon support | Mass of added compositions (mg) | | | | Acid leaching |
|---|---|---|---|---|---|---|---|---|
| | | | | Metal precursor | Carbon | EDTA | melamine | |
| $CN_x$ | - | - | AC | - | 100 | 400 | 500 | - |
| 1.0-Co-AC | $Co(NO_3)_2{\cdot}6H_2O$ | 1.0 | AC | 10.1 | 100 | 200 | 500 | no |
| 2.5-Ni-AC | $Ni(NO_3)_2{\cdot}6H_2O$ | 2.5 | AC | 55.1 | 100 | 400 | 500 | yes |
| 1.6-Cu-AC | $Cu(NO_3)_2{\cdot}3H_2O$ | 1.6 | AC | 42.3 | 100 | 400 | 500 | yes |
| 5.6-Cu-AC | $Cu(NO_3)_2{\cdot}3H_2O$ | 5.6 | AC | 126.7 | 100 | 400 | 500 | yes |
| 3.7-Mo-AC | $Na_2MoO_4{\cdot}2H_2O$ | 3.7 | AC | 28.0 | 100 | 400 | 500 | yes |
| 0.8-Pd-AC | $PdCl_2$ | 0.8 | AC | 7.0 | 100 | 400 | 500 | yes |
| 7.5-Pd-AC | $PdCl_2$ | 7.5 | AC | 111.1 | 100 | 800 | 500 | yes |
| 1.0-Ir-AC | $IrCl_3{\cdot}xH_2O$ | 1.0 | AC | 3.8 | 100 | 200 | 500 | no |
| 3.4-Ir-AC | $IrCl_3{\cdot}xH_2O$ | 3.4 | AC | 20.4 | 100 | 350 | 500 | no |
| 1.1-Pt-AC | $PtCl_4$ | 1.1 | AC | 7.2 | 100 | 400 | 500 | yes |
| 11.7-Pt-AC | $PtCl_4$ | 11.7 | AC | 115.2 | 100 | 800 | 500 | yes |

*Table 2. 2: List of metal single atom catalyst samples and synthesis details.*

## 2.2 Characterization

### 2.2.1 Physicochemical characterization

#### 2.2.1.1 Powder X-ray Diffraction analyses

X-ray diffraction (XRD) is an important and non-destructive technique used in the field of materials characterization to obtain the crystalline structure of materials. X-rays are high-energy electromagnetic radiation with wavelength ranging from about $10^{-3}$ to 10 nm which is close to the atomic length scale in crystals. These X-rays are produced by a cathode ray tube and filtered to obtain a monochromatic radiation. A beam of the generated monochromatic wave is then directed towards a powder sample (Figure 2.3). The crystalline sample consists of planes of atoms, with a space $d_{hkl}$, reflecting the incident X-rays. The reflected X-Rays will interfere with each other. These interferences can be constructive (the waves add together

in superposition) or destructive (the waves add together but cancel out). The interference will be constructive only if the path-length difference $2d_{hkl}\cdot\sin\theta$ equals an integer multiple of the wavelength of X-rays. This is summarized in the Bragg's law equation:

$$n\lambda = 2dsin\theta \qquad \text{Equation 2.1}$$

where *n* is an integer, $\lambda$ is the wavelength of the incident X-rays, *d* is the spacing of the crystal planes and $\theta$ is the angle between the specimen surface and the incident (or diffracted) beam. These diffracted waves are then detected and counted. The wavelength in XRD experiments is known and the distance *d* between the lattice planes of the material can be determined.

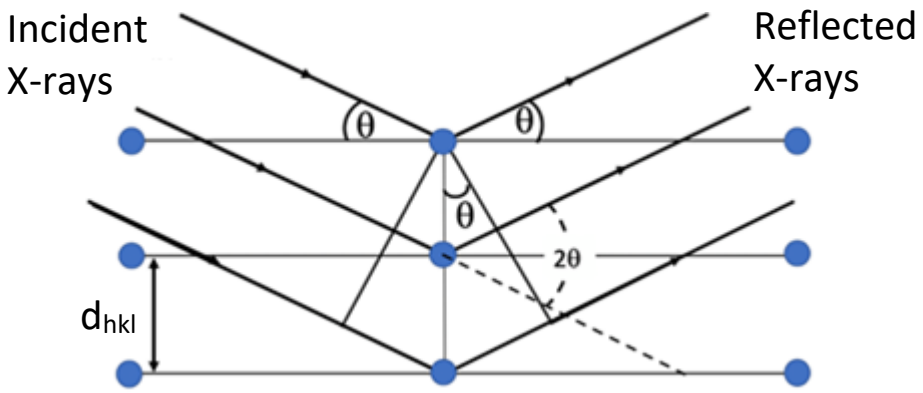


*Figure 2. 3: Bragg reflection for X-ray diffraction.*

In this work, the diffractometer used is a Bruker-D8 Advanced with Bragg-Brentano geometry. The $2\theta$ range used is 10˚ to 90˚ at a scan rate of 1.33˚/min. The source used is a copper anticathode ($\lambda_{K\alpha1}$ = 1.5406 Å) working at 40 kV and 40 mA.

### 2.2.1.2 Scanning Electron Microscopy

Scanning electron microscopy (SEM) is a technique of choice to analyze the specimen surfaces. A typical SEM consists of an electron gun to emit electron source and accelerate by an anode, electromagnetic lenses to focus the electrons, a vacuum chamber to accommodate the specimen, and a selection of detectors to collect the signals emitted by the specimen. A schematic illustration of a SEM is displayed in Figure 2.4.

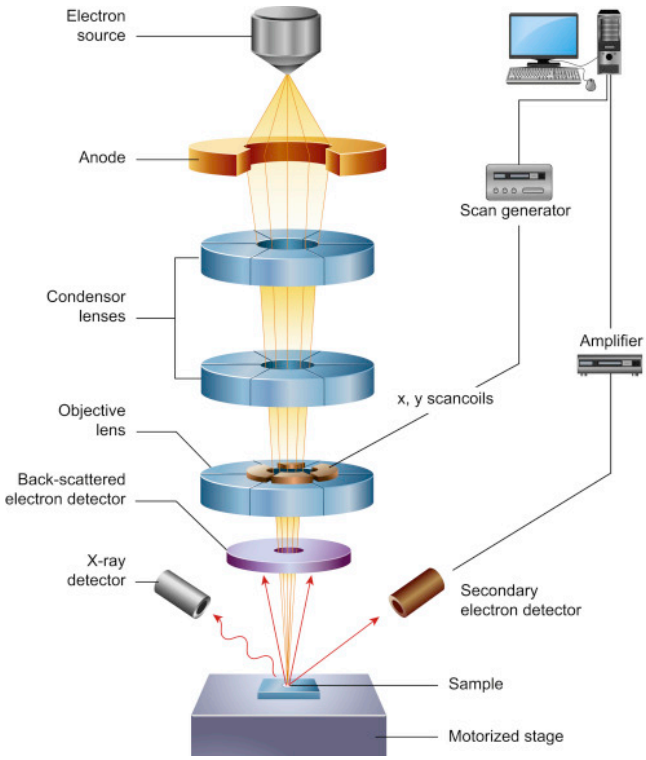


*Figure 2. 4: Schematic diagram of an SEM microscope.*[2]

Electrons are created by a thermionic electron gun and accelerated toward the specimen using a positive electrical potential (1-30 kV). The accelerated electrons are confined and focused using electromagnetic lenses into a thin beam. The beam interacts with the atoms of the specimen, producing secondary electrons, backscattered electrons and X-rays that contain information about its surface morphology and chemical composition. These interactions and effects are detected and transformed into images or quantitative chemical information.

In this project, SEM was used for simple imaging purposes. The analysis was carried out on a Zeiss Merlin microscope complemented from Oxford Instruments (Aztec EDS Advanced). The sample in powder form was placed on a carbon double-sided tape for direct analysis.

#### 2.2.1.3 Transmission Electron Microscopy

Transmission electron microscopy (TEM) is an analytical tool to reveal sub-micrometer, internal fine structure in solids. It allows to obtain detailed micro-structural examination through high resolution and high magnification imaging because it produces images from a

sample by illuminating the sample with a focused beam of high energy electrons. A schematic illustration of a TEM is shown in Figure 2.5.

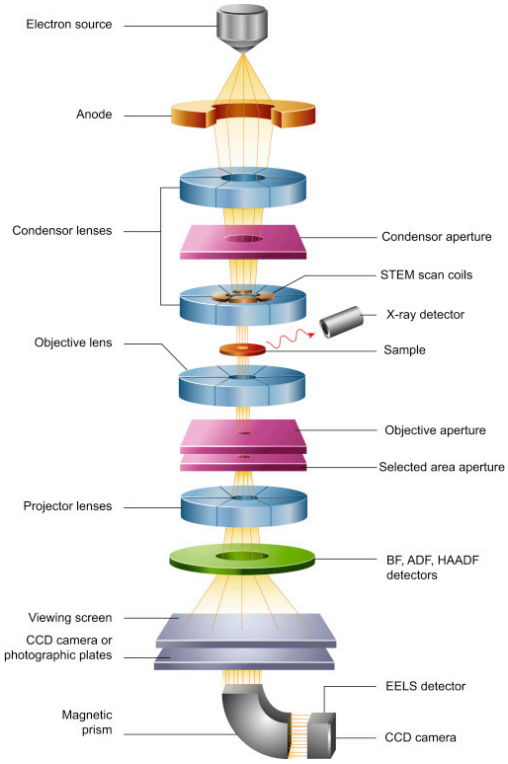


*Figure 2. 5: Schematic of core components of a TEM microscope.*[2]

TEM needs a high-vacuum system, *i.e.*, $10^{-7}$ to $10^{-10}$ mbar is necessary in the area of the electron source. The column is evacuated to a vacuum of $10^{-5}$ to $10^{-7}$ mbar. Electrons are produced by thermionic emission (a tungsten filament, a LaB6 crystal or a ZrO/W Schottky emitter) or cold field emission. The emitted electrons have a low energy and are accelerated to a high speed through an acceleration voltage of 80-300 kV. The accelerated electron beam hits the specimen and either passes the sample unaffected or interacts with it to produce a wide range of secondary signals, some of these are summarized in Figure 2.6. A conventional bright-field (BF) image can be formed by using an objective aperture to select the direct (transmitted) electrons. In BF image, areas with crystalline or high mass materials which result in a strong weakening of the direct beam will appear dark. On the contrary, the objective aperture can also block unscattered (transmitted) beam and select the scattered electrons to form dark field (DF) image. The backscattered electrons and secondary electrons are used in scanning electron microscope (SEM). X-ray photons (EDS analysis: Energy Dispersive Spectroscopy) emitted from the sample are used to characterize both qualitatively and quantitatively the type of elements that are present in the sample and the percentage of each

element's concentration. Finally, the electron energy loss spectrometry (EELS) evaluates the energy loss of inelastically scattered electrons and is very useful to determine the distribution of chemical elements including lighter elements, *e.g.*: B, C, N and O.

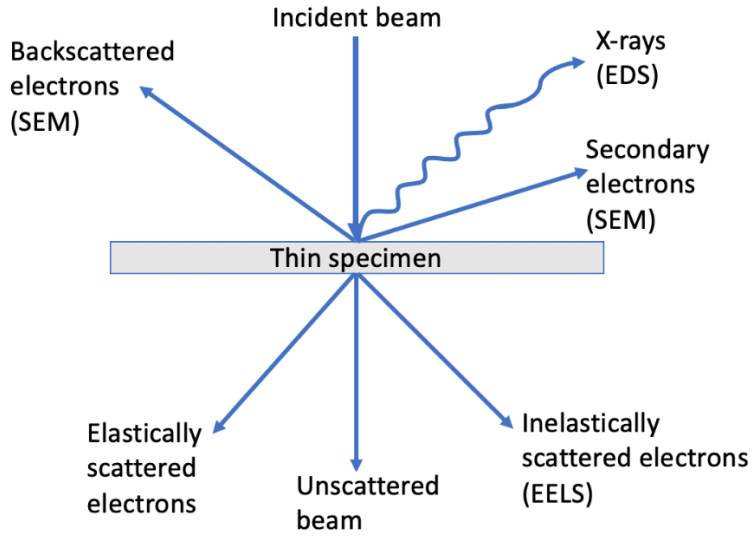


*Figure 2. 6: The interaction of incoming primary electrons with a specimen.*

In this project, the samples are metal nanoparticles or single atoms supported on carbon materials which are in the form of powders. The metal nanoparticles have been fully characterized in the laboratory ICMPE on a FEI Tecnai F20 (point-point resolution 2.4 Å) operated at 200 kV. The single atoms samples (SACs) were firstly characterized to ensure that there was no formation of metal nanoparticles or clusters. For sample preparation, the sample powder was dispersed by ultrasonication in ethanol solvent, then small drops of the suspension are placed on a carbon hollow grid. BF TEM images were collected. For metal nanoparticle samples, the metal nanoparticle size distribution and the average size have been determined by statistical analyses of several TEM images using the software ImageJ. For the SACs, samples were sent to the laboratory IPCMS to study their dispersion by Scanning transmission electron microscopy (STEM) with high-angle annular dark field (HAADF) detection on a Jeol 2100F (point point-to-point resolution 1.1 Å), equipped with a Cs-corrected condenser at the probe level and operated at 200 kV. For sample preparation, the powder was dispersed in ethanol through ultrasonication, dropped onto a holey carbon hollow grid, and dried by a lamp. To avoid contamination during analysis and remove any residual carbon, the samples were Ar plasma-cleaned for 20 s (Plasma Prep 5, GaLa Instrumente). No filtering was applied on the STEM images.

### 2.2.1.4 Specific surface area & porosity

Porous materials are characterized by their texture properties, such as specific surface area and porosity. The specific surface area is defined as the accessible area of solid surface per unit mass of material and the porosity which consists of pore shape and size, describes the ratio of the total pore volume to the volume of the particle. The pores are classified according to their size by the IUPAC (International Union of Pure and Applied Chemistry) as follows:[3]

- Micropores have width smaller than 2 nm;
- Mesopores have width between 2 and 50 nm;
- Macropores have widths larger than 50 nm.

Gas adsorption is the most common experimental method used for characterization of the surface and pore size distribution of porous materials. In practice, $N_2$ is chosen as adsorption gas and the experiment is carried out at its boiling temperature (77.35 K). The physisorption isotherms are obtained experimentally, it describes the amount adsorbed $N_2$ as a function of the equilibrium relative pressure $P/P_0$, where the $P$ is the equilibrium pressure of the adsorbate $N_2$ and $P_0$ is the saturation pressure. The sorption properties are depending on the type of porosity and consequently, the IUPAC classifies the following 8 types of physisorption isotherms (Figure 2.7).

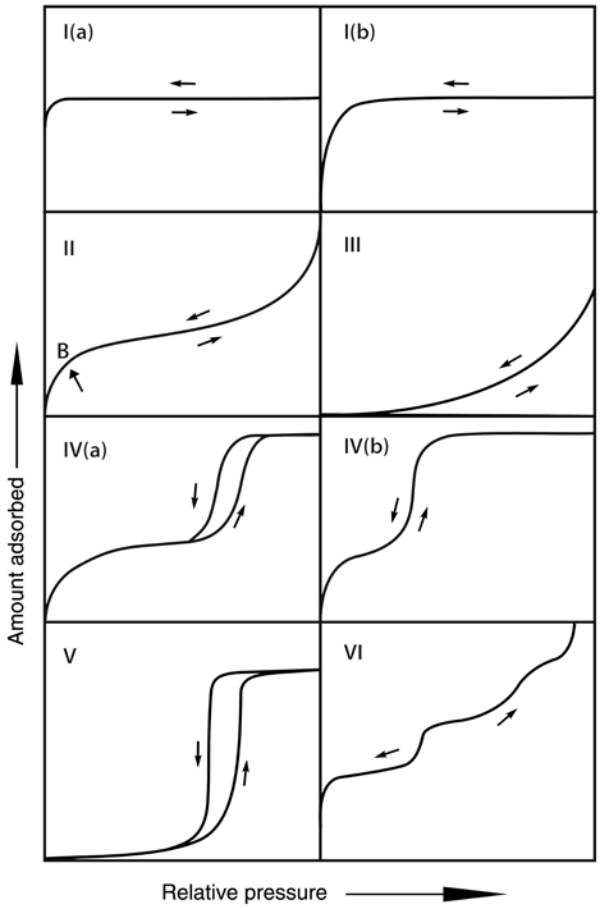


*Figure 2. 7: IUPAC classification of sorption isotherms.*[4]

Type I isotherms are given by monolayer adsorption of microporous solids which have high uptakes of $N_2$ at relatively low pressures because of the narrow pore width. Type I(a) isotherms are found for materials having mainly narrow micropores ($< \sim 1\ nm$), and type 1(b) isotherms correspond to materials having broader pore size range including wider micropores and possibly narrow mesopores ($< \sim 2.5\ nm$).

Type II isotherms are given by the nonporous or macroporous materials, which have an unrestricted monolayer-multilayer adsorption. The inflection point B indicates the step that monolayer coverage is finished, and multilayer adsorption starts.

There is no point B in the Type III isotherms, consequently the monolayer formation is not discernible on the surface of nonporous or macroporous solid. The adsorbate-adsorbent interactions are weak.

Type IV isotherms are given by mesoporous materials. The sorption process which begins with the monolayer-multilayer adsorption on the mesopore walls as the Type II

isotherm, is accompanied by capillary condensation. Capillary condensation is a phenomenon of gas condensation in pores at a pressure smaller than saturation pressure of the bulk phase. Type IV(a) curve shows capillary condensation with hysteresis. Hysteresis usually occurs when mesopore width exceeds a certain critical width ($> \sim 4\ nm$). With mesopores of shorter width, type IV(b) isotherms without hysteresis are found. They are also observed on materials with conical and cylindrical mesopores closed at tapered end.

Type V isotherms show a hysteresis loop. However, the sorption isotherm is similar to sorption isotherms of type (III) which indicate weak attractive adsorbate-adsorbent interactions. This is characteristic of mesoporous materials with low energy of adsorption.

Type VI isotherms show layer-by-layer adsorption – adsorption on a highly uniform nonporous surface. The step-height represents the energies of adsorption for each adsorbed layer.

The specific surface area of materials used in this project is determined by $N_2$ sorption at liquid $N_2$ temperature (77.35 K) by using the volumetric method. It measures the amount of $N_2$ that adsorbs on the surface of porous solid as a function of gas pressure at equilibrium. The Brunauer-Emmett-Teller (BET) method is used to determine the specific surface area via the equation 2.2:

$$1/n[\left(\frac{P_0}{P}\right) - 1] = \frac{1}{n_m C} + \frac{C-1}{n_m C} * \frac{P}{P_0} \qquad \text{Equation 2.2}$$

Where *n* is the quantity of the gas adsorbed at the relative pressure and $n_m$ is the quantity of adsorbate gas in a completed monolayer. *C* is the BET constant that can be expressed as Equation 2.3:

$$C = \exp(\frac{E_1 - E_L}{RT}) \qquad \text{Equation 2.3}$$

Where $E_1$ is the adsorption energy of the first layer, $E_L$ is liquefaction energy of the second and higher layers and *R* is the ideal gas constant.

Generally, in the range 0.05 and 0.35 of $P/P_0$, the plot of $1/n[\left(\frac{P_0}{P}\right) - 1]$ versus $P/P_0$ is a straight line, as shown in Figure 2.8:

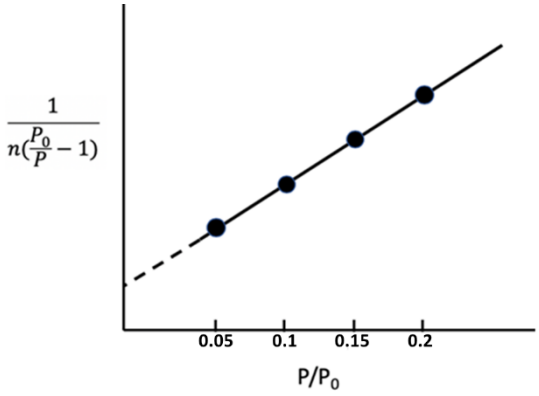


*Figure 2. 8: Typical BET plot.*

By the linearization of the BET plot, the slope *s* and the intercept *i* are given by equations 2.4 and 2.5, respectively:

$$s = \frac{C-1}{n_m C}$$ Equation 2.4

$$i = \frac{1}{n_m C}$$ Equation 2.5

Therefore, the $n_m$, the quantity of adsorbate gas in a completed monolayer is expressed as

$$n_m = \frac{1}{s+i}$$ Equation 2.6

Finally, the specific surface area is calculated by:

$$S_t = n_m \cdot N_A \cdot \sigma_{N_2}$$ Equation 2.7

Where $N_A$ is the avogadro constant ($N_A$ = 6.02214076×$10^{23}$ $mol^{-1}$) and $\sigma_{N_2}$ is cross-sectional area of $N_2$ ($\sigma_{N_2}$= 16.2x$10^{-20}$ $m^2$).

The textural properties were determined with an Auto IQ Quantachrome instrument. Prior to the experiment, 60 mg of sample was outgassed under secondary vacuum at 220 °C for 18 hours. The specific surface area was obtained by the BET method in the range of 0.05-0.2 $P/P_0$.

**2.2.1.5 Raman Spectroscopy**

Raman spectroscopy technique is used to determine the vibrational, rotational and other low-frequency modes in molecular systems. This is a non-destructive analysis tool for the structural characterization of carbon materials. It is based on the interactions of incident light inelastically scattered by vibrating molecules within a material.

In Raman spectroscopy, sample is illuminated with a monochromatic light, usually formed from a laser in the visible, near infrared or near ultraviolet. The monochromatic laser beam interacts with the sample and produced scattered light. The Raman spectroscopy is used to study the structure disorder of carbon materials. As shown in Figure 2.9, two intense bands are present in Raman spectrum of an activated carbon material. The band at about 1610 $cm^{-1}$ (G band) is a commonly assigned to the bond stretching of pairs of $sp^2$ carbon atoms (G mode). The D band close to 1350 $cm^{-1}$ is usually assigned to a lattice breathing mode with $A_{1g}$ symmetry (D mode). This band cannot be seen for a highly crystalline carbon, however it becomes Raman active owing to the presence of structural disorder.

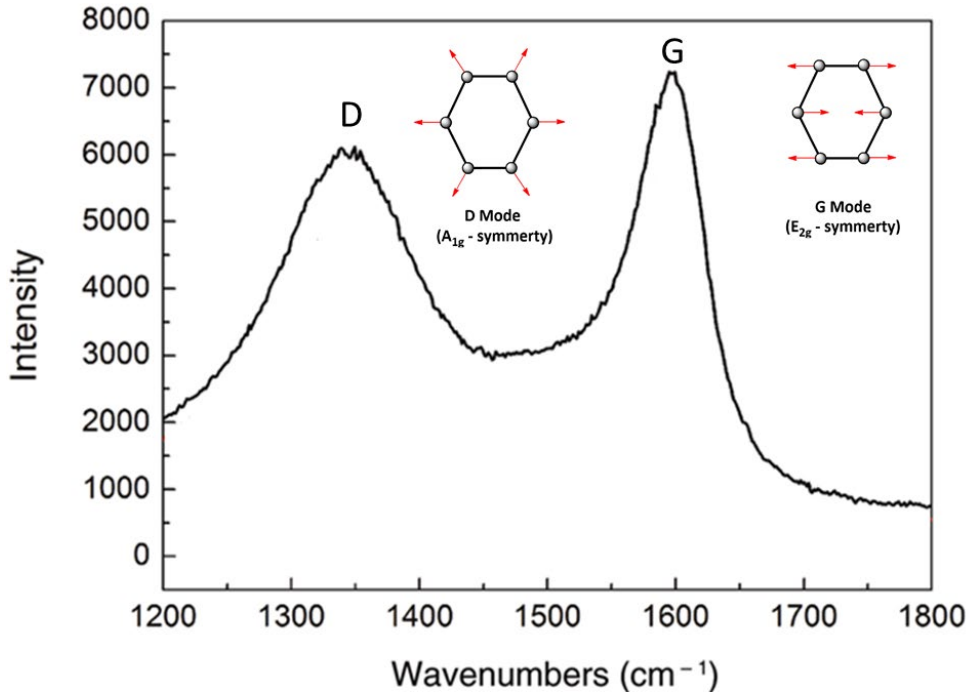


*Figure 2. 9: Raman spectrum of activated carbon materials, collected with an excitation λ = 514 nm, and assignment of the main bands. The insets show a scheme of the vibrational modes associated with the two main bands.*[5]

In this project, the structure of carbon materials was investigated using a Raman spectrometer XPloRA PLUS from Horiba Jobin Yvon equipped with a diode laser emitting at 532 nm.

### 2.2.1.6 X-Ray Photoelectron Spectroscopy

X-ray photoelectron spectroscopy (XPS) is a technique for analyzing the surface chemistry of a material. XPS can measure the elemental composition, chemical state and electronic state within the surface (1-10 nm depth) of a material.

The principle of XPS analysis can be described as follows: X-rays beam with energy, $h\nu$, provided by electron bombardment of a Mg or Al cathode in a high vacuum system, interacts with the electrons in the atomic shell with binding energy, $E_b$, and photoelectrons are generated. The photoelectrons overcome the work function of the sample, $\Phi_s$, and are emitted to the vacuum with kinetic energy: $E_{kin} = h\nu - E_b - \Phi_s$. The kinetic energy of emitted electrons is then measured by the analyzer with $\Phi_A$ the work function. Thus, the binding energy of the chemical element is determined: $E_b = h\nu - E_{kin} - \Phi_A$. This is summarized in the Figure 2.10.

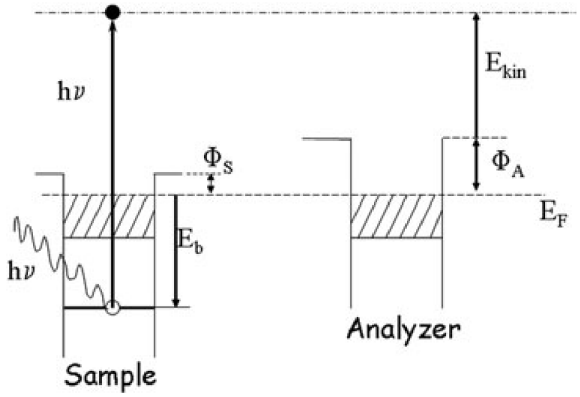


*Figure 2. 10: Schematic explanation of relevant energy terms in XPS of solid surfaces.*[6]

The XPS experiment was carried out at the laboratory IRCELYON. It was carried out using a commercial instrument KRATOS Axis Ultra DLD equipped with an Al K$\alpha$ (1486.6 eV) radiation source.

### 2.2.1.7 X-Ray Absorption Spectroscopy

X-ray Absorption Spectroscopy (XAS) is a powerful technique for determining the local structure of selected elements contained within a material. It consists in measuring the X-ray absorption coefficient $\mu$ of a specimen as a function of photon energy *E* of the incident X-ray beam which is usually produced at a synchrotron radiation facility. In the experiment (Figure 2.11), the absorption coefficient $\mu$ is calculated by:

$$\mu(E)x = ln\frac{I_0}{I}$$ Equation 2.10

where $x$ is the sample thickness, $I_0$ and $I$ are the intensities of the incident and transmitted beams.

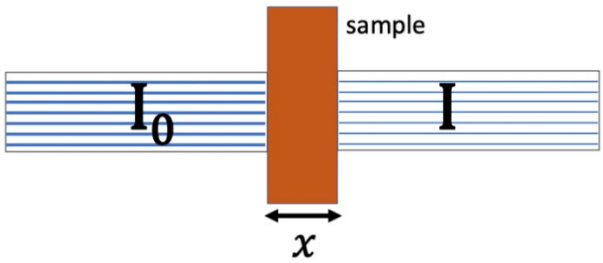


*Figure 2. 11: Incident and transmitted X-ray beams in the presence of a sample with x thickness.*

As shown in Figure 2.12, XAS spectrum consists of two energy regions: the first is X-ray absorption near-edge spectroscopy (XANES) which encompasses three parts: the pre-edge, the edge and the post-edge 50 eV above the edge and the second is Extended X-ray absorption fine structure (EXAFS) which extends from ~50 eV to 1000 eV above the edge. The XANES date are valuable for investigation of the local site symmetry and the valence state of the X-ray absorbing element, while the EXAFS provides information about the interatomic distances, near neighbor coordination numbers and degree of disorder. In our experiment, the EXAFS region is mostly exploited but the XANES is also used to identify the charge state of the absorbing atom.

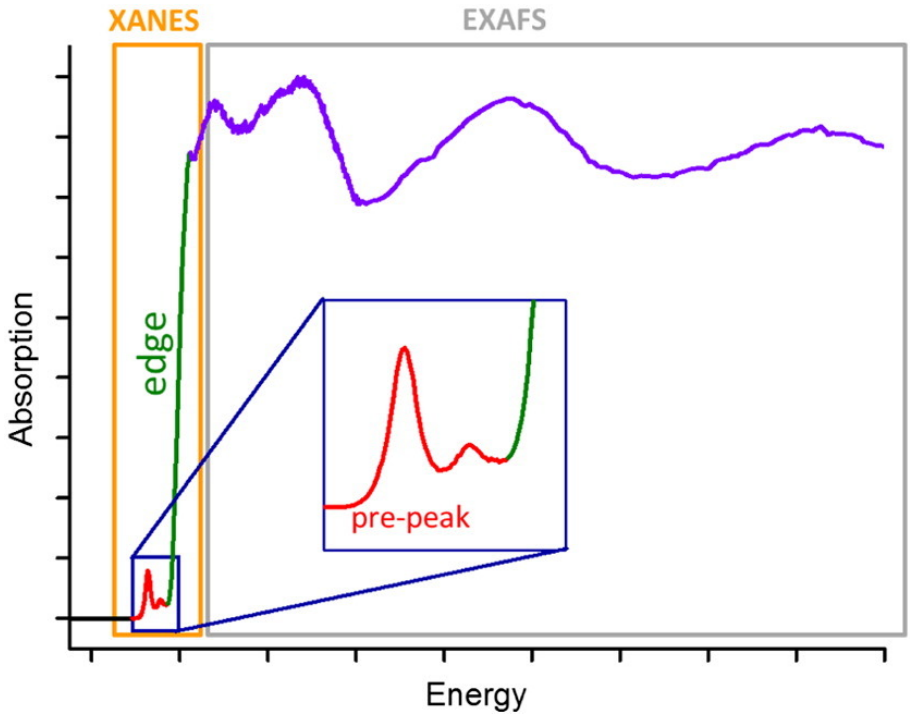


*Figure 2. 12: X-ray absorption spectrum showing the X-ray absorption region near edge structure (XANES) including the pre-edge feature and extended X-ray absorption fine structure (EXAFS) region.*[7]

In the EXAFS region, a core electron can be ejected from an atom to the continuum and this emitted photoelectron can be represented as an outgoing spherical wave. If the absorbing atom is surrounded by neighboring atoms, the outgoing photoelectron wave can be backscattered by the neighboring atoms and causing an incoming electron wave. The outgoing and incoming waves can interfere with each other either constructively or destructively, which result in the sinusoidal variation of the absorption coefficient $\mu$ *versus E* in the EXAFS spectrum. The EXAFS fine-structure function, $x(E)$, can be defined as

$$x(E) = \frac{\mu(E) - \mu_0(E)}{\Delta\mu_0(E)} \qquad \text{Equation 2.11}$$

where $\mu(E)$ is the measured absorption coefficient, $\mu_0(E)$ is a smooth background function corresponding to the absorption of an isolated atom, and $\Delta\mu_0(E)$ is the measured jump in the absorption $\mu(E)$ at the threshold energy $E_0$ of the absorption edge. The energy *E* is converted into the photoelectron wavevector $k$, $k = \sqrt{\frac{2m(E-E_0)}{\hbar^2}}$. The EXAFS signal $x(k)$ in $k$ space can be modeled by the following formula[8]:

$$x(k) = \sum_j \frac{N_j S_0^2}{kR_j^2} F_j(k) e^{-2R_j/\lambda_j(k)} e^{-2k^2\sigma_j^2} sin[2kR_j + \Phi_j(k)] \qquad \text{Equation 2.12}$$

where $F_j(k)$ is the photoelectron backscattering amplitude from each of the $N_j$ neighboring atoms of $j^{th}$ type, $S_0^2$ is the amplitude reduction factor, $R_j$ is the interatomic distance, $\lambda_j(k)$ is the photoelectron inelastic mean free path, $\sigma_j$ is the Debye-Waller factor (thermal vibration and static disorder), $F_j$ is the photoelectron (back-)scattering amplitude, $\Phi_j(k)$ is the corresponding (back-)scattering phase for the $j^{th}$ atomic shell, and $e^{-2r_j/\lambda_j(k)}$ is related to inelastic losses in the scattering process.

The local structures of metal nanoparticles and single atom catalysts (SACs) were investigated by XAS in transmission mode on the ROCK beamline at the SOLEIL synchrotron.[9,10] Three types of XAS experiments have been carried out. Simple acquisitions at room temperature were realized for certain metal SAC samples: Co, Mo, Ir and Pt. For Pd nanoparticle samples we have performed *in situ* XAS under controlled atmosphere (He and $H_2$) at room temperature. Finally, the Ir SAC and nanoparticle samples were investigated by *operando* XAS coupled with mass spectroscopy during the reaction of the hydrogenation of butadiene:

***Simple XAS acquisition***: The local structure of metal SAC samples: Co, Mo, Ir and Pt, and their corresponding metal bulks, was investigated by XAS at room temperature. The powder samples were placed inside a Lytle-type cell.[11] The XAS spectra at the K-edge of Co ($E_0$ = 7709 eV), the K-edge of Mo ($E_0$ = 20000 eV), $L_3$-edge of Ir ($E_0$ = 11215 eV) and $L_3$-edge of Pt ($E_0$ = 11564 eV) were measured in air and at room temperature for an acquisition time of 20 minutes. 1.0-Co-AC, 3.7-Mo-AC, 3.4-Ir-AC, 1.1-Pt-AC, 11.7-Pt-AC as well as 1.0-Ir-AC after the catalysis of hydrogenation of levulinic acid were also measured. The metal bulks (Co, Mo, Ir or Pt) were used as references.

***In situ* XAS**: The local structure of Pd bulk and Pd nanoparticles samples was studied by *in situ* XAS. The X-ray absorption spectra at the K-edge of Pd ($E_0$ = 24350 eV) were measured at isothermal conditions at 25 °C. The powder samples were placed inside a Lytle-type cell which was connected to a gas distribution system that controls the gas flow composition at atmospheric pressure. Prior to any isothermal measurement the samples were treated under $H_2$ flow (30 ml/min) at room temperature for 10-15 minutes to remove any oxide at the surface of nanoparticles, as demonstrated earlier.[12] Then the $H_2$ flow was replaced by He (30

ml/min) and the samples were heat-treated with the following temperature profile: heating to 250 °C with a ramp of 10 °C $min^{-1}$, dwell at 250 °C for 10 minutes followed by cooling to 25 °C with a ramp of 15 °C/min. The purpose of this treatment is to completely remove water molecules formed during reduction of the surface oxide layer at room temperature together with hydrogen atoms possibly adsorbed/absorbed in Pd nanoparticles. Such pre-treatment ensures the exploration of hydrogen sorption properties of clean nanoparticles without oxide layer or other interstitial impurities. Four samples: Pd bulk and 3 Pd nanoparticles: 10-Pd@HSAG-500, 10-Pd@HSAG-300 and 10-Pd@AC-300, were measured under several $H_2$ partial pressures in a He flow (30 ml/min). The sequence of $H_2$ partial pressures was the following: 0, 0.05, 0.25, 0.5 and 1 bar in absorption as well as 1, 0.5, 0.25, 0.05 and 0 bar $H_2$ in desorption at 25 °C. A Pd foil was used as reference.

**Operando XAS**: *Operando* XAS on 1.0-Ir-AC SAC and 1-Ir@AC-700 nanoparticles samples during the hydrogenation of butadiene were carried out at the $L_3$-edge of Ir ($E_0$ = 11215 eV). Metal Ir foil and $IrO_2$ were used as reference. The powder samples were placed inside a Lytle-type cell. The experiment followed as close as possible the laboratory reaction conditions (described in **2.2.3.1 hydrogenation of butadiene**). Prior to each operando experiment, the samples were pretreated to remove contaminants at the surface by heating to 250 °C for 1 h under continuous He/$H_2$ flow (15 ml/min He and 15 ml/min $H_2$) and then cooled down to 25 °C. Afterward, the catalysts were exposed to the reactive gas mixture (35 mL/min): 0.5% $C_4H_6$ + 2.5% $H_2$ + 97% He and temperature was raised to 200 °C with a ramp of 1 °C/min. The temperature was maintained at 200 °C for 1 h under reaction conditions. The XAS measurements were coupled with continuous mass spectrometry (MS) to determine the reaction kinetics and catalytic products.

All XANES spectra were calibrated in energy and normalised at SOLEIL Synchrotron. The XAS data treatment and EXAFS refinements were performed with the MAX program package (CHEROKEE and Roundmidnight). The normalised spectrum was first treated by the software “CHEROKEE” to remove background, then the spectra of EXAFS and FT (Fourier transform) were obtained. The filtered spectra of EXAFS was extracted in the range of 3 - 15 $Å^{-1}$ of FT for Pd and 4 - 15 $Å^{-1}$ for Co, Mo, Ir and Pt.[13,14] EXAFS fitting was performed on first-sphere filtered spectra with the filtered spectra by the software “Roundmidnight”. Theoretical phases and amplitudes were computed with FEFF8 based on *fcc* Pd metal

structure for Pd samples and $X$-$N_4$ ($X$ = Co, Mo, Ir or Pt) for SACs samples. The refined parameters are the coordination number ($N$), the Debye-Waller factor ($\sigma^2$), the nearest neighbour distance ($R$) and, for small Pd nanoparticles only, the $C_3$ cumulant factor to account for deviations from Gaussian distribution. The energy shift $\Delta E_0$ was refined first for the metal reference and then fixed for further refinements. The goodness of fit was evaluated using the quality factor ($QF$).

#### 2.2.1.8 Inductively Coupled Plasma Spectroscopy

Inductively Coupled Plasma (ICP) spectroscopy is an analytical technique that can be used to measure quantitatively the chemical elements at trace levels in materials. The first step in ICP is the sample preparation: solid samples are normally dissolved by acid treatment in a solution, *e.g.*, HCl, $HNO_3$ and aqua regia. The liquid solution of the sample is then transformed into a coarse aerosol form through a nebulizer. The aerosol is introduced in an argon-induced plasma, at around 7000-10000 K. At such high temperature, the aerosol is first dried to a solid, then atomization and ionization take place. Two kinds of detector technologies are used: Atomic Emission Spectroscopy (AES) and Mass Spectroscopy (MS).

Atomic Emission Spectroscopy (ICP-AES) involves the measurement of the characteristic wavelength of light emitted from the atoms of samples. At high temperature, atoms are capable of absorbing radiation and electrons are excited from the ground state to higher energy levels. When the electrons return to the initial state, an emission of light (photons) occurs, as shown in Figure 2.13. Each element has a characteristic emission spectrum. The wavelengths are separated and identified, and the light intensity of each wavelength is measured with a spectrometer. Mass spectroscopy (ICP-MS) measures the ratio mass/charge ($m/z$) of ions produced by high temperature argon plasma. In the mass spectrometer, the ions are separated according to their $m/z$ ratio and measured in function of their abundance.

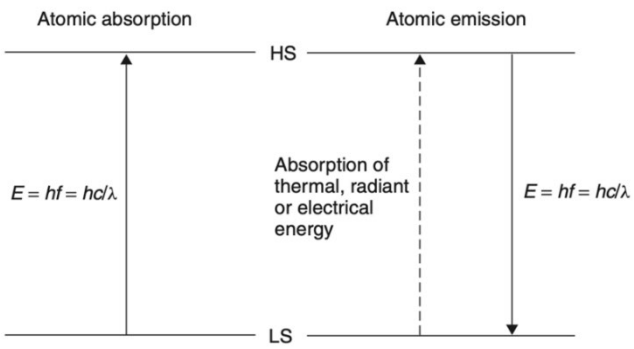


*Figure 2. 13: Schematic representation of atomic absorption and atomic emission energy transitions: LS, lower-energy state or ground state; HS, higher-energy state.*[15]

In this work, in order to determine the metal content in the SACs samples, ICP-AES was performed at IRCELYON using an ICP-AES ACTIVA DE HORIBA JOBIN YVON. The samples were dissolved by using the mixture of concentrated $H_2SO_4$ and aqua regia at 350 °C.

**2.2.1.9 Thermogravimetric Analysis**

Thermogravimetric Analysis (TGA) is a method of thermal analysis in which the mass of a sample is measured as a function of temperature changes in a controlled atmosphere. The experiment is carried out on a thermogravimetric analyzer. It contains a sample pan weighed by a precision balance. This sample pan is placed inside a furnace with a controlled temperature and environment. The sample is generally heated at constant rate to a fixed temperature under a variety of atmospheres, *e.g.*, ambient air, vacuum and Argon. The temperature and mass of sample are recorded as function of increasing temperature with a constant rate. The TGA is often coupled with a spectrometer (FTIT: Fourier Transform Infrared Spectroscopy, or MS: Mass Spectroscopy) to analyze the volatile species and pyrolysis products, which can lead to understand how a compound or formulation decomposes and what components it contains.

In this work, the formation of 1.0-Ir-AC has been monitored by the TGA-MS at IRCELYON. TGA-MS analysis was conducted on a Setaram Setsys Evolution 12 thermoanalyzer via a heated (*ca.* 150 °C) capillary with a Pfeiffer Omnistar quadrupole mass spectrometer (QMS). Degassed sample (20 mg of mixture of $IrCl_3$, EDTA, AC and melamine) was placed in a Pt-based open crucible and heated from ambient temperature to 800 °C for 2 h , at a constant rate of 3 °C/min, under a flow of pure argon (40 ml/min).

Other samples were analyzed for the thermal stability of materials under continuous dry air flow condition by TGA at ICMPE. A SETARAM evo TGA 1160 evolution was used for this analysis. Degassed sample (20 mg) was placed in a Pt-based open crucible and heated up to 800 °C with a ramp of 10 °C/min, under a flow of dry air (20 ml/min).

### 2.2.2 Hydrogenation properties

#### 2.2.2.1 Pressure-Composition Isotherm

Hydrogen sorption properties have been investigated by the Sievert method, also known as volumetric method. A general Sievert's apparatus is schematically shown in Figure 2.14 a. The system is composed of the following components: $H_2$ gas supply, vacuum supply, pressure measurement, and two chambers (reference chambre: $V_{ref}$ and sample chambre: $V_{cell}$) connected by an isolation valve. The measurement follows an iterative process. Sample is placed in the sample chambre and separated from the reference chamber with a determined pressure and temperature. Hydrogen is loaded into the reference chamber at a pressure of $p_i = i \cdot \Delta p_{inc}$ with $\Delta p_{inc}$ being a selected pressure increment. After the stabilization of the gas temperature into the reference volume, the isolation valve is opened and the $H_2$ gas expands to the sample cell. The gas expansion results in the drop of pressure in the reference chamber and the rise of pressure in the sample chambre. An equilibrium pressure ($p_{eq,i}$) is reached for the sample after a suitable stabilization time.. Afterwards, the sample chamber is again isolated from the reference chamber. The absorption process is repeated at $p_{i+1} = (i+1) \cdot \Delta p_{inc}$ up to the desired final pressure. The desorption process is identical as the absorption process except with a pressure decrement down to zero pressure. A schematic representation of pressure evolution of the absorption process is shown in Figure 2.14 b.

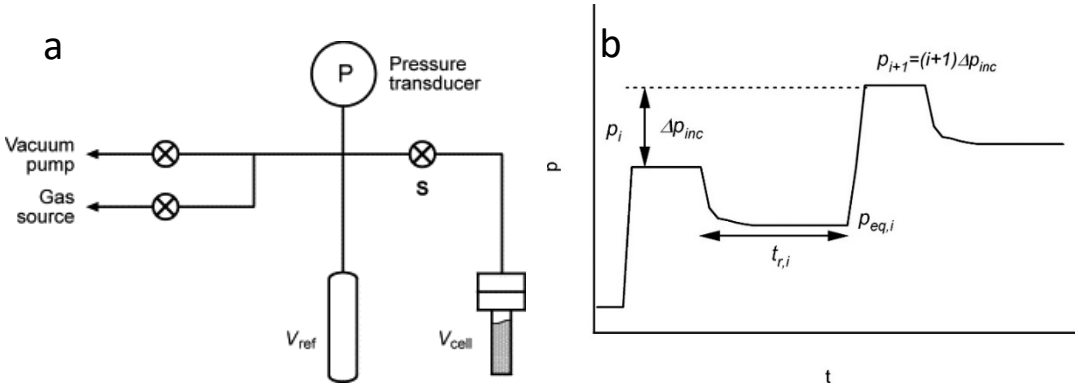


*Figure 2. 14: a) Schematic representation of a Sievert's apparatus,*[16] *and b) Schematics of the measurement procedure in a Sieverts apparatus. The schematics illustrates the acquisition of point i+1.*[17]

The amount of hydrogen absorbed or desorbed by a certain mass of sample can be calculated by the collected data $p_i$, $p_{eq,i}$ and $V_{ref}$, with the formula: $n(H_2\ absorbed) = \frac{P_i \cdot V_{ref} - P_{eq}(V_{ref}+V_{cell})}{RT}$, where *R* is ideal gas constant and *T* is temperature and a pressure-composition isotherms (PCI) curve can be constructed by measuring the equilibrium pressure and the hydrogen concentration in the sample. A typical PCI curve of Pd bulk at room temperature is shown in Figure 2.15. At low hydrogen pressure, $H_2$ is slightly dissolved by the metal and forms a solid-solution phase ($\alpha$ phase). When the gas pressure increases, the hydride phase ($\beta$ phase) begins to form and the Pd starts to absorb large quantities of hydrogen at constant pressure (plateau pressure). The pressure augments rapidly after the Pd has totally been transformed into Pd hydride. This process is reversible by lowering the hydrogen pressure.

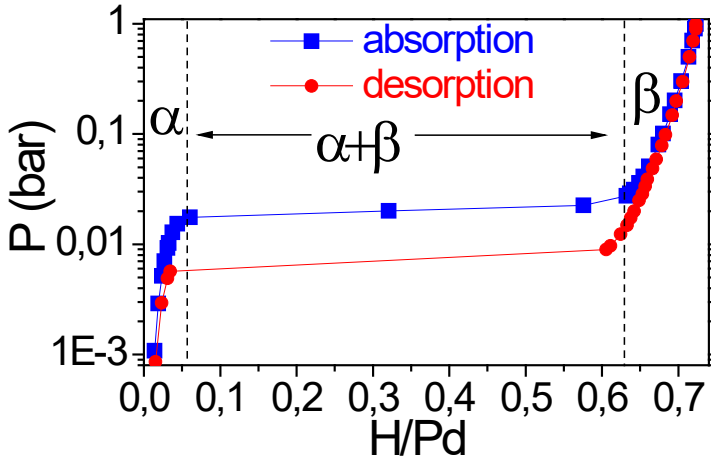


*Figure 2. 15: Example of Pressure-Composition Isotherm of Pd bulk at RT.*

In this work, the experiments were carried out to measure pressure composition isotherm (PCI) curves at different temperatures up to a maximum hydrogen pressure of 1 bar by an automated volumetric apparatus (Quantachrome Autosorb IQ). Prior to the experiment, the samples were degassed under secondary vacuum at 220 °C for 18h.

### 2.2.2.2 Thermo-Desorption Spectroscopy

Thermal desorption spectroscopy (TDS) is originally a surface characterization technique for the study of the interaction of reaction gases with solid surfaces as a function of sample temperature. It is widely used to investigate the hydrogen sorption behavior in metallic materials. The basic concept of this method is that the hydrogen absorbed by the material can be desorbed when it is heated to a higher temperature.

A schematic illustration of TDS apparatus is shown in Figure 2.16. The experiment is performed at a high vacuum condition (typically, $10^{-6}$ bar). The sample is usually cooled to a certain temperature by liquid He, liquid $N_2$ or simply at room temperature and then heated at a programed heating rate. The hydrogen desorbed from the sample is measured by a mass spectrometer (*e.g.*, quadrupole mass spectrometer). The quantity of desorbed gas is recorded as a function of the sample temperature , *i.e.*, a TDS spectrum.

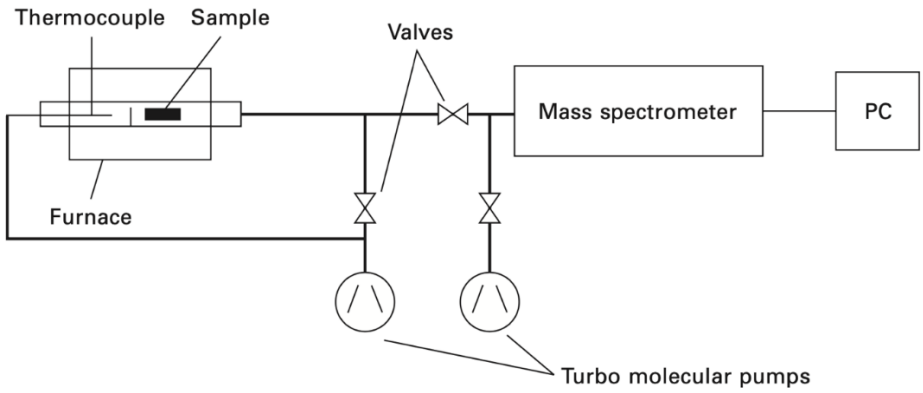


*Figure 2. 16: Schematic illustration of thermal desorption spectroscopy apparatus.*[18]

The Kissinger method is usually used to estimate the activation energy of desorption. The Kissinger equation[19] is described by the equation below:

$$\ln\left(\frac{\beta}{T_m^2}\right) = -\frac{E_a}{RT_m} + \ln k_0 \qquad \text{(Equation 2.13)}$$

Where: $E_a$ is the activation energy, $\beta$ is the heating rate, $T_m$ is the temperature that corresponds to maximum desorption rate, $R$ is the gas constant and $k_0$ is a pre-exponential

factor. By varying the heating rate $\beta$, a Kissinger linear plot of $\ln\left(\frac{\beta}{T_m^2}\right)$ vs. $\frac{1}{T_m}$ is obtained, and the activation energy is related to the value of the slope of the Kissinger plot.

In this work, three experimental protocols were carried out at different temperature range. For our convenience, the unity of temperature used in TDS at cryogenic condition is Kelvin (K) instead of Celsius (°C), typically used in the high temperature range:

**(1) High-temperature TDS** in the temperature range 25 – 225 °C (298-498 K): The samples were exposed to 1 bar $H_2$ at room temperature and subsequently evacuated under secondary vacuum. Afterwards, the desorbed $H_2$ partial pressure was recorded while heating to 225 °C with a constant heating rate of 5 °C/min.

**(2) Medium cryogenic TDS** in the temperature range 78 – 310 K: The experience was carried out using an Oxford Instrument cryostat (ITC 5035) that uses liquid nitrogen as a coolant. The hydrogen partial pressure was recorded from 77 to 310 K with heating a heating rate of 2 – 10 K/min.

**(3) Low cryogenic TDS** in the temperature range 35 – 300 K: The experience was carried out using an ARS-4HW Compressor cryostat that employs liquid helium as a coolant. The hydrogen partial pressure was recorded from 35 to 300 K with a heating of 5 K/min.

### 2.2.3 Catalysis

The samples were evaluated in catalytic reaction of selective hydrogenations in different mediums at laboratory IRCELYON: hydrogenation of butadiene in gaseous condition and hydrogenation of levulinic acid (LA) in aqueous solution.

#### 2.2.3.1 Hydrogenation of butadiene

Two protocols were carried out in the hydrogenation of butadiene, the first is the **main reaction, hydrogenation of butadiene**, and the second is the **isomerization of butenes**.

**Main reaction**: The equipment of hydrogenation of butadiene is described in Figure 2.17. The hydrogenation of butadiene was carried out under atmospheric pressure in a continuous flow fixed-bed stainless steel U shape reactor. The reactor was placed in a ceramic furnace and the temperature is controlled via a thermocouple. Before the reaction, 40 mg of catalyst was mixed with 100 mg $Al_2O_3$ and activated *in situ* with hydrogen by heating from room temperature (RT) to 250 °C at a heating rate of 4 °C/min and maintained at 250 °C for 1

h. Then the reactor was cooled down to RT under $H_2$. The feed flow rate was set to 100 ml/min. The reactive gases ($C_2H_2$:$H_2$:He) were mixed using mass flow controllers (Brooks and Vögtlin) with a ratio of 2:10:88. The temperature was heated to 200 °C with a ramp of 1°C/min and maintained at 200 °C for 1 h under reaction gases. The feed and effluent gases were analyzed online using Shimadzu GC-2014 gas chromatograph equipped with a Supelco alumina sulfate plot coupled with a silica capillary column and an FID detector.

Butadiene conversion (%) is based on the initial concentration of butadiene in the reactive gases ([butadiene]$_0$) and defined by: $butadiene\ conversion\ (\%) = \frac{[butadiene]_0 - [butadiene]_t}{[butadiene]_0} \times 100$, where [butadiene]$_t$ refers to the concentration of butadiene detected by GC at time *t*. The selectivity to butenes (1-butene, trans-2-butene and cis-2-butene) is defined as $\sum P_{butenes} / (\sum P_{\sum P_{butane}} + \sum P_{butenes})$ where $P_i$ is the partial pressure of product *i*.

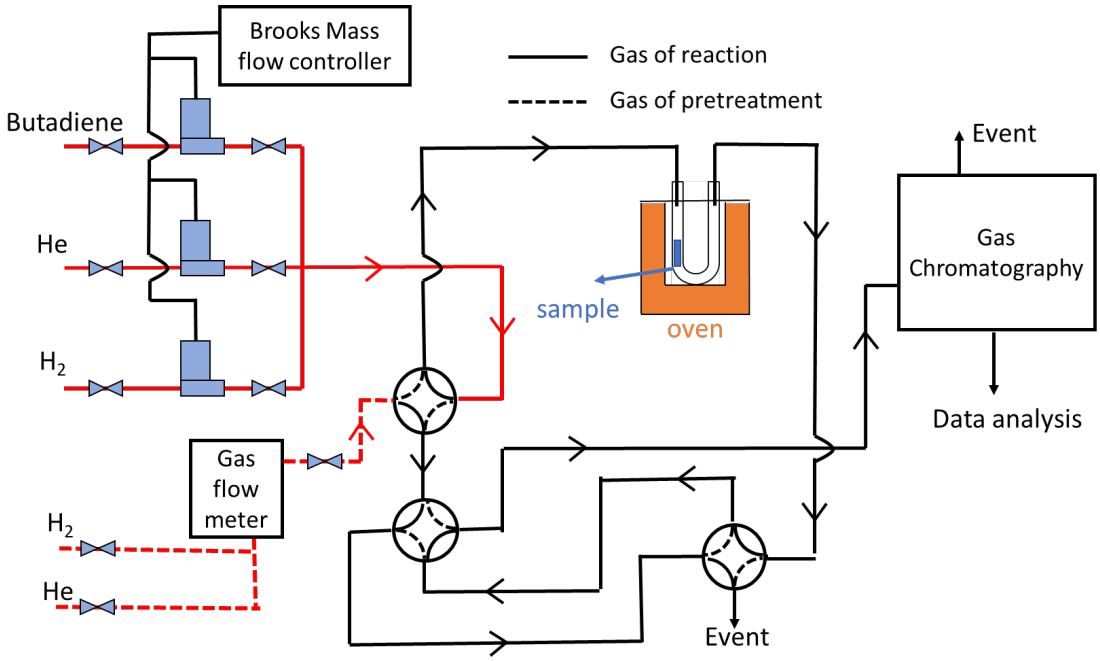


*Figure 2. 17: Schematic diagram of catalytic hydrogenation of butadiene test system.*

**Isomerization of butenes**: In order to understand the mechanism of hydrogenation of butadiene, the isomerization of butenes was realized on the same reaction instrument. Before the reaction, 40 mg of catalyst was mixed with 100 mg $Al_2O_3$ and activated *in situ* with hydrogen by heating from room temperature (RT) to 250 °C at a heating rate of 4 °C/min and maintained at 250 °C for 30 min. Then the reactor was cooled down to RT under He. After the

pretreatment, the feed flow rate was set to 100 ml/min with a mixture of 0.04% butenes/$N_2$ (10.5% 1-butene, 50.9% isobutene, 21.7% trans-2-butene and 16.9% cis-2-butene). The temperature was heated to 350 °C with a ramp of 1°C/min. The feed and effluent gases were analyzed online using the gas chromatograph mentioned above.

#### 2.2.3.2 Hydrogenation of levulinic acid

The aqueous catalytic hydrogenation experiments were performed using a 300 mL high-pressure batch (Parr 4560) Hastelloy autoclave, equipped with a magnetically driven impeller and a liquid sampling system. The reaction temperature was monitored by a thermocouple probe, which was present inside a thermowell, in the reactor. A 150 mL aqueous solution of levulinic acid (LA) (0.17 M) and 0.8 g (or 0.4 g) of the catalyst were loaded into the reactor. After sealing, the autoclave was purged three times with Ar, heated up to 160 °C, then pressurized with $H_2$ up to 50 bar (or 150 bar) and stirred at 900 rpm. The reactions were conducted for 24 h, and the samples were collected periodically every 2 h during the day to follow the evolution of the reaction. The collected liquid samples were analyzed by a GC Agilent Technologies 6890N with a flame ionization detector employing a VF-WAXms column (30 m × 0.25 mm × 0.25 µm). The temperature was increased up to 190 °C under helium as a carrier gas.

LA conversion (%) is based on the initial concentration of LA ($[LA]_0$) and defined by: $LA\ conversion\ (\%) = \frac{[LA]_0 - [LA]_t}{[LA]_0} \times 100$, where $[LA]_t$ refers to the concentration of LA at time $t$. Selectivity and yield of a product $i$ are given by $selectivity\ (\%) = \frac{[P_i]_t}{[LA]_0 - [LA]_t} \times 100$ and $product\ yield\ (\%) = \frac{[Pi]t}{[LA]_0} x100$, where $[P_i]_t$ refers to the concentration of the product $i$ at time $t$.

## 2.3 References

(1) Zlotea, C.; Campesi, R.; Cuevas, F.; Leroy, E.; Dibandjo, P.; Volkringer, C.; Loiseau, T.; Férey, G.; Latroche, M. Pd Nanoparticles Embedded into a Metal-Organic Framework: Synthesis, Structural Characteristics, and Hydrogen Sorption Properties. *Journal of the American Chemical Society* **2010**, *132* (9), 2991–2997. https://doi.org/10.1021/ja9084995.

(2) Inkson, B. J. Scanning Electron Microscopy (SEM) and Transmission Electron Microscopy (TEM) for Materials Characterization. In *Materials Characterization Using Nondestructive Evaluation (NDE) Methods*; Elsevier, 2016; pp 17–43. https://doi.org/10.1016/B978-0-08-100040-3.00002-X.

(3) Rouquerol, J.; Avnir, D.; Fairbridge, C. W.; Everett, D. H.; Haynes, J. H.; Pernicone, N.; Ramsay, J. D. F.; Sing, K. S. W.; Unger, K. K. Recommendations for the Characterization of Porous Solids. https://doi.org/10.1515/iupac.66.0925.

(4) Thommes, M.; Kaneko, K.; Neimark, A. V.; Olivier, J. P.; Rodriguez-Reinoso, F.; Rouquerol, J.; Sing, K. S. W. Physisorption of Gases, with Special Reference to the Evaluation of Surface Area and Pore Size Distribution (IUPAC Technical Report). *Pure and Applied Chemistry* **2015**, *87* (9–10), 1051–1069. https://doi.org/10.1515/pac-2014-1117.

(5) Cheng, S.; Zhang, L.; Xia, H.; Peng, J. Characterization and Adsorption Properties of La and Fe Modified Activated Carbon for Dye Wastewater Treatment. *Green Processing and Synthesis* **2017**, *6* (5), 487–498. https://doi.org/10.1515/gps-2016-0120.

(6) Hofmann, S. *Auger- and X-Ray Photoelectron Spectroscopy in Materials Science*; Springer Series in Surface Sciences; Springer Berlin Heidelberg: Berlin, Heidelberg, 2013; Vol. 49. https://doi.org/10.1007/978-3-642-27381-0.

(7) Kowalska, J.; DeBeer, S. The Role of X-Ray Spectroscopy in Understanding the Geometric and Electronic Structure of Nitrogenase. *Biochimica et Biophysica Acta (BBA) - Molecular Cell Research* **2015**, *1853* (6), 1406–1415. https://doi.org/10.1016/j.bbamcr.2014.11.027.

(8) Teo, B. K. *EXAFS: Basic Principles and Data Analysis*; Springer Berlin: Berlin, 2014.

(9) Briois, V.; Fontaine, C. L.; Belin, S.; Barthe, L.; Moreno, T.; Pinty, V.; Carcy, A.; Girardot, R.; Fonda, E. ROCK: The New Quick-EXAFS Beamline at SOLEIL. *J. Phys.: Conf. Ser.* **2016**, *712*, 012149. https://doi.org/10.1088/1742-6596/712/1/012149.

(10) La Fontaine, C.; Belin, S.; Barthe, L.; Roudenko, O.; Briois, V. ROCK: A Beamline Tailored for Catalysis and Energy-Related Materials from Ms Time Resolution to Mm Spatial Resolution. *Synchrotron Radiation News* **2020**, *33* (1), 20–25. https://doi.org/10.1080/08940886.2020.1701372.

(11) La Fontaine, C.; Barthe, L.; Rochet, A.; Briois, V. X-Ray Absorption Spectroscopy and Heterogeneous Catalysis: Performances at the SOLEIL's SAMBA Beamline. *Catalysis Today* **2013**, *205* (0), 148–158. https://doi.org/10.1016/j.cattod.2012.09.032.

(12) Zlotea, C.; Oumellal, Y.; Provost, K.; Matei Ghimbeu, C. Experimental Challenges in Studying Hydrogen Absorption in Ultra-Small Metal Nanoparticles. *Frontiers in Energy Research* **2016**, *4* (24), 24. https://doi.org/10.3389/fenrg.2016.00024.

(13) Michalowicz, A.; Moscovici, J.; Muller-Bouvet, D.; Provost, K. MAX: Multiplatform Applications for XAFS. *Journal of Physics: Conference Series* **2009**, *190* (1), 012034.

(14) Michalowicz, A.; Moscovici, J.; Muller-Bouvet, D.; Provost, K. MAX (Multiplatform Applications for XAFS) New Features. *Journal of Physics: Conference Series* **2013**, *430* (1), 012016.

(15) Dean, J. R. *Practical Inductively Coupled Plasma Spectroscopy*.

(16) Blach, T. P.; Gray, E. MacA. Sieverts Apparatus and Methodology for Accurate Determination of Hydrogen Uptake by Light-Atom Hosts. *Journal of Alloys and Compounds* **2007**, *446–447*, 692–697. https://doi.org/10.1016/j.jallcom.2006.12.061.

(17) Bielmann, M.; Kato, S.; Mauron, P.; Borgschulte, A.; Züttel, A. Characterization of Hydrogen Storage Materials by Means of Pressure Concentration Isotherms Based on the Mass Flow Method. *Review of Scientific Instruments* **2009**, *80* (8), 083901. https://doi.org/10.1063/1.3186731.

(18) Verbeken, K. Analysing Hydrogen in Metals: Bulk Thermal Desorption Spectroscopy (TDS) Methods. In *Gaseous Hydrogen Embrittlement of Materials in Energy Technologies*; Elsevier, 2012; pp 27–55. https://doi.org/10.1533/9780857095374.1.27.

(19) Blaine, R. L.; Kissinger, H. E. Homer Kissinger and the Kissinger Equation. *Thermochimica Acta* **2012**, *540*, 1–6. https://doi.org/10.1016/j.tca.2012.04.008.

# CHAPTER III: POROUS CARBONS WITH PALLADIUM

### 3.1 Synthesis of Palladium carbon materials

The aim of this chapter is to study the interaction between hydrogen and ultra-small sized Pd and to follow $H_2$ effect of down scaling from bulk material to nano, sub-nano and until single atom state (Figure 3.1).

The following samples will be investigated:

- 3 samples composed of Pd nanoparticles supported on two porous carbons (High Surface Area Graphite - HSAG - with 500 $m^2/g$ from Imerys Graphite & Carbon and the activated carbon, AC with 1400 $m^2/g$ from STREM Chemicals).

-2 samples containing Pd single atom catalyst (SACs) with different concentrations dispersed on a nitrogen-rich activated carbon (AC, a commercial porous carbon - with 1400 $m^2/g$ from STREM Chemicals),

-for the sake of comparison, Pd bulk in powder form was also studied.

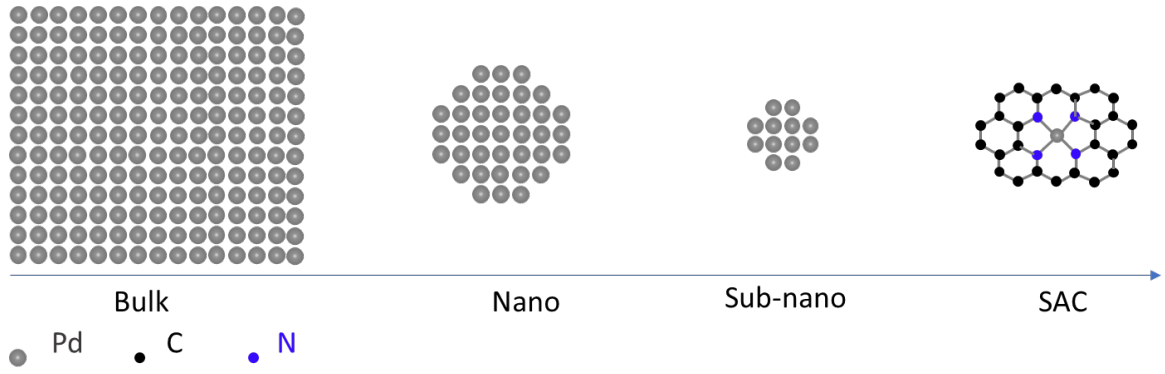


*Figure 3. 1: Illustration of downsizing Pd size from bulk state to single atom state.*

The synthesis of nanoparticles and SAC was detailed in **Chapter II**.

The Pd SAC was prepared by a cascade anchoring strategy adapted from Zhao *et al.*[1] The Pd SAC was dispersed on a nitrogen-rich AC by the liquid impregnation of the pristine AC with $PdCl_2$ precursor in an aqueous solution in the presence of a chelating agent (EDTA) followed by pyrolysis under Ar at 800 °C in the presence of a source of nitrogen (melamine). This treatment allows the simultaneous preparation of metal SAC and doping of carbon with nitrogen. The pyrolyzed sample was further leached with aqua regia for 6 h to remove possible large clusters/nanoparticles formed during pyrolysis. The samples are named *x*-Pd-AC, where *x* (0.8 or 7.5 wt.%) stands for the metal content over the entire sample mass. A

nitrogen doped carbon sample ($CN_x$) was prepared with same method without the addition of Pd precursor.

The Pd nanoparticles samples were prepared by a simple method based on the liquid impregnation of the carbon supports (AC or HSAG) with a $H_2PdCl_4$ precursor aqueous solution, followed by reduction under $H_2$/Ar flow at 300 °C or 500 °C, as described earlier.[2] The samples are named *x*-Pd@Y-*z*, where *x* (10 wt.%) is the metal content over the entire sample mass, Y (AC or HSAG) stands for the carbon support and *z* (300 or 500 °C) represents the reduction temperature.

### 3.2 Pd nanoparticles supported on carbons

First, we will discuss the physicochemical and hydrogen sorption properties of the three nanosized Pd supported on carbons prepared by liquid impregnation and subsequent reduction.

#### 3.2.1 Physicochemical properties of materials

The synthesized materials were firstly characterized by X-Ray Diffraction (XRD) for the determination of their structural properties (Figure 3.2). Two carbon materials were used here: HSAG and AC.

The HSAG is a crystalline graphite with the main diffraction peak at 26.4° (Miller index (002)). The HSAG maintains its crystalline structure after the synthesis of Pd nanoparticles. The sample 10-Pd@HSAG-500 (Figure 3.2 a) shows sharp Pd diffraction peaks indexed (111), (200), (220) and (311) along with the ones from graphite. However, the diffraction peaks broaden for the sample 10-Pd@HSAG-300 (Figure 3.2 b) and only the diffraction peak (111) can be noticed. This indicates that Pd nanoparticles formed in the latter sample might have a smaller size distribution than the former sample.[3]

The AC is mainly amorphous with a small graphitic component, as proven by the presence of the (002) sharp peak at 26.4°. Nevertheless, some impurities are also present which give rise to several small additional diffraction peaks. The diffraction peaks of Pd are hardly visible in the diffractogram of 10-Pd@AC-300 (Figure 3.2 c), only the plane (111) is slightly noticeable as a broad contribution overlapping the carbon contribution at around 40-50°. This suggests probably that the size of Pd nano-objects is too small to be detected by XRD

(too short coherence lengths for X-ray diffraction). This hypothesis will be further verified by transmission electron microscopy.

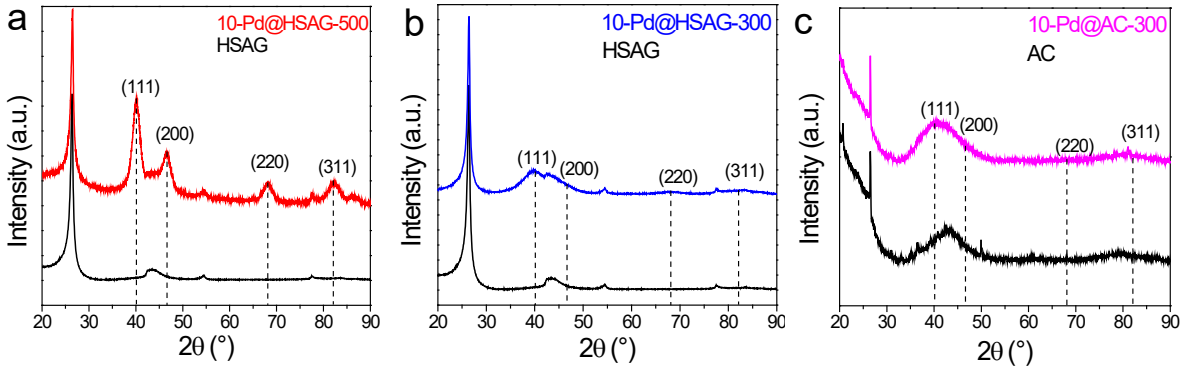


*Figure 3. 2: XRD patterns of a) HSAG and 10-Pd@HSAG-500, b) HSAG and 10-Pd@HSAG-300 and c) AC and 10-Pd@AC-300.*

These materials were characterized by Transmission Electron Microscopy (TEM) to analyse the dispersion of Pd on the carbon hosts as well as the formation of metal nanoparticles or clusters.

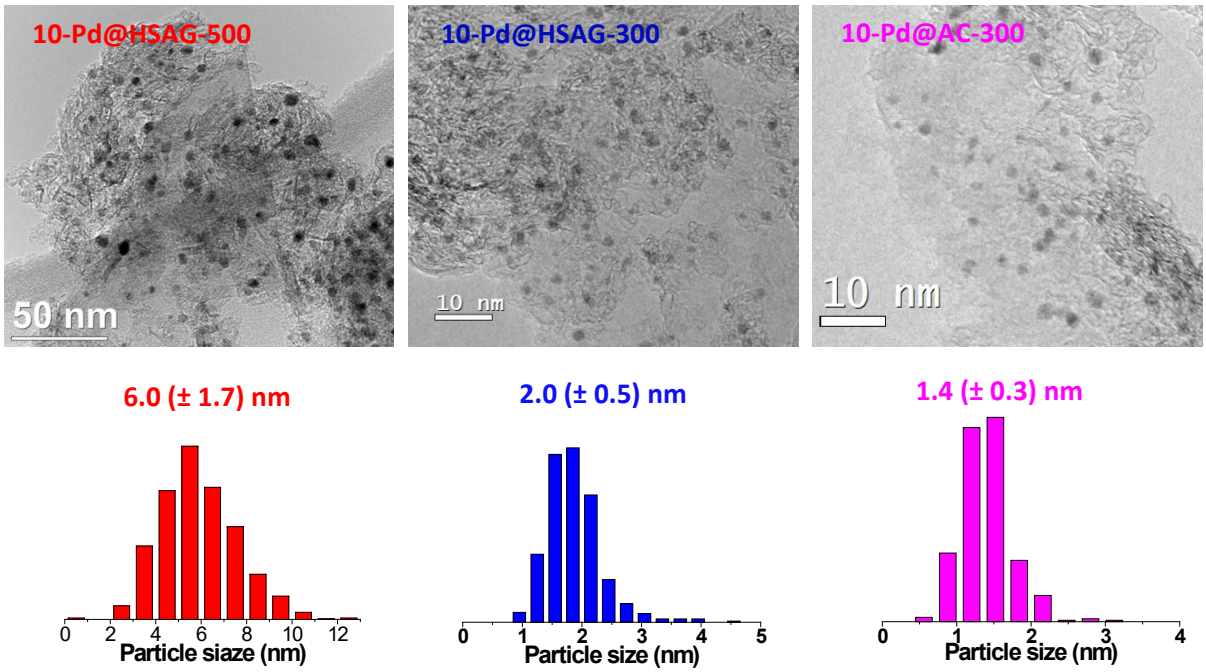


*Figure 3. 3: TEM images of 10-Pd@HSAG-500, 10-Pd@HSAG-300 and 10-Pd@AC-300, together with the particle size distribution of Pd nanoparticles.*

The TEM bright field images of different Pd samples are shown in Figure 3.3. For the samples 10-Pd@HSAG-500, 10-Pd@HSAG-300, 10-Pd@AC-300, Pd nanoparticles are noticed as the black spots. They are well dispersed on the carbon supports. The average particle size

was determined by the statistical analysis of particles size histograms. Pd nanoparticles embedded on HSAG have a mean size of 6.0(±1.7) nm for the reduction temperature 500 °C. The average particle size reduced to 2.0(±0.5) nm when the reduction temperature decreased to 300 °C. Pd nanoparticles supported on AC, which has a larger surface area than HSAG (AC: 1400 $m^2/g$ > HSAG: 500 $m^2/g$ ), has the smallest average size, 1.4(±0.3) nm at a reduction temperature of 300 °C. Consequently, it can be concluded that the size of Pd nanoparticles decreases with decreasing the reduction temperature and with increasing the specific surface area of support. For the sake of the convenience and clarity, the samples containing Pd nanoparticles 10-Pd@HSAG-500, 10-Pd@HSAG-300 and 10-Pd@AC-300 will be further named 6.0 nm Pd, 2.0 nm Pd and 1.4 nm Pd, respectively.

The textural properties were characterized by nitrogen adsorption/desorption measurements at 77 K. Figure 3.4 shows the $N_2$ adsorption/desorption curves for HSAG, AC and the Pd samples. A hysteresis loop can be observed for both HSAG and AC, meaning that they contain mesopores. The micropores contribution is relatively high at low pressure values for AC, indicating that the AC is more microporous than the HSAG.

The surface area, as determined by BET method in the relative pressure range $P/P_0$ = 0.05 – 0.20 decreases with the Pd nanoparticles dispersed on the support (Table 3.1). There are two reasons to explain the diminution of the surface area. First, the volumetric mass density of Pd (12.02 $g/cm^3$) is bigger than C (graphite: 2.09-2.23 $g/cm^3$, AC: 1.80-2.10 $g/cm^3$). Therefore, adding Pd in carbon increases the density of the material. The specific surface area is defined as the total surface area per unit of mass. Thus, for the same kind of material, the higher the density, the smaller the specific surface area. Secondly, Pd nanoparticles supported on carbons can block the pores of the materials and consequently the accessible pores, and specific surface area decreases after the synthesis of Pd nanoparticles.

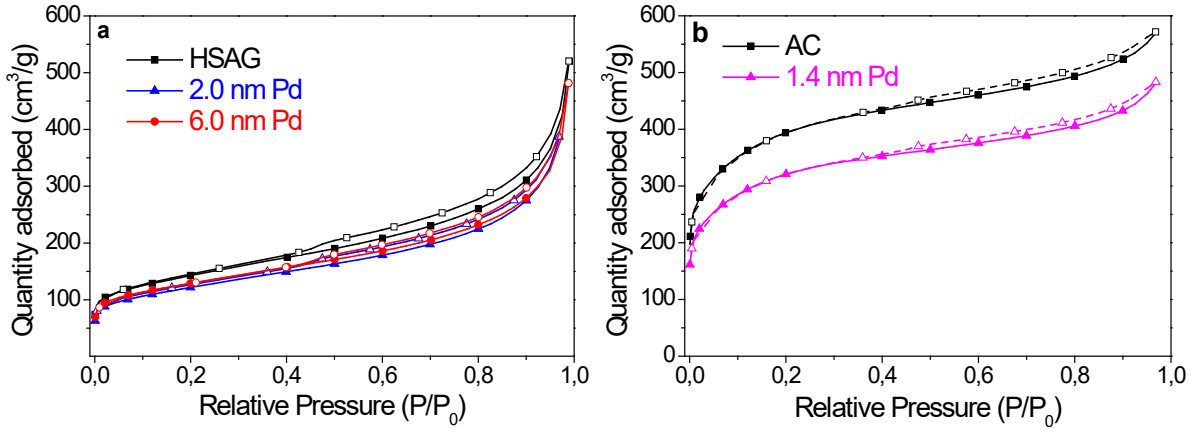


*Figure 3. 4: $N_2$ adsorption/desorption curves at 77 K of (a) HSAG, 6.0 nm and 2.0 nm Pd, and (b) AC and 1.4 nm Pd.*

| sample | Surface area ($m^2/g$) |
|---|---|
| **HASG** | 500(±10) |
| **6.0 nm** | 450(±10) |
| **2.0 nm** | 430(±10) |
| **AC** | 1400(±10) |
| **1.4 nm** | 1170(±10) |

*Table 3. 1: Specific surface area of HSAG, AC, 6.0 nm, 2.0 nm and 1.4 nm Pd.*

### 3.2.2 Nanosized Pd interaction with hydrogen

The hydrogen sorption properties of Pd nanoparticles were characterized by several techniques including: Pressure-Composition Isotherms (PCI), *in situ* X-Ray Diffraction (*in situ* XRD), *in situ* X-Ray Absorption (*in situ* XAS), Thermal Desorption Spectroscopy (TDS) as well as a theoretical approach based on atomic simulations.

#### 3.2.2.1 Hydrogen sorption properties at room temperature

The Pressure-Composition Isotherms (PCI) of these materials have been studied firstly at room temperature up to 1 bar $H_2$. Figure 3.5 shows the details of absorption/desorption $H_2$ curves of 1.4 nm, 2.0 nm, 6.0 nm Pd nanoparticles as well as Pd bulk. The carbon supports have negligible $H_2$ uptake under present conditions[4] (see also in **section 3.3.1**, **Figure 3.24**). Consequently, all $H_2$ capacity can be related to H absorption in Pd, and the H absorbed can be expressed as H/Pd in *x*-axis. The PCI curves clearly show size effects when Pd size decreases. These effects can be summarized as followed:

1) The total capacity at 1 bar $H_2$ pressure diminishes with the decrease of Pd size;

2) The $\alpha_{max}$ solubility limit (solid solution) increases with the decrease of Pd size;
3) The $\beta_{min}$ solubility limit (hydride phase) decreases with the decrease of Pd size;
4) The plateau becomes slopped for 6.0 nm and 2.0 nm Pd, and it completely disappears for 1.4 nm Pd;
5) Absorption and desorption show only partial reversibility for Pd nanoparticles at low pressure, contrary to Pd bulk.

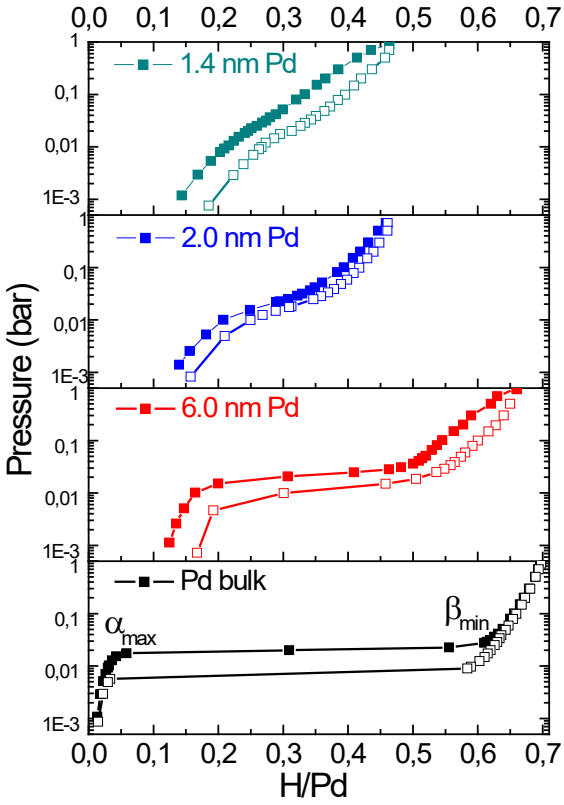


*Figure 3. 5: Pressure-composition-isotherms curves for Pd bulk, 6.0 nm, 2.0 nm and 1.4 nm Pd at 25 °C. Full and empty symbols stand for absorption and desorption, respectively.*

Overall, the hydrogen absorption capacity diminishes with decreasing the particles size. For example, at 1 bar $H_2$ pressure, the total amounts absorbed are 0.70, 0.65, 0.45 and 0.45 H/Pd for Pd bulk, 6.0 nm, 2.0 nm and 1.4 nm Pd nanoparticles, respectively. Nützenadel *et al.*[5] explained that the diminution of hydrogen absorption capacity is due to the relative number of interstitial sites which reduces with decreasing nanoparticle size. In fact, Pd atoms on surface provide only 50% of interstitial sites because they are half outside. Surface Pd atoms can be neglected for Pd bulk, while they can no longer be ignored for Pd nanoparticles. Normally, the proportion of surface atoms increases with decreasing particle size.

Consequently, the available interstitial sites decrease as the Pd size diminishes, along with the hydrogen capacity. The most recognized hypothesis to explain the increase of $\alpha_{max}$ is that there exist subsurface sites which are more favourable to form solid solution and a bulk-like inner core that acts like Pd bulk[6–8]. Upon this hypothesis, the interstitial sites of the subsurface are more favourable to be occupied and to form solid solutions with hydrogen than the bulk-like ones.

There are several explanations regarding the plateau which becomes steeper with reducing the particle size: surface tension, broad size distribution of nanoparticles, interfacial stress of the nanoparticles with the stabilizer/host.[9–11] The absence of the plateau for 1.4 nm Pd indicates that the hydride phase is no longer formed and only solid solutions with H are expected, in very good agreement with previous findings for 1.0 nm Pd supported on MIL-101.[12]

The non-closing absorption/desorption PCI curves for Pd nanoparticles are ascribed to the hydrogen trapping in strong interstitial sites of the lattice, which will be discussed in detail later.

To better understand hydrogen sorption properties with Pd at room temperature, *in situ* XRD under 1 bar $H_2$ was carried out (Figure 3.6). The sample was first analysed by XRD under vacuum (initial state). Then 1 bar $H_2$ was filled in the sample holder to check the hydride formation. Finally, XRD was recorded at dynamic vacuum (desorbed state). As shown in these diffractograms, the peaks of Pd shift to smaller 2θ angles under $H_2$ as compared to Pd under vacuum owing to the formation of Pd hydride phase for Pd bulk, 6.0 nm and 2.0 nm Pd, while no noticeable shift for 1.4 nm Pd is observed. The latter observation can be explained by two plausible propositions. Firstly, as discussed previously, only the diffraction peak of Pd (111) is slightly noticeable for 1.4 nm Pd supported on AC due to the ultra-small particles size. Moreover, it overlaps with the diffraction peaks of AC support. Consequently, it is very difficult to discern the shift of diffraction peak under $H_2$. Secondly, perhaps there is no hydride formation for 1.4 nm Pd under 1 bar $H_2$ at room temperature to give rise to a remarkable shift of the diffraction peaks. The latter hypothesis is supported by the result obtained from PCI experiment at room temperature. We can also observe that the shift of the peaks becomes smaller as the Pd size reduces, which indicates smaller lattice parameter change with decreasing the Pd size. The lattice constants (*a*) have been determined for Pd samples under

vacuum and 1 bar $H_2$ (Table 3.2). In order to have a clear comparison with the nearest $R_{Pd\text{-}Pd}$ obtained from *in situ* XAS experiment discussed in the next paragraph, the nearest Pd-Pd distance ($R_{Pd\text{-}Pd}$) values have also been also determined by employing formula: $R_{Pd-Pd} = a/\sqrt{2}$ (Face-Centred Cubic) lattice (Table 3.2). All Pd samples have the same $R_{Pd\text{-}Pd}$ distance (2.752 Å) under vacuum, in agreement with previous reported values for Pd bulk.[13,14] The $R_{Pd\text{-}Pd}$ is 2.863, 2.844 and 2.822 Å for Pd bulk, 6.0 nm and 2.0 nm Pd under 1 bar $H_2$, respectively. The decrease of the lattice parameter expansion with reducing Pd size under 1 bar $H_2$ suggests that the $H_2$ absorption capacity diminishes. This is consistent with the PCI curves shown in Figure 3.5.

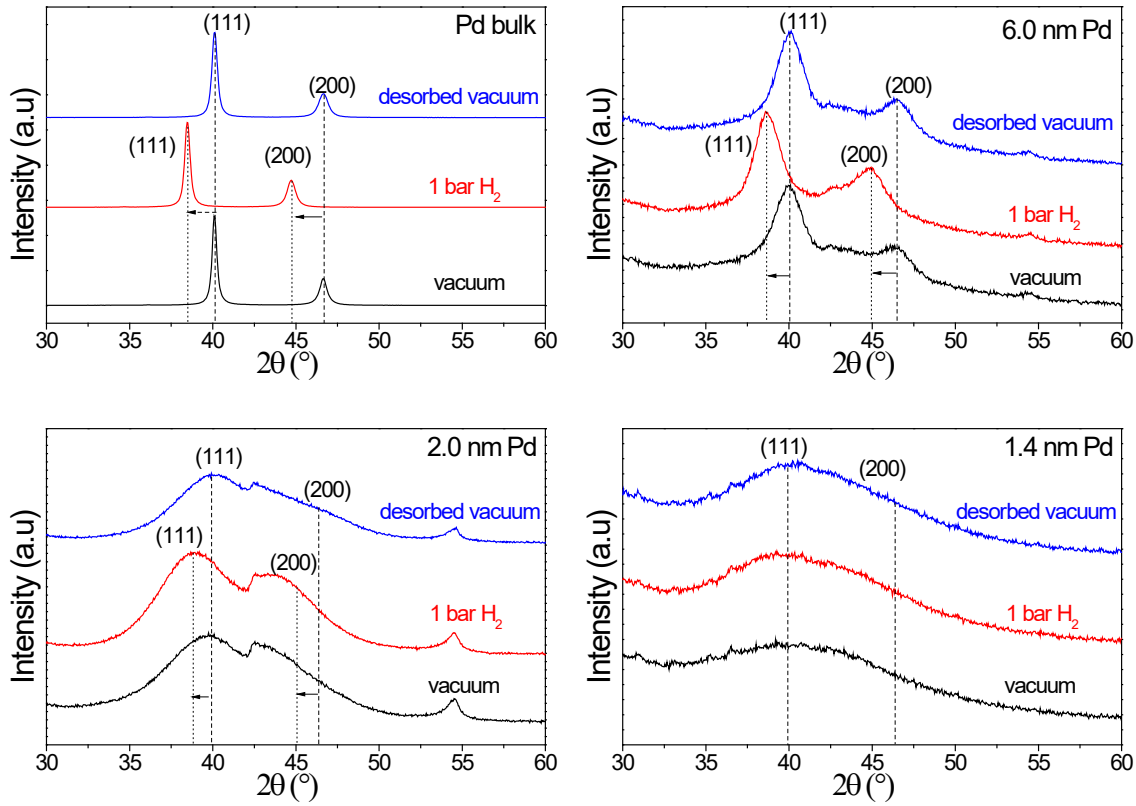


*Figure 3. 6: In situ XRD under vacuum (initial state), under 1 bar $H_2$ (absorbed state) followed by vacuum (desorbed state) for Pd bulk, 6.0 nm, 2.0 nm and 1.4 nm Pd at 25 °C.*

| Sample | Bulk | | 6,0 nm | | 2,0 nm | | 1,4 nm |
|---|---|---|---|---|---|---|---|
| | a (Å) | $R_{Pd-Pd}$ (Å) | a (Å) | $R_{Pd-Pd}$ (Å) | a (Å) | $R_{Pd-Pd}$ (Å) | - |
| Initial state | 3,891 | 2,751 | 3,891 | 2,751 | 3,892 | 2,752 | - |
| 1 bar $H_2$ | 4,049 | 2,863 | 4,022 | 2,844 | 3,991 | 2,822 | - |
| *ΔR/R* | - | 4,10% | - | 3,40% | - | 2,50% | - |

*Table 3. 2: Lattice parameter and the distance of nearest Pd-Pd ($R_{Pd-Pd}$) for Pd bulk, 6.0 nm, 2.0 nm and 1.4 nm Pd determined by XRD under vacuum and under 1 bar $H_2$, and the variation of $R_{Pd-Pd}$ (ΔR/R) for Pd samples under 1 bar $H_2$ as compared to initial state.*

In order to investigate the local structure change of Pd samples under absorption/desorption process at room temperature, *in situ* XAS was carried out under different $H_2$ partial pressures at room temperature. Prior to the experiment, Pd samples were pre-treated under $H_2$ and then He at high temperature, 250 °C, to completely remove water molecules formed during reduction of the surface oxide layer at room temperature together with hydrogen atoms possibly adsorbed/absorbed in Pd samples. Afterward, the samples were exposed under several $H_2$ partial pressures: 0, 50, 250, 500 and 1000 mbar in absorption as well as, 1000, 500, 250, 50 and 0 mbar in desorption under isothermal conditions at 25 °C (Figure 3.7). More details of the experiment can be seen in **Chapiter II materials and methods**.

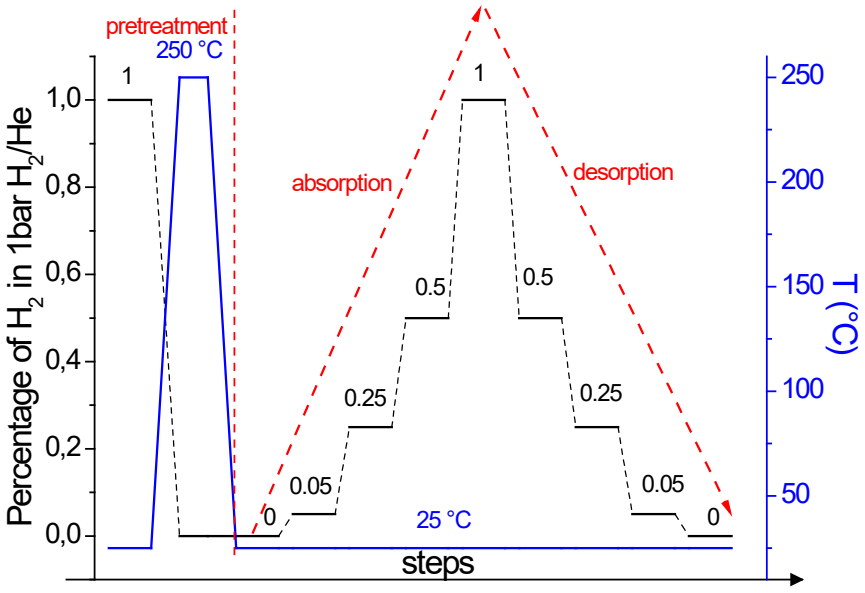


*Figure 3. 7: Steps of in situ XAS experiment for Pd Bulk, 6.0 nm, 2.0 nm and 1.4 nm Pd.*

The Fourier Transform (FT) of EXAFS spectra for Pd bulk, 6.0 nm, 2.0 nm and 1.4 nm Pd nanoparticles under different $H_2$ partial pressures at 25 °C are shown in Figure 3.8. Under

$H_2$, the main FT peak intensity decreases with decreasing the Pd size. FT peaks shift to larger distances and their intensity decreases with increasing $H_2$ pressure. The latter observation is size dependent: the smaller the size, the minor the effect on FT.

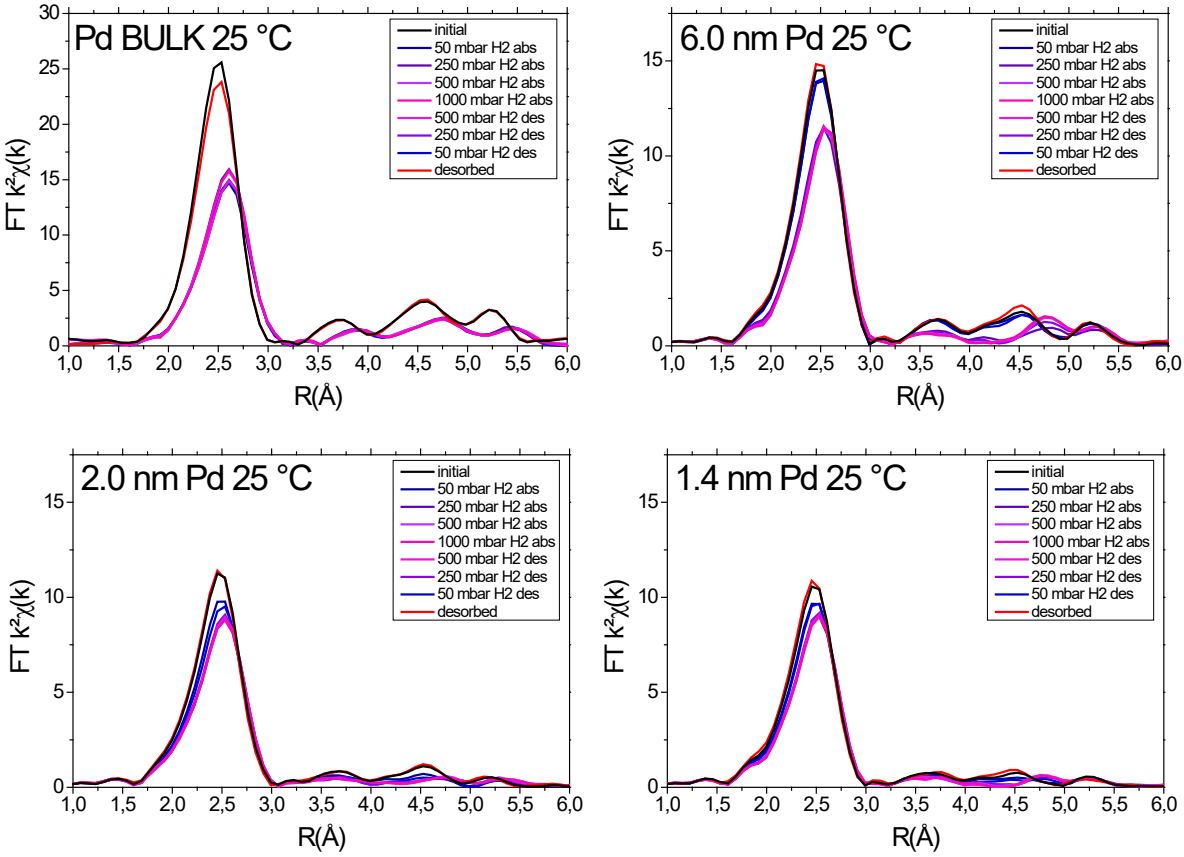


*Figure 3. 8: FT of the EXAFS spectra ($k^2x(k)$) for Pd bulk and 6.0 nm, 2.0 nm and 1.4 nm Pd under various partial pressures of $H_2$ at 25 °C.*

The EXAFS refinement results for all samples are displayed in Table 3.3. Typical refinements are plotted in Figure 3.9. The average coordination number, *N*, (average of all experiment points) decreases from 11.5 for bulk (12 typical for bulk fcc metals) to 10.3, 7.9 and 7.5 for 6.0 nm, 2.0 nm and 1.4 nm Pd, respectively. The decrease of *N* can be understood by an enlarged number of dangling bonds of surface atoms increasingly important with decreasing the size.[15] The initial value of the Debye–Waller factor shows an increase from 0.0066 to 0.0087 from Pd bulk to 1.4 nm particle size. This finding can be explained as an increase of the static disorder in nanoparticles due to the relaxation of bond lengths at the surface, which undergoes substantial strain. Moreover, within the same material, the Debye–Waller factor rises with increasing the hydrogen pressure, which can be linked to the hydride phase formation and consequently, to the rise of the static disorder by hydrogen insertion

within the interstitials. It is worth noticing that the coordination numbers and Debye–Waller factors do not differ significantly for 2.0 nm and 1.4 nm Pd because the discrimination among these sizes is within the error bar by this experimental technique.

| Sample | $H_2$ pressure (mbar) | $R_{Pd-Pd}$ (Å) | N | $\sigma^2$ (Å$^2$) | $C_3$ ($10^{-4}$ Å$^3$) | QF |
|---|---|---|---|---|---|---|
| **Bulk** | 0 | 2.748(1) | 11.5(5) | 0.0066(1) | - | 1.4 |
| | 50 | 2.842(1) | 11.5(5) | 0.0088 (1) | - | 0.8 |
| | 250 | 2.848(1) | 11.5(5) | 0.0084(1) | - | 1.5 |
| | 500 | 2.849(1) | 11.5(5) | 0.0084(1) | - | 1.5 |
| | 1000 | 2.852(1) | 11.5(5) | 0.0084(1) | - | 1.4 |
| | 500 | 2.850(1) | 11.5(5) | 0.0087(1) | - | 1.3 |
| | 250 | 2.848(1) | 11.5(5) | 0.0087(1) | - | 1.3 |
| | 50 | 2.842(1) | 11.5(5) | 0.0087(1) | - | 1.2 |
| | 0 | 2.747(1) | 12.0(5) | 0.0072(1) | - | 2.3 |
| **6.0 nm** | 0 | 2.748(1) | 10.4(5) | 0.0076(1) | - | 3.3 |
| | 50 | 2.804(1) | 10.2(5) | 0.0090(2) | - | 2.1 |
| | 250 | 2.823(1) | 10.2(5) | 0.0086(2) | - | 2.3 |
| | 500 | 2.826(1) | 10.2(5) | 0.0086(2) | - | 2.3 |
| | 1000 | 2.828(1) | 10.2(5) | 0.0086(2) | - | 2.3 |
| | 500 | 2.826(1) | 10.3(5) | 0.0086(2) | - | 2.4 |
| | 250 | 2.824(1) | 10.2(5) | 0.0086(2) | - | 2.3 |
| | 50 | 2.816(1) | 10.2(5) | 0.0086(2) | - | 2.2 |
| | 0 | 2.758(1) | 10.4(5) | 0.0076(2) | - | 3.2 |
| **2.0 nm** | 0 | 2.748(1) | 7.6(5) | 0.0085(2) | 1.1(4) | 3.5 |
| | 50 | 2.777(1) | 7.7(5) | 0.0091(2) | 1.1(4) | 2.0 |
| | 250 | 2.793(1) | 7.9(5) | 0.0098(2) | 1.1(4) | 2.1 |
| | 500 | 2.797(1) | 8.0(5) | 0.0098(2) | 1.1(4) | 2.3 |
| | 1000 | 2.799(1) | 8.0(5) | 0.0098(2) | 1.5(4) | 2.5 |
| | 500 | 2.798(1) | 8.0(5) | 0.0097(2) | 1.1(4) | 2.1 |
| | 250 | 2.795(1) | 8.1(5) | 0.0097(2) | 1.1(4) | 2.4 |
| | 50 | 2.785(1) | 7.9(5) | 0.0094(2) | 1.1(4) | 2.1 |
| | 0 | 2.768(1) | 7.8(5) | 0.0086(2) | 1.5(4) | 2.2 |
| **1.4 nm** | 0 | 2.745(1) | 7.5(5) | 0.0087(2) | 1.1(3) | 2.0 |
| | 50 | 2.772(1) | 7.5(5) | 0.0090(2) | 1.1(3) | 1.5 |
| | 250 | 2.789(1) | 7.5(5) | 0.0095(3) | 1.1(3) | 1.2 |
| | 500 | 2.794(1) | 7.6(5) | 0.0094(3) | 1.1(3) | 1.1 |
| | 1000 | 2.798(1) | 7.5(5) | 0.0094(3) | 1.1(3) | 1.1 |

| | | | | | | |
|---|---|---|---|---|---|---|
| | 500 | 2.795(1) | 7.4(5) | 0.0093(3) | 1.1(3) | 1.1 |
| | 250 | 2.792(1) | 7.5(5) | 0.0093(3) | 1.1(3) | 1.0 |
| | 50 | 2.779(1) | 7.6(5) | 0.0091(2) | 1.1(3) | 1.3 |
| | 0 | 2.764(1) | 7.5(5) | 0.0087(2) | 1.1(3) | 1.3 |

*Table 3. 3: EXAFS refinement result for Pd bulk and 6.0 nm, 2.0 nm and 1.4 nm Pd under various $H_2$ pressures at 25 °C. The nearest Pd-Pd distance ($R_{Pd-Pd}$), the coordination number (N), the Debye-Waller factor ($\sigma^2$), $C_3$ cumulant and the confidence factor (QF) are given.*

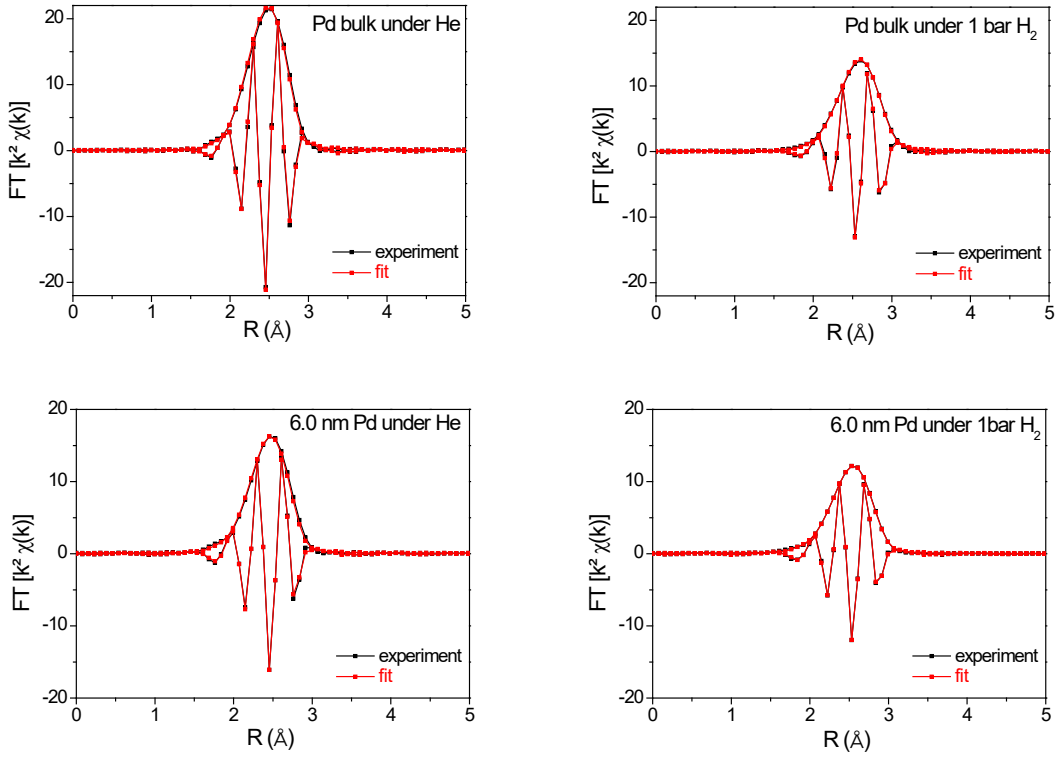

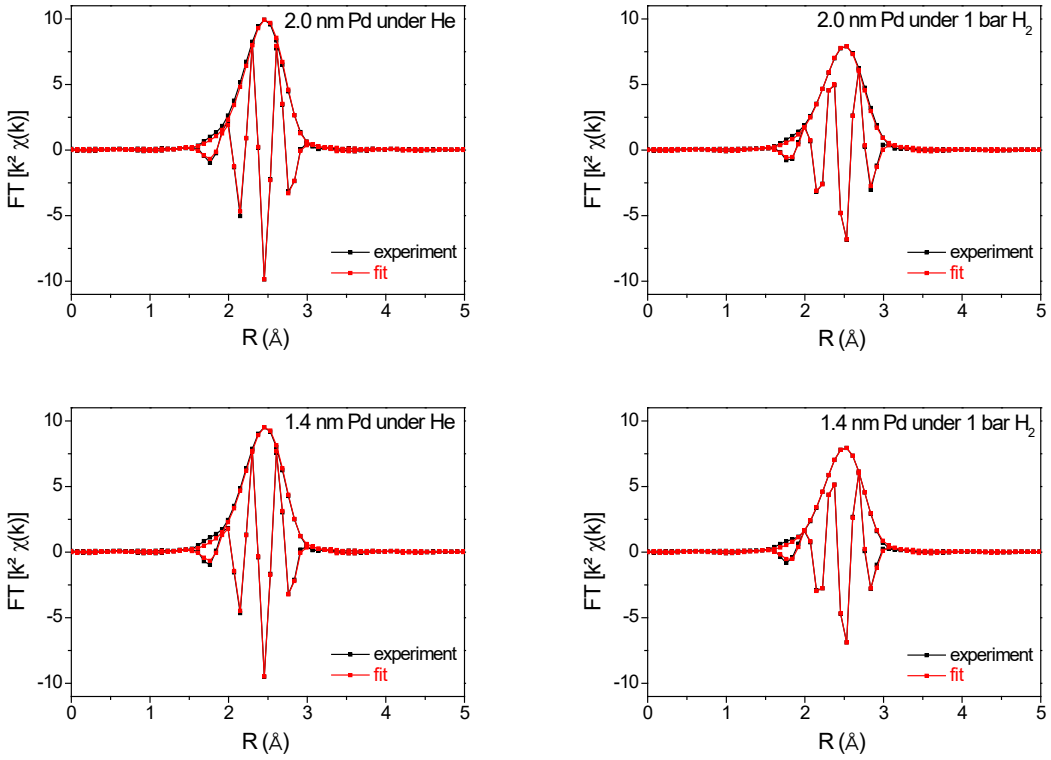


*Figure 3. 9: Selected EXAFS refinements between FT (black) and fitted (red) for Pd bulk and 6.0 nm, 2.0 nm and 1.4 nm Pd under He and 1 bar $H_2$ at room temperature.*

The initial $R_{Pd-Pd}$ (clean surfaces and H-free nanoparticles after heat-treatment, as described above) for 6.0 and 2.0 nm Pd particles is similar to the bulk value (2.748(1) Å). For 1.4 nm Pd, the initial $R_{Pd-Pd}$ is slightly smaller than the bulk value (2.745(1) Å). After exposed at 1 bar $H_2$, the values become 2.852(1), 2.828(1), 2.799(1) and 2.798(1) Å for Pd bulk, 6.0 nm, 2.0 nm and 1.4 nm Pd nanoparticles, respectively. A comparison of results obtained from *in situ* XRD and *in situ* XAS is shown in the Table 3.4. There is a good agreement between XRD and XAS results.

| EXAFS | $R_{Pd-Pd}$ (Å) FCC | | | |
|---|---|---|---|---|
| Sample | Bulk | 6.0 nm | 2.0 nm | 1.4 nm |
| Vacuum | 2.748(1) | 2.748(1) | 2.748(1) | 2.745(1) |
| 1 bar H2 | 2.852(1) | 2.828(1) | 2.799(1) | 2.798(1) |
| ΔR/R **XAS** | 3.8% | 2.9% | 2.0% | 2.0% |
| ΔR/R **XRD** | 4.1% | 3.4% | 2.5% | - |

*Table 3. 4: The distance of nearest Pd-Pd ($R_{Pd-Pd}$) for Pd bulk, 6.0 nm, 2.0 nm and 1.4 nm Pd under vacuum and under 1 bar $H_2$ determined by in situ **XAS** and comparison of $\Delta R_{Pd-Pd}/R_{Pd-Pd}$ found by in situ **XAS** and in situ **XRD** for desorbed Pd and Pd under 1 bar $H_2$.*

Comparisons between the PCI curves and the $R_{Pd-Pd}$ as function of pressure are shown in Figure 3.10. A good agreement is noticed between the PCI curves and the evolution of $R_{Pd-Pd}$ as function of pressure, irrespective of the particle size.

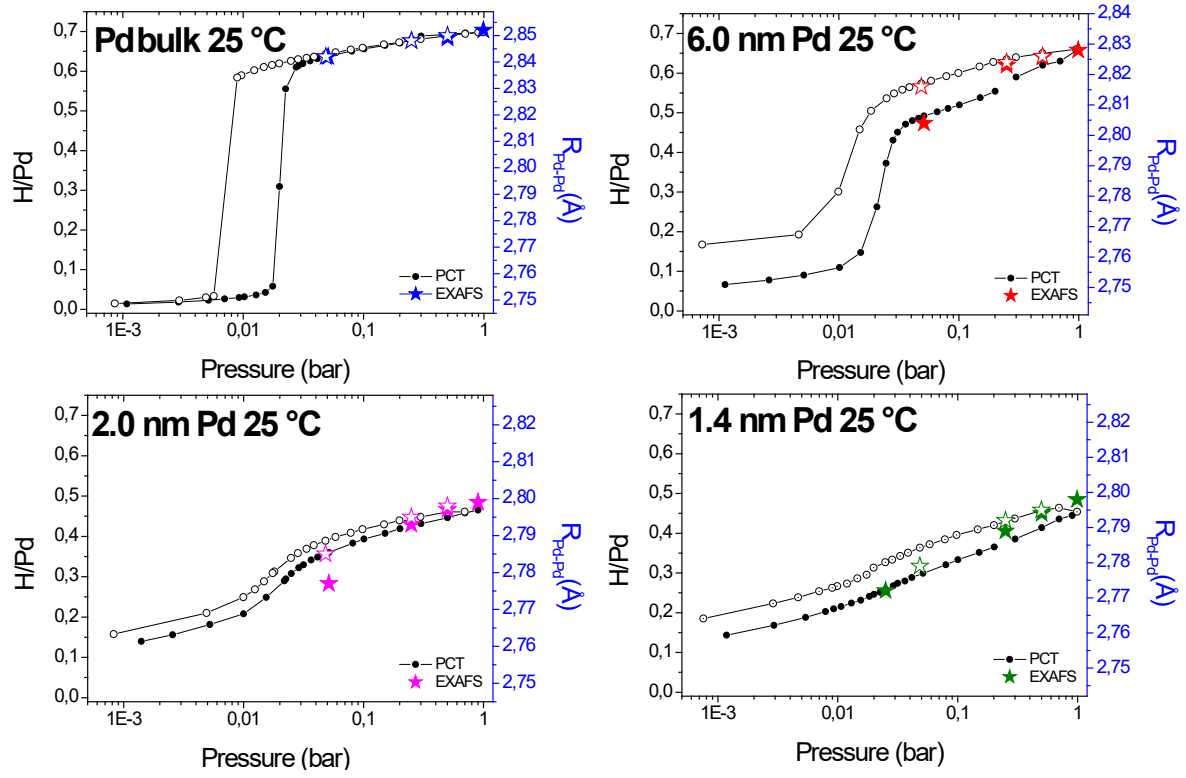


*Figure 3. 10: Comparison between the PCI curves (expressed as H/Pd vs. Pressure) and the nearest Pd-Pd distances determined by EXAFS as function of $H_2$ pressure for Pd bulk, 6.0 nm, 2.0 nm and 1.4 nm Pd at 25 °C. Full and empty symbols stands for absorption and desorption, respectively.*

A thorough analysis of the refinements results in Table 3.3 allows us to draw several remarks:

(1) For Pd bulk the absorption/desorption is fully reversible.

(2) For all Pd nanoparticles the values of $R_{Pd–Pd}$ after desorption are all systematically larger than the initial ones: 2.758 vs. 2.748 Å for 6.0 nm Pd, 2.768 vs. 2.748 Å for 2.0 nm Pd and 2.764 vs. 2.745 Å for 1.4 nm Pd.

These findings are in good agreement with PCI curves proving that hydrogen absorption/desorption is not fully reversible in nano scaled Pd and H is irreversibly trapped inside the lattice of Pd nanoparticles. Moreover, the larger $R_{Pd–Pd}$ observed after desorption suggests that H is trapped inside the volume of nanoparticles and not at the surface as adsorbed species, as recently suggested for Pd thin films.[16] This is supported by the hypothesis that H atoms chemisorbed at the surface of Pd nanoparticles have a negligible effect on the overall nearest neighbour distances determined by EXAFS.

To highlight the size dependence of this behaviour, Figure 3.11 displays the evolution of $R_{Pd–Pd}$ as function of the inverse of particle size in three states: initial clean metal, absorbed state under 1 bar of $H_2$ and desorbed state under He. Obviously, there is a size dependence of the quantity of trapped H (irreversible part): the smaller the size, the larger the irreversible H amount (the dashed area in Figure 3.11).

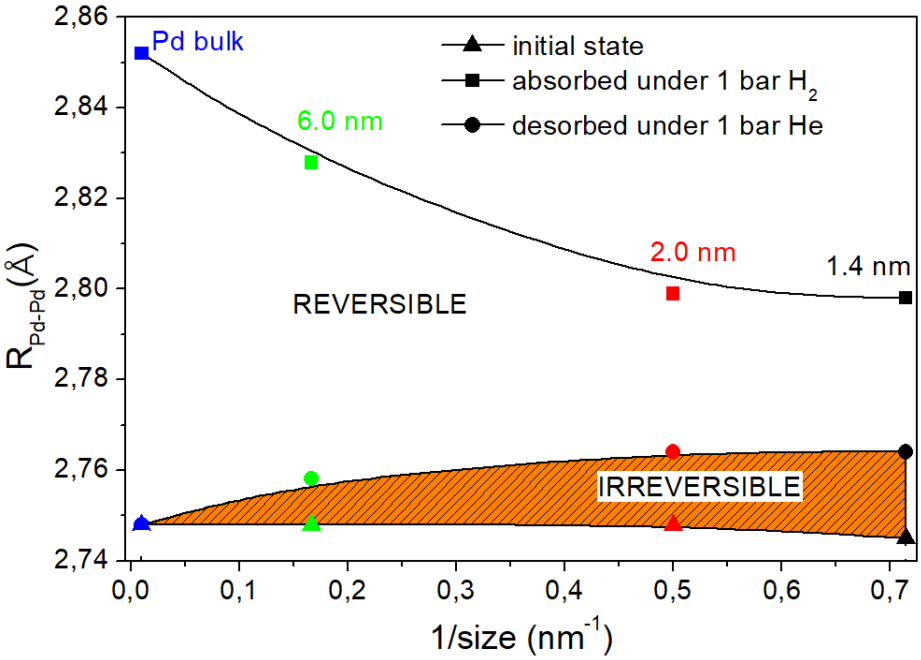


*Figure 3. 11: The variation of $R_{Pd-Pd}$ as function of the inverse of particle size for several sizes of Pd bulk, 6.0 nm, 2.0 nm and 1.4 nm Pd as initial state (triangle), absorbed state under 1 bar $H_2$ (square) and desorbed phase (circle).*

However, one might object that nanoparticles are possibly not fully desorbed because of kinetic issues rather than H trapping, although this may seem counterintuitive since kinetics of hydrogen desorption for nanoparticles are enhanced relative to bulk. We have demonstrated that our results listed in Table 3.3 were obtained at thermodynamic equilibrium (see Figure 3.12). Pd bulk has the slowest kinetics for hydrogen desorption and reaches the initial metal value after around 400 s whereas, all nanoparticles attain a stable value of $R_{Pd\text{-}Pd}$ distance in less than 200 s. However, the stabilisation values for all nanoparticles are above the Pd bulk, clearly indicating a H trapping, which is size dependent: the smaller the size, the larger final $R_{Pd\text{-}Pd}$ value. Consequently, this is a clear size effect not a kinetic issue that can be explained by the H trapping inside the lattice of Pd.

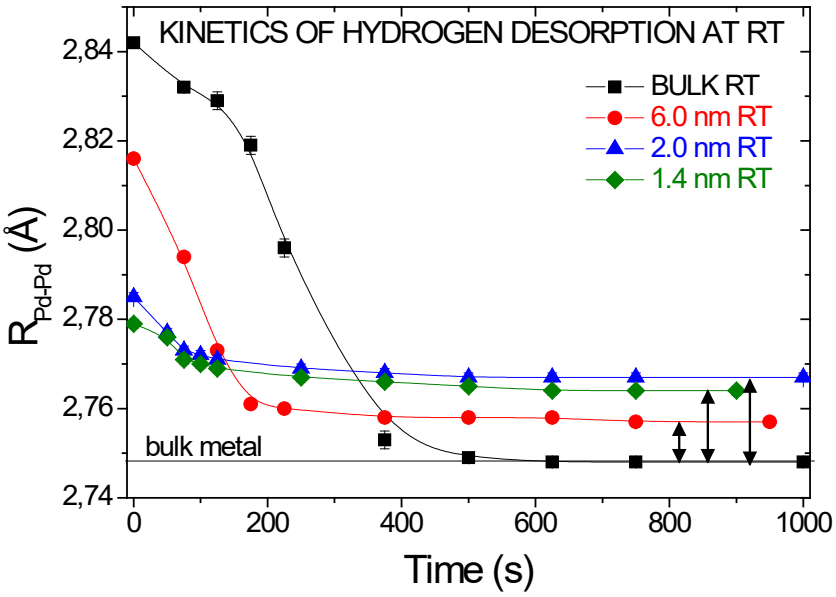


*Figure 3. 12: Kinetics of hydrogen desorption for Pd bulk, 6.0 nm, 2.0 nm and 1.4 nm Pd at 25 °C. The data are recorded during a pressure drop from 50 to 0 mbar $H_2$ partial pressure in He flow.*

The total amounts of absorbed H in Pd nanoparticles at 1 bar $H_2$ pressure and 25 °C are 0.65, 0.45 and 0.45 H/M for 6.0 nm, 2.0 nm and 1.4 nm Pd, respectively (from the PCI curves). The amount of trapped H can be calculated by dividing the expansion of the cell volume due to H trapping (from EXAFS results) per metal atom to the volume of the interstitial H atom in Pd. The latter one was determined from the variation of the lattice cell volume from Pd bulk metal to the hydride phase under 1 bar at 25 °C and the total amount of absorbed H in Pd bulk, as taken from the PCI curve. This value was found to be around 2.5(±0.2)

Å$^3$ per H atom, close to 2.9 Å$^3$ proposed by Peisl[17] for various *hcp*, *bcc*, and *fcc* metals and alloys. Using this approach, the quantities of trapped H in Pd nanoparticles are approximately 0.06, 0.12 and 0.12 H/M for 6.0 nm, 2.0 nm and 1.4 nm Pd, respectively. These values represent around 9, 26 and 26% of the total H sorption capacity for nanoparticles with average sizes 6.0, 2.0 and 1.4 nm, respectively. Consequently, the H trapping in Pd nanoparticles is increasingly important with decreasing the particle size. The amount of trapped H can be as high as 26% of the initial capacity for the smaller Pd nanoparticles (with 2.0 and 1.4 nm average sizes).

In order to check if H trapped inside Pd nanoparticles can be desorbed at high temperature, we have performed *in situ* XAS under He flow during heating to 250 °C (10 °C min$^{-1}$). The results of EXAFS refinements (nearest neighbour distance) are plotted in Figure 3.13. The nearest neighbour distance for Pd bulk steadily increases in agreement with the expected linear thermal expansion of metallic Pd (dotted line in Figure 3.13). However, Pd nanoparticles show a different behaviour with first a contraction of the nearest neighbour distance up to 150–170 °C followed by a linear rise almost parallel to the linear thermal expansion of Pd metal. The desorption at high temperature was also checked by the Thermo-desorption Spectroscopy at high temperature.

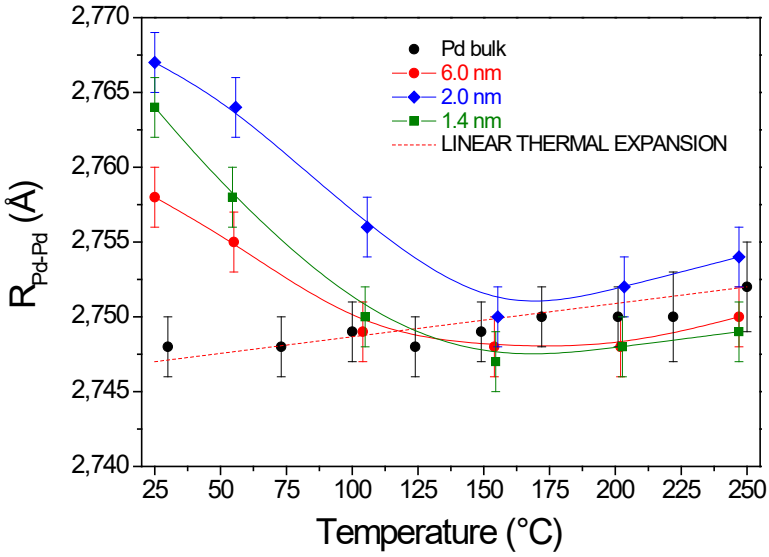


*Figure 3. 13: The thermal variation of $R_{Pd-Pd}$ in in situ XAS under He flow during heating to 250 °C for desorbed Pd bulk, 6.0 nm, 2.0 nm and 1.4 nm Pd (10 °C/min).*

In summary, size-dependent hydrogen trapping has been demonstrated in 6.0 nm, 2.0 nm and 1.4 nm Pd nanoparticles: smaller the size, larger the amount of trapped hydrogen in Pd nanoparticles. However, the experiment results indicate that the trapped H are located in the volume of nanoparticles without providing a clear localization of H within the core or the subsurface of nanoparticles, therefore a theoretical approach based on simulations is required to better understand this phenomenon.

### 3.2.2.2 Atomic Simulation

To get insight at the atomic scale and investigate the stability of H inside the Pd nanoparticles, theoretical approach based on tight-binding (TB) and Density Functional Theory (DFT) calculations was performed by our collaborators Hakim Amara, Daniel Förster from ONERA-CNRS and Yann Magnin from MIT.[18] More precisely, the formation energy ($E_f$) of H inserted in octahedral or tetrahedral interstitial sites along the radius of the nanoparticle was calculated according to the following equation :

$$E_f = E_{Pd+1H} - E_{Pd} - \frac{1}{2}E_{H_2} \qquad \text{(Equation 3.3)}$$

where $E_{Pd+1H}$ is the total energy of the Pd system (*fcc* bulk or nanoparticle) containing one hydrogen atom, $E_{Pd}$ is the total energy of the pure Pd system and $E_{H_2}$ is the total energy of the $H_2$ molecule. The more negative $E_f$ is, the more strongly the H atom is bound to neighbouring Pd atoms.

The formation energy of H atoms located in interstitial sites along the radius of the nanoparticles containing 147 and 309 atoms in cuboctahedron form, *i.e.*, from the centre to the outer surface, was calculated. The results are presented in Figure 3.14, where only the case of a nanoparticle containing 309 atoms is depicted, since the same conclusions can be drawn for the 147 atoms nanoparticle.

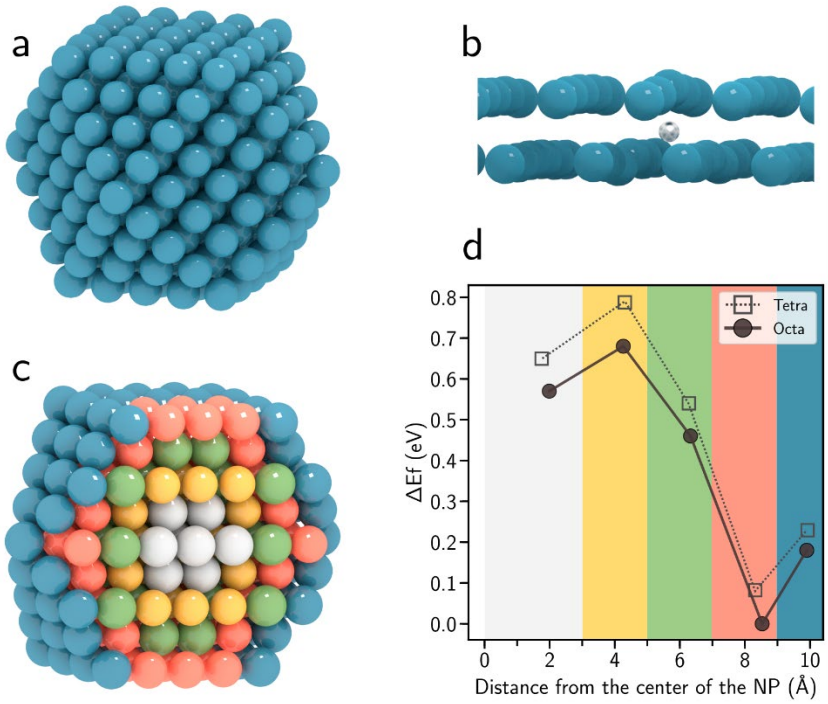


*Figure 3. 14. (a) Cuboctahedron NP of Pd containing 309 atoms. (b) Presence of the hydrogen atom (white) in the subsurface position of the NP inducing a local distortion of the first layers. (c) Slide view showing the different planes within the NP. (d) Formation energy of a hydrogen atom occupying different sites (octahedral and tetrahedral) along the radius of the NP. The different coloured areas correspond to the regions indicated in (c) : blue and red correspond to the surface and subsurface, respectively. The most stable configuration is set to zero.*

First of all, for each location within the nanoparticle, the octahedral position is the most stable, in agreement with the bulk case. More interestingly, it is clearly observed that the further away from the core (surface and subsurface sites), the more stable the H atom (Figure 3.14 d). This is particularly true for H atoms occupying subsurface sites, which are the most stable configurations (red part in Figures 3.14 c and d). The energy gain of an atom located at the subsurface in comparison with a bulk position is significant in the order of 1 eV. Indeed, in the presence of a surface the relaxation process is easier and the elastic energy cost is lower. Analysis of the local distortions around the incorporated H atom clearly shows this effect (Figure 3.14 b). On the one hand, the H atom located at the core is strongly constrained and cannot distort the structure leading to low distortion (1 %). In contrast, the H atom in the subsurface octahedral position can maximize the formation of Pd-H bonds, which are favourable, while at the same time it is able to strongly distort the structure to relax

the stresses (around 7%). Such a configuration is more stable than in the surface position since by occupying an octahedral site, the H atom forms stronger bonds. As a result, the formation of Pd-H bonds and the elastic effect required to relax the structures favour the segregation of strongly energetic interstitial sites toward subsurface positions. It is to be noted that the subsurface position has often been put forward to explain the catalytic activity of transition or noble metals [19,20]. Consequently, these DFT calculations suggest that hydrogen atoms are trapped at subsurface sites that are very stable and more favourable than bulk sites. It can be noted that no significant difference was observed for the two sizes of nanoparticles considered in the present work (147 and 309 atoms), since they have fairly similar diameters (1.7 and 2.1 nm, respectively). In both cases, the H atoms at subsurface positions are strongly bound to the Pd atoms and therefore less prone to leave the particle at room temperature, as observed experimentally. A higher temperature, around 150 °C, is needed for complete H desorption from these trapping sites.

#### 3.2.2.3 Thermodynamic properties

In order to study the thermodynamic properties of Pd interaction with hydrogen, enthalpy ($\Delta H$) and entropy ($\Delta S$) change of hydride formation have been determined from the PCI at variable temperatures for Pd bulk, 6 nm and 2.0 nm Pd (Figure 3.15). 1.4 nm Pd was not studied because it did not show a clear phase transition from metal to hydride phase at room temperature in the PCI curves.

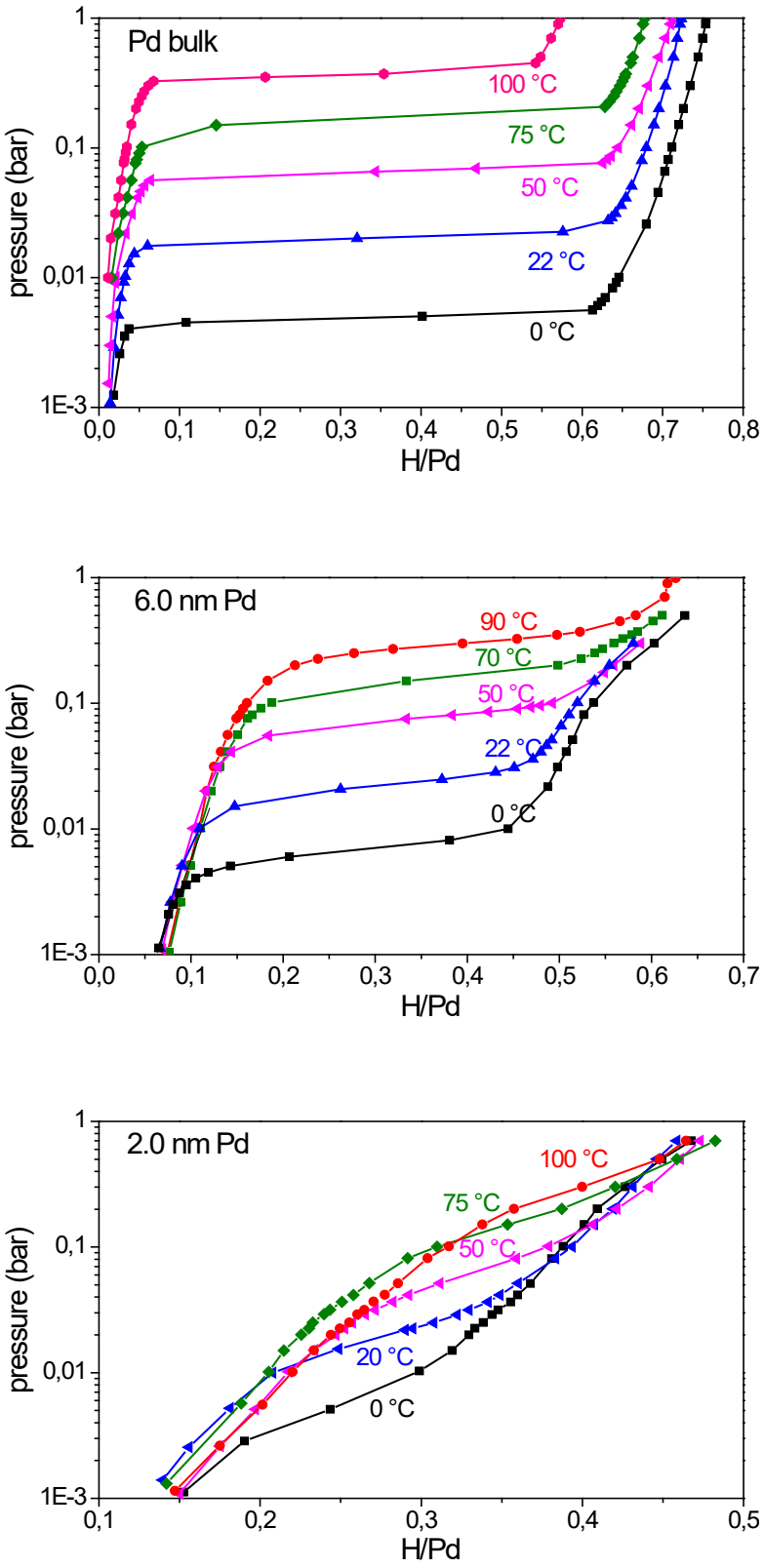


*Figure 3. 15: Absorption PCI curves for Pd bulk, 6.0 nm and 2.0 nm at variable temperature (0 - 100 °C).*

As described in Chapter 2, the plateau pressure ($P_{eq}$) (determined as the halfway pressure between $\alpha_{max}$ and $\beta_{min}$) is related to the reaction $\Delta H$ and $\Delta S$, expressed by Van't Hoff equation (Equation 3.1):

$$lnP_{eq} = \frac{\Delta H}{RT} - \frac{\Delta S}{R} \qquad \text{(Equation 3.1)}$$

The Van't Hoff plot of Pd samples is displayed below (Figure 3.14). By employing Van't Hoff equation, $\Delta H$ and $\Delta S$ can be determined. $\Delta H$ and $\Delta S$ for Pd bulk are -36.2(±1.2) KJ·mol$^{-1}$ $H_2$ and -89.1(±3.9) J·mol$^{-1}$·K$^{-1}$ $H_2$, in agreement with previous studies.[21] For 6.0 nm Pd these values are -34.7(±0.7) KJ·mol$^{-1}$ $H_2$ and -85.2(±2.2) J·mol$^{-1}$·K$^{-1}$ $H_2$, whereas they are -31.4(±1.6) KJ·mol$^{-1}$ $H_2$ and -73.9(±5.0) J·mol$^{-1}$·K$^{-1}$ $H_2$ for 2.0 nm Pd. Clearly, it was found that -$\Delta H$ and -$\Delta S$ decrease with decreasing particle size. Yamauchi *et al.*[22] pointed out that the -$\Delta H$ value could be seen as the bond strength between hydrogen (H) and Pd in the hydride phase. This result indicates that the bond strength for Pd-H becomes weaker as the Pd size decreases. The entropy change during the hydride formation originates principally from the entropy loss of hydrogen gas.[23] The diminution of -$\Delta S$ value implies that hydrogen atoms in nanoparticles have larger entropy with decreasing the size. However, another hypothesis was proposed by Griessen *et al.*[24] They pointed out that the discrepancy between $\Delta H$ and $\Delta S$ values obtained for a wide range of Pd nanoparticles might came from the statistical errors of the determination of accurate values of plateau pressure ($P_{eq}$), as it is not easy to ascertain the $P_{eq}$ at constant concentration for slopped plateaus in the case of Pd nanoparticles.

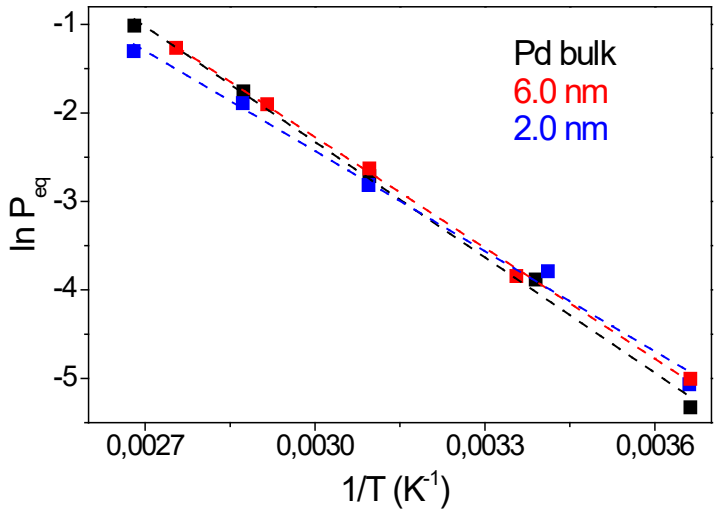


*Figure 3. 16: Van't Hoff plots of Pd bulk, 6.0 nm and 2.0 nm Pd. The correlation coefficients for the linear regressions are $R > 0.99$ for all the samples.*

### 3.2.2.4 Desorption properties

Hydrogen desorption properties from hydrogenated Pd samples were studied by the Thermo-Desorption Spectroscopy (TDS) technique. Two desorption protocols were used, depending on the temperature range to be studied.

#### 3.2.2.4.1 TDS in the temperature range 25 – 225 °C (298-498 K)

As demonstrated by PCI and *in situ* XAS experiment, H is trapped inside the Pd nanoparticles after the desorption at ambient temperature and the trapped H can be completely desorbed at high temperature (around 150 °C). A TDS experiment between 25 - 225 °C was carried out to supplement this study. The first protocol of the TDS experiment at high temperature for Pd bulk, 6.0 nm, 2.0 nm and 1.4 nm Pd is described as follows. The Pd sample was first exposed to 1 bar of hydrogen at room temperature and the hydrogen gas was subsequently evacuated under secondary vacuum. Finally, the desorbed $H_2$ partial pressure was recorded while applying 5 °C/min heating rate up to 225 °C.

The thermo-desorption spectra are shown in Figure 3.17. No desorption peak of $H_2$ is found for Pd bulk while desorption features are present in Pd nanoparticles. This confirms the H trapping in Pd nanoparticles, which is consistent with the results from PCI and *in situ* XAS. The maximum desorption peaks are around 75 °C, 85 °C and 105 °C for 6.0 nm, 2.0 nm and 1.4 nm Pd, respectively. So, the desorption temperature increases as the Pd size decreases. This may suggest that the stability of trapped H increases with the reduction of Pd size.

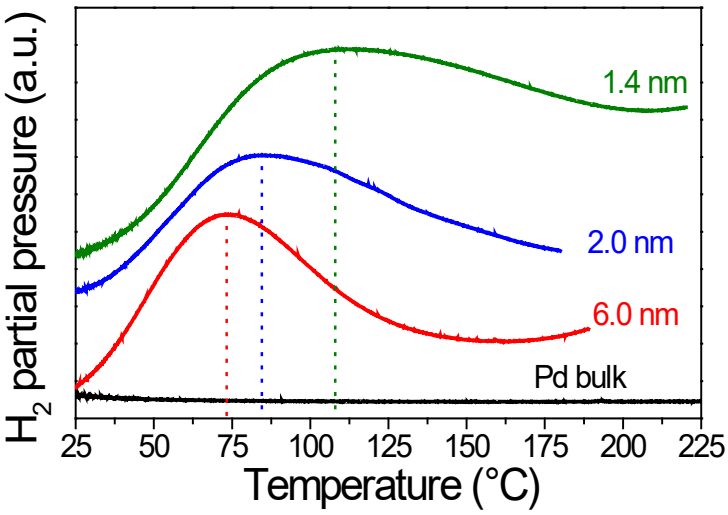


*Figure 3. 17: Thermo-desorption spectra of Pd bulk, 6.0 nm Pd, 2.0 nm and 1.4 nm Pd with a heating rate of 5 °C/min.*

### 3.2.2.4.2 TDS in the temperature range 78 – 310 K

The second protocol of the TDS experiment was carried out to study the kinetic properties of the hydrogen desorption of Pd nanoparticles at low temperature range. For our convenience, the unity of temperature used in TDS at cryogenic condition is Kelvin (K) instead of Celsius (°C), typically used in the high temperature range. The protocol of the experiment for Pd bulk, 6.0 nm, 2.0 nm and 1.4 nm Pd is described as follows. Prior to the measurement, the sample was degassed at 473 K for 10 h under high vacuum. The desorbed sample was first exposed to 1 bar of hydrogen at room temperature then cooled down under gas pressure to 77 K (liquid $N_2$ coolant). The gaseous $H_2$ was subsequently evacuated under secondary vacuum. Next, the desorbed $H_2$ partial pressure was recorded while applying different constant heating rates (from 2 to 15 K/min) up to 310 K. Here, all Pd nanoparticles samples can form hydride phase at 77 K under 1 bar $H_2$ as reported earlier for 1.0 nm Pd.[12]

Thermo-desorption spectra of Pd bulk, 6.0 nm, 2.0 nm and 1.4 nm Pd with a heating rate of 5 K/min are plotted in Figures 3.18. As shown in Figure 3.18, there are 2 desorption peaks for Pd bulk while 3 peaks for Pd nanoparticles. The first desorption peak for Pd nanoparticles samples at around 100-110 K is ascribed to the physisorption of $H_2$ on the porous supports (HSAG and AC). The second desorption peak ($T_\beta$) points to the dehydrogenation from the $\beta$ phase, and the third peak ($T_{\beta\rightarrow\alpha}$) corresponds to desorption that accompanies the $\beta$ to $\alpha$ phase transformation.[14,25] The second desorption peaks for the Pd nanoparticles are more evident in the spectra compared to the one for Pd bulk which is very broad peak. Vons *et al*.[26] proposed that the areas of the $T_\beta$ peaks can be used to estimate the amount of hydrogen absorbed beyond $\beta_{min}$ at room temperature and 1 bar $H_2$. The fraction of hydrogen released in these peak increases with decreasing Pd size. Meanwhile, the areas of the $T_{\beta\rightarrow\alpha}$ can be used to estimate the amount of hydrogen from the $\beta$ to $\alpha$ phase transformation which corresponds to the absorption/desorption plateau in PCI curves (Figure 3.5). It decreases with decreasing Pd size. This finding is consistent with the result obtained from PCI characterization that shows that the relative amount of hydrogen absorbed after $\beta_{min}$ increases with the reduction of Pd size along with the narrowing of plateau. Moreover, the maximum desorption temperatures ($T_\beta$ and $T_{\beta\rightarrow\alpha}$) decrease as the Pd size decreases. This indicates that the thermal stability of Pd hydride ($\beta$ phase) diminishes as the Pd size decreases.

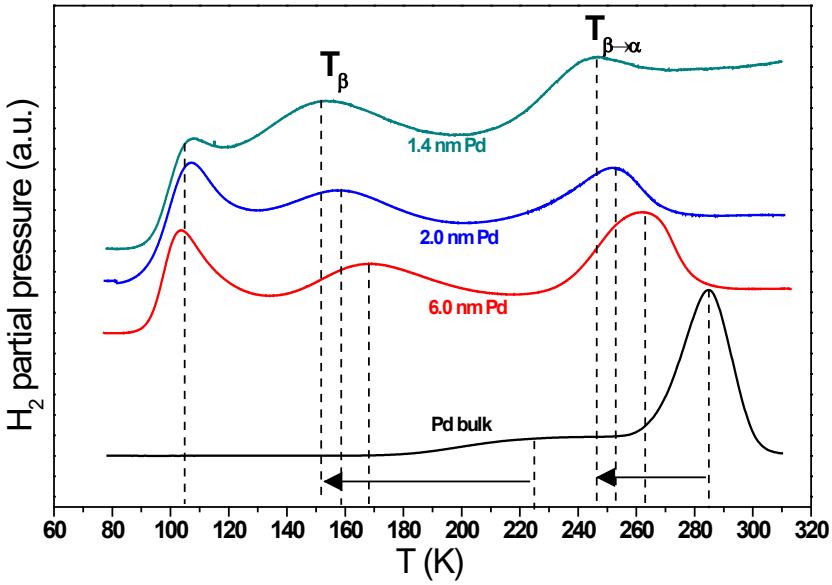


*Figure 3. 18: Thermo-desorption spectra of Pd bulk, 6.0 nm Pd, 2.0 nm and 1.4 nm Pd with a heating rate of 5 K/min.*

The TDS spectra with variant heating rates are shown in Figure 3.19. The activation energy of desorption is calculated using the Kissinger method[27] illustrated by the equation below:

$$\ln\left(\frac{\beta}{T_m^2}\right) = -\frac{E_a}{RT_m} + \ln k_0 \qquad \text{(Equation 3.2)}$$

Where: $E_a$ is the activation energy, $\beta$ is the heating rate, $T_m$ is taken equal to $T_{\beta\to\alpha}$, $R$ is the gas constant and $k_0$ is a pre-exponential factor. A linear dependence between $\ln\left(\frac{\beta}{T_m^2}\right)$ and $\frac{1}{T_m}$ is expected, as depicted in Figure 3.20. The calculated values of $E_a$ are 0.49(3), 0.33(1), 0.28(1) and 0.26(1) eV for Pd bulk, 6.0 nm, 2.0 nm and 1.4 nm Pd, respectively (Table 3.5). The value obtained for Pd bulk is in good agreement with previous results.[28] The strong decrease of the activation energy of desorption from bulk to Pd nanoparticles shows that the Pd nanoparticle samples have lower thermal stability than Pd bulk, and it decreases with the reduction of Pd size. The values for 2.0 nm and 1.4 nm Pd are comparable with the result of 1.0 nm Pd (0.27(2) eV) supported on MIL-101 reported by Malouche *et al.*[12] They suggest that the diminution of activation energy is due to change of the rate limiting step from surface recombination or $\beta \to \alpha$ phase transformation in Pd bulk to hydrogen diffusion into $\alpha$ and $\beta$ phases in Pd nanoparticles due to the shorter diffusion path and larger surface area.

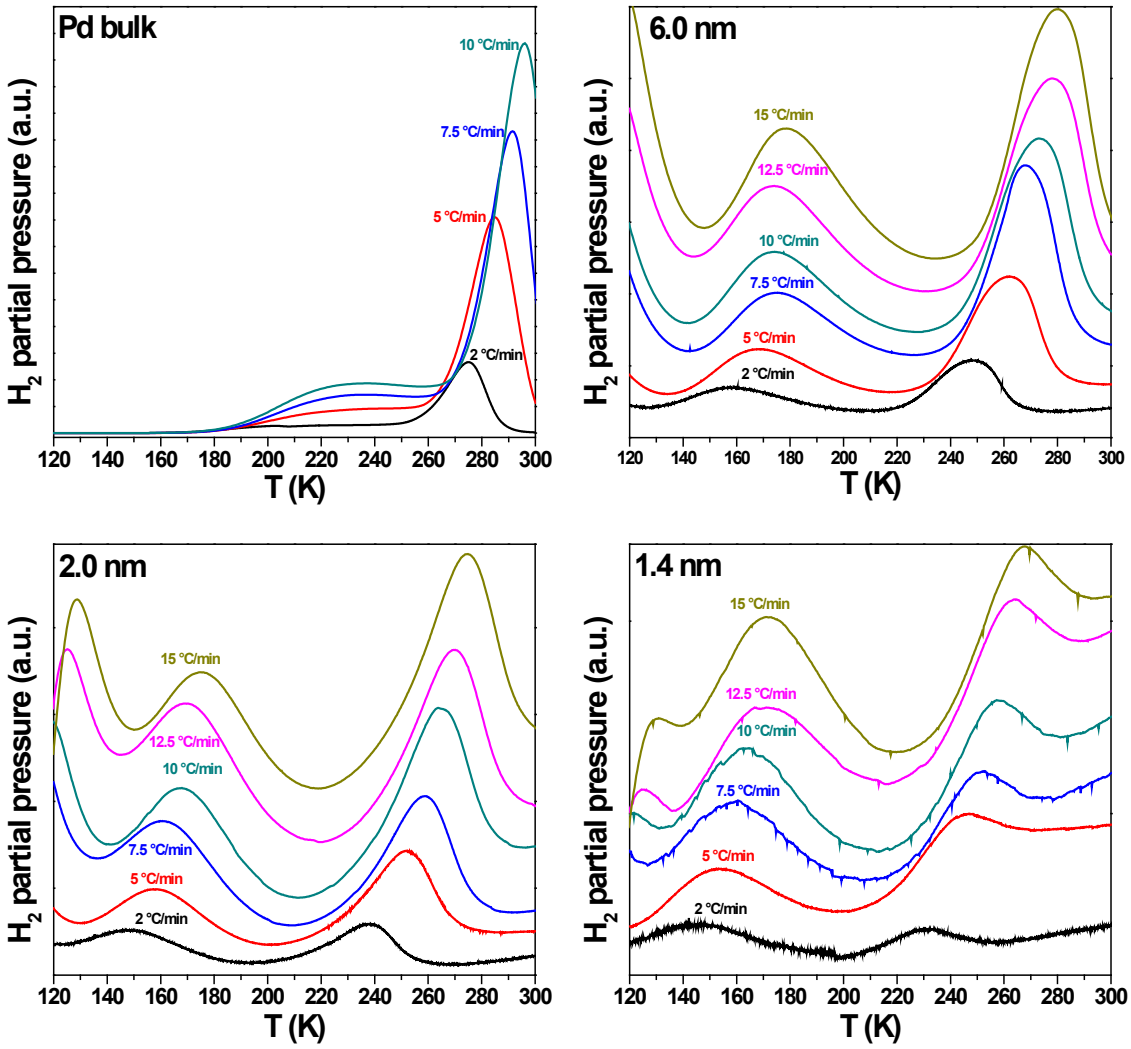


*Figure 3. 19: Thermo-desorption spectra performed at different heating rate for Pd bulk, 6.0 nm, 2.0 nm and 1.4 nm Pd.*

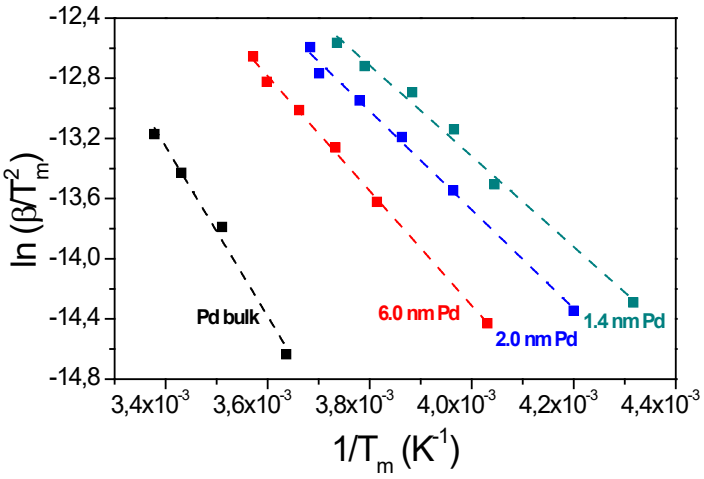


*Figure 3. 20: The Kissinger plots for Pd bulk, 6.0 nm, 2.0 nm and 1.4 nm Pd. The correlation coefficients for the linear regressions are $R > 0.99$ for all the samples.*

| samples | *Ea* (eV) |
|---|---|
| Pd bulk | 0.49(3) |
| 6.0 nm Pd | 0.33(1) |
| 2.0 nm Pd | 0.28(1) |
| 1.4 nm Pd | 0.26(1) |

*Table 3. 5: The calculated values of activation energy for Pd bulk, 6.0 nm, 2.0 nm and 1.4 nm Pd.*

### 3.3 Pd single atoms supported on carbons

In this subchapter, we will discuss the physicochemical and hydrogen sorption properties of two samples formed by Pd single atoms supported on carbons and prepared by liquid impregnation and subsequent pyrolysis with EDTA and melamine, along with a nitrogen doped carbon $CN_x$ without metal.

#### 3.3.1 Physicochemical properties of materials

The synthesized materials were characterized by X-Ray Diffraction (**XRD**) for the determination of their structural properties (Figure 3.21). As described in **section 3.2.1**, the AC is mainly amorphous with some impurities which give rise to several small additional diffraction peaks. For $CN_x$, 0.8-Pd-AC and 7.5-Pd-AC samples, no extra diffraction peaks could be observed. This suggests that either the size of Pd nano-objects is too small to be detected by XRD (too short coherence lengths for X-ray diffraction) or they do not have a periodic arrangement as in the case of random distribution of SACs on the carbon support. This hypothesis will be verified by transmission electron microscopy.

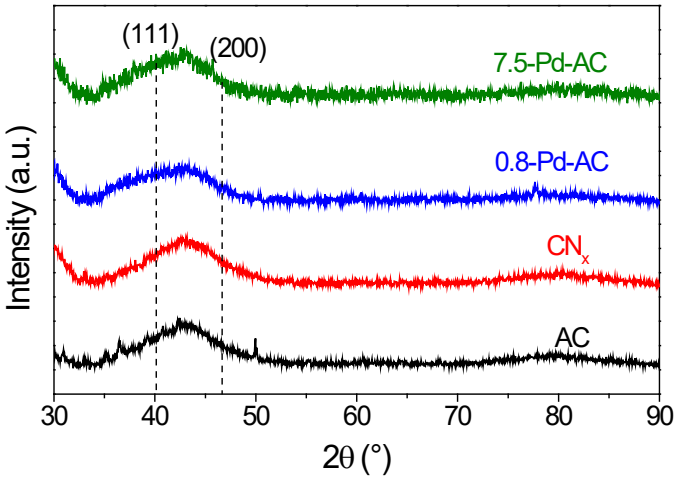


*Figure 3. 21: XRD patterns of AC, $CN_x$, 0.8-Pd-AC and 7.5-Pd-AC.*

These materials were characterized by Transmission Electron Microscopy (TEM) to analyse the dispersion of Pd on the carbon hosts as well as the formation of metal nanoparticles, clusters, or possibly single atoms.

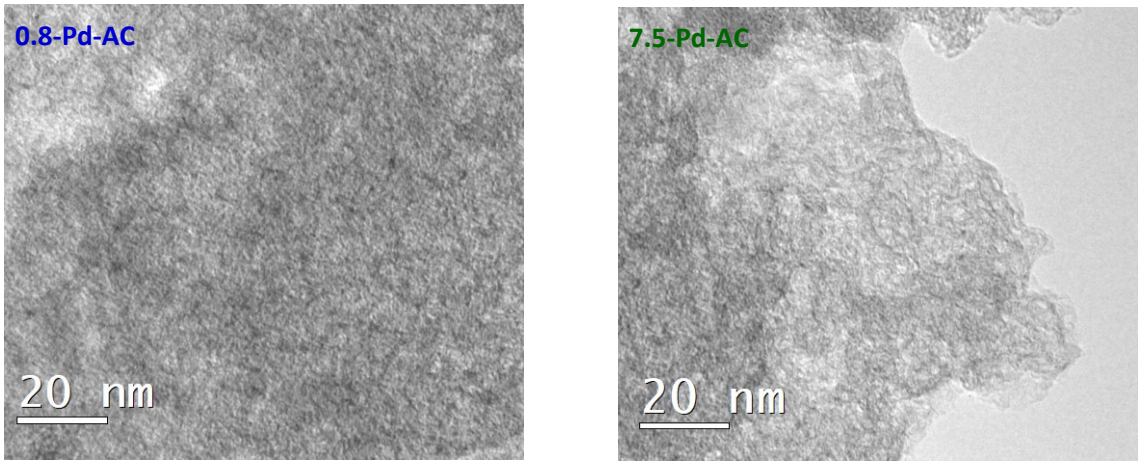


*Figure 3. 22: TEM images of 0.8-Pd-AC and 7.5-Pd-AC.*

Pd nanoparticles could not be observed in the TEM images of the 0.8-Pd-AC and 7.5-Pd-AC samples (Figure 3.22), indicating that the Pd is distributed as sub-nanometric clusters and/or SACs. However, the Pd clusters or SACs are too small to be detected by classic TEM (resolution 0.24 nm). These results are consistent with the ones obtained from XRD which showed an absence of diffraction peaks for the 0.8-Pd-AC and 7.5-Pd-AC samples.

To determine the Pd distribution in the samples 0.8-Pd-AC and 7.5-Pd-AC, Scanning Transmission Electron Microscopy (STEM) was realised by Mounib Bahri and Ovidiu Ersen at IPCMS (Strasbourg). The high-angle annular dark-filed scanning TEM (HAADF–STEM) images are presented in Figure 3.23. The bright spots displayed are expected to be Pd atoms, as Pd has a higher atomic number Z than C and N. They have a higher density in 7.5-Pd-AC than in 0.8-Pd-AC because the former is more concentrated in Pd. In conclusion, we successfully synthesized Pd single atoms with a homogenous distribution on a nitrogen doped carbon.

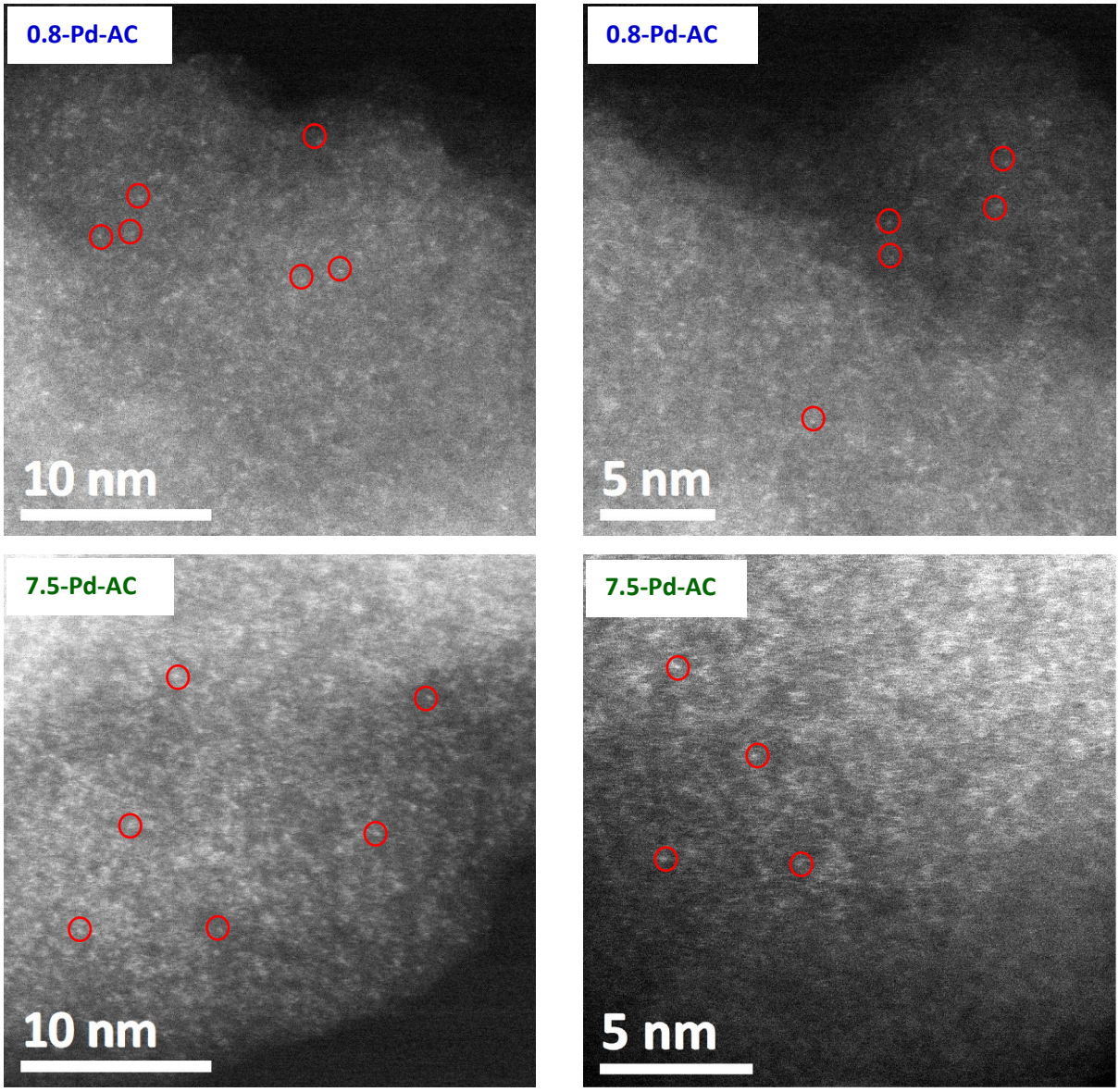


*Figure 3. 23: HAADF-STEM images of 0.8-Pd-AC and 7.5-Pd-AC, the bright spots in the red circles are Pd atoms.*

The textural properties were characterized by nitrogen adsorption/desorption measurements at 77 K. Figure 3.24 shows the $N_2$ adsorption/desorption curves for AC, $CN_x$ and the Pd SACs materials. A hysteresis loop can be observed for AC, meaning that AC contain mesopores. The high adsorption at low pressure shows that it is also a highly microporous material.

The surface area, as determined by BET method in the relative pressure range $P/P_0$ = 0.05 – 0.20 decreases drastically after pyrolysis (Table 3.6). The specific surface area reduces drastically for $CN_x$ (364 $m^2/g$), 0.8-Pd-AC (425 $m^2/g$) and 7.5-Pd-AC (281 $m^2/g$), as compared

to the initial AC (1400 $m^2/g$) probably due to loss of porosities after the pyrolysis reaction with melamine and EDTA.

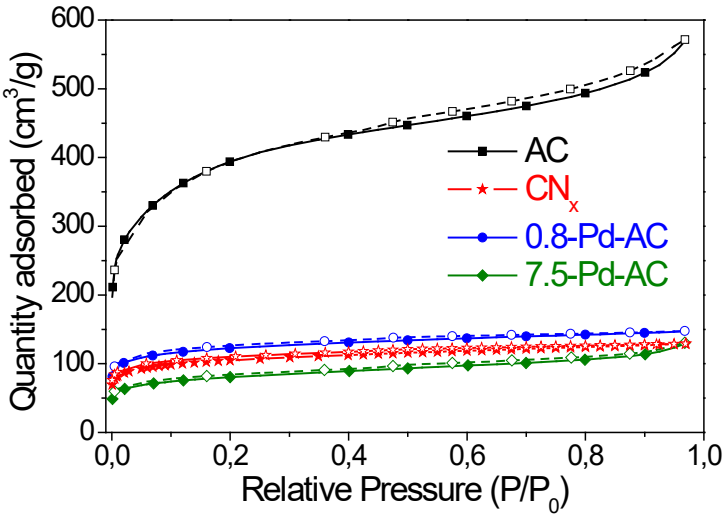


*Figure 3. 24: Liquid $N_2$ adsorption/desorption curves of AC, $CN_x$, 0.8-Pd-AC and 7.5-Pd-AC.*

| sample | Surface area ($m^2/g$) |
|---|---|
| **AC** | 1400(10) |
| **$CN_x$** | 364(10) |
| **0.8-Pd-AC** | 425(10) |
| **7.5-Pd-AC** | 281(10) |

*Table 3. 6: BET specific surface area of AC, $CN_x$, 0.8-Pd-AC and 7.5-Pd-AC.*

To gain more information of the textural change of $CN_x$ and Pd-SACs after pyrolysis, the SEM analysis was carried out for AC, $CN_x$ and 0.8-Pd-AC. According to textural properties analysis, the pristine AC possesses both micropores and mesopores. Some mesopores can be clearly seen from the SEM images (Figure 3.25 b). After the pyrolysis with EDTA and melamine, the particle size of $CN_x$ and 0.8-Pd-AC increased. It seems that a crust is formed on the surface of AC and its porosity was lost during this process (Figure 3.25 d and f).

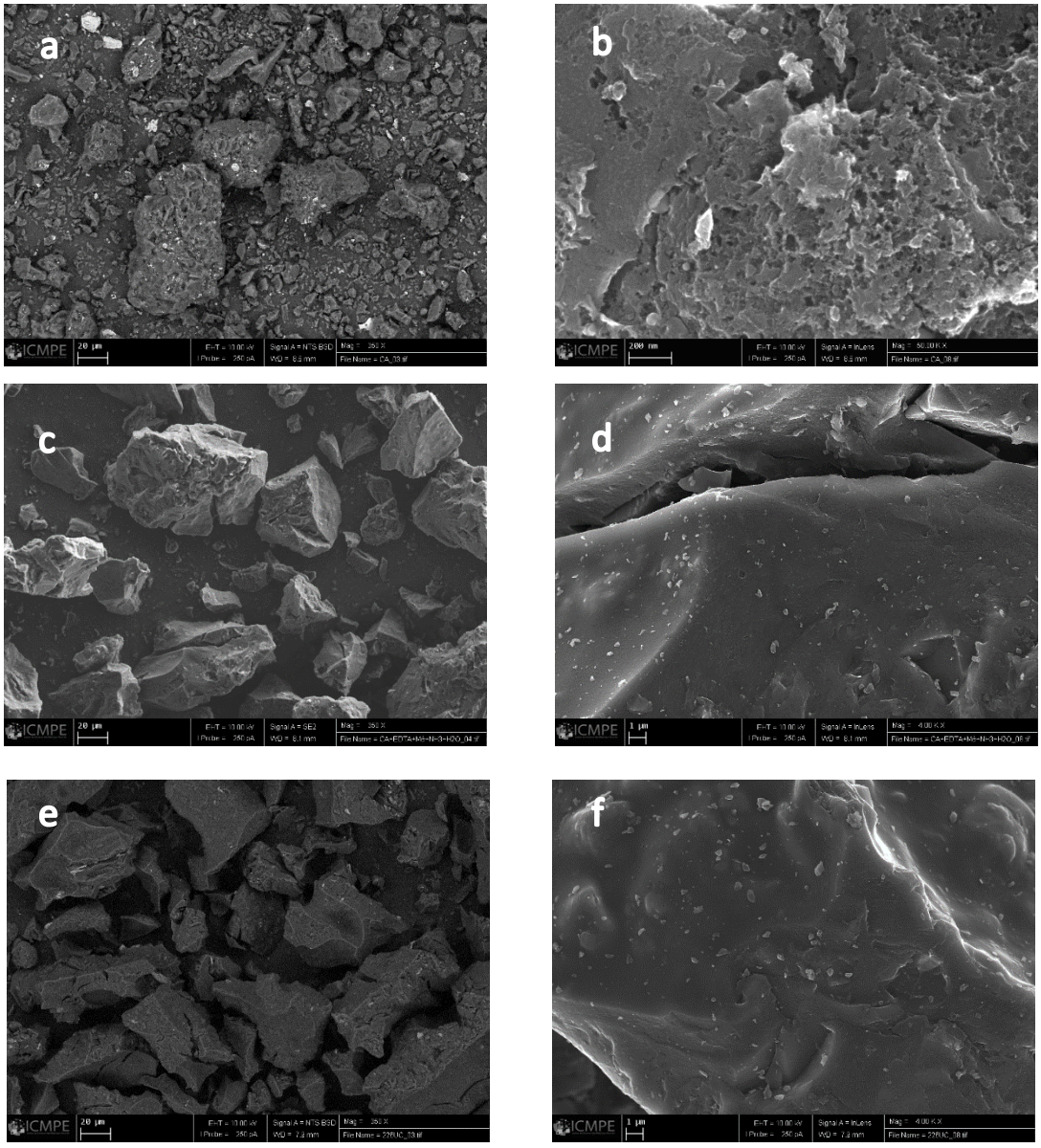


*Figure 3. 25: SEM images of a, b) AC; c, d) $CN_x$ and e, f) 0.8-Pd-AC.*

### 3.3.2 Pd single atoms interaction with hydrogen

Pressure-Composition-Isotherms (PCI) of these materials have been studied at room temperature and cryogenic temperature (77 K) up to 1 bar $H_2$. A comparison of PCI curves at room temperature of 1.4 nm Pd nanoparticles and Pd single atom materials (0.8-Pd-AC and 7.5-Pd-AC) with $CN_x$ and initial activated carbon is shown in Figure 3.26 a.

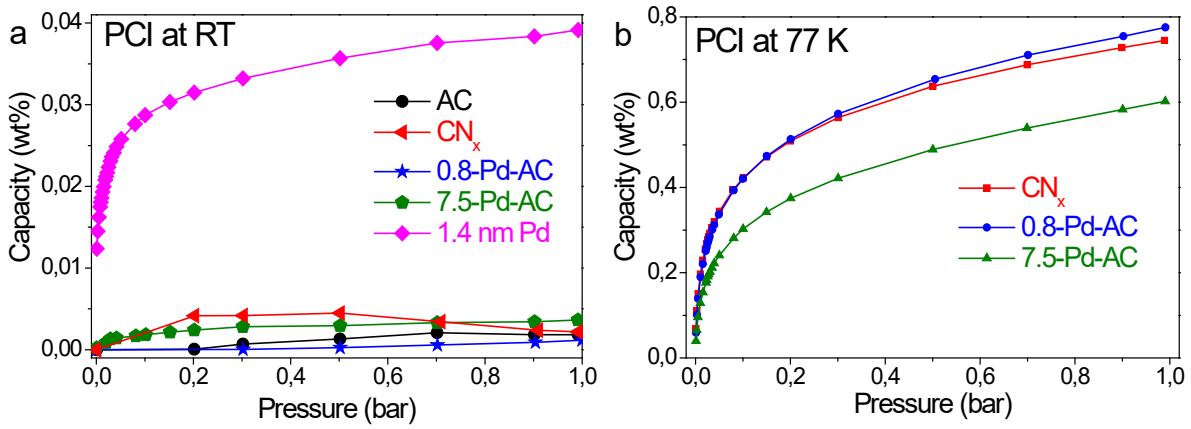


*Figure 3. 26: Pressure-composition-isotherms curves of a) AC, 1.4 nm Pd, 0.8-Pd-AC and 7.5-Pd-AC at room temperature and b) $CN_x$, 0.8-Pd-AC and 7.5-Pd-AC at cryogenic temperature (77K).*

As displayed in the figure above, there is very little interaction between hydrogen and AC, $CN_x$ up to atmospheric pressure at room temperature with very small uptake under these conditions. Interestingly, the SAC samples also show low sorption of $H_2$, close to the initial carbon. On the contrary, Pd nanoparticles with average size 1.4 nm have higher sorption capacity than Pd single atoms. This is due to hydrogen absorption in the volume of nanoparticles with formation of solid solution or hydride, as described in **section 3.2.1**. Thus, this result indicates that Pd single atoms has little interaction with hydrogen molecules as compared to Pd nanoparticles but also confirm that nanoparticles are not present in any of SAC samples. This agrees with the results obtained from XRD and HAADF-STEM images, showing no formation of Pd nanoparticles or clusters for 0.8-Pd-AC and 7.5-Pd-AC samples.

The PCI curves for Pd single atom materials (0.8-Pd-AC and 7.5-Pd-AC) and $CN_x$ at cryogenic temperature (77 K) are shown in Figure 3.26 b. The hydrogen uptake capacity at 1 bar is correlated to the specific surface area of materials and it enhances with increasing the surface area. Furthermore, it seems to be adhered to Chahine's rule, which predicts a linear correlation of hydrogen adsorption capacity, at 77 K, with surface area (1 wt.% per 500 $m^2/g$) (Figure 3.27).[4,29,30]

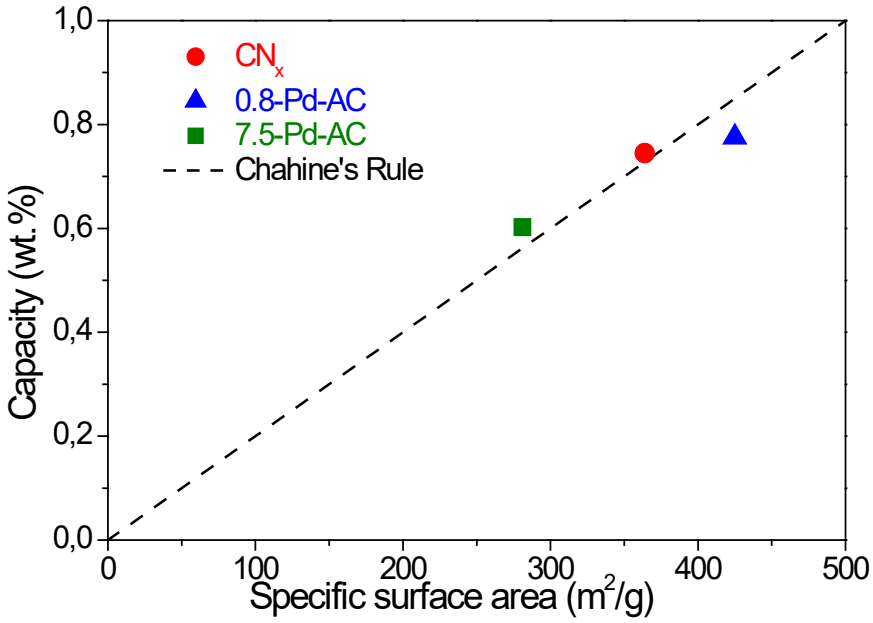


*Figure 3. 27: Correlation between the BET surface area and the hydrogen storage capacity (at 1 bar $H_2$ and 77 K) of CNx, 0.8-Pd-AC and 7.5-Pd-AC. The dashed line represents Chahine's rule.*

The experiment of Thermo-Desorption Spectroscopy (**TDS**) in the temperature range 35 – 300 K was carried out to study the difference of hydrogen desorption properties for 3 samples based on the same AC material: $CN_x$, 7.5-Pd-AC and 1.4 nm Pd. The protocol of the third TDS experiment is described as follows. Prior to the measurement, the sample was degassed at 473 K for 10 h under high vacuum. The desorbed sample was first exposed to 1 bar of hydrogen at room temperature then cooled down under gas pressure to 35 K (closed He cooling circuit). After reaching the minimum temperature, the $H_2$ gas is subsequently evacuated under secondary vacuum. Finally, the desorbed $H_2$ partial pressure is recorded while applying a constant heating rate of 5 K/min up to 300 K.

The thermo-desorption spectra are shown in Figure 3.28. The desorption before 120 K can be attributed to the physisorption of $H_2$ in the porosity of supports, and there are slight differences between the porous supports due to the different textural properties and the effects of the heteroatoms in the supports (N or Pd). The $H_2$ desorption is completed at around 120 K for 1.4 nm Pd while it is finished at around 170 K for $CN_x$ and 7.5-Pd-AC with about 50 K high temperature difference (Figure 3.28, red rectangle). This feature might be due to the presence of N atoms dopped in carbon materials which may lead to larger interaction with $H_2$ molecules. After 120 K, the 1.4 nm Pd shows a two-peak desorption

features ($T_\beta$ and $T_{\beta\to\alpha}$) (Figure 3.28, green rectangle) as discussed above (Figure 3.18). The 7.5-Pd-AC shows no $H_2$ desorption, same as sample $CN_x$. This finding confirms that Pd nanoparticles are not formed in the 7.5-Pd-AC, which is consistent with the results obtained from STEM images and PCI experiment.

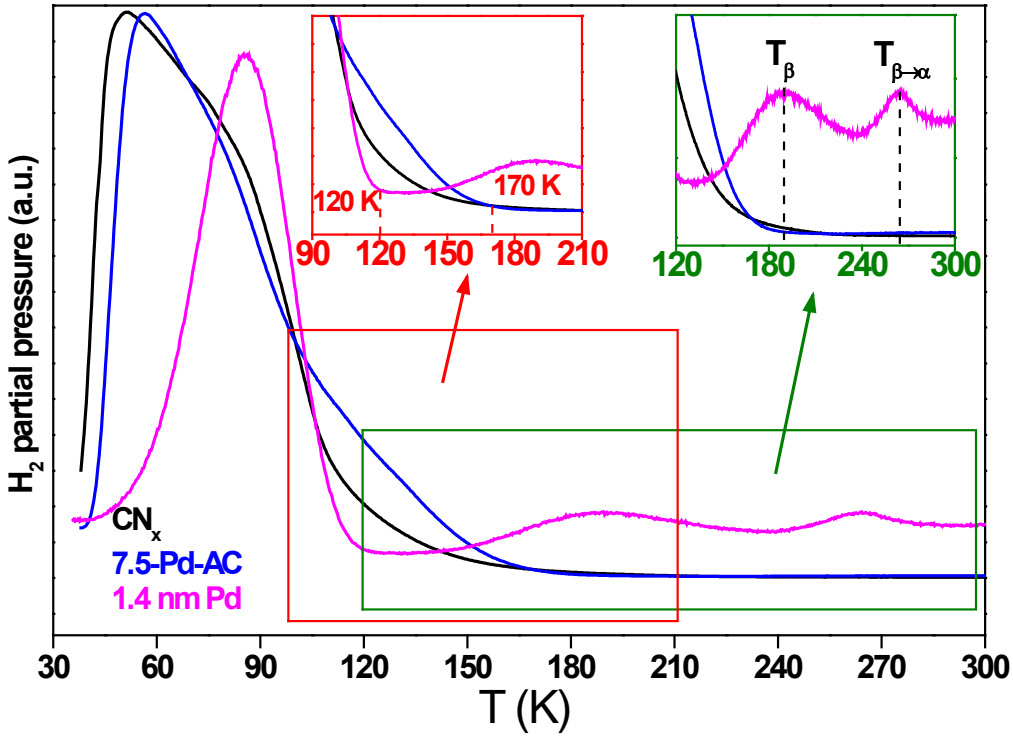


*Figure 3. 28: Thermo-desorption spectra of $CN_x$, 7.5-Pd-AC and 1.4 nm Pd with a heating rate of 5 K/min.*

**3.4 Conclusion**

In this chapter, a study of the interaction between hydrogen and ultra-small size of Pd nanoparticles with different sizes and single atoms, was carried out.

The first part of this chapter consists of the Pd nanoparticles supported on carbons. First, structural, nanostructural and textural characterization confirmed the successful preparation of Pd nanoparticles with 6.0, 2.0 and 1.4 nm average sizes embedded in two porous carbons: HSAG and AC. The hydrogen sorption properties of Pd nanoparticles had been thoroughly studied by means of both laboratory and synchrotron facilities. According to PCI curves at room temperature, the absorption capacity at 1 bar $H_2$ diminishes with the decrease of Pd size, the plateau becomes more and more sloped for 6.0 and 2.0 nm Pd, and it completely disappears for 1.4 nm Pd. The absorption and desorption show only partial

reversibility for Pd nanoparticles at low pressure, while they are completely reversible for Pd bulk. The decrease of absorption capacity was confirmed by *in situ* XRD and *in situ* XAS, reflected by the decrease of the lattice expansion with reducing Pd size under 1 bar $H_2$. The H trapping inside the lattice of Pd nanoparticles after the desorption process was also confirmed by *in situ* XAS and there is a size dependence of the quantity of trapped H: the smaller the size, the larger the irreversible H amount and the larger the binding energy of the trapped H inside of Pd nanoparticles. The DFT and TB simulations suggest that the strong H trapping sites are located at the subsurface of nanoparticles. The trapped H can be desorbed by heating to around 150–170 °C under vacuum or inert gas flow. The enthalpy and entropy change of hydride formation decrease with decreasing Pd size, indicating that the bond strength for Pd-H becomes weaker as the Pd size decreases and hydrogen atoms in nanoparticles have larger entropy with decreasing the Pd size. The TDS experiment showed that the thermal stability of hydrogenated Pd nanoparticles decreases as compared to Pd bulk. The Pd nanoparticles have lower activation energy of desorption as compared to Pd bulk. The diminution of activation energy is due to change of the rate limiting step from surface recombination or $\beta \rightarrow \alpha$ phase transformation in Pd bulk to hydrogen diffusion into $\alpha$ and $\beta$ phases in Pd nanoparticles.

The second part of this chapter focused on the Pd single atoms supported on carbon material. Pd single atoms samples were successfully synthesized and embedded on nitrogen-based carbon host, as confirmed by XRD and HAADF-STEM characterization. The interaction between hydrogen and Pd single atoms were studied by PCI at room temperature and at cryogenic temperature (77 K), as well as TDS at low cryogenic temperature range (35-310 K). The PCI and TDS experiments shows that there is very little interaction between hydrogen and Pd single atoms supported on carbon host, contrary to Pd nanoparticles.

## 3.5 References

(1) Zhao, L.; Zhang, Y.; Huang, L.-B.; Liu, X.-Z.; Zhang, Q.-H.; He, C.; Wu, Z.-Y.; Zhang, L.-J.; Wu, J.; Yang, W.; Gu, L.; Hu, J.-S.; Wan, L.-J. Cascade Anchoring Strategy for General Mass Production of High-Loading Single-Atomic Metal-Nitrogen Catalysts. *Nat. Commun.* **2019**, *10* (1). https://doi.org/10.1038/s41467-019-09290-y.

(2) Bastide, S.; Zlotea, C.; Laurent, M.; Latroche, M.; Cachet-Vivier, C. Direct Assessment from Cyclic Voltammetry of Size Effect on the Hydrogen Sorption Properties of Pd Nanoparticle/Carbon Hybrids. *J. Electroanal. Chem.* **2013**, *706*, 33–39. https://doi.org/10.1016/j.jelechem.2013.07.036.

(3) Vannice, M. A. *Kinetics of Catalytic Reactions*; Springer: New York, 2005.

(4) Poirier, E.; Chahine, R.; Bose, T. K. Hydrogen Adsorption in Carbon Nanostructures. *Int. J. Hydrog. Energy* **2001**, *26* (8), 831–835. https://doi.org/10.1016/S0360-3199(01)00014-3.

(5) Nützenadel, C.; Züttel, A.; Chartouni, D.; Schmid, G.; Schlapbach, L. Critical Size and Surface Effect of the Hydrogen Interaction of Palladium Clusters. *Eur. Phys. J. - At. Mol. Opt. Phys.* **2000**, *8* (2), 245–250. https://doi.org/10.1007/s100530050033.

(6) Sachs, C.; Pundt, A.; Kirchheim, R.; Winter, M.; Reetz, M. T.; Fritsch, D. Solubility of Hydrogen in Single-Sized Palladium Clusters. *Phys. Rev. B* **2001**, *64* (7), 075408. https://doi.org/10.1103/PhysRevB.64.075408.

(7) Pundt, A.; Sachs, C.; Winter, M.; Reetz, M. T.; Fritsch, D.; Kirchheim, R. Hydrogen Sorption in Elastically Soft Stabilized Pd-Clusters. *J. Alloys Compd.* **1999**, *293–295*, 480–483. https://doi.org/10.1016/S0925-8388(99)00469-7.

(8) Pundt, A.; Kirchheim, R. HYDROGEN IN METALS: Microstructural Aspects. *Annu. Rev. Mater. Res.* **2006**, *36* (1), 555–608. https://doi.org/10.1146/annurev.matsci.36.090804.094451.

(9) Salomons, E.; Griessen, R.; Groot, D. G. de; Magerl, A. Surface Tension and Subsurface Sites of Metallic Nanocrystals Determined from H-Absorption. *Europhys. Lett. EPL* **1988**, *5* (5), 449–454. https://doi.org/10.1209/0295-5075/5/5/012.

(10) Shegai, T.; Langhammer, C. Hydride Formation in Single Palladium and Magnesium Nanoparticles Studied By Nanoplasmonic Dark-Field Scattering Spectroscopy. *Adv. Mater.* **2011**, *23* (38), 4409–4414. https://doi.org/10.1002/adma.201101976.

(11) Narehood, D. G.; Kishore, S.; Goto, H.; Adair, J. H.; Nelson, J. A.; Gutiérrez, H. R.; Eklund, P. C. X-Ray Diffraction and H-Storage in Ultra-Small Palladium Particles. *Int. J. Hydrog. Energy* **2009**, *34* (2), 952–960. https://doi.org/10.1016/j.ijhydene.2008.10.080.

(12) Malouche, A.; Blanita, G.; Lupu, D.; Bourgon, J.; Nelayah, J.; Zlotea, C. Hydrogen Absorption in 1 Nm Pd Clusters Confined in MIL-101(Cr). *J. Mater. Chem. A* **2017**, *5* (44), 23043–23052. https://doi.org/10.1039/C7TA07159K.

(13) KubotaTakeshi; KitajimaYoshinori; AsakuraKiyotaka; IwasawaYasuhiro. Pd L3-Edge XANES Spectra of Supported Pd Particles Induced by the Adsorption and the Absorption of Hydrogen. *Bull. Chem. Soc. Jpn.* **2003**. https://doi.org/10.1246/bcsj.72.673.

(14) Zlotea, C.; Cuevas, F.; Paul-Boncour, V.; Leroy, E.; Dibandjo, P.; Gadiou, R.; Vix-Guterl, C.; Latroche, M. Size-Dependent Hydrogen Sorption in Ultrasmall Pd Clusters Embedded in a Mesoporous Carbon Template. *J. Am. Chem. Soc.* **2010**, *132* (22), 7720–7729. https://doi.org/10.1021/ja101795g.

(15) Frenkel, A. I.; Hills, C. W.; Nuzzo, R. G. A View from the Inside: Complexity in the Atomic Scale Ordering of Supported Metal Nanoparticles. *J. Phys. Chem. B* **2001**, *105* (51), 12689–12703. https://doi.org/10.1021/jp012769j.

(16) Wagner, S.; Pundt, A.; Wagner, S.; Pundt, A. Hydrogen as a Probe for Defects in Materials: Isotherms and Related Microstructures of Palladium-Hydrogen Thin Films. *AIMS Mater. Sci.* **2020**, *7* (4), 399–419. https://doi.org/10.3934/matersci.2020.4.399.

(17) Peisl, H. Lattice Strains Due to Hydrogen in Metals. In *Hydrogen in Metals I: Basic Properties*; Alefeld, G., Völkl, J., Eds.; Topics in Applied Physics; Springer: Berlin, Heidelberg, 1978; pp 53–74. https://doi.org/10.1007/3540087052_42.

(18) Liu, W.; Magnin, Y.; Förster, D.; Bourgon, J.; Len, T.; Morfin, F.; Piccolo, L.; Amara, H.; Zlotea, C. Size-Dependent Hydrogen Trapping in Palladium Nanoparticles. *J. Mater. Chem. A* **2021**, *9* (16), 10354–10363. https://doi.org/10.1039/D0TA12174F.

(19) Teschner, D.; Borsodi, J.; Wootsch, A.; Révay, Z.; Hävecker, M.; Knop-Gericke, A.; Jackson, S. D.; Schlögl, R. The Roles of Subsurface Carbon and Hydrogen in Palladium-Catalyzed Alkyne Hydrogenation. *Science* **2008**, *320* (5872), 86–89. https://doi.org/10.1126/science.1155200.

(20) Aleksandrov, H. A.; Kozlov, S. M.; Schauermann, S.; Vayssilov, G. N.; Neyman, K. M. How Absorbed Hydrogen Affects the Catalytic Activity of Transition Metals. *Angew. Chem. Int. Ed.* **2014**, *53* (49), 13371–13375. https://doi.org/10.1002/anie.201405738.

(21) Lässer, R.; Klatt, K.-H. Solubility of Hydrogen Isotopes in Palladium. *Phys. Rev. B* **1983**, *28* (2), 748–758. https://doi.org/10.1103/PhysRevB.28.748.

(22) Yamauchi, M.; Ikeda, R.; Kitagawa, H.; Takata, M. Nanosize Effects on Hydrogen Storage in Palladium. *J. Phys. Chem. C* **2008**, *112* (9), 3294–3299. https://doi.org/10.1021/jp710447j.

(23) *Nanostructured Materials for Next-Generation Energy Storage and Conversion: Hydrogen Production, Storage, and Utilization*, 1st ed. 2017.; Bashir, S., Chen, Y.-P., Liu, J. L., Eds.; Springer Berlin Heidelberg : Imprint: Springer: Berlin, Heidelberg, 2017. https://doi.org/10.1007/978-3-662-53514-1.

(24) Griessen, R.; Strohfeldt, N.; Giessen, H. Thermodynamics of the Hybrid Interaction of Hydrogen with Palladium Nanoparticles. *Nat. Mater.* **2016**, *15* (3), 311–317. https://doi.org/10.1038/nmat4480.

(25) Stern, A.; Resnik, A.; Shaltiel, D. Thermal Desorption Spectra of the PdHxsystem in a Powder Form. *J. Phys. F Met. Phys.* **1984**, *14* (7), 1625–1639. https://doi.org/10.1088/0305-4608/14/7/012.

(26) Vons, V. A.; Leegwater, H.; Legerstee, W. J.; Eijt, S. W. H.; Schmidt-Ott, A. Hydrogen Storage Properties of Spark Generated Palladium Nanoparticles. *Int. J. Hydrog. Energy* **2010**, *35* (11), 5479–5489. https://doi.org/10.1016/j.ijhydene.2010.02.118.

(27) Blaine, R. L.; Kissinger, H. E. Homer Kissinger and the Kissinger Equation. *Thermochim. Acta* **2012**, *540*, 1–6. https://doi.org/10.1016/j.tca.2012.04.008.

(28) Leardini, F.; Fernández, J. F.; Bodega, J.; Sánchez, C. Isotope Effects in the Kinetics of Simultaneous H and D Thermal Desorption from Pd. *J. Phys. Chem. Solids* **2008**, *69* (1), 116–127. https://doi.org/10.1016/j.jpcs.2007.08.005.

(29) Bénard, P.; Chahine, R. Storage of Hydrogen by Physisorption on Carbon and Nanostructured Materials. *Scr. Mater.* **2007**, *56* (10), 803–808. https://doi.org/10.1016/j.scriptamat.2007.01.008.

(30) Balderas-Xicohténcatl, R.; Schlichtenmayer, M.; Hirscher, M. Volumetric Hydrogen Storage Capacity in Metal–Organic Frameworks. *Energy Technol.* **2018**, *6* (3), 578–582. https://doi.org/10.1002/ente.201700636.

# CHAPTER IV: POROUS CARBONS WITH IRIDIUM FOR SELECTIVE HYDROGENATION REACTIONS

## 4.1 Synthesis of Iridium carbon materials

In this chapter, Ir single atom catalyst (SAC) and Ir nanoparticles (NP) samples were prepared, and they were tested in two catalytic reactions of selective hydrogenation in different mediums: hydrogenation of butadiene in gaseous condition and hydrogenation of levulinic acid (LA) in aqueous solution.

Ir single atom catalyst (SAC) was prepared by a cascade anchoring strategy adapted from Zhao *et al.*[1] The Ir SAC was dispersed on a nitrogen-rich AC (a commercial activated carbon - AC - with 1400 $m^2/g$ from STREM Chemicals) by the liquid impregnation of the pristine carbon AC with $IrCl_3 \cdot xH_2O$ precursor in aqueous solution in the presence of a chelating agent (EDTA) followed by pyrolysis under Ar at 800 °C in the presence of a source of nitrogen (melamine). The sample was named χ-Ir-AC, where χ stands for the metal content (1.0 wt. %) over the entire sample mass. Carbon nitride ($CN_x$) sample was also prepared with same method without addition of Ir precursor.

For the sake of comparison, we have also prepared Ir nanoparticle (NPs) catalyst by a simple method based on the liquid-phase impregnation of the AC support with a $IrCl_3 \cdot xH_2O$ precursor aqueous solution, followed by reduction under $H_2$/Ar flow at 700 °C, as described earlier.[2] The sample was named χ-Ir@AC-700, where χ stands for the metal content (3.7 wt. %) over the entire sample mass.

## 4.2 Physicochemical characterization

The synthesized Ir samples have been characterized by a large panel of techniques for their physicochemical properties.

The synthesized hybrid material, together with $CN_x$ and initial AC, were characterized firstly by X-Ray Diffraction (XRD) for their structural properties (Figure 4.1). XRD patterns of 1.0-Ir-AC and 3.7-Ir@AC-700 samples showed only contribution from activated carbon support and no diffraction peaks from *fcc* metal Ir (40.699 ° -(111); 47.326 ° -(200)). This suggests that Ir is well dispersed on the carbon host, either as ultra-small nanoparticles with too short coherence length to diffract X-rays,[3] or as smaller size such as, sub-nanometric to single atom states (without periodic arrangement). This will be further verified by transmission electron microscopy for both metal containing samples.

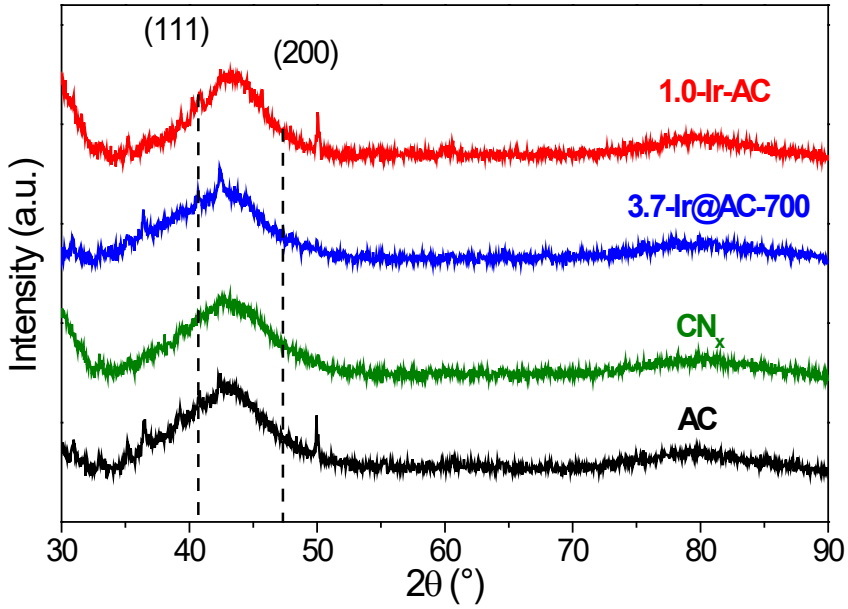


*Figure 4. 1: XRD patterns of AC, $CN_x$, 3.7-Ir@AC-700 and 1.0-Ir-AC.*

The Ir hybrid materials were characterized by Transmission Electron Microscopy secondly (TEM) to see the dispersion of Ir on the carbon hosts as well as the distribution of Ir nanoparticles, sub-nanoparticles, nanoclusters, or possibly single atoms.

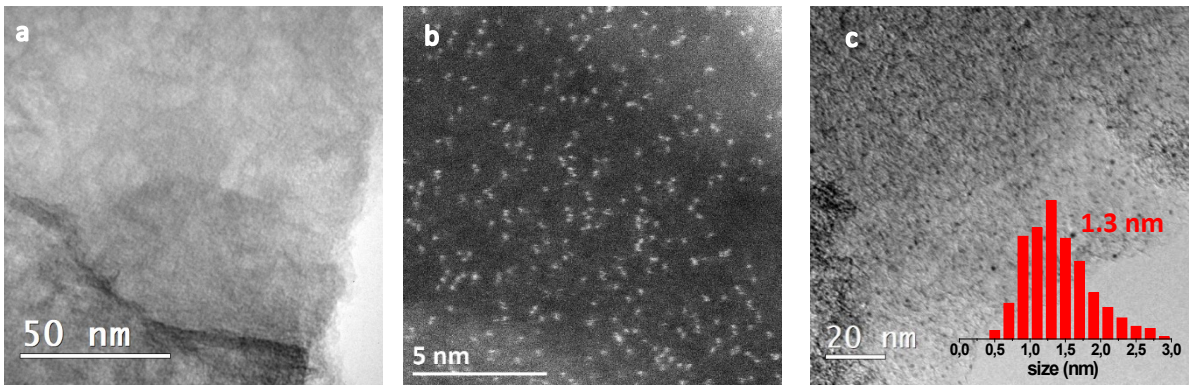


*Figure 4. 2: a) TEM image of 1.0-Ir-AC, b) HAADF-STEM image of 1.0-Ir-AC, and c) TEM image of 3.7-Ir@AC-700.*

While no Ir nanoparticles nor clusters could be found by classic TEM for 1.0-Ir-AC sample (Figure 4.2 a), the high-resolution aberration-corrected high-angle annular dark-field scanning transmission electron microscopy (HAADF-STEM) images showed isolated bright spots homogeneously dispersed on the support (Figure 4.2 b). The bright spots displayed in the images are Ir atoms as Ir has a higher atomic number Z than C, N and O. The size of spots of 1.0-Ir-AC is measured manuelly, the mean size is 2.0 (±0.4) Å on a basis of statistical analysis over 100 bright spots, corroborating that these Ir atoms are mainly in single atomic state. On

the contrary, Ir is agglomerated in the form of well dispersed nanoparticles on the carbon support for 3.7-Ir@AC-700 sample, as revealed by TEM images (Figure 4.2 c); the mean size is very small around 1.3 (±0.5) nm. For the sake of the convenience and clarity, the samples 1.0-Ir-AC and 3.7-Ir@AC-700 will be further named Ir-SAC and Ir-NP, respectively.

The textural properties were characterized by liquid nitrogen adsorption/desorption measurements (Brunauer–Emmett–Teller (**BET**)). Figure 4.3 shows the $N_2$ adsorption/desorption curves for AC, $CN_x$ and Ir-SAC. As shown in this figure, AC and Ir-SAC are microporous and mesoporous materials, whereas $CN_x$ is poorly porous with small microporosity still present. The specific surface area of $CN_x$ (364 $m^2/g$) and Ir-SAC (671 $m^2/g$) reduces tremendously compared to initial AC (1400 $m^2/g$) probably due to loss of porosities after the pyrolysis reaction with melamine and EDTA.

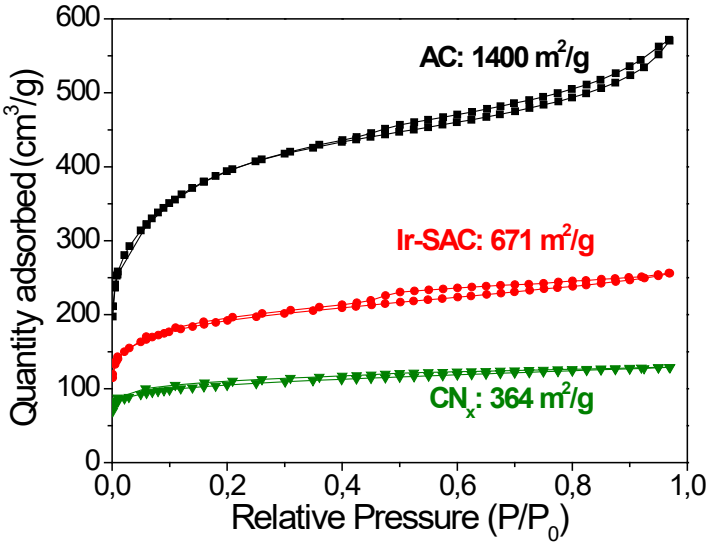


*Figure 4. 3: Liquid $N_2$ adsorption/desorption curves of AC, $CN_x$, and Ir-SAC, determined at ICMPE.*

To gain more information on the physicochemical changes induced by pyrolysis, the SEM analysis was carried out for AC and Ir-SAC (Figure 4.4). According to the textural properties analysis, the pristine AC possesses both microporous and mesoporous (Figure 4.3). Some mesopores can be clearly seen from the SEM images (Figure 4.4 b). After the pyrolysis with EDTA and melamine, the particle size of Ir-SAC increased as compared to AC (22.9 µm > 7.6 µm). It seems that a crust is formed at the surface of AC after pyrolysis and some of its porosity was lost during this process (Figure 4 d), which is in good agreement with the results obtained from BET analysis.

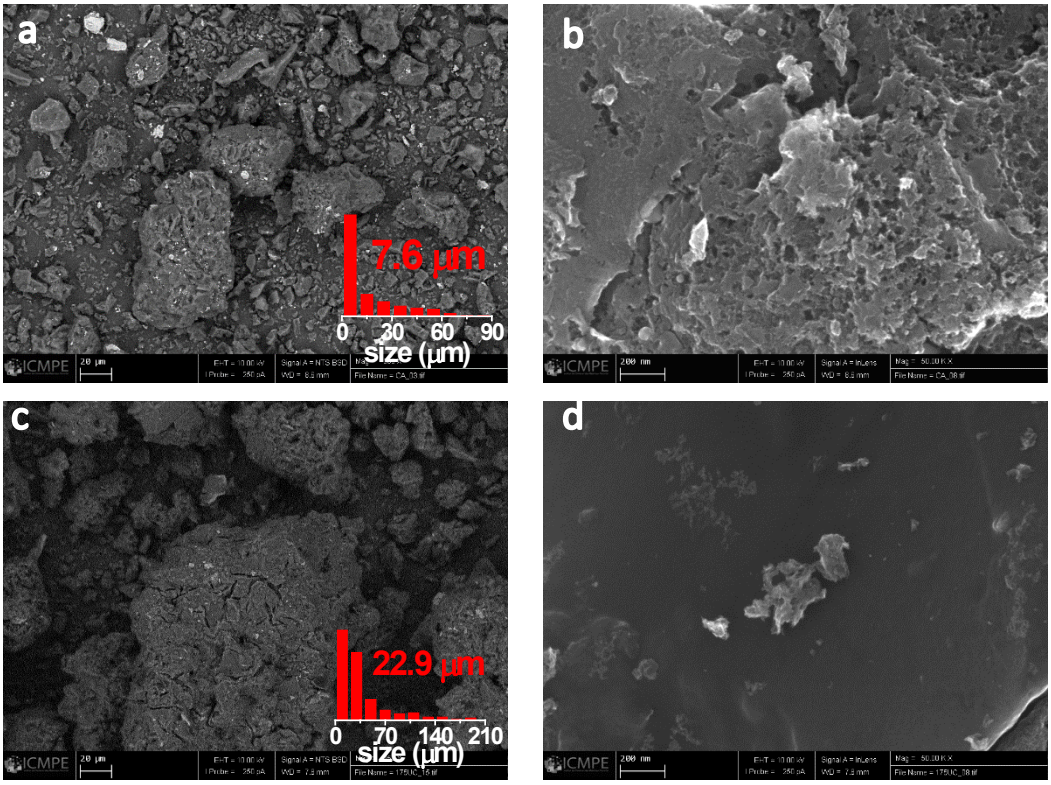


*Figure 4. 4: SEM images of a, b) initial AC; c, d) Ir-SAC.*

The Ir-SAC, $CN_x$ and initial AC were further studied by Raman spectroscopy. The latter signals arising from lattice vibrations of graphitic materials are very sensitive to the degree of structural disorder (defects). A common feature of all graphene and carbon graphitic materials is the presence of the G band (G for graphite) located around 1610 $cm^{-1}$, which corresponds to the zone center vibration of carbon atoms against each other's in the layer planes. The presence of disorder in the graphitic lattice is associated with the occurrence of the D band (D for defect) around 1350 $cm^{-1}$. All samples show these two dominant D and G peaks (Figure 4.5) proving a typical signature of amorphous carbon.[4]

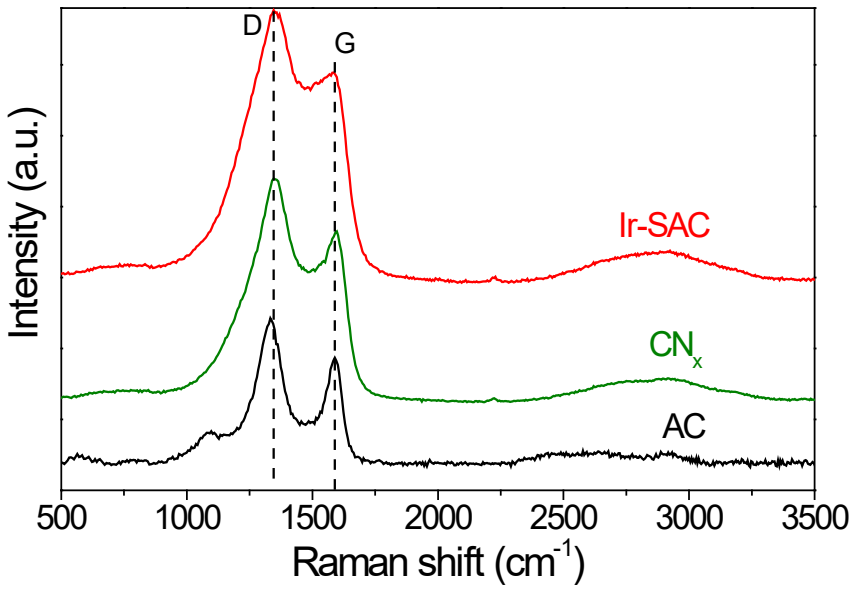


*Figure 4. 5: Raman spectra of AC, $CN_x$, and Ir-SAC.*

To obtain further information from the surface as well as the chemical state of nitrogen atoms and metal atoms as single atoms and nanoparticles, X-ray photoelectron spectroscopy (XPS) was performed for Ir samples. N 1s spectrum of Ir-SAC are presented in Figure 4.6 a. The N 1s spectrum shows four different bonding configurations of N atoms, which are attributed to pyridinic-N (398.6 eV), pyrrolic-N (399.7 eV), graphitic-N (401.2 eV) and oxidized-N (404.2 eV), respectively. Pyridinic-N and pyrrolic-N are the nitrogen species at the edges or in the vacancies of the graphitic host, respectively. The pyridinic–N bonds with two C atoms and contributes one *p* electron to the $\pi$ system. Pyrrolic–N refers to N atoms incorporated in pentagonal ring and contributes two *p* electrons to the $\pi$ system. Graphitic–N refers to N atoms that substitute C atoms in the hexagonal ring.

The Ir 4f spectrum of Ir-SAC is shown in Figure 4.6 b and compared with Ir-NP sample and Ir bulk. For Ir-SAC, Ir 4f has two main peaks at 62.5 eV ($4f_{7/2}$) and 65.5 eV ($4f_{5/2}$), the binding energies are higher than Ir in Ir-NP and Ir bulk. The results imply the positively charged nature of Ir species in Ir-SAC, which are different from Ir species in Ir-NP and Ir bulk. It should be noted that due to the partial oxidation of Ir nanoparticles in air, the binding energy of Ir 4f in Ir-NP is slightly larger than Ir bulk (61.6 eV > 60.8 eV).

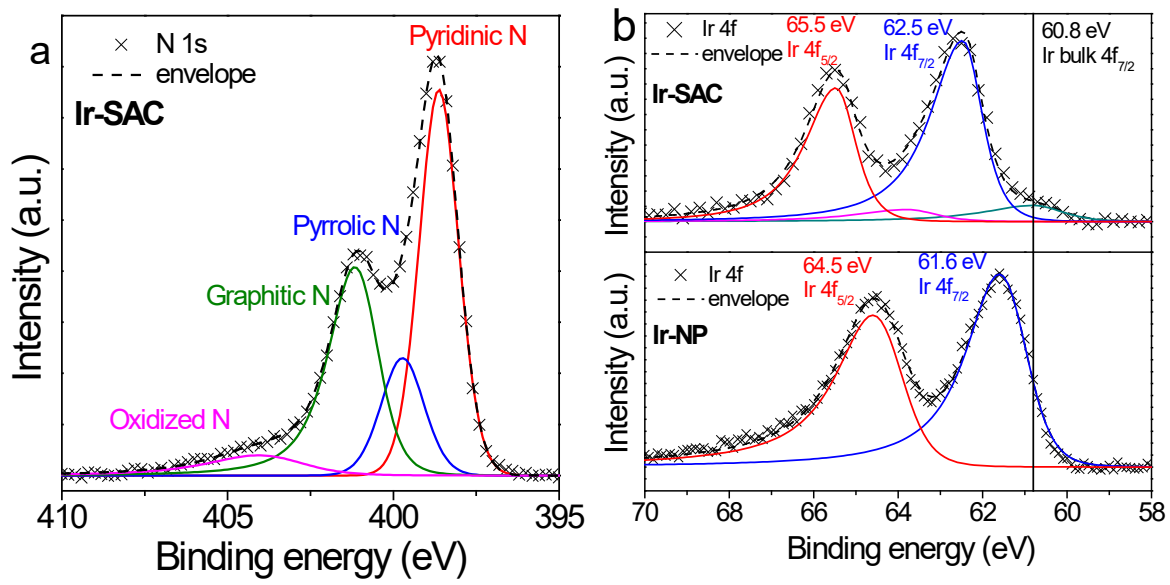


*Figure 4. 6: a) N 1s XPS spectrum of Ir-SAC and b) Ir 4f XPS spectra of Ir-SAC and Ir-NP; The black line at 60.8 eV is the binding energy of Ir bulk $4f_{7/2}$ taken from literature.*[5]

The Ir concentration in the different composites was determined by ICP-AES and the content of light elements: N, C and H, was analysed by CHNS technique. The results are listed in Table 4.1. The C content decreased for the synthesized materials compared to the pristine AC, while the concentration of N significantly increased for Ir-SAC and $CN_x$. The content of oxygen is not measured due to the presence of impurities, such as aluminosilicates in the pristine AC, thus the sum of metal content as well as the light elements (N, C and H) is not 100%.

| sample | ICP-AES | CHNS | | |
|---|---|---|---|---|
| | Metal content (wt. %) | N (wt. %) | C (wt. %) | H (wt. %) |
| AC | - | 0.47 (±0.08) | 78.39 (±0.81) | 0.22 (±0.04) |
| $CN_x$ | - | 18.78 (±0.11) | 62.92 (±0.30) | 0.74 (±0.11) |
| Ir-SAC | 0.99(±0.01) | 14.07 (±0.15) | 68.97 (±0.11) | 0.43 (±0.03) |
| Ir-NP | 3.70(±0.02) | - | - | - |

*Table 4. 1: Ir content of Ir-SAC and Ir-NP, determined by ICP-AES, and N, C and H concentration of AC, $CN_x$ and Ir-SAC, determined by CHNS.*

## 4.3 Formation process and stability of Ir-SAC sample

### 4.3.1 Formation process of Ir SAC sample

The formation process of Ir-SAC was investigated by the thermogravimetric analysis coupled with mass spectroscopy (TGA-MS). A mixture of $IrCl_3$, AC, EDTA and melamine (0.3 wt.% $IrCl_3$, 12.5 wt.% AC, 25.0 wt.% EDTA and 62.5 wt.% melamine) following the grinding procedure (**Chapiter 2.1.3**) before calcination was heated to 800 °C with a ramp of 3 °C/min under Ar flow (40 ml/min). The evolution of sample mass and gaseous products as well as the sample temperature were recorded by TGA-MS, as shown in Figure 4.7.

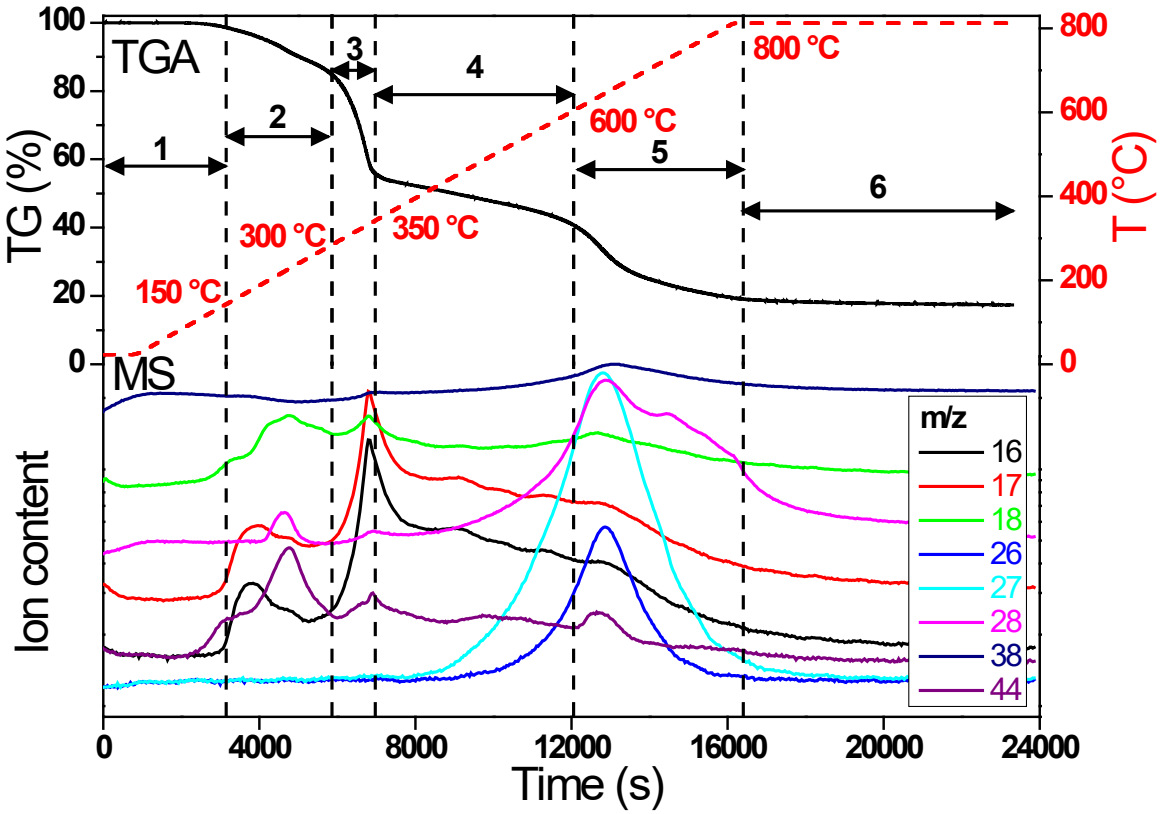


*Figure 4. 7: TGA-MS data of the mixture of $IrCl_3$, AC, EDTA and melamine (0.3 wt.% $IrCl_3$, 12.5 wt.% AC, 25 wt.% EDTA and 62.5 wt.% melamine), the final product after TGA is Ir-SAC.*

The pyrolysis process can be deconvoluted into several steps with the evolution of temperature and time, as shown in Figure 4.7:

(1) 0 – 150 °C: At temperature lower than 150 °C, no significant weight loss is observed.

(2) 150-300 °C: The mixture exhibits a smooth loss of about 15 wt.% in this range of temperature. This can be attributed to the sublimation and decomposition of EDTA, which begins to decompose at about 150 °C. The material undergoes decarboxylation and hydrolysis

process of the ethylene C-N link to form amine-based carbon materials with the release of $CO_2$ and $H_2O$.[6] This attribution is confirmed by the presence of ion current peaks in the MS analysis associated to the mass of $CO_2^+$ ($m/z = 44$), $CO^+$ ($m/z = 28$), and $H_2O^+$ ($m/z = 18$). Two peaks at $m/z = 16$ and $m/z = 17$ were also detected, this can be ascribed to the ammonium solution ($NH_3 \cdot H_2O$) added during the synthesis.

(3) 300-350 °C: The mixture shows a more marked weight loss with a steep decrease. This may be explained by the sublimation and condensation of melamine, accompanied by the formation of melem ($C_6N_{10}H_6$) and the elimination of ammonium. This is highlighted by the presence of ion peaks of ammonia species: $NH_4^+$ ($m/z = 18$), $NH_3^+$ ($m/z = 17$) and $NH_2^+$ ($m/z = 16$).

(4) 350 -600 °C: At the higher temperature of up to 600 °C, melem begins to polymerize forming melon ($C_6N_9H_3$) with a small loss of sample weight.

(5) 600 – 800 °C: At high temperatures above 600 °C, melon polymerize to form graphitic carbon nitride, g-$C_3N_4$. The latter becomes unstable at about 650 °C and pyrolyzes into a new nitrogen-based carbon material ($CN_x$).[7–9] In this region, the fragment of carbon-nitrogen compounds was detected in the MS analysis: $CN^+$ ($m/z = 26$), $HCN^+$ ($m/z = 27$), and $H_2CN^+$ ($m/z = 28$).

(6) 800 °C: No weight loss nor gas product is discerned, therefore the newly formed $CN_x$ is stable at 800 °C.

The thermal decomposition of melamine and the formation of graphitic carbon nitride are shown in Figure 4.8. HCl ($m/z = 38$) was also detected during the pyrolysis process owning to the chloride from the $IrCl_3 \cdot xH_2O$ precursor. During the calcination, Ir ions sequestered by EDTA can be subsequently incorporated into the newly formed nitrogen-based carbon network ($CN_x$) from the pyrolysis of EDTA and melamine, preventing them from aggregation to form large metal clusters, as evidenced by XRD, HAADF-STEM and XPS analyses.

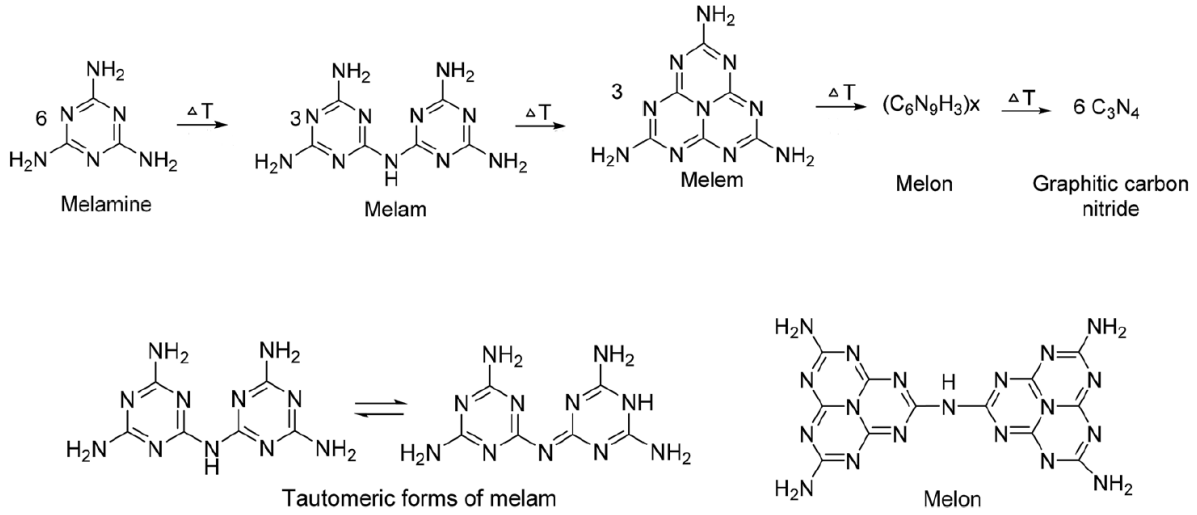


*Figure 4. 8: Thermal decomposition of melamine and the formation of graphitic carbon nitride.*[7]

### 4.3.2 Stability of Ir-SAC sample

The thermal stability of Ir-SAC was studied by TGA analysis under air flow. The Ir-SAC is stable up to around 450 °C, as shown in Figure 4.9. The Ir-SAC is less air resistant than the pristine AC while $CN_x$ is more stable than the pristine carbon. This can be explained by the existence of Ir atoms catalysing the oxidation process.[10] The high oxidation resistance of $CN_x$ may be possibly originated from the strong covalent carbon nitrogen bonds.[11] The mass loss at high temperature does not reach 0% due to the presence of around 10% impurity such as, alumina-silicates (also confirmed by ICP chemical analysis), which are very stable under these conditions.

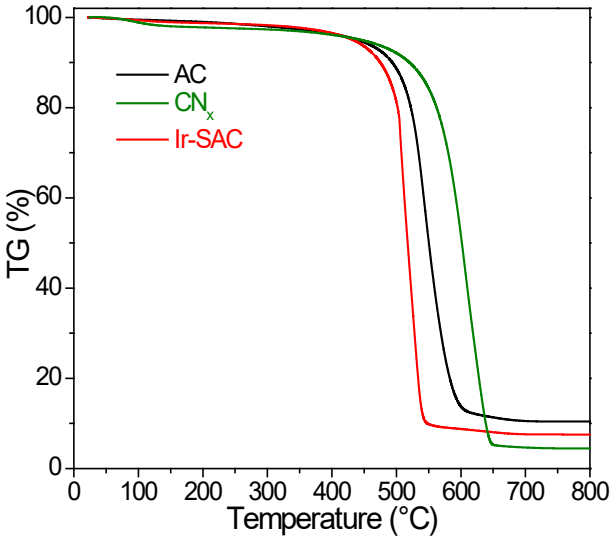


*Figure 4. 9:TGA under dry air flow of pristine AC, $CN_x$, and Ir-SAC.*

The stability of Ir single atoms against aggregation was studied at high temperature. Ir-SAC was heated to 400 °C for 30 min with a ramp of 10 °C/min under 5% $H_2$/Ar (200 ml/min). The hydrogen treated sample was then characterized by HAADF-STEM (Figure 4.10). No Ir clusters nor nanoparticles after the thermal reduction treatment could be noticed, suggesting that the Ir-SAC is stable up to 400 °C.

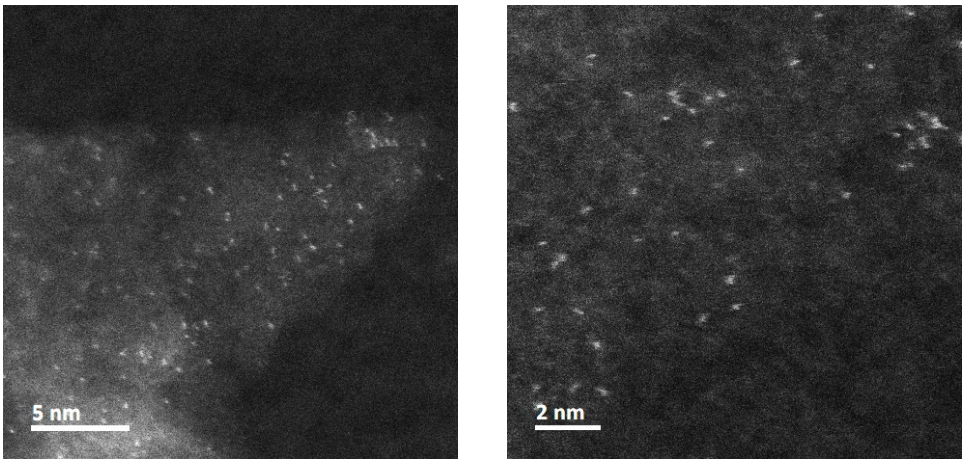


*Figure 4. 10: HAADF-STEM images of Ir-SAC after $H_2$ treatment at 400 °C.*

In conclusion, Ir single atom catalyst sample supported on a nitrogen-based carbon material was successfully synthesized by wet chemistry and pyrolysis method. The presence of Ir single atoms was confirmed by XRD, TEM and XPS characterizations, comparing with the Ir nanoparticles sample. Ir-SAC is a microporous and mesoporous amorphous carbon material, which has less surface area than the initial AC. The material shows high stability against oxidation under air condition (> 400 °C) and the Ir single atoms are stable up to 400 °C against aggregation.

### 4.4 Catalytic test

The synthesized Ir samples were evaluated in the catalytic reactions of selective hydrogenation in different mediums at laboratory IRCELYON: hydrogenation of butadiene in gaseous condition and hydrogenation of levulinic acid (LA) in aqueous solution.

#### 4.4.1 Hydrogenation of butadiene

The catalytic test of hydrogenation of butadiene was carried out at laboratory IRCELYON. The hydrogenation of butadiene was performed under atmospheric pressure in a continuous flow fixed-bed reactor. Before the reaction, 40 mg of catalyst was mixed with 100 mg $Al_2O_3$ and activated *in situ* with hydrogen by heating from room temperature (RT) to

250 °C at a heating rate of 4 °C/min and maintained at 250 °C for 1 h. Then the reactor was cooled down to RT under $H_2$. The reaction was then carried out from RT to 200 °C with a reaction gas flow of 100 ml/min ($C_2H_2$:$H_2$:He = 2:10:88). The conversion and selectivity of Ir-SAC and Ir-NP during the hydrogenation of butadiene reaction are shown in Figure 4.11. Ir-SAC shows an impressive nearly 100% selectivity to butenes starting from 25 °C with high stability in the temperature range. The conversion increases steadily with rising the temperature reaching 80% at maximum temperature 200 °C. Furthermore, for Ir-SAC, the majority product is trans-2-butene which is rarely reported in the literature, where 1-butene is the majority product.[12–14] Ir-NP behaves differently with high selectivity at low temperature and low conversion (below 30%). However, when the conversion exceeds 30% a sudden drop of the selectivity occurs to almost full hydrogenation to butane at high temperatures.

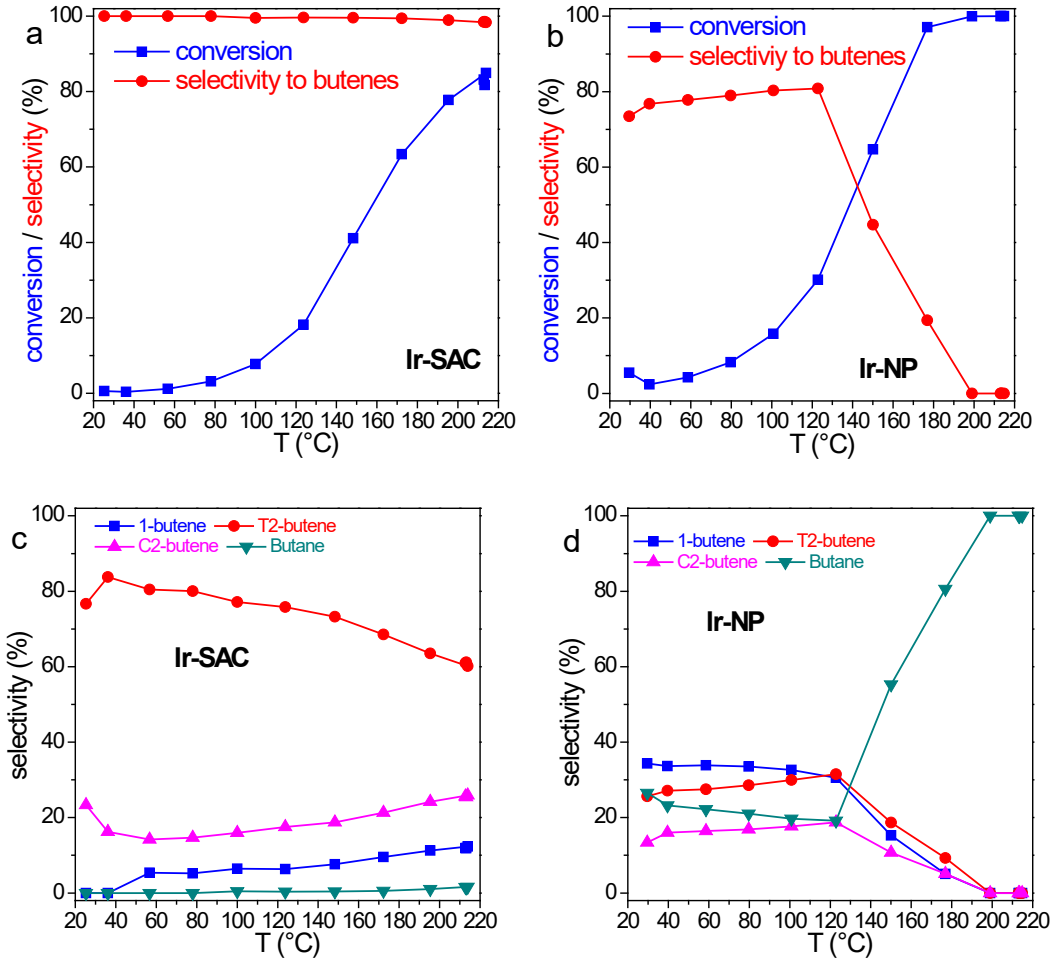


*Figure 4. 11: Catalytic performance in hydrogenation of butadiene of Ir-SAC and Ir-NP. Conversion and selectivity to butenes as a function of temperature for Ir-SAC (a) and Ir-NP (b); Product distribution for Ir-SAC (c) and Ir-NP (d).*

In order to understand the high selectivity for trans-2-butene of Ir-SAC, the isomerization of butenes was performed over Ir-SAC and $CN_x$ samples in the same reactor of the hydrogenation of butadiene. Ir-SAC or $CN_x$ was mixed with $Al_2O_3$ and pre-treated at 250 °C for 30 min under $H_2$ and then under He to eliminate the $H_2$ in the sample. After the pre-treatment, the isomerisation reaction was realised from RT to 350 °C with a reaction gas flow of 100 ml/min of 0.4 % butenes/$N_2$ (10% 1-butene, 51% isobutene, 17% cis-2-butene and 22% trans-2-butene). The results are shown in Figure 4.12. Interestingly, there is no isomerization reaction over the $CN_x$ support, the composition of butenes does not vary with the increase of temperature. However, Ir-SAC promotes the isomerization reaction from ambient temperature to go towards the thermodynamic equilibrium, with the increase of trans-2-butene and the decrease of 1-butene in the beginning of the reaction. Therefore, this finding may be used to explain the high selectivity on trans-2-butene for Ir-SAC. In hydrogenation of butadiene over Ir-SAC, 1-butene may be the majority product in the first step. Thereafter, 1-butene isomerizes probably to trans-2-butene to make a more thermodynamically stable mixture of butenes. Thus, trans-2-butene becomes the principal product in hydrogenation of butadiene over Ir-SAC catalyst.

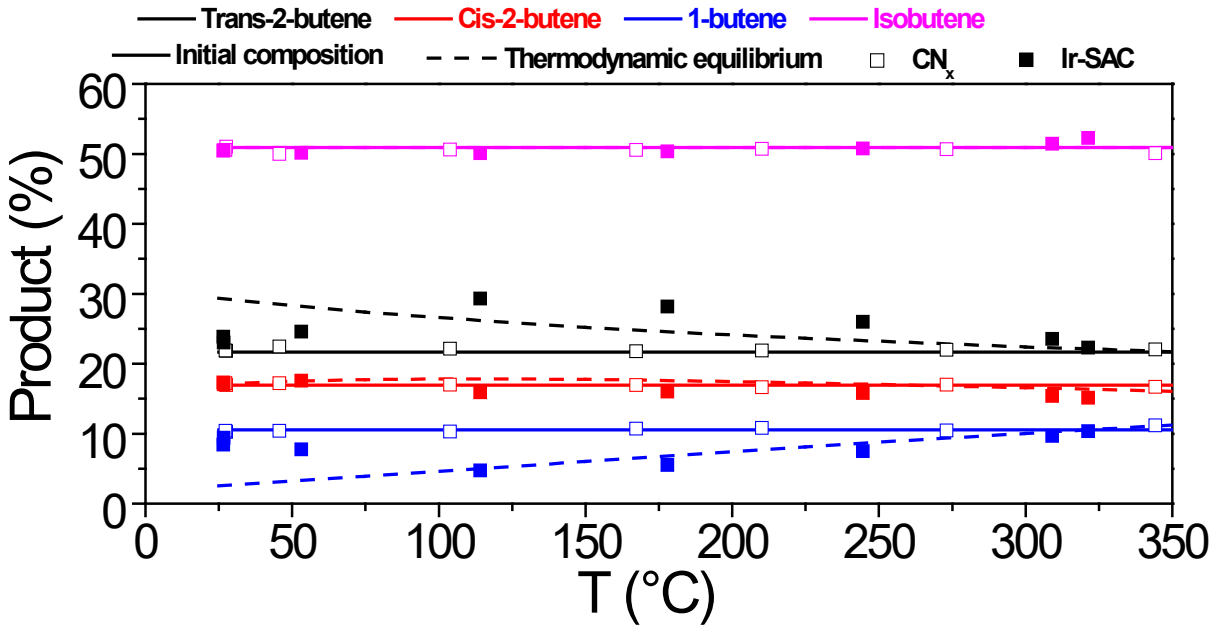


*Figure 4. 12: Isomerization of butenes over Ir-SAC and $CN_x$. The solid line represents the initial composition of butenes, the dashed line represents the thermodynamic equilibrium composition as a function of temperature (without considering the isobutene), the void square represents the results of $CN_x$ and the solid square represents the results of Ir-SAC.*

To gain in-depth knowledge of the local structure of Ir-SAC such as, the chemical coordination environments and electronic feature in reactive conditions of hydrogenation of butadiene, we have performed *operando* X-ray absorption energy spectroscopy (XAS) for Ir-SAC. For the sake of comparison, we have also investigated Ir-NP under the same reactive conditions. The experiment was followed as close as possible to the laboratory reaction conditions. Samples were heated to 250 °C for 1 h under He/$H_2$ flow (15 ml/min He and 15 ml/min $H_2$) and then cooled down to room temperature. Afterward, the catalysts were exposed to the reactive gas mixture (35 mL/min): 0.5% $C_4H_6$ + 2.5% $H_2$ + 97% He and temperature were heated to 200 °C with a ramp of 1 °C/min. The temperature was maintained at 200 °C for 1 h under reaction condition (Figure 4.13). The XAS measurements were coupled with continuous mass spectrometry (MS) to determine the reaction kinetics and catalytic data.

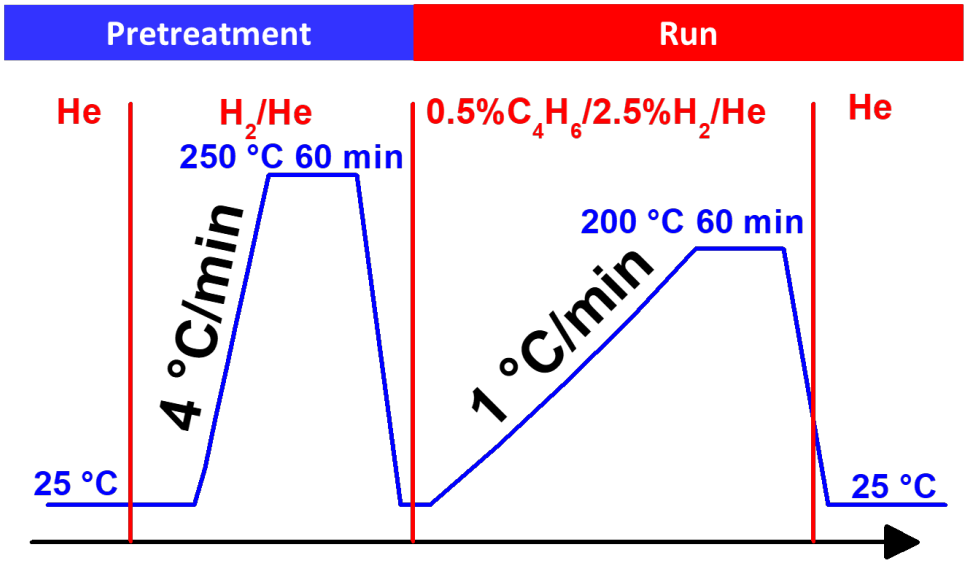


*Figure 4. 13: Process of operando XAS experiment Ir-SAC and Ir-NP.*

The X-ray absorption near edge structure (XANES) and extended X-ray absorption fine structure (EXAFS) spectra before reaction at RT are shown in Figure 4.14. Ir bulk and $IrO_2$ were used as references. As shown in Figure 4.14 a, the intensity of the white line of Ir-SAC is close to $IrO_2$ which indicates that its oxidation state approaches that of $IrO_2$. For Ir-NP, the white line peak is situated at almost the same level of that of Ir bulk demonstrating metallic species. The oxidation states of Ir in Ir-SAC and Ir-NP were calculated according to the method proposed by Hambley *et al*[15] and compared to those of well-known references: bulk metal $Ir^{(0)}$ and oxide $Ir^{(IV)}O_2$ (Figure 4.15). The oxidation state of Ir was estimated using the following

equation: $OS_{sample} = 4 \times \left[\left(\frac{a}{b}\right)_{sample} - \left(\frac{a}{b}\right)_{Ir\ bulk}\right] / \left[\left(\frac{a}{b}\right)_{IrO_2} - \left(\frac{a}{b}\right)_{Ir\ bulk}\right]$, where *a* refers to the maximum of the intensity of the white line and *b* is the lowest point of the trough after the white line.

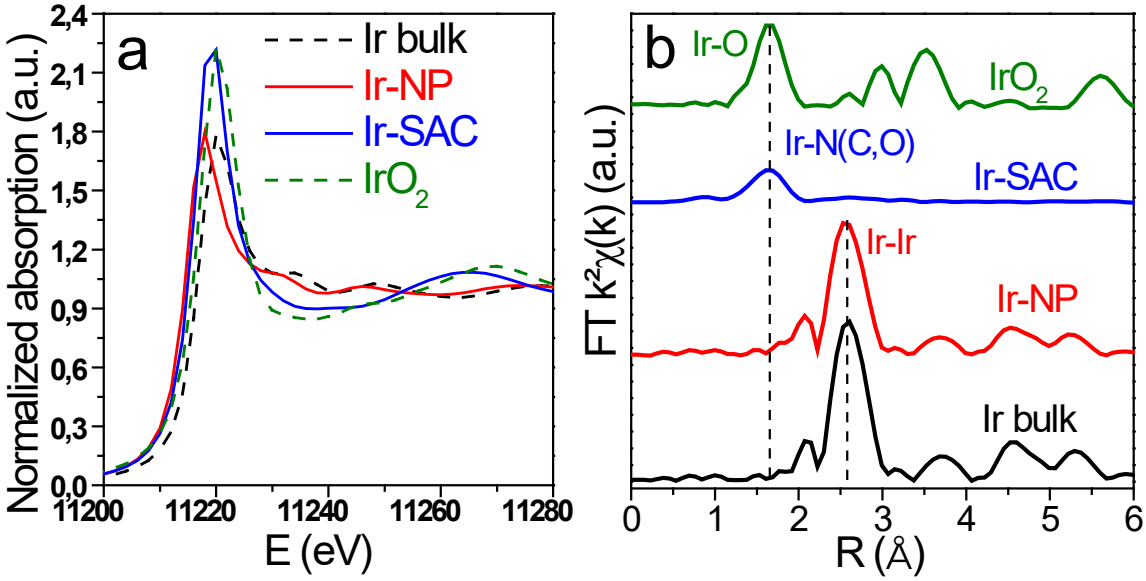


*Figure 4. 14: a) XANES spectra at the Ir $L_3$-edge of Ir bulk (black), Ir-NPs (red), Ir-SAC (blue) and $IrO_2$ (green) before reaction at RT, and b) their corresponding Fourier transform. For the sake of comparison, FT have been stacked.*

Initially, Ir in Ir-SAC has an oxidation state of +3.2, while Ir in Ir-NP displays +0.1 (slightly oxidized nanoparticles). This further confirms that Ir exists as single atoms well dispersed in Ir-SAC. To follow the change in the electronic properties of Ir-SAC in *operando* conditions we have applied the same data treatment (Table 4.2 and Figure 4.15).

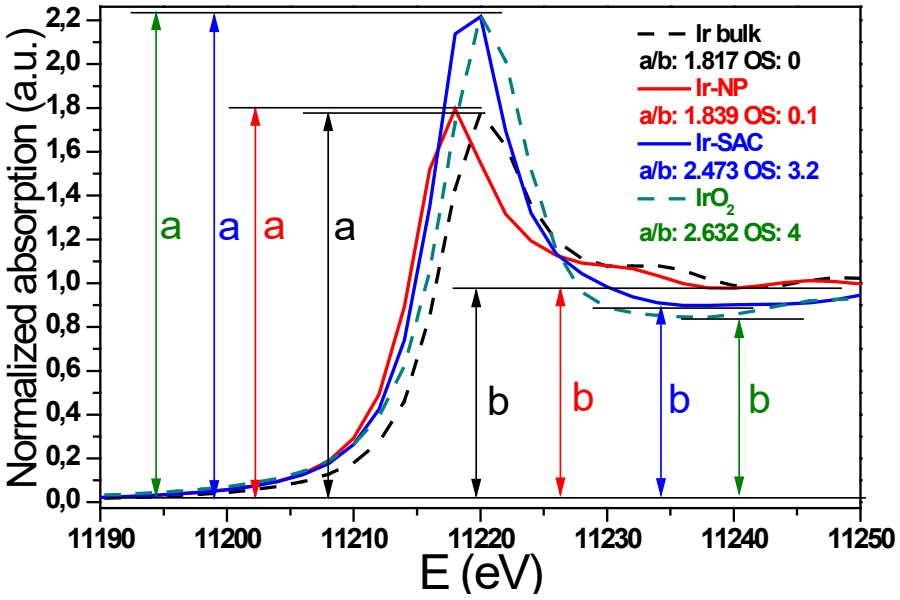


*Figure 4. 15: XANES spectra of Ir bulk (black), Ir-NP (red), Ir-SAC (blue) and $IrO_2$ (green) showing the difference in peak heights for these samples, and the parameters a and b used for the assessment of the oxidation state.*

The Fourier transforms of EXAFS spectra of the initial samples are compared to Ir bulk and $IrO_2$ in Figure 4.14 b. Ir bulk shows typical peaks for the *fcc* metal with the dominant one at approximately 2.58 Å (Ir-Ir nearest distances). The $IrO_2$ shows distinct features compared to bulk with a main peak at around 1.62 Å corresponding to the Ir-O nearest neighbours of the tetragonal structure of the oxide. The FT of Ir-SAC is clearly different comparative to metal and oxide samples and features a single peak at around 1.6 Å with low intensity. This peak can be ascribed to the backscattering from the nearest neighbours of Ir-*X* (*X* = N/C/O). However, EXAFS cannot distinguish between light elements close to each other such as, C, N or O because of their close scattering amplitude. It is worth noting that Ir-Ir scattering peak (around 2.6 Å) is not visible, which clearly confirms atomic dispersion of Ir in Ir-SAC without any metal agglomeration. On the other side, the FT of Ir-NP is nearly the same as Ir bulk.

To reveal the local structure of Ir-SAC under reactive conditions, we have performed EXAFS refinements based on a structural model where one metal iridium is coordinated with four light atoms Ir-$(N,C)_xO_y$ (x + y = 4), as proposed in the literature.[16,17] The EXAFS fitting results such as, the coordination number-*N*, the Debye-Waller factor-$\sigma^2$ and the nearest neighbours Ir-*X* distance-*R* are listed in Table 4.2. Typical refinements results are plotted in Figure 4.16.

| Conditions | | | EXAFS | | | | XANES |
|---|---|---|---|---|---|---|---|
| Step | Gas | T (°C) | N | $\sigma^2$ (Å$^2$) | R (Å) | QF | a/b |
| Initial state | air | 25 | 4.0 (1) | 0.0052 (3) | 2.016 (1) | 0.14 | 2.473 |
| Initial state | He | 25 | 4.0 (1) | 0.0052 (3) | 2.016 (1) | 0.11 | 2.473 |
| Introduction of reduction gas | $H_2$/He | 25 | 4.0 (1) | 0.0052 (3) | 2.016 (2) | 0.12 | 2.468 |
| Pretreatment ramp | $H_2$/He | 25 | 4.0 (1) | 0.0053 (3) | 2.016 (1) | 0.10 | 2.465 |
| | | 50.5 | 4.0 (1) | 0.0055 (3) | 2.015 (2) | 0.10 | 2.446 |
| | | 84.2 | 3.9 (1) | 0.0061 (4) | 2.012 (1) | 0.07 | 2.407 |
| | | 117.6 | 3.6 (1) | 0.0059 (4) | 2.008 (1) | 0.06 | 2.349 |
| | | 150.6 | 3.3 (1) | 0.0059 (4) | 2.005 (1) | 0.06 | 2.312 |
| | | 183.6 | 3.2 (1) | 0.0059 (4) | 2.001 (1) | 0.05 | 2.283 |
| | | 216.3 | 3.1 (1) | 0.0057 (4) | 1.999 (1) | 0.04 | 2.249 |
| | | 252 | 3.0 (1) | 0.0057 (5) | 1.997 (1) | 0.05 | 2.216 |
| Pretreatment at 250 °C | $H_2$/He | 250 | 2.9 (1) | 0.0057 (5) | 1.996 (1) | 0.05 | 2.228 |
| | | 250 | 2.9 (1) | 0.0056 (4) | 1.995 (1) | 0.04 | 2.204 |
| | | 250 | 2.9 (1) | 0.0052 (5) | 1.995 (1) | 0.05 | 2.194 |
| | | 250 | 2.9 (1) | 0.0053 (4) | 1.995 (1) | 0.05 | 2.189 |
| | | 250 | 2.8 (1) | 0.0052 (4) | 1.995 (1) | 0.04 | 2.185 |
| Pretreatment cooling | $H_2$/He | 34.1 | 2.9 (1) | 0.0049 (4) | 1.996 (1) | 0.06 | 2.199 |
| Introduction of reactive gas mixture | $C_4H_6$/$H_2$/He | 24.9 | 3.0 (1) | 0.0049 (5) | 1.997 (1) | 0.06 | 2.222 |
| Reaction ramp | $C_4H_6$/$H_2$/He | 24.8 | 3.0 (1) | 0.0048 (4) | 1.998 (1) | 0.05 | 2.225 |
| | | 64.7 | 3.1 (1) | 0.0051 (5) | 2.001 (1) | 0.06 | 2.250 |
| | | 106.5 | 3.1 (1) | 0.0053 (4) | 2.001 (1) | 0.05 | 2.244 |
| | | 147.7 | 3.1 (1) | 0.0054 (4) | 1.999 (1) | 0.05 | 2.232 |
| | | 198.6 | 3.0 (1) | 0.0055 (4) | 1.996 (1) | 0.05 | 2.206 |
| Reaction at 200 °C | $C_4H_6$/$H_2$/He | 200 | 3.0 (1) | 0.0054 (4) | 1.996 (1) | 0.05 | 2.206 |
| | | 200 | 2.9 (1) | 0.0051 (5) | 1.997 (1) | 0.06 | 2.204 |
| | | 200 | 3.0 (1) | 0.0053 (4) | 1.996 (1) | 0.05 | 2.204 |
| Final state | He | 33.4 | 3.1 (1) | 0.0053 (4) | 1.996 (1) | 0.05 | 2.232 |

*Table 4. 2: EXAFS refinements result for Ir-SAC under operando conditions. The coordination number (N), the Debye–Waller factor ($\sigma^2$) and the nearest Ir–X (X=N,C,O) distance (R) are given. The values of the ratio of a/b from XANES analysis are also given.*

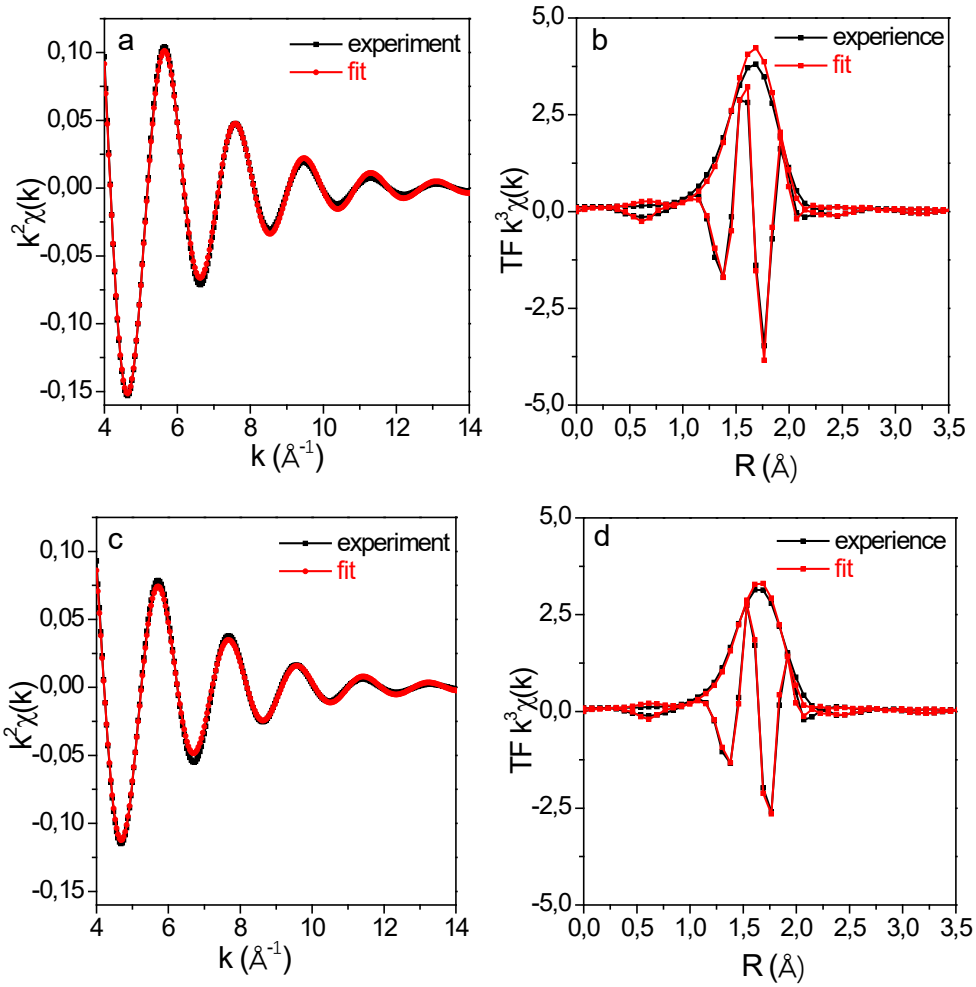


*Figure 4. 16: EXAFS fitting of Ir-SAC before pretreatment under He flow at 25°C (a, b) and after reaction under He flow at 25°C (c, d).*

The evolution of the coordination number-*N*, and the nearest neighbours Ir-*X* distance-*R* are plotted in Figure 4.17. Initially the Ir atoms are surrounded by 4 light atoms (N/C/O) and the valence state is +3.2 (Table 4.2), which is similar to $Ir^{3+}$ in homogeneous iridium (III) porphyrins and phthalocyanines complexes.[18–20]

During the pre-treatment under $H_2$ gas at 250 °C, the coordination number (*N*) reduces from 4.0 to 3.0 and further stabilizes to this latter value during the reaction at 200 °C. The coordination number reduction is accompanied by the diminution of the nearest distance Ir-*X* ($R_{Ir\text{-}x}$) (2.016 to 1.996 Å). Same tendency was found for the Ir oxidation state, it gradually reduces from +3.2 to +2.0, as shown in Figure 4.18. Therefore, a partial reduction of Ir occurs during the pre-treatment under $H_2$ accompanied by a loss of approximately 1 neighbor light atom. This hints to Ir atoms surrounded by 3 light elements (N/C/O) as being the main reactive species in the hydrogenation of butadiene. The coordination configuration *M* (metal) -$X_3$ has

been already reported for Cu, Mn and Co single atom catalysts supported on carbon nitride based materials,[21–23] and Ir (II) complexes ($^{R}$N4)Ir(COD)$^{2+}$ where Ir was found to be coordinated with 3 nitrogen atoms.[24] Moreover, Fang *et al*.[25] found that Pt in $Pt_1$/N-C SAC shows the same diminution of the coordination number (*N*) (from 4 to 2) and the oxidation state (+ 1.89 to + 1.12) under electroreduction conditions, as evidenced by *operando* XAS.[25] These authors hypothesized that the high catalytic activity of the electrochemical hydrogen evolution reaction was mainly due to this evolution of the electronic and the atomic structures.

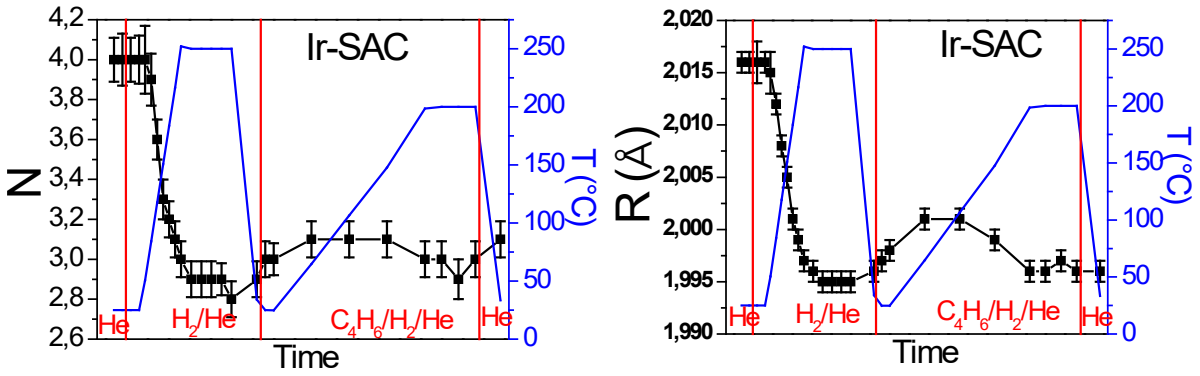


*Figure 4. 17: Variation of coordination number (N) and the nearest neighbor distance Ir-X ($R_{Ir-X}$) in operando XAS conditions.*

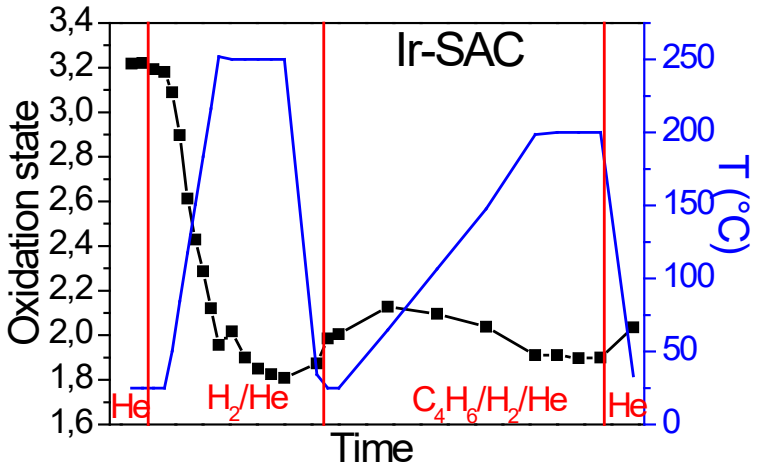


*Figure 4. 18: Variation of Ir oxidation state in Ir-SAC in operando XAS conditions.*

The decrease of the distance Ir-*X* (Figure 4.17) associated to the reduction of coordination number might be explained by the de-coordination of one longer distance Ir-*X* amongst Ir-$X_4$. As can be seen from the literature, the bond lengths of *M*-N are noticeable smaller than *M*-O in metal SACs. For example, the distances Cu-N and Cu-O were found to be 1.91 Å and 2.01 Å, respectively, in a Cu SAC supported on carbon dots.[26] In a $ZnN_x$/C catalysts,

the distances Zn-N and Zn-O are 2.00 Å and 2.14 Å, respectively.[27] Furthermore, the bond length of Ir-N in an Iridium Pincer complex, (NCN)Ir($CH_2CH_3$)Cl($OH_2$), is 2.051 Å which is significantly shorter than $R_{Ir-O}$ 2.259 Å.[28] Therefore, we hypothesize that $R_{Ir-N}$ is shorter than $R_{Ir-O}$ in Ir single atom catalysts based on nitrogen doped carbon materials. Assuming that the initial configuration is Ir-$(N,C)_xO_y$ (x + y = 4), it evolves into Ir-$(N,C)_xO_{y-1}$ during the reduction pre-treatment. Thus, the loss of one longer bond length may result in the decrease of $R_{Ir-x}$, as observed in our results (Figure 4.17).

The variation of the geometric and the electronic configuration is reflected by the reduction of the intensity of both the white-line and the FT peak of Ir-SAC before pretreatment and after reaction (Figure 4.19 a). Furthermore, it is important to notice that Ir-SAC are stable during reaction without coalescence and formation of metallic aggregates since any new peak at 2.6 Å could not be observed after reaction (Figure 4.19 b), in agreement with our previous study of stability at high temperature under $H_2$ (section **4.2.2**).

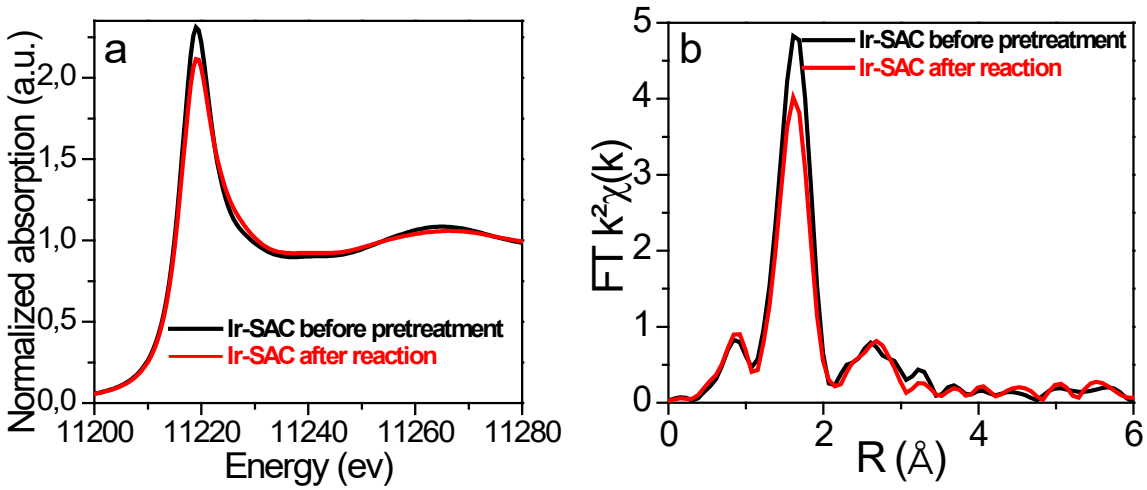


*Figure 4. 19: a) XANES spectra at the Ir $L_3$-edge of Ir-SAC before pretreatment and after reaction; b) Fourier transform of $k^2$-weighted Ir $L_3$-edge EXAFS data.*

The gaseous product distributions during reaction of both Ir-SAC and Ir-NP were detected by mass spectroscopy. The molecular masses of butadiene, butene and butane are 54, 56 and 58, respectively. As shown in Figure 4.20, the peaks of their fragments in MS spectrum range from $m/z = 15$ to $m/z = 59$ and their product pools are very similar. After a careful selection, $m/z = 54$, $m/z = 56$ and $m/z = 58$ were chosen to represent butadiene, butene and butane, respectively, although they are not the principal peaks. As shown in Figure 4.21, Ir-SAC was highly active and selective to butene while butane was the

principal product for Ir-NP. The result is consistent with laboratory catalytic tests, confirming that *operando* XAS experiments were conducted in same laboratory conditions.

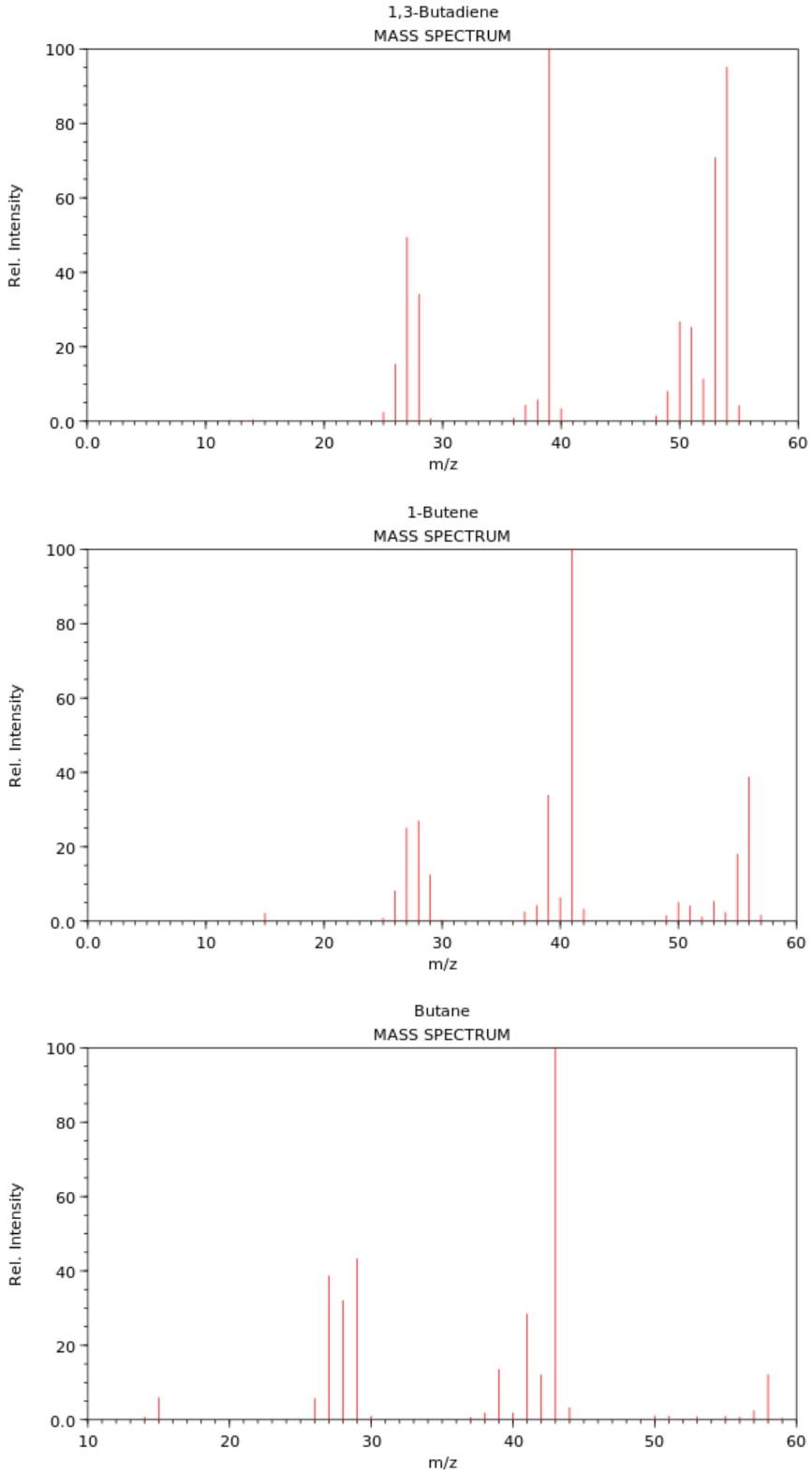


*Figure 4. 20: Mass Spectrum of butadiene, 1-butene and butane. (From NIST chemistry Webbook)*

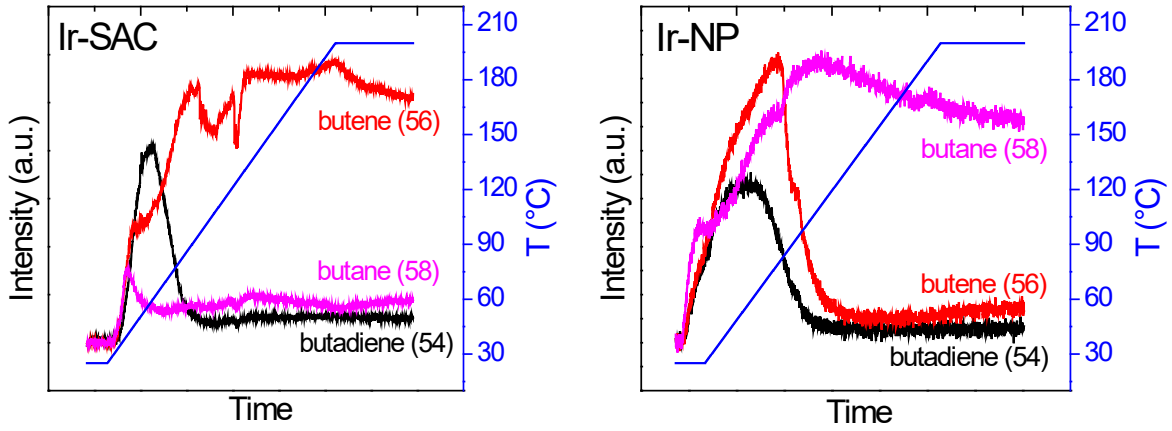


*Figure 4. 21: Product distribution during the reaction of hydrogenation of butadiene for Ir-SAC and Ir-NP, as detected by mass spectroscopy during operando XAS experiments.*

### 4.4.2 Hydrogenation of levulinic acid

As discussed above, Ir-SAC are reactive and highly selective in hydrogenation of butadiene. Furthermore, the catalyst is proved to be very stable in this gaseous reaction condition. Another study was carried out to find out their reactivity and stability in aqueous reaction condition: hydrogenation of levulinic acid (LA). The latter reaction was realised in a batch reactor at 160 °C and under 50 bar $H_2$ pressure (the molar ratio of LA to Ir was 620), and the results are shown in Figure 4.22.

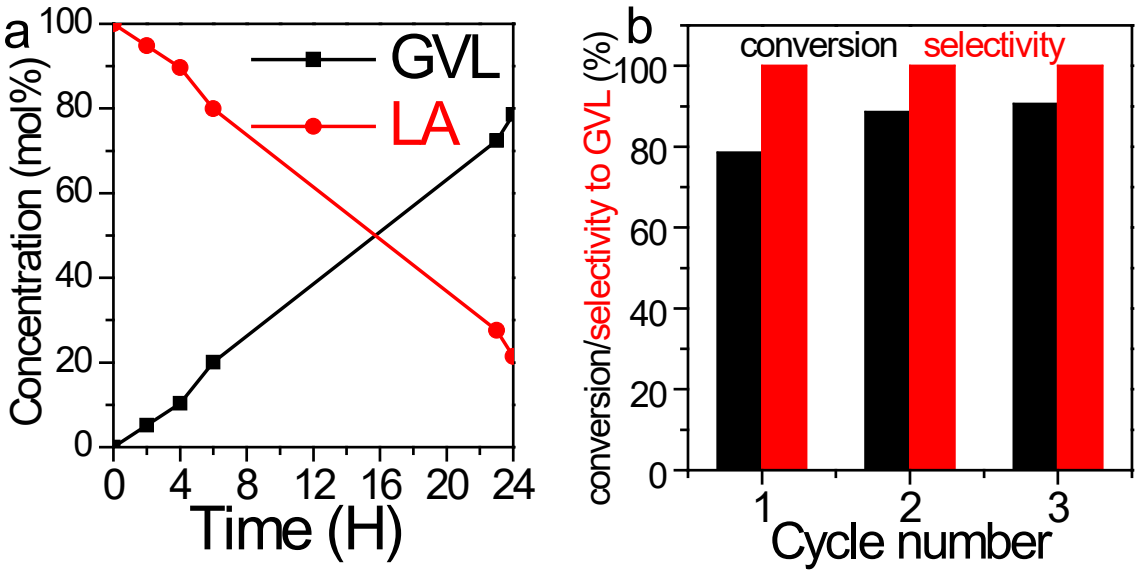


*Figure 4. 22: a) Conversion of levulinic acid in water for Ir-SAC catalyst, b) Recycling experiments of the Ir-SAC catalyst. Reaction conditions: LA (0.17 M in 150 ml water), 800 mg catalyst (the molar ratio of LA to Ir was 620), $H_2$ (50 bar), 160 °C, 24 h.*

Figure 4.22 a shows the evolution of the LA concentration and its products over reaction time. The LA conversion at 24 h is near 80% with a selectivity 100% to y-valerolactone (GVL). This result is comparable with a Ir SACs (0.6% Ir@ZrO2@C) sample reported in the literature, which achieved a LA conversion of 99% and a GVL selectivity of 98.8% after 10 h reaction under 180 °C and 40 bar $H_2$ condition (LA/Ir = 500).[29] However, the Ir SACs are less reactive than the Ir nanoparticle catalysts. For example, Du *et al.*[30] synthesized 1.9 nm nanoparticles 4.5% Ir catalyst supported on carbon nanotubes, it showed complete conversion of LA to GVL in less than 1 h in aqueous solution at 50 °C under 20 bar $H_2$ (LA/Ir = 445). Moreover, Wang *et al.*[31] reported that 100% conversion of LA to GVL in 1.5 h was attained with a 1.5 nm 3.0% Ir/SiC nanoparticles catalyst under 50 °C and 2 bar $H_2$ reaction condition (LA/Ir = 500).

The stability of Ir-SAC was investigated by performing multiple recycling test in the same reaction condition, the result is shown in Figure 4.22 b. Surprisingly, the recycled sample shows a slight activation through recycling runs. An increase in LA conversion from 80% to 90% is observed for the 2nd cycling reaction, and the LA conversion stabilizes at 90% for the 3rd cycling run. Two hypotheses could be attributed to the increase of the catalytic reactivity of Ir-SAC, such as: the increase of surface area and the formation of Ir nanoparticles. Several characterization analyses have been performed in order to understand this behaviour. The liquid nitrogen adsorption/desorption measurements were firstly realized to check the BET surface area after the 1st cycling sample.

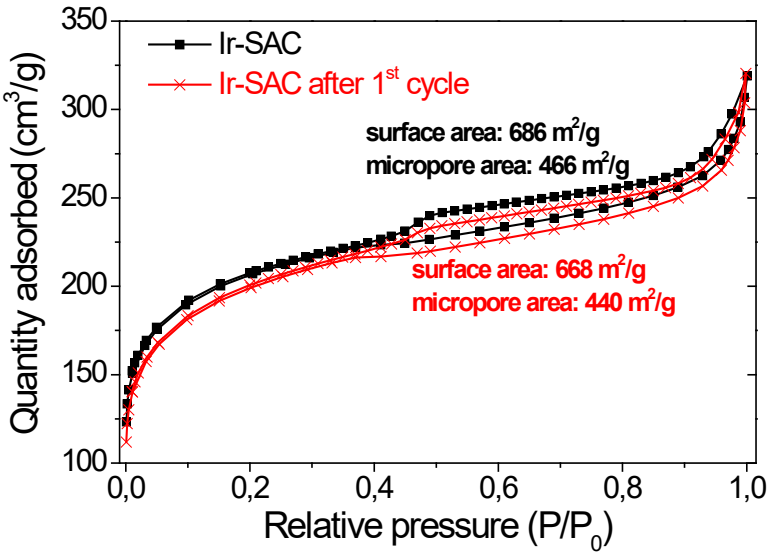


*Figure 4. 23: Liquid $N_2$ adsorption/desorption curves of Ir-SAC and Ir-SAC after 1st cycle.*

As shown in Figure 4.23, Ir-SAC has a surface area of 686 $m^2/g$ and micropore area of 466 $m^2/g$, while the surface area and the micropore area decrease slightly to 668 $m^2/g$ and 440 $m^2/g$, respectively, for Ir-SAC after 1st cycling sample. Therefore, marginal changes in the BET surface area were observed in Ir-SAC after reaction, the increase of surface area as the reason for catalytic activity activation could be excluded. For this reason, the used sample was characterized by HAADF-STEM to check the distribution of Ir atoms (Figure 4.24). According to the STEM images, no noticeable agglomeration is observed and Ir atoms exist mainly as single atom states or as multimers.

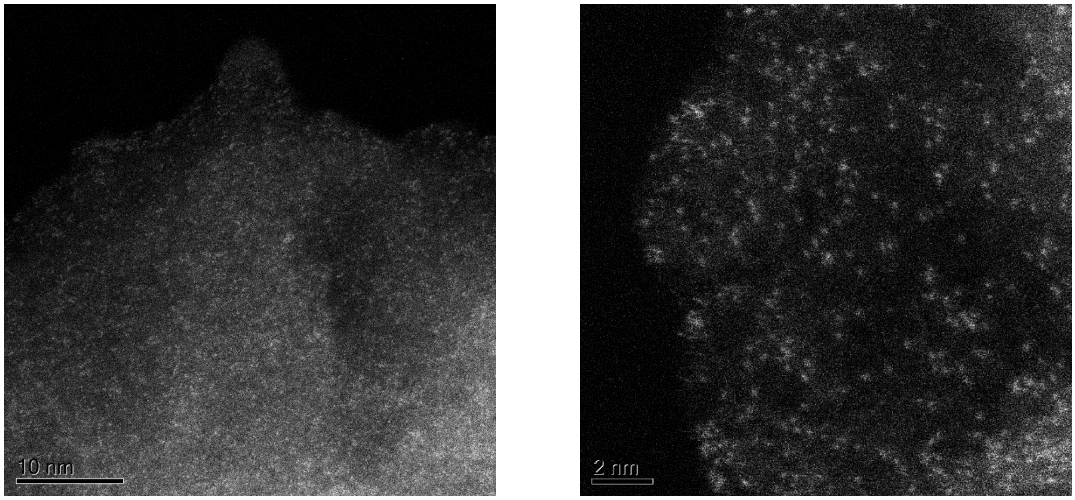


*Figure 4. 24: HAADF-STEM images of Ir-SAC after 1st cycle.*

To gain more information over the Ir sample after the reaction, the Ir content in the reaction solution of 1st cycle run was determined by ICP-AES, and the content of light elements for all the used samples: N, C and H, was analysed by CHNS technique. As shown in Table 4.3, 4 mg Ir is presented in the Ir-SAC sample, while the Ir content found in the reaction solution is less than 0.02 mg. Thus, the catalyst is stable against the leaching process. However, the N content decreases from 14.07% to 12.20% after the 1st cycle reaction and retain at around 12% after 3rd reaction. Meanwhile, the C content and H content increase slightly. This indicates that there is a loss of N in the nitrogen-based carbon support under high temperature and high hydrogen pressure condition. This loss of N could probably result in the de-coordination of Ir species, which may aggregate to form Ir rafts or nanoclusters.

| sample | ICP-AES | CHNS | | |
|---|---|---|---|---|
| | Ir content (mg) | N (wt.%) | C (wt.%) | H (wt.%) |
| Ir-SAC | 4 | 14.07 (±0.15) | 68.97 (±0.11) | 0.43 (±0.03) |
| 1st cycle | < 0.02 | 12.20 (±0.03) | 70.49 (±0.34) | 1.05 (±0.07) |
| 2nd cycle | - | 12.27 (±0.04) | 72.64 (±0.86) | 0.88 (±0.01) |
| 3rd cycle | - | 12.51 (±0.10) | 75.22 (±0.15) | 1.05 (±0.01) |

*Table 4. 3: Ir content of I.0-Ir-AC and in the reaction solution of 1st cycle run, determined by ICP-AES, and N, C and H concentration of Ir-SAC, 1st cycle, 2nd cycle, and 3rd cycle run samples, determined by CHNS.*

In order to confirm the hypothesis of formation of Ir rafts or nanoclusters, the spent sample was characterized by XAS (Figure 4.25). The XANES of spent sample shows slightly different feature than the initial sample, and the difference is highlighted by the FT of EXAFS spectra. The Ir-Ir scattering peak (around 2.6 Å) is observed for the used sample, which clearly confirms the formation of Ir-Ir metal bond, suggesting the formation of Ir rafts or nanoclusters.

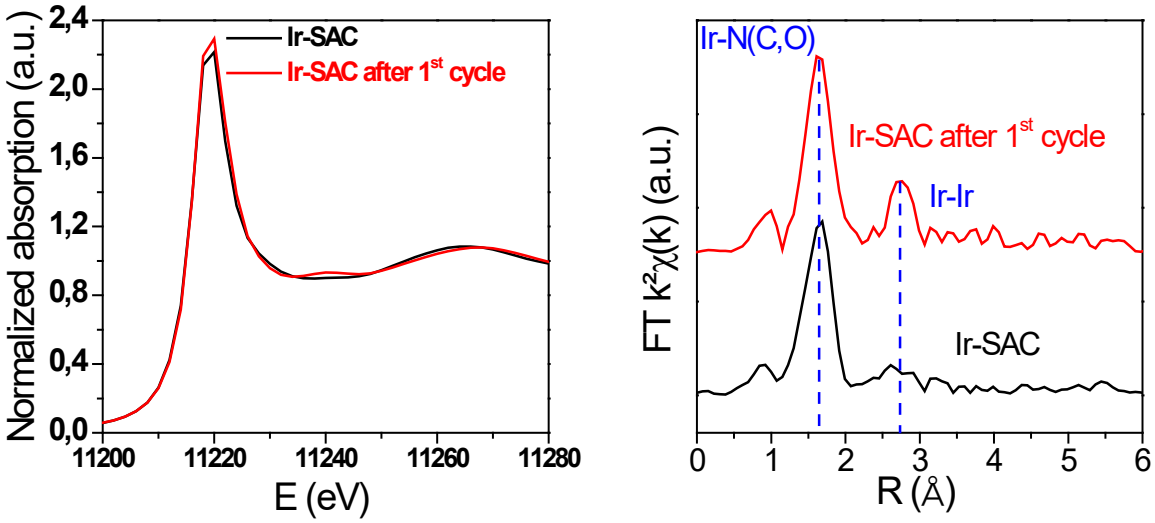


*Figure 4. 25: a) XANES spectra at the Ir $L_3$-edga of Ir-SAC (black) and Ir-SAC after 1st cycle (red) and b) their corresponding Fourier transform. For the sake of comparison, FT have been stacked.*

In conclusion, Ir-SAC is reactive and selective in hydrogenation of butadiene to butenes in gaseous condition, in particular highly selective on trans-2-butene. It also showed moderate reactivity in hydrogenation of levulinic acid in aqueous solution to GVL. The Ir single atoms is proved to be stable against aggregation in gaseous condition, however the coalescence of Ir single atoms is observed after the reaction of hydrogenation of levulinic acid.

## 4.5 Conclusion

In this chapter, Ir single atom catalyst (Ir-SAC) has been extensively studied for its physicochemical properties, formation process and stability under high temperature and hydrogen atmosphere. Afterwards, the catalytic reactivity of Ir-SAC was studied in hydrogenation of butadiene in gaseous condition and hydrogenation of levulinic acid (LA) in aqueous solution. Ir nanoparticles sample (Ir-NP) was also synthesized and its catalytic performance in hydrogenation of butadiene was determined for comparison to Ir-SAC.

The first part of this chapter consists of the physicochemical characterization of Ir-SAC and Ir-NP. Ir single atoms or Ir nanoparticles were successfully synthesized and embedded on nitrogen-based carbon ($CN_X$) host or AC host, respectively. The newly formed CNx is microporous and mesoporous amorphous material, which has less surface area than the initial AC. The Ir atoms in Ir-SAC have a higher binding energy than Ir in Ir-NP and Ir bulk, by XPS.

The second part of this chapter focused on the study of the formation process of Ir-SAC and its stability. Nitrogen-based carbon network (CNx) was formed by the pyrolysis of EDTA at low temperature (150 – 300 °C) accompanied by the pyrolysis of melamine at high temperature (300 – 800 °C). During the calcination, Ir ions sequestered by EDTA can be subsequently incorporated into the $CN_x$ framework, preventing them from aggregation to form large metal clusters. The synthesized Ir-SAC shows high stability under air and hydrogen atmosphere up to 400 °C.

The last part of this chapter is dedicated to the study of the catalytic reactivity of Ir-SAC. In the hydrogenation of butadiene, the conversion of Ir-SAC increases with the increase of reaction temperature and it reaches 80% at 200 °C. It shows an impressive nearly 100% selectivity to butenes, with the majority product trans-2-butene, throughout the course of the reaction. To the best of our knowledge, it is the first time that trans-2-butene as a majority product is observed in hydrogenation of butadiene. In comparison, Ir-NP behaves differently with low selectivity to butenes while the conversion exceeds 30%. By means of *operando* XAS experiment, it is believed that Ir forms stable bond with 4 N (and/or C, O) and its oxidation state (OS) is + 3.2 before the reaction. The coordination number (N) and the oxidation state (OS) are partially reduced to around 3 and + 2.0, respectively, during the pretreatment and reaction condition. This evolution of the electronic and atomic structure of Ir-SAC is the

possible reason of the high catalytic activity of Ir-SAC in the hydrogenation of butadiene. In hydrogenation of LA, Ir-SAC shows moderate catalytic activity. Ir-SAC is proved to be stable against aggregation in hydrogenation of butadiene, while not in hydrogenation of LA, as confirmed by XAS characterization.

## 4.6 Reference

(1) Zhao, L.; Zhang, Y.; Huang, L.-B.; Liu, X.-Z.; Zhang, Q.-H.; He, C.; Wu, Z.-Y.; Zhang, L.-J.; Wu, J.; Yang, W.; Gu, L.; Hu, J.-S.; Wan, L.-J. Cascade Anchoring Strategy for General Mass Production of High-Loading Single-Atomic Metal-Nitrogen Catalysts. *Nat. Commun.* **2019**, *10* (1). https://doi.org/10.1038/s41467-019-09290-y.

(2) Malouche, A.; Oumellal, Y.; Ghimbeu, C. M.; de Yuso, A. M.; Zlotea, C. Exploring the Hydrogen Absorption into Pd–Ir Nanoalloys Supported on Carbon. *J. Nanoparticle Res.* **2017**, *19* (8), 270. https://doi.org/10.1007/s11051-017-3978-4.

(3) Malouche, A.; Blanita, G.; Lupu, D.; Bourgon, J.; Nelayah, J.; Zlotea, C. Hydrogen Absorption in 1 Nm Pd Clusters Confined in MIL-101(Cr). *J. Mater. Chem. A* **2017**, *5* (44), 23043–23052. https://doi.org/10.1039/C7TA07159K.

(4) Marton, M.; Vojs, M.; Zdravecká, E.; Himmerlich, M.; Haensel, T.; Krischok, S.; Kotlár, M.; Michniak, P.; Veselý, M.; Redhammer, R. Raman Spectroscopy of Amorphous Carbon Prepared by Pulsed Arc Discharge in Various Gas Mixtures. *J. Spectrosc.* **2013**, *2013*, 1–6. https://doi.org/10.1155/2013/467079.

(5) Pfeifer, V.; Jones, T. E.; Velasco Vélez, J. J.; Massué, C.; Arrigo, R.; Teschner, D.; Girgsdies, F.; Scherzer, M.; Greiner, M. T.; Allan, J.; Hashagen, M.; Weinberg, G.; Piccinin, S.; Hävecker, M.; Knop-Gericke, A.; Schlögl, R. The Electronic Structure of Iridium and Its Oxides: The Electronic Structure of Iridium and Its Oxides. *Surf. Interface Anal.* **2016**, *48* (5), 261–273. https://doi.org/10.1002/sia.5895.

(6) Chen, J.; Gao, J.; Wang, X. Thermal Decomposition of Ethylenediaminetetraacetic Acid in the Presence of 1,2-Phenylenediamine and Hydrochloric Acid. *J. Braz. Chem. Soc.* **2006**, *17*, 880–885. https://doi.org/10.1590/S0103-50532006000500010.

(7) Liu, X.; Hao, J.; Gaan, S. Recent Studies on the Decomposition and Strategies of Smoke and Toxicity Suppression for Polyurethane Based Materials. *RSC Adv.* **2016**, *6* (78), 74742–74756. https://doi.org/10.1039/C6RA14345H.

(8) Praus, P.; Svoboda, L.; Ritz, M.; Troppová, I.; Šihor, M.; Kočí, K. Graphitic Carbon Nitride: Synthesis, Characterization and Photocatalytic Decomposition of Nitrous Oxide. *Mater. Chem. Phys.* **2017**, *193*, 438–446. https://doi.org/10.1016/j.matchemphys.2017.03.008.

(9) Thomas, A.; Fischer, A.; Goettmann, F.; Antonietti, M.; Müller, J.-O.; Schlögl, R.; Carlsson, J. M. Graphitic Carbon Nitride Materials: Variation of Structure and Morphology and Their Use as Metal-Free Catalysts. *J. Mater. Chem.* **2008**, *18* (41), 4893. https://doi.org/10.1039/b800274f.

(10) Dibandjo, P.; Zlotea, C.; Gadiou, R.; Matei Ghimbeu, C.; Cuevas, F.; Latroche, M.; Leroy, E.; Vix-Guterl, C. Hydrogen Storage in Hybrid Nanostructured Carbon/Palladium Materials: Influence of Particle Size and Surface Chemistry. *Int. J. Hydrog. Energy* **2013**, *38* (2), 952–965. https://doi.org/10.1016/j.ijhydene.2012.10.050.

(11) Liu, J.; Wang, H.; Antonietti, M. Graphitic Carbon Nitride "Reloaded": Emerging Applications beyond (Photo)Catalysis. *Chem. Soc. Rev.* **2016**, *45* (8), 2308–2326. https://doi.org/10.1039/C5CS00767D.

(12) Zhang, X.; Shi, H.; Xu, B.-Q. Catalysis by Gold: Isolated Surface Au3+ Ions Are Active Sites for Selective Hydrogenation of 1,3-Butadiene over Au/ZrO2 Catalysts. *Angew. Chem. Int. Ed.* **2005**, *44* (43), 7132–7135. https://doi.org/10.1002/anie.200502101.

(13) Yan, H.; Cheng, H.; Yi, H.; Lin, Y.; Yao, T.; Wang, C.; Li, J.; Wei, S.; Lu, J. Single-Atom Pd $_1$ /Graphene Catalyst Achieved by Atomic Layer Deposition: Remarkable Performance in Selective Hydrogenation of 1,3-Butadiene. *J. Am. Chem. Soc.* **2015**, *137* (33), 10484–10487. https://doi.org/10.1021/jacs.5b06485.

(14) Furlong, B. K.; Hightower, J. W.; Chan, T. Y.-L.; Sarkany, A.; Guczi, L. 1,3-Butadiene Selective Hydrogenation over Pd/Alumina and CuPd/Alumina Catalysts. *Appl. Catal. Gen.* **1994**, *117* (1), 41–51. https://doi.org/10.1016/0926-860X(94)80157-6.

(15) Hall, M. D.; Foran, G. J.; Zhang, M.; Beale, P. J.; Hambley, T. W. XANES Determination of the Platinum Oxidation State Distribution in Cancer Cells Treated with Platinum(IV) Anticancer Agents. *J. Am. Chem. Soc.* **2003**, *125* (25), 7524–7525. https://doi.org/10.1021/ja0354770.

(16) Li, Z.; Chen, Y.; Ji, S.; Tang, Y.; Chen, W.; Li, A.; Zhao, J.; Xiong, Y.; Wu, Y.; Gong, Y.; Yao, T.; Liu, W.; Zheng, L.; Dong, J.; Wang, Y.; Zhuang, Z.; Xing, W.; He, C.-T.; Peng, C.; Cheong, W.-C.; Li, Q.; Zhang, M.; Chen, Z.; Fu, N.; Gao, X.; Zhu, W.; Wan, J.; Zhang, J.; Gu, L.; Wei, S.; Hu, P.; Luo, J.; Li, J.; Chen, C.; Peng, Q.; Duan, X.; Huang, Y.; Chen, X.-M.; Wang, D.; Li, Y. Iridium Single-Atom Catalyst on Nitrogen-Doped Carbon for Formic Acid Oxidation

Synthesized Using a General Host–Guest Strategy. *Nat. Chem.* **2020**. https://doi.org/10.1038/s41557-020-0473-9.

(17) Chen, Z.; Xiao, M.; Zhu, J.; Li, G.; Li, N.; Li, S.; Cano, Z. P.; Ma, L.; Cui, P. X.; Xu, P.; Jiang, G.; Jin, H.; Wang, S.; Wu, T.; Lu, J.; Yu, A.; Su, D. Single Atom Iridium Heterogeneous Catalyst in Oxygen Reduction Reaction. *Angew. Chem.* **2019**, ange.201905241. https://doi.org/10.1002/ange.201905241.

(18) Castro, M. C. R.; Sedrine, N. B.; Monteiro, T.; Machado, A. V. Iridium(III)Porphyrin Arrays with Tuneable Photophysical Properties. *Spectrochim. Acta. A. Mol. Biomol. Spectrosc.* **2020**, *235*, 118309. https://doi.org/10.1016/j.saa.2020.118309.

(19) Cui, H.; Wang, Y.; Wang, Y.; Fan, Y.-Z.; Zhang, L.; Su, C.-Y. A Stable and Porous Iridium( III )-Porphyrin Metal–Organic Framework: Synthesis, Structure and Catalysis. *CrystEngComm* **2016**, *18* (12), 2203–2209. https://doi.org/10.1039/C6CE00358C.

(20) Murata, K.; Ishii, K. Near Infra-Red $S_0 \leftrightarrow T_1$ Transitions of Iridium(III) Phthalocyanine: Degeneracy of the $T_1$ State Evidenced by Magnetic Circular Dichroism: Near Infra-Red $S_0 \leftrightarrow T_1$ Transitions of Iridium(III) Phthalocyanine: Degeneracy of the $T_1$ State Evidenced by Magnetic Circular Dichroism. *Eur. J. Inorg. Chem.* **2017**, *2017* (44), 5103–5107. https://doi.org/10.1002/ejic.201700668.

(21) Yang, P.; Zuo, S.; Zhang, F.; Yu, B.; Guo, S.; Yu, X.; Zhao, Y.; Zhang, J.; Liu, Z. Carbon Nitride-Based Single-Atom Cu Catalysts for Highly Efficient Carboxylation of Alkynes with Atmospheric CO2. *Ind. Eng. Chem. Res.* **2020**, *59* (16), 7327–7335. https://doi.org/10.1021/acs.iecr.0c00547.

(22) Liu, W.; Hu, W.; Yang, L.; Liu, J. Single Cobalt Atom Anchored on Carbon Nitride with Well-Defined Active Sites for Photo-Enzyme Catalysis. *Nano Energy* **2020**, *73*, 104750. https://doi.org/10.1016/j.nanoen.2020.104750.

(23) Feng, J.; Gao, H.; Zheng, L.; Chen, Z.; Zeng, S.; Jiang, C.; Dong, H.; Liu, L.; Zhang, S.; Zhang, X. A Mn-N 3 Single-Atom Catalyst Embedded in Graphitic Carbon Nitride for Efficient CO 2 Electroreduction. *Nat. Commun.* **2020**, *11* (1), 4341. https://doi.org/10.1038/s41467-020-18143-y.

(24) Fuchigami, K.; Rath, N. P.; Mirica, L. M. Mononuclear Rhodium(II) and Iridium(II) Complexes Supported by Tetradentate Pyridinophane Ligands. *Inorg. Chem.* **2017**, *56* (16), 9404–9408. https://doi.org/10.1021/acs.inorgchem.7b01619.

(25) Fang, S.; Zhu, X.; Liu, X.; Gu, J.; Liu, W.; Wang, D.; Zhang, W.; Lin, Y.; Lu, J.; Wei, S.; Li, Y.; Yao, T. Uncovering Near-Free Platinum Single-Atom Dynamics during Electrochemical Hydrogen Evolution Reaction. *Nat. Commun.* **2020**, *11* (1), 1029. https://doi.org/10.1038/s41467-020-14848-2.

(26) Cai, Y.; Fu, J.; Zhou, Y.; Chang, Y.-C.; Min, Q.; Zhu, J.-J.; Lin, Y.; Zhu, W. Insights on Forming N,O-Coordinated Cu Single-Atom Catalysts for Electrochemical Reduction CO 2 to Methane. *Nat. Commun.* **2021**, *12* (1), 586. https://doi.org/10.1038/s41467-020-20769-x.

(27) Song, P.; Luo, M.; Liu, X.; Xing, W.; Xu, W.; Jiang, Z.; Gu, L. Zn Single Atom Catalyst for Highly Efficient Oxygen Reduction Reaction. *Adv. Funct. Mater.* **2017**, *27* (28), 1700802. https://doi.org/10.1002/adfm.201700802.

(28) Wingard, L. Accessing Intermediate and High Oxidation States with Tungsten and Iridium Pincer Complexes, University of North Carolina at Chape Hill, 2012.

(29) Cao, W.; Lin, L.; Qi, H.; He, Q.; Wu, Z.; Wang, A.; Luo, W.; Zhang, T. In-Situ Synthesis of Single-Atom Ir by Utilizing Metal-Organic Frameworks: An Acid-Resistant Catalyst for Hydrogenation of Levulinic Acid to γ-Valerolactone. *J. Catal.* **2019**, *373*, 161–172. https://doi.org/10.1016/j.jcat.2019.03.035.

(30) Du, X.; Liu, Y.; Wang, J.; Cao, Y.; Fan, K. Catalytic Conversion of Biomass-Derived Levulinic Acid into γ-Valerolactone Using Iridium Nanoparticles Supported on Carbon Nanotubes. *Chin. J. Catal.* **2013**, *34* (5), 993–1001. https://doi.org/10.1016/S1872-2067(11)60522-6.

(31) Wang, J.; Wang, Y.; Tong, X.; Wang, Y.; Jin, G.; Guo, X. Highly Active Ir/SiC Catalyst for Aqueous Hydrogenation of Levulinic Acid to γ-Valerolactone. *Catal. Commun.* **2020**, *139*, 105971. https://doi.org/10.1016/j.catcom.2020.105971.

# CHAPTER V: POROUS CARBONS WITH VARIOUS TRANSITION METALS FOR HYDROGENATION REACTIONS

## 5.1 Synthesis of single atom catalysts with various transition metals supported on activated carbon

The main aim of this chapter is to synthesize low loading (< 5 wt.%) single atom catalysts (SACs) with various transition metals: Co, Ni, Cu, Mo, Pd, Ir and Pt, supported on nitrogen-based activated carbon (AC) and then to evaluate them in catalytic reactions of selective hydrogenation in different mediums: hydrogenation of butadiene in gaseous condition and hydrogenation of levulinic acid (LA) in aqueous solution. Besides, the synthesis with high metal loading (> 5 wt.%) SACs for Cu, Pd and Pt metals was also tested, and some preliminary studies are shown in this chapter.

The metal (*M*) SAC was prepared by a cascade anchoring strategy adapted from Zhao *et al.*[1] The *M*-SAC was dispersed on a nitrogen-rich AC by the liquid impregnation of the pristine AC with metal precursor in an aqueous solution in the presence of a chelating agent (EDTA) followed by pyrolysis under Ar at 800 °C in the presence of a source of nitrogen (melamine). This treatment allows the simultaneous preparation of metal SAC and doping of carbon with nitrogen. The pyrolyzed sample was further washed with aqua regia for 6 h to remove possible large clusters/nanoparticles formed during pyrolysis, except for Co and Ir samples. The samples are named *x*-*M*-AC, where *x* (wt.%) stands for the metal content over the entire sample mass and *M* = Co, Ni, Cu, Mo, Pd, Ir or Pt. More details of synthesis can be found in **Chapter II Materials and Methods**.

For the purpose of comparison, except for iridium, the corresponding metal nanoparticles samples were prepared by a simple method based on the liquid impregnation of the activated carbon support with the metal precursor aqueous solution, followed by reduction under 5% $H_2$/Ar flow at high temperature (250 – 800 °C). The samples are named *X*-*M*@AC-*Y*, where *X* (wt.%) is the metal content over the entire sample mass, *M* = Co, Ni, Cu, Mo, Pd or Pt and *Y* represents the reduction temperature.

## 5.2 Physicochemical characterization

The metal single atom catalysts (SACs) are divided into two categories according to the metal loading: low metal loading SACs (< 5 wt.%) and high metal loading SACs (> 5 wt.%). The physicochemical properties of the low metal loading SACs will be presented first, afterwards the high metal loading SACs will be discussed.

### 5.2.1 Low metal loading SACs (< 5 wt.%)

The synthesized low loading (< 5 wt.%) SACs materials were firstly characterized by X-Ray Diffraction (XRD) for the determination of their structural properties (Figure 5.1).

The AC is an amorphous carbon with some impurities which give rise to several small sharp diffraction peaks in the range 30 - 50.0°. XRD patterns of all metal SAC samples showed contribution from activated carbon support and no diffraction peaks from metals can be discerned. This suggests that the metals are very well dispersed on the carbon support, same as discussed in **Chapter IV** for Ir samples. The metal can be either as ultra-small clusters with too short coherence length to diffract X-rays, or as even smaller size such as, single atom sates. This will be further verified by transmission electron microscopy.

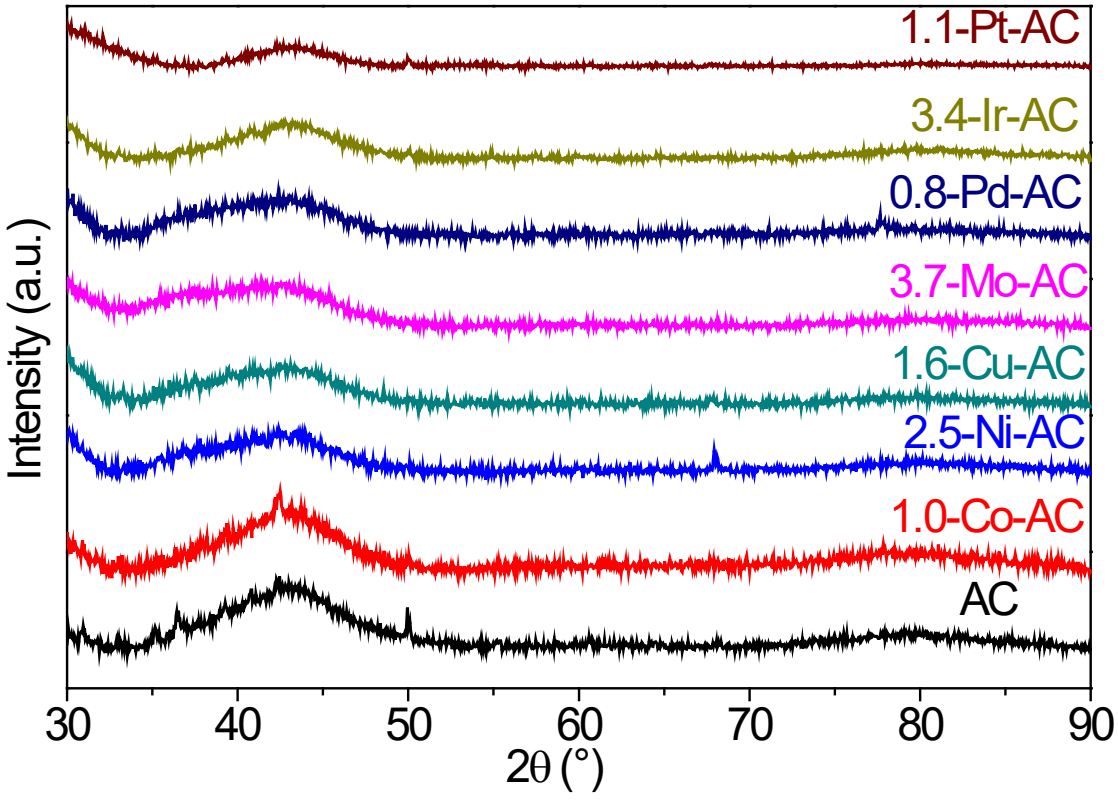


*Figure 5. 1: XRD pattern of pristine AC, 1.0-Co-AC, 2.5-Ni-AC, 1.6-Cu-AC, 3.7-Mo-AC, 0.8-Pd-AC, 3.4-Ir-AC, and 1.1-Pt-AC.*

The SACs materials were characterized by Transmission Electron Microscopy (TEM) to analyse the dispersion of metals on the carbon host. One detailed example for 3.4-Ir-AC is given in Figure 5.2. In classic bright field TEM images as displayed by Figure 5.2 a and b, no Ir nanoparticles nor clusters could be observed, while high-resolution aberration-corrected

high-angle annular dark field scanning electron microscopy (HAADF-STEM) images showed that Ir existed at atomic scale as isolated bright spots homogeneously dispersed on the carbon support (Figure 5.2 c and d).

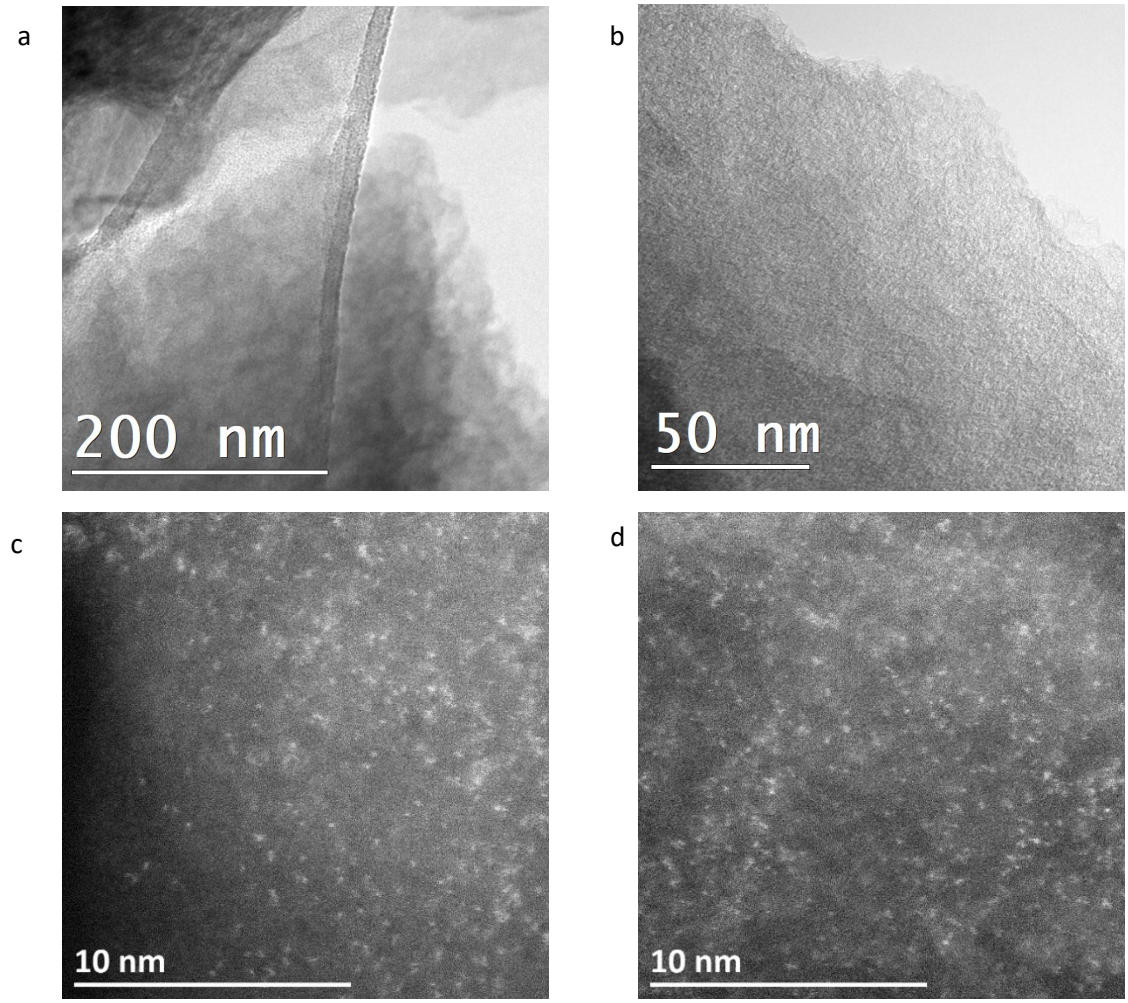


*Figure 5. 2: a), b) Classic bright field TEM images and c), d) HAADF-STEM images of 3.4-Ir-AC.*

The HAADF-STEM images of the other samples, Co, Ni, Cu, Mo, Pd and Pt SACs, are shown in Figure 5.3, together with their counterpart nanoparticles samples for comparison. The white spots of 1.0-Co-Ac, 2.5-Ni-AC and 1.6-Cu-AC are not clearly noticeable in the annular dark field (ADF) microscopy images possibly due to small contrast between these metals and the carbon support. In fact, it has been reported that ADF signal is approximately proportional to the second power of the atomic number, $Z$.[2] Some of the white spots are indicated by the yellow arrows and they are in the size of atomic scale. As the atomic number increases, the contrast in the STEM images enhances for 3.7-Mo-AC, 0.8-Pd-AC and 1.1-Pt-AC samples. Large amount of subnanometric clusters or rafts of atoms (< 1 nm) of Mo are

observed to be homogeneously dispersed on the carbon support for 3.7-Mo-AC, while Pd and Pt atoms are well dispersed on the supports as isolated single atoms. On the contrary, the metal nanoparticles are shown as blacks spots in the bright field TEM images, and they are homogeneously dispersed on the activated carbon support with different average size ranging from 2 to 9 nm: Co ≈ 2.3 ± 0.4 nm, Ni ≈ 4.9 ± 1.0 nm, Cu ≈ 7.4 ± 2.4 nm, Mo ≈ 8.2 ± 3.7 nm, Pd ≈ 5.5 ± 1.7 nm and Pt ≈ 5.0 ± 1.8 nm.

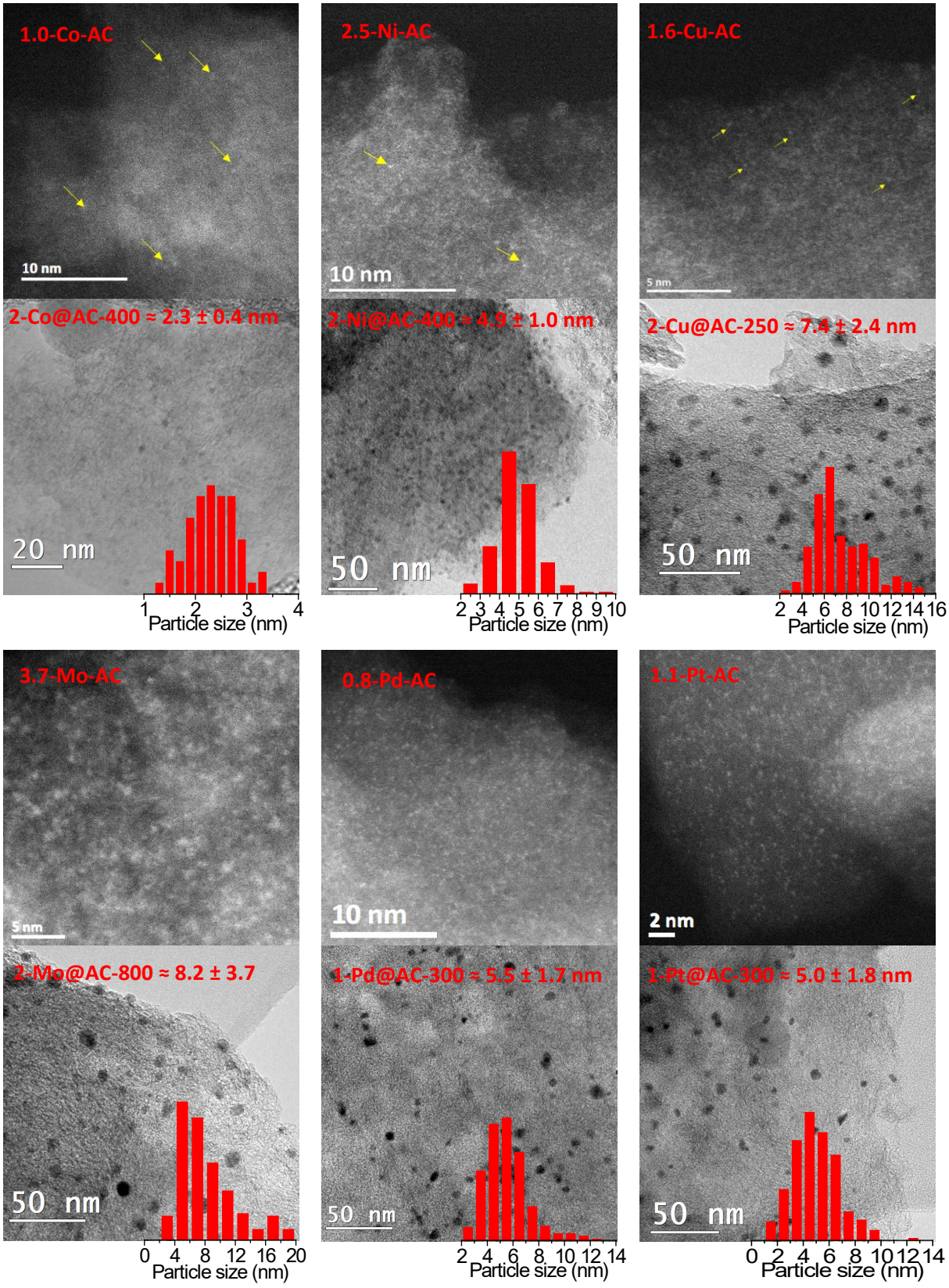


*Figure 5. 3: HAADF-STEM images of 1.0-Co-AC, 2.5-Ni-AC, 1.6-Cu-AC, 3.7-Mo-AC, 0.8-Pd-AC and 1.1-Pt-AC (top), and TEM images of 2-Co@AC-400, 2-Cu@AC-250, 2-Ni@AC-400, 2-Mo@AC-800, 1-Pd@AC-300, 1-Pt@AC-300 (bottom).*

The metal concentration in the different composites was determined by ICP-AES and the content of light elements, N, C and H, was analysed by CHNS technique. The results are listed in Table 5.1. The C content decreased for the synthesized materials compared to the pristine AC, while the concentration of N significantly increased for SACs samples. The N content is nearly zero in AC and reaches around 14-19 wt.% after the pyrolysis, except for 3.7-Mo-AC, which has only 6.8 wt.% of nitrogen. The N content is in large excess as compared to metal loading and it plays a key role to stabilize/coordinate the metal atoms. The relatively low content of nitrogen in 3.7-Mo-AC sample is a possible reason for the formation of Mo atomic rafts. The hydrogen content increased slightly after the synthesis for all the SACs materials. It should be noted that the content of oxygen is not measured due to the presence of impurities, such as aluminosilicates in the pristine AC, the sum of metal content as well as the light elements (N, C and H) is not 100%.

| sample | ICP-AES | CHNS | | |
|---|---|---|---|---|
| | Metal content (wt. %) | N (wt. %) | C (wt. %) | H (wt. %) |
| AC | - | 0.47 (±0.08) | 78.39 (±0.81) | 0.22 (±0.04) |
| 1.0-Co-AC | 0.95 (±0.01) | 13.95 (±0.33) | 68.97 (±0.54) | 0.43 (±0.13) |
| 2.5-Ni-AC | 2.50 (±0.01) | 17.21 (±0.10) | 60.34 (±0.20) | 1.46 (±0.23) |
| 1.6-Cu-AC | 1.55 (±0.01) | 15.52 (±0.07) | 61.56 (±0.15) | 1.07 (±0.02) |
| 3.7-Mo-AC | 3.67 (±0.06) | 6.80 (±0.02) | 69.52 (±0.15) | 0.69 (±0.09) |
| 0.8-Pd-AC | 0.77 (±0.02) | 19.01 (±0.81) | 64.39 (±0.26) | 0.94 (±0.20) |
| 3.4-Ir-AC | 3.44 (±0.05) | 17.06 (±0.03) | 60.04 (±0.09) | 1.07 (±0.14) |
| 1.1-Pt-AC | 1.10 (±0.01) | 19.64 (±0.53) | 63.27 (±0.24) | 1.13 (±0.01) |

*Table 5. 1: Metal content of AC, 1.0-Co-AC, 2.5-Ni-AC, 1.6-Cu-AC, 3.7-Mo-AC, 0.8-Pd-AC, 3.4-Ir-AC and 1.1-Pt-AC, determined by ICP-AES and their corresponding concentration of N, C and H determined by CHNS.*

To obtain further information from the surface as well as the chemical state of nitrogen atoms and metal atoms in SACs materials, X-ray photoelectron spectroscopy (XPS) was performed. As an example, N 1s and Co 2p spectra of 1.0-Co-AC are presented in Figure 5.4. As discussed in **Chapter IV** for 1.0-Ir-AC sample, the N 1s spectrum (Figure 5.4 a) of Co sample shows four different bonding configurations of N atoms, which are attributed to pyridinic-N (398.6 eV), pyrrolic-N (399.7 eV), graphitic-N (401.2 eV) and oxidized-N (404.2 eV), respectively. Pyridinic-N and pyrrolic-N are the nitrogen species at the edges or in the

vacancies of the graphitic host. The pyridinic–N bonds with two C atoms and contributes one *p* electron to the $\pi$ system. Pyrrolic–N refers to N atoms incorporated in pentagonal ring and contributes two *p* electrons to the $\pi$ system. Graphitic–N refers to N atoms that substitute C atoms in the hexagonal ring. The Co 2p can be deconvoluted into four peaks as well. As shown in Figure 5.4 b, two main peaks at 781.2 eV and 796.9 eV correspond to Co $2p_{3/2}$ and Co $2p_{1/2}$, respectively, these values are similar to the Co 2p binding energy in cobalt oxide.[3,4] Two satellite peaks are observed at 786.2 eV and 803.6 eV suggesting the presence of $Co^{2+}$.[5] No signal from zero valence Co metal (binding energy of bulk Co $2p_{2/3}$: 778.2 eV) could be observed from the XPS data.[6] These findings are consistent with the results found for other Co single atoms supported on nitrogen-based carbon materials. For example, Li *et al.*[7] reported an atomically dispersed cobalt dispersed onto nitrogen-doped graphene, the Co 2p spectra of XPS showed two main peaks at 780.9 eV and 796.2 eV, and with the presence of two satellite peaks. Moreover, similar binding energy was reported by Liu *et al.*[8] for a Co SACs dispersed on carbon nitride nanosheet.

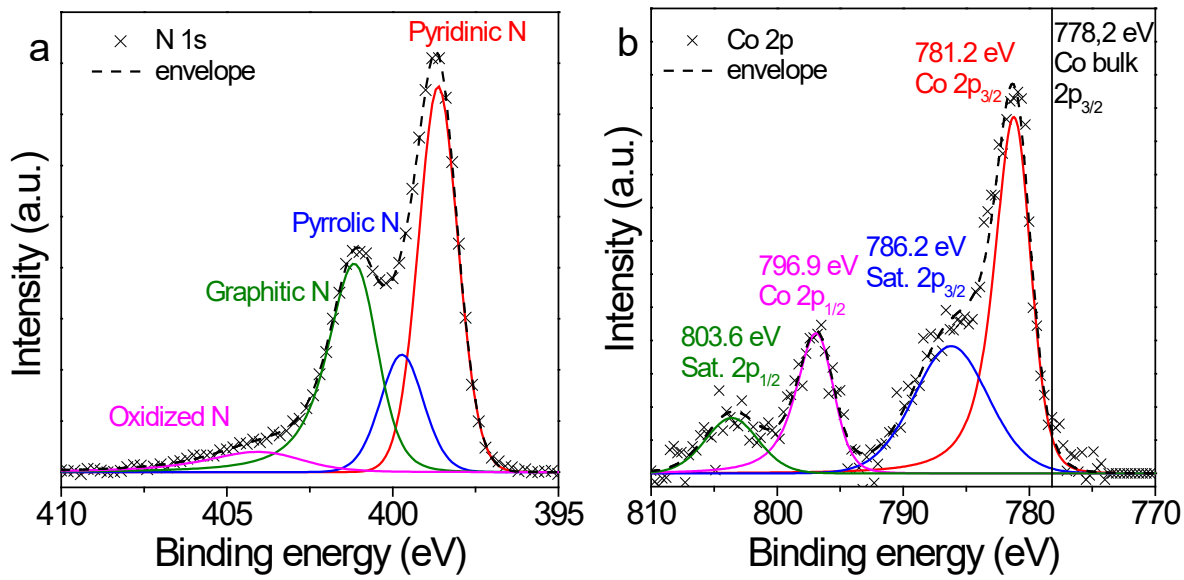


*Figure 5. 4: a) N 1s and b) Co 2p XPS spectra of 1.0-Co-AC; The black line at 778.2 eV is the binding energy of Co bulk $2p_{3/2}$ taken from literature.[6]*

To gain more information on the chemical coordination environments and atomic dispersion of single atom catalysts, 1.0-Co-AC, 3.7-Mo-AC, 3.4-Ir-AC and 1.1-Pt-AC were investigated by X-ray absorption (XAS) spectroscopy. The X-ray absorption near edge structure (XANES) and X-ray absorption fine structure (EXAFS) spectra are shown in Figure 5.5.

Bulk metals foils were used as references. As shown in Figure 5.5 a, c, e and g, the XANES spectra of 1.0-Co-AC, 3.7-Mo-AC, 3.4-Ir-AC and 1.1-Pt-AC show distinct features as compared to their counterpart metal. They have a higher intensity of the "white line" than metal bulks, which indicates that they have a different oxidation state.

The Fourier transforms (FT) of EXAFS spectra of 1.0-Co-AC, 3.7-Mo-AC, 3.4-Ir-AC and 1.1-Pt-AC are compared to Co, Mo, Ir and Pt bulk in Figure 5.5 b, d, f and h. Co bulk shows typical peaks for the close-packed-hexagonal metal structure with the dominant one at approximately 2.18 Å (Co-Co nearest distances), while 1.0-Co-AC shows a single dominant peak at around 1.53 Å. This peak can be ascribed to the backscattering from the nearest Co neighbours *X* (*X* = N/C/O). However, EXAFS cannot distinguish between light elements close to each other such as, C, N or O because of their close scattering amplitude. Thus, we can conclude that Co-Co metal bond scattering peak (around 2.18 Å) are absent for 1-Co-AC, suggesting that no metal nanoparticles were formed in this sample. The FT of Ir, Pt SAC samples are similar to the Co one. Ir bulk (or Pt bulk) (face-centred-cubic structure) has its dominant peak at 2.58 Å (or 2.59 Å) (Ir-Ir (or Pt-Pt) nearest distances), whereas the single dominant peak is at around 1.62 Å (or 1.67 Å) originating from the backscattering of Ir-*X* (or Pt-*X* where *X* = N/C/O) for the 3.4-Ir-AC (or 1.1-Pt-AC). The metal-metal scattering paths could not be observed for these two SAC samples: 3.4-Ir-AC and 1.1-Pt-AC. On the contrary, Mo bulk (body-centred cubic) shows two main peaks at approximately 2.38 and 2.85 Å for the first and second coordination shell of Mo-Mo bond, respectively.[9] For the 3.7-Mo-AC, besides the peak of Mo-*X* (*X* = N/C/O) at around 1.33 Å, a significant peak at about 2.85 Å is noticed which can be hypothetically ascribed to the Mo-Mo metal bond. This finding might indicate the formation of Mo rafts or nanoclusters with bonds close to a 2D structure that might be distinct to the 3D bulk lattice. These results confirm the atomic dispersion of cobalt atoms in the 1.0-Co-AC, iridium atoms in the 3.4-Ir-AC and platinum atoms in the 1.1-Pt-AC, as well as the formation of both Mo SACs and rafts in 3.7-Mo-AC, in very good agreement with HAADF-STEM.

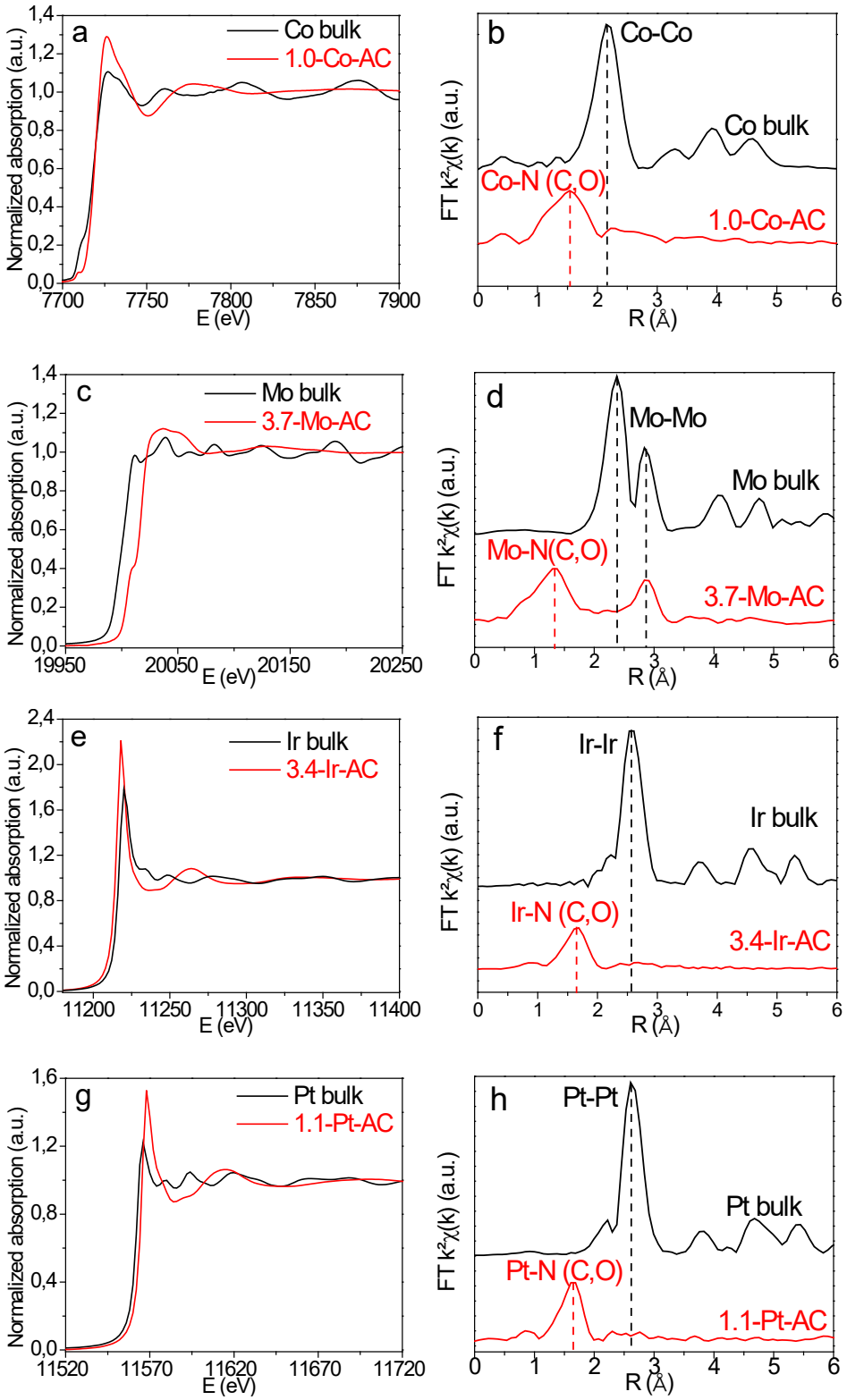


*Figure 5.5: XANES spectra at the, a) K-edge of Co bulk (black) and 1.0-Co-AC (red), c) K-edge of Mo bulk (black) and 3.7-Mo-AC (red), e) $L_3$-edge of Ir bulk (black) and 3.4-Ir-AC (red), and g) $L_3$-edge of Pt bulk (black) and 1.1-Pt-AC (red); their corresponding Fourier Transform, b)*

*Co bulk and 1.0-Co-AC, d) Mo bulk and 3.7-Mo-AC, f) Ir bulk and 3.4-Ir-AC, and h) Pt bulk and 1.1-Pt-AC.*

To reveal the local structure of metal *M* (*M* = Co, Ir, Mo or Pt) SACs, EXAFS refinements were performed based on a known structural model where one metal atom is coordinated with four light atoms *M*-(N, C)$_x$O$_y$ (x + y = 4), as proposed for 1.0-Ir-AC sample in **Chapter IV**. The EXAFS fitting results such as, the coordination number (*N*), the Debye-Waller factor ($\sigma^2$), the nearest neighbours *M-X* distance and the confidence factor (*QF*) are listed in Table 5.2. The results of 3.7-Mo-AC are not listed because of the poor quality of the EXAFS data and complex fit for Mo rafts. Typical refinements results are plotted in Figure 5.6. The fitted Co, Ir and Pt coordination numbers are around 4, indicating that each metal atoms coordinate with four light atoms (N/C/O) on the support. Notably, the four-configuration mode is found in metal porphyrins complexes.[10–12] The nearest distance of *M-X* is found to be 1.990(3) Å for 1.0-Co-AC, 2.015(3) Å for 3.4-Ir-AC and 1.996(4) Å for 1-Pt-AC. These values are consistent with results reported in the literature. For example, the distance Co-*X* was found to be 1.96(2) Å in a Co SAC supported on a hierarchically ordered pours N-doped carbon.[13] In a Ir/CN catalyst, the distance Ir-*X* was 2.00(2) Å.[14] Moreover, the bond length of Pt-*X* in a Pt SAC on nitrogen doped carbon dots was 1.99(2) Å.[15]

| Sample | N | $\sigma^2$ (Å$^2$) | $R_{M-X}$ (Å) | QF |
|---|---|---|---|---|
| 1.0-Co-AC | 4.0(2) | 0.0147(14) | 1.990(3) | 0.1 |
| 3.4-Ir-AC | 4.0(1) | 0.0050(4) | 2.015(3) | 0.2 |
| 1.1-Pt-AC | 4.0(3) | 0.0043(7) | 1.996(4) | 0.7 |

*Table 5. 2: EXAFS refinements result for 1.0-Co-AC, 3.4-Ir-AC and 1.1-Pt-AC at 25 °C. The coordination number (N), the Debye–Waller factor ($\sigma^2$), the nearest M–X (M = Co, Ir or Pt, X = N,C,O) distance (R) and the confidence factor (QF) are given.*

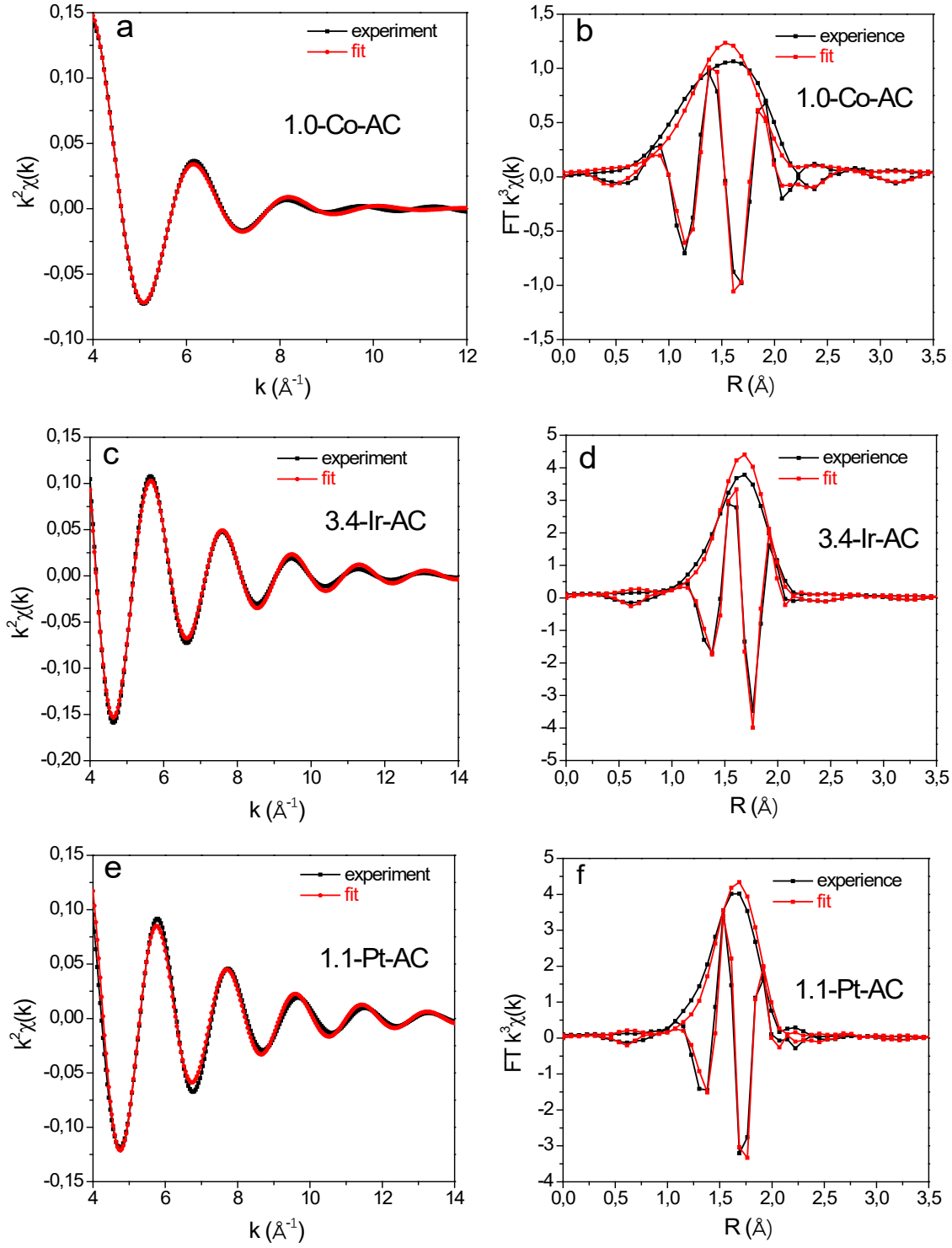


*Figure 5. 6: EXAFS fitting of SACs at 25 °C, a, b) 1.0-Co-AC, c, d) 3.4-Ir-AC, and e, f) 1.1-Pt-AC.*

### 5.2.2 High loading SACs (> 5 wt.%)

The synthesized high loading SACs materials (> 5 wt.%) were firstly characterized by XRD for the determination of their structural properties. As shown in Figure 5.7, no diffraction

peaks of pure metals can be observed suggesting that they are well dispersed on the carbon support. HAAF-STEM characterization is then used to verify the dispersion of the metals.

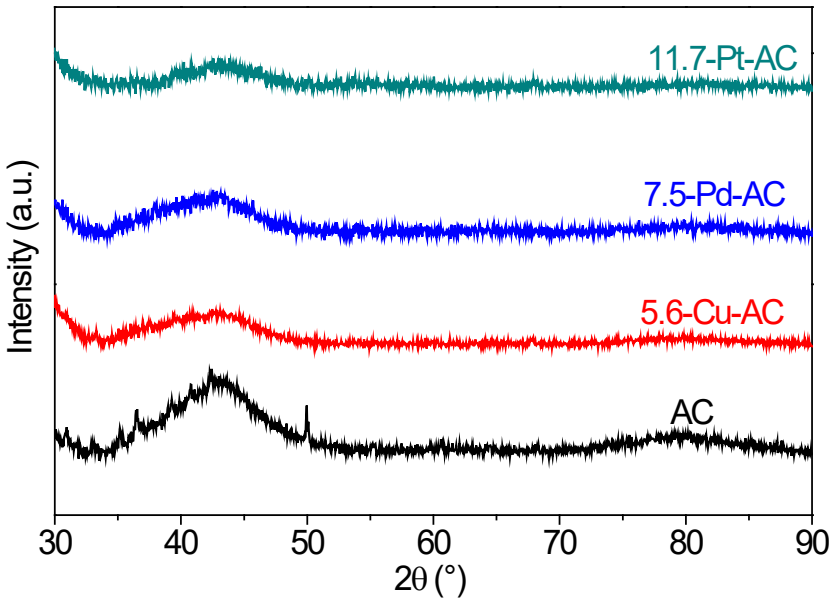


*Figure 5. 7: XRD pattern of pristine AC, 5.6-Cu-AC, 7.5-Pd-AC and 11.7-Pt-AC.*

The HAADF-STEM images of 5.6-Cu-AC, 7.5-Pd-AC and 11.7-Pt-AC are shown in Figure 5.8. At low magnification, no metals nanoparticles can be observed. However, well dispersed bright spots can be observed in the high magnification images. For 5.6-Cu-AC, some white spots are indicated by the yellow arrows and they are in the size of atomic scale. As the metal concentration is very high, the bright spots are very densely dispersed on the carbon support, in particular for 7.5-Pd-AC and 11.7-Pt-AC. Single atoms as well as oligomers such as, dimers, trimers, tetramers, are observed in STEM images, however it is difficult to distinguish among them.

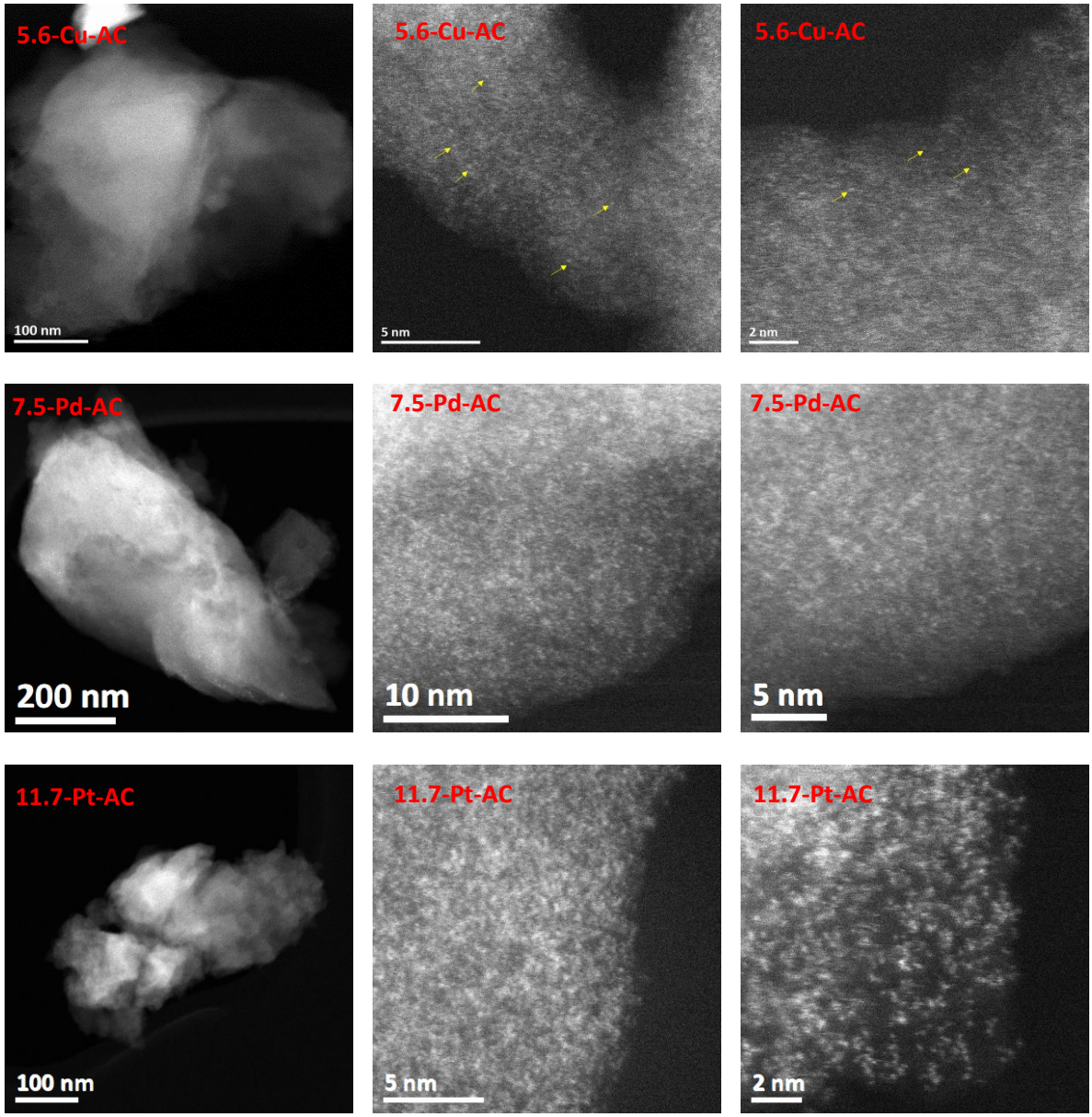


*Figure 5. 8: HAADF-STEM images of 5.6-Cu-AC, 7.5-Pd-AC and 11.7-Pt-AC.*

The metal concentration in the different composites was determined by ICP-AES, the results are shown in Table 5.3. The metal concentrations are 5.64, 7.45 and 11.72 wt.% for 5.6-Cu-AC, 7.5-Pd-AC and 11.7-Pt-AC, respectively.

| sample | Metal content (wt. %) |
|---|---|
| 5.6-Cu-AC | 5.64(±0.05) |
| 7.5-Pd-AC | 7.45(±0.04) |
| 11.7-Pt-AC | 11.72(±0.08) |

*Table 5. 3: Metal content of 5.6-Cu-AC, 7.5-Pd-AC and 11.7-Pt-AC, determined by ICP-AES.*

The 11.7-Pt-AC was investigated by XAS to check the chemical coordination environments and the Pt atomic dispersion. The results were compared with 1.1-Pt-AC and Pt bulk. The XANES and EXAFS spectra are shown in Figure 5.9. The XANES spectrum of 11.7-Pt-AC is very similar to 1.1-Pt-AC but different when compared to Pt bulk. The intensity of white line is between those of Pt bulk and 1.1-Pt-AC, indicating that the oxidation state is among the metallic Pt bulk and the pure SAC form of 1.1-Pt-AC. The FT of EXAFS spectra of the Pt bulk, 1.1-Pt-AC and 11.7-Pt-AC are shown in Figure 5.9 b. Same as the 1.1-Pt-AC, Pt-*X* (*X* = N,C or O) back-scattering peak is observed at approximately 1.67 Å, which means the formation of Pt single atoms. Moreover, no Pt-Pt metal distances (around 2.59 Å) could be found, consequently, metal nanoparticles were not formed in the 11.7-Pt-AC sample. However, a small peak at around 2.0 Å is found which might be ascribed to the Pt-Cl bond formed during the leaching of the sample with the aqua regia ($HNO_3$ + 3HCl). In fact, the leaching mechanism of metallic Pt can be explained with the oxidation of Pt by $HNO_3$, then the oxidized Pt ions react with chloride ions (HCl) resulting in hexachloroplatinate(IV) ($PtCl_6^{2-}$) ions. As reported in literature, the scattering peak of Pt-Cl in $H_2PtCl_4$ is around at 2 Å in EXAFS analyses.[16,17]

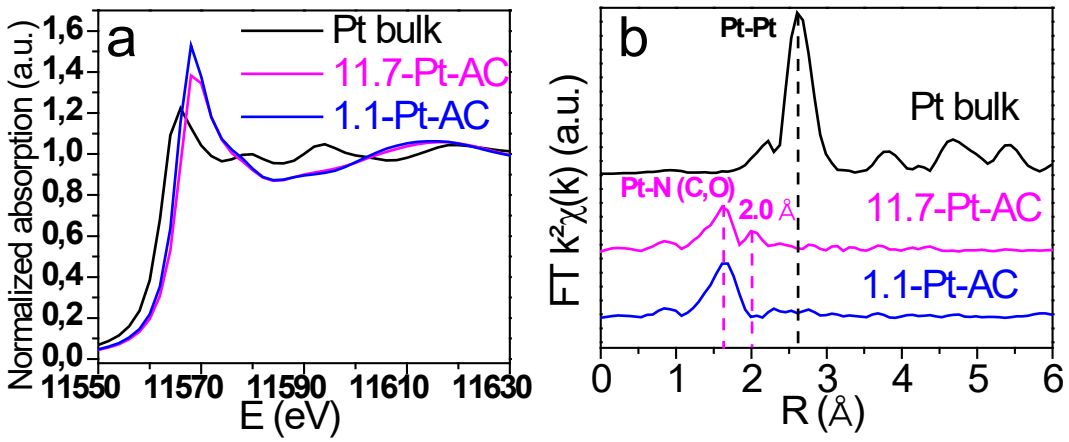


*Figure 5. 9: a) XANES spectra at the $L_3$-edge of Pt bulk (black), 1.1-Pt-AC (blue) and 11.7-Pt-AC (rose); b) their corresponding Fourier Transform.*

The local structure of Pt is revealed by EXAFS refinements based on a two-shell structural model where the first shell is Pt coordinated with four light atoms *M*-$(N, C)_xO_y$ (x + y = 4) as for the pure SAC sample, and the second shell corresponds to nearest neighbours of the rhombohedral structure of $PtCl_2$ ($R\bar{3}m$). The EXAFS fitting results such as, the coordination number (*N*), the Debye-Waller factor ($\sigma^2$), the nearest Pt-*X* and Pt-Cl distance and the

confidence factor (QF) are listed in Table 5.4. Typical refinements results are plotted in Figure 5.10. The fitted Pt coordination numbers of the first shell are around 4 and the nearest distance of *Pt-X* is found to be 1.989(3) Å, similar to the 1.1-Pt-AC. Pt is also found to be coordinated with around 1 Cl at a distance around 2.198 Å.

| Sample | Shell | N | $\sigma^2$ (Å$^2$) | $R_{M-X}$ (Å) | QF |
|---|---|---|---|---|---|
| **11.7-Pt-AC** | Pt-*X* | 4.2(3) | 0.0040(6) | 1.989(3) | 0.27 |
| | Pt-Cl | 0.8(0.6) | | 2.198(14) | |

*Table 5. 4: EXAFS refinements result for 11.7-Pt-AC under He flow at 25 °C. The coordination number (N), the Debye–Waller factor ($\sigma^2$), the nearest Pt–X and Pt-Cl distance (R) and the confidence factor (QF) are given.*

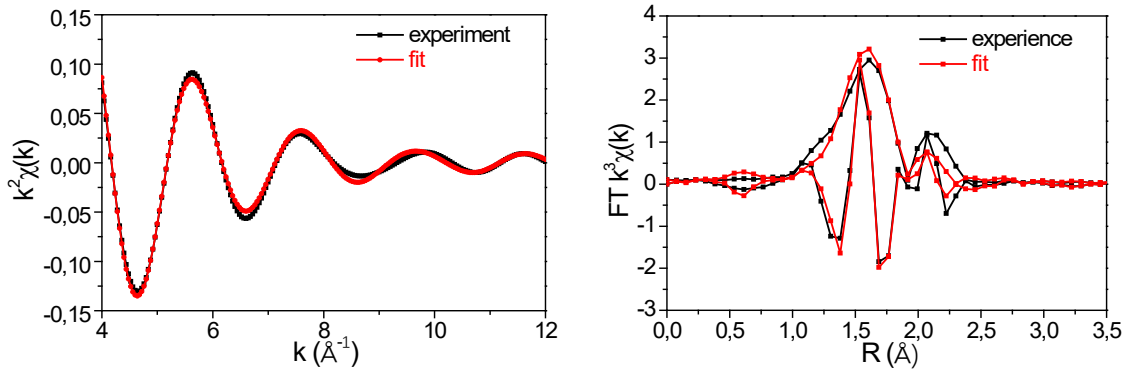


*Figure 5. 10: EXAFS fitting of 11.7-Pt-AC under He flow at 25 °C.*

In conclusion, single atom catalysts with several transition metals were synthesized with low loading (< 5 wt.%) and high loading (> 5 wt.%) concentration. The metal SACs were studied by several characterization techniques: XRD, HAADF-STEM, XPS and XAS, which showed that the metal atoms were ultra-dispersed on nitrogen-based carbon supported as single atoms or multimers (clusters or rafts).

### 5.3 Catalytic test

The low metal loading SACs materials were evaluated in catalytic reaction of selective hydrogenations in different mediums at laboratory IRCELYON: hydrogenation of butadiene in gaseous condition and hydrogenation of levulinic acid (LA) in aqueous solution.

#### 5.3.1 Hydrogenation of butadiene

The low loading SACs materials were firstly tested in hydrogenation of butadiene. The catalytic reaction was performed under atmospheric pressure in a continuous flow fixed-bed

reactor. Before the reaction, 40 mg of catalyst was mixed with 100 mg $Al_2O_3$ and activated *in situ* with hydrogen by heating from room temperature (RT) to 250 °C at a heating rate of 4 °C/min and maintained at 250 °C for 1 h. Then the reactor was cooled down to RT under $H_2$. The reaction was then carried out from RT to 200 °C with a reaction gas flow of 100 ml/min ($C_2H_2$:$H_2$:He = 2:10:88). The catalytic performance of SACs samples is compared with the corresponding metal nanoparticles, and the results are shown in the figures (Figure 5.11 – 5.16) as follows.

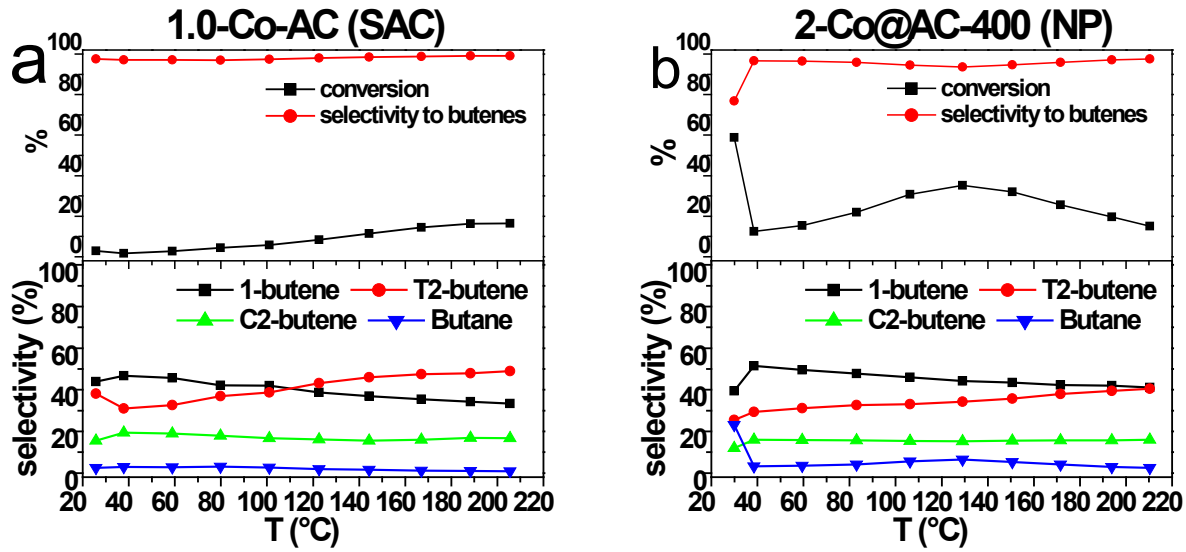


*Figure 5. 11:Catalytic performance in hydrogenation of butadiene of a) 1.0-Co-AC (SAC) and b) 2-Co@AC-400 (NP). Conversion and selectivity to butenes as a function of temperature, as well as their corresponding product distributions.*

1.0-Co-AC (SAC) is slightly reactive in this reaction, below 20% conversion at high temperature. The conversion increases with the rise of the temperature and it is about 16% when the temperature is superior to 180 °C. The selectivity to butenes attains nearly 100% during the whole reaction. The major products are 1-butene and T2-butene.

The Co nanoparticle sample, 2-Co@AC-400, is very reactive in the beginning of the reaction, nearly 60% conversion is achieved at room temperature. However, it deactivates rapidly and only 12% conversion is found at 40 °C. The reactivity increases slowly with the rise in temperature, the maximum being reached at 130 °C with 35% conversion. The selectivity to butenes reaches 90%, except at room temperature. Same as 1.0-Co-AC, the main products are 1-butene and T2-butene. The 1-butene decreases and T2-butene increases with temperature during the reaction for both samples.

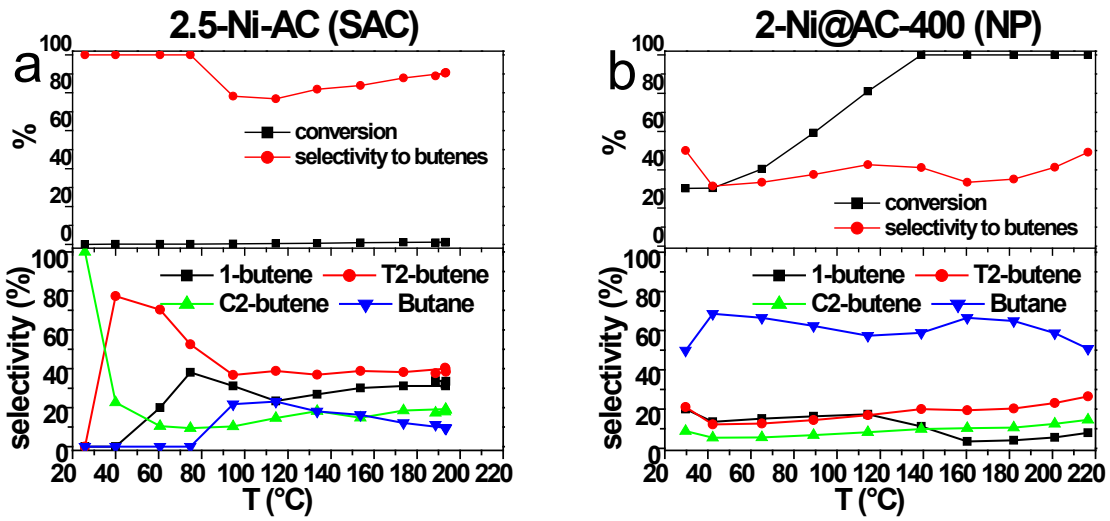


*Figure 5. 12:Catalytic performance in hydrogenation of butadiene of a) 2.5-Ni-AC (SAC) and b) 2-Ni@AC-400 (NP). Conversion and selectivity to butenes as a function of temperature, as well as their corresponding product distributions.*

2.5-Ni-AC is not reactive during the reaction whereas, Ni nanoparticles, 2-Ni@AC-400, are highly reactive in this reaction. They show complete conversion above 140 °C, and butane is the main product during the reaction.

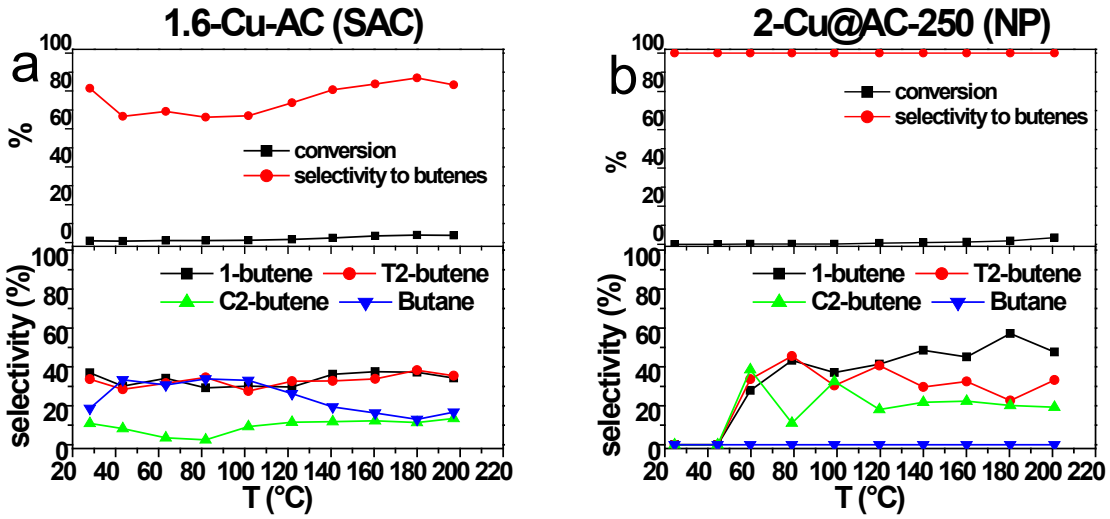


*Figure 5. 13:Catalytic performance in hydrogenation of butadiene of a) 1.6-Cu-AC (SAC) and b) 2-Cu@AC-250 (NP). Conversion and selectivity to butenes as a function of temperature, as well as their corresponding product distributions.*

The Cu single atom catalysts and nanoparticles catalyst are both not active during the reaction. The conversion is nearly zero, irrespective the reaction temperature.

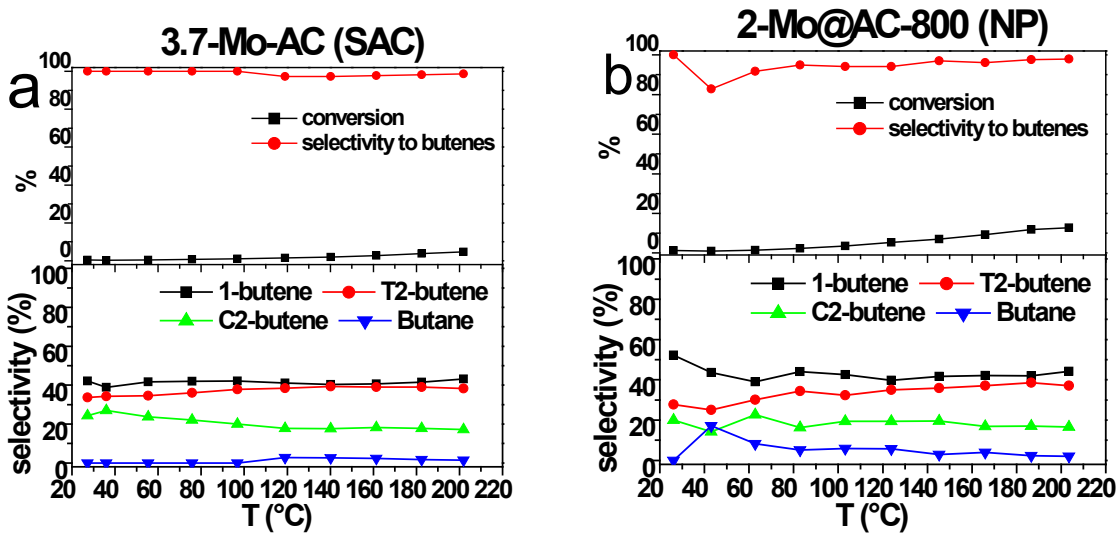


*Figure 5. 14:Catalytic performance in hydrogenation of butadiene of a) 3.7-Mo-AC (SAC) and b) 2-Mo@AC-800 (NP). Conversion and selectivity to butenes as a function of temperature, as well as their corresponding product distributions.*

The Mo catalysts are not very active for this reaction. The conversion increases slowly from 0% to 5% for SAC samples, 3.7-Mo-AC, and from 0% to 10% for nanoparticles, 2-Mo@AC-800, with rising the temperature from room temperature to around 200 °C. The selectivity to butenes is high around 90% but the catalysts are not reactive.

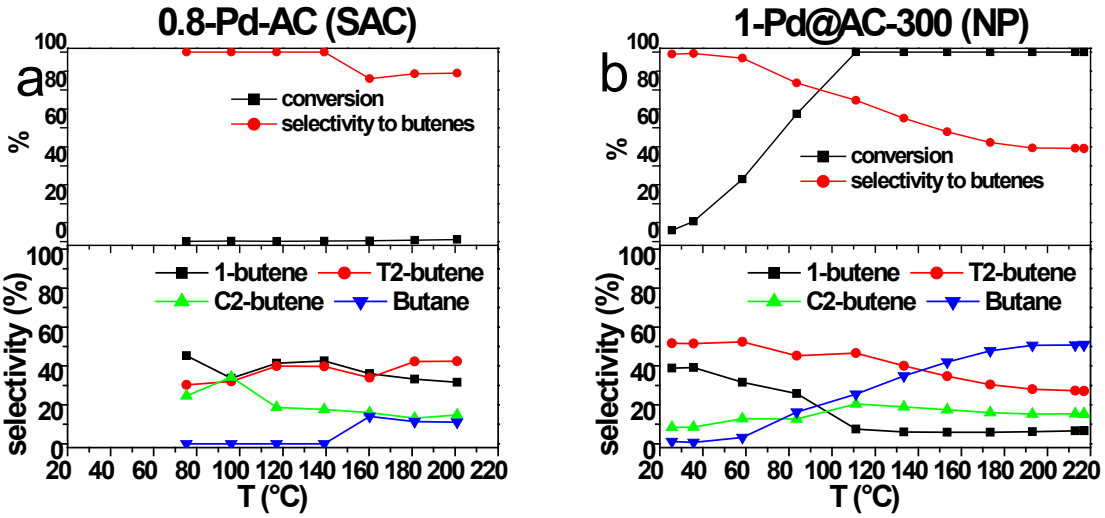


*Figure 5. 15:Catalytic performance in hydrogenation of butadiene of a) 0.8-Pd-AC (SAC) and b) 1-Pd@AC-300 (NP). Conversion and selectivity to butenes as a function of temperature, as well as their corresponding product distributions.*

No reactivity is found for Pd SAC catalyst, 0.8-Pd-AC. However, Pd nanoparticles, 1-Pd@AC-300, has a good performance for this reaction. The conversion increases progressively

with temperature and reaches full conversion at 110 °C and higher temperatures. Pd nanoparticles have a high selectivity to butenes at low temperature (< 60 °C) and T2-butene and 1-butene are primary products. As the temperature rises, the selectivity to butane increases along with the decrease of 1-butene and T2-butene. The butane becomes the main product when the temperature surpasses 140 °C.

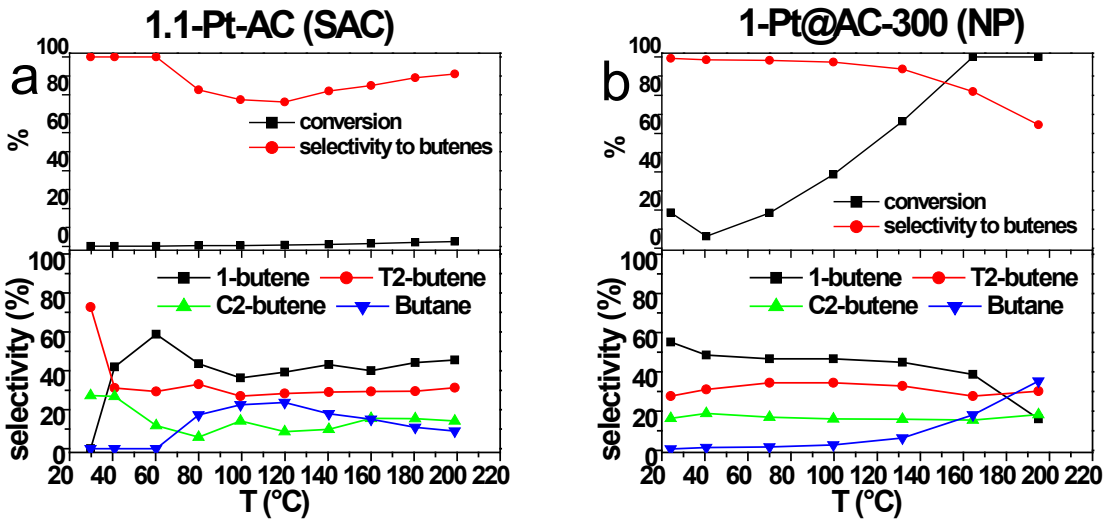


*Figure 5. 16:Catalytic performance in hydrogenation of butadiene of a) 1.1-Pt-AC (SAC) and b) 1-Pt@AC-300 (NP). Conversion and selectivity to butenes as a function of temperature, as well as their corresponding product distributions.*

Similar to Pd SAC, Pt SAC catalyst, 1.1-Pt-AC, shows no reactivity for this reaction. Nevertheless, the Pt nanoparticles, 1-Pt@AC-300, are reactive, like Pd case discussed before. 20% conversion is observed at the beginning of the reaction with 100% selectivity to butenes. The Pt nanoparticles deactivates at 40°C but regain activity with the increases of the temperature. The selectivity to butenes declines with increasing reaction temperature. The butane becomes the major product after 180 °C at full conversion.

The metal SACs catalysts: 1.0-Co-AC, 3.7-Mo-AC and 0.8-Pd-AC after the catalytic test were verified by TEM analysis (Figure 5.17). No metal clusters nor nanoparticles after the hydrogenation of butadiene could be noticed, suggesting that the Co, Mo and Pd single atoms are stable up to 250 °C under hydrogen atmosphere and up to 200 °C under reaction condition.

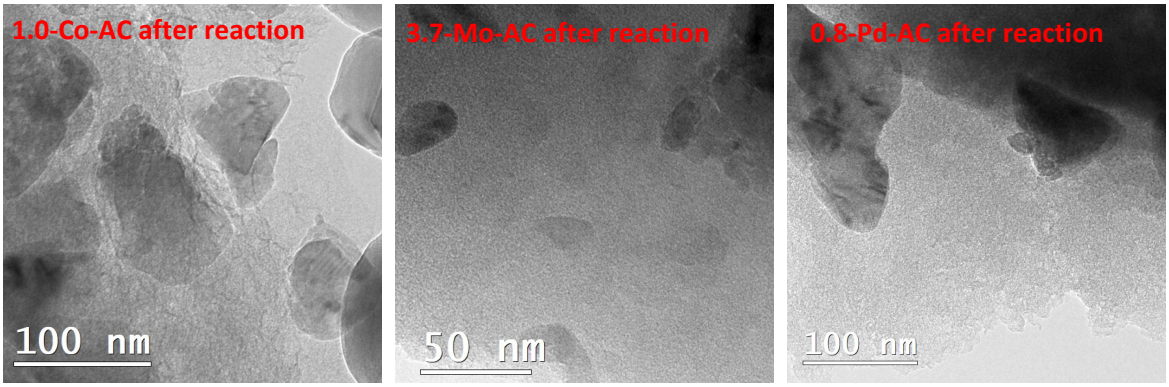


*Figure 5. 17: TEM images of 1.0-Co-AC, 3.7-Mo-AC and 0.8-Pd-AC after the hydrogenation of butadiene.*

### 5.3.2 Hydrogenation of levulinic acid

As discussed above, single atom catalysts showed different reactivity and selectivity in gaseous reaction of hydrogenation of butadiene as compared to metal nanoparticles. Another study was carried out to find out their catalytic performance in aqueous reaction condition: hydrogenation of levulinic acid (LA). The latter reaction was realised in a batch reactor at 160 °C and under 150 bar $H_2$ pressure, the detail of reaction condition can be found in **Chapter 2 Materials and Methods**. The results of hydrogenation of LA for these low loading SACs samples are shown in Figure 5.18.

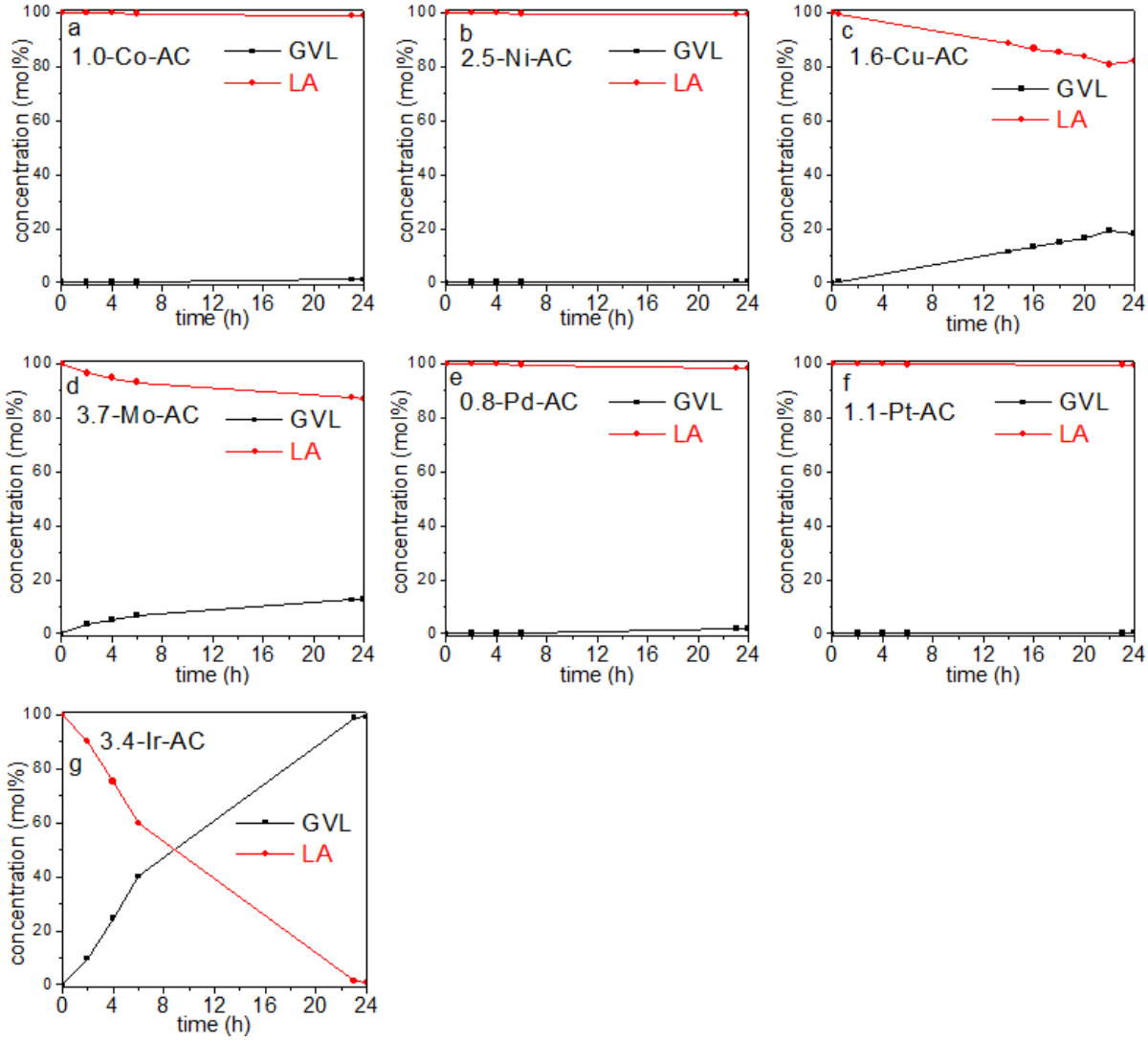


*Figure 5. 18: Conversion of levulinic acid in water for a) 1.0-Co-AC, b) 2.5-Ni-AC, c) 1.6-Cu-AC, d) 3.7-Mo-AC, e) 0.8-Pd-AC, f) 1.1-Pt-AC and g) 3.4-Ir-AC; reaction conditions: LA (0.17 M in 150 ml water), 400 mg catalyst, $H_2$ (150 bar), 160 °C, 24 h.*

The Co, Ni, Pd and Pt SACs are not reactive for this reaction. The conversion of LA was nearly zero after 24 h reaction. On the other side, 1.6-Cu-AC and 3.7-Mo-AC catalysts were slightly more active and the conversion of LA to GVL was 18% and 13%, respectively. The 3.4-Ir-AC showed a full conversion after 24 h reaction.

The tested SACs catalysts showed poor catalytic reactivity in the hydrogenation of levulinic acid as compared to metal nanoparticles catalysts found in the literature.[18,19] For example, Liu *et al.*[20] reported that 100% conversion of LA to GVL in 4h was attained with a 22 nm 5% Ni nanoparticles catalyst supported on nitrogen-doped mesoporous carbon under 200 °C, 30 bar $H_2$ and dioxane solvent reaction condition. Moreover, Hengne et al.[21]

synthesized 13.5 nm nanoparticles 5% Cu catalyst supported on $ZrO_2$, it showed complete conversion of LA to GVL in 5h in aqueous solution at 200 °C under 34.5 bar $H_2$. In addition, Upare et al. reported that a 5% Pd supported on carbon catalyst gave excellent reactivity of 100% conversion of LA in dioxane solution within 50h at 265 °C and under hydrogen pressure.

Single atom catalyst has been studied in many catalytic reactions, such as, electrochemical reactions (ORR: oxygen reduction reaction, MOR: methanol oxidation reaction and HER: hydrogen evolution reaction) and various hydrogenation reactions.[22,23] However, few studies concern the hydrogenation of levulinic acid. Cao *et al.*[24] synthesized an Ir@$ZrO_2$@C SAC which showed complete conversion in 10 h in the hydrogenation of LA to GVL in acidic aqueous solution at 180 °C under 40 bar $H_2$. Zhang *et al.*[25] designed a Ru/$TiO_2$@CN SAC and LA could be completely converted to GVL within 13 h at room temperature under 60 bar $H_2$. Obviously, the SACs reported in literature have much better catalytic reactivity than our SACs materials based on Co, Ni, Cu, Mo, Pd and Pt. However, we can recall that the 1.0-Ir-AC catalyst described in **Chapter IV** reaches a conversion of 49% LA to GVL under the same reaction conditions, which outperformed all our tested catalysts in this chapter, except 3.4-Ir-AC.

## 5.4 Conclusion

In this chapter, a study of physicochemical properties of single atom catalysts with various transition metals supported on carbon-based materials, as well as their performance in catalytic reaction of hydrogenation of butadiene and hydrogenation of levulinic acid (LA) was carried out. For the purpose of comparison, metal nanoparticles samples were also synthesized and studied for its catalytic performance in hydrogenation of butadiene.

The first part of this chapter consists of the physicochemical characterization of the metal SACs with two different categories according to the metal content: low metal loading (< 5 wt.%) and high metal loading (> 5 wt.%). The low metal (Co, Ni, Cu, Mo, Ir, Pd and Pt) loading SACs were proved to be ultra-dispersed on the nitrogen-based carbon support as single atoms or multimers (clusters or rafts), as confirmed by XRD, HAADF-STEM, XPS and XAS characterization. Moreover, three high metal loading SACs were successfully synthesized for Cu, Pd and Pt.

The second part of this chapter focused on the study of the catalytic reactivity of low metal loading SACs. In hydrogenation of butadiene, Co, Cu and Mo SACs and nanoparticles show poor conversion of butadiene: < 20%. The Ni, Pd and Pt SACs show nearly zero reactivity, while their corresponding nanoparticles samples reaches full conversion of butadiene at high temperature with the butane as the majority product. The metal SACs catalysts seem stable against reaction condition. In hydrogenation of LA, the metal SACs catalysts show mediocre reactivity, except Ir SACs which has a full conversion of LA to GVL after 24h. Co, Ni, Pd, Pt SACs are not reactive for this reaction. The conversions for Cu and Mo samples are 18% and 13%, respectively.

## 5.5 Reference

(1) Zhao, L.; Zhang, Y.; Huang, L.-B.; Liu, X.-Z.; Zhang, Q.-H.; He, C.; Wu, Z.-Y.; Zhang, L.-J.; Wu, J.; Yang, W.; Gu, L.; Hu, J.-S.; Wan, L.-J. Cascade Anchoring Strategy for General Mass Production of High-Loading Single-Atomic Metal-Nitrogen Catalysts. *Nat. Commun.* **2019**, *10* (1). https://doi.org/10.1038/s41467-019-09290-y.

(2) Midgley, P. A.; Weyland, M.; Thomas, J. M.; Johnson, B. F. G. Z-Contrast Tomography: A Technique Inthree-Dimensional Nanostructural Analysis Based on Rutherfordscattering. *Chem. Commun.* **2001**, No. 10, 907–908. https://doi.org/10.1039/B101819C.

(3) Lukashuk, L.; Yigit, N.; Rameshan, R.; Kolar, E.; Teschner, D.; Hävecker, M.; Knop-Gericke, A.; Schlögl, R.; Föttinger, K.; Rupprechter, G. Operando Insights into CO Oxidation on Cobalt Oxide Catalysts by NAP-XPS, FTIR, and XRD. *ACS Catal.* **2018**, *8* (9), 8630–8641. https://doi.org/10.1021/acscatal.8b01237.

(4) Christoskova, St. G.; Stoyanova, M.; Georgieva, M.; Mehandjiev, D. Preparation and Characterization of a Higher Cobalt Oxide. *Mater. Chem. Phys.* **1999**, *60* (1), 39–43. https://doi.org/10.1016/S0254-0584(99)00053-X.

(5) Barreca, D.; Gasparotto, A.; Lebedev, O. I.; Maccato, C.; Pozza, A.; Tondello, E.; Turner, S.; Tendeloo, G. V. Controlled Vapor-Phase Synthesis of Cobalt Oxide Nanomaterials with Tuned Composition and Spatial Organization. *CrystEngComm* **2010**, *12* (7), 2185–2197. https://doi.org/10.1039/B926368N.

(6) Yin, D.; Tang, J.; Bai, R.; Yin, S.; Jiang, M.; Kan, Z.; Li, H.; Wang, F.; Li, C. Cobalt Phosphide (Co2P) with Notable Electrocatalytic Activity Designed for Sensitive and Selective Enzymeless Bioanalysis of Hydrogen Peroxide. *Nanoscale Res. Lett.* **2021**, *16* (1), 11. https://doi.org/10.1186/s11671-020-03469-9.

(7) Li, M.; Wu, S.; Yang, X.; Hu, J.; Peng, L.; Bai, L.; Huo, Q.; Guan, J. Highly Efficient Single Atom Cobalt Catalyst for Selective Oxidation of Alcohols. *Appl. Catal. Gen.* **2017**, *543*, 61–66. https://doi.org/10.1016/j.apcata.2017.06.018.

(8) Gao, X.; Zhou, Y.; Liu, S.; Cheng, Z.; Tan, Y.; Shen, Z. Single Cobalt Atom Anchored on N-Doped Graphyne for Boosting the Overall Water Splitting. *Appl. Surf. Sci.* **2020**, *502*, 144155. https://doi.org/10.1016/j.apsusc.2019.144155.

(9) Mao, J.; Chen, W.; He, D.; Wan, J.; Pei, J.; Dong, J.; Wang, Y.; An, P.; Jin, Z.; Xing, W.; Tang, H.; Zhuang, Z.; Liang, X.; Huang, Y.; Zhou, G.; Wang, L.; Wang, D.; Li, Y. Design of Ultrathin Pt-Mo-Ni Nanowire Catalysts for Ethanol Electrooxidation. *Sci. Adv.* **2017**, *3* (8), e1603068. https://doi.org/10.1126/sciadv.1603068.

(10) Nakazono, T.; Parent, A. R.; Sakai, K. Cobalt Porphyrins as Homogeneous Catalysts for Water Oxidation. *Chem. Commun.* **2013**, *49* (56), 6325. https://doi.org/10.1039/c3cc43031f.

(11) Lam, T.-L.; Tong, K.-C.; Yang, C.; Kwong, W.-L.; Guan, X.; Li, M.-D.; Lo, V. K.-Y.; Chan, S. L.-F.; Phillips, D. L.; Lok, C.-N.; Che, C.-M. Luminescent Ruffled Iridium(III) Porphyrin Complexes Containing N-Heterocyclic Carbene Ligands: Structures, Spectroscopies and Potent Antitumor Activities under Dark and Light Irradiation Conditions. *Chem. Sci.* **2018**, *10* (1), 293–309. https://doi.org/10.1039/C8SC02920B.

(12) Zems, Y.; Moiseev, A. G.; Perepichka, D. F. Convenient Synthesis of a Highly Soluble and Stable Phosphorescent Platinum Porphyrin Dye. *Org. Lett.* **2013**, *15* (20), 5330–5333. https://doi.org/10.1021/ol402590c.

(13) Sun, T.; Zhao, S.; Chen, W.; Zhai, D.; Dong, J.; Wang, Y.; Zhang, S.; Han, A.; Gu, L.; Yu, R.; Wen, X.; Ren, H.; Xu, L.; Chen, C.; Peng, Q.; Wang, D.; Li, Y. Single-Atomic Cobalt Sites Embedded in Hierarchically Ordered Porous Nitrogen-Doped Carbon as a Superior Bifunctional Electrocatalyst. *Proc. Natl. Acad. Sci.* **2018**, *115* (50), 12692–12697. https://doi.org/10.1073/pnas.1813605115.

(14) Li, Z.; Chen, Y.; Ji, S.; Tang, Y.; Chen, W.; Li, A.; Zhao, J.; Xiong, Y.; Wu, Y.; Gong, Y.; Yao, T.; Liu, W.; Zheng, L.; Dong, J.; Wang, Y.; Zhuang, Z.; Xing, W.; He, C.-T.; Peng, C.; Cheong, W.-C.; Li, Q.; Zhang, M.; Chen, Z.; Fu, N.; Gao, X.; Zhu, W.; Wan, J.; Zhang, J.; Gu, L.; Wei, S.; Hu, P.; Luo, J.; Li, J.; Chen, C.; Peng, Q.; Duan, X.; Huang, Y.; Chen, X.-M.; Wang, D.; Li, Y. Iridium Single-Atom Catalyst on Nitrogen-Doped Carbon for Formic Acid Oxidation Synthesized Using a General Host–Guest Strategy. *Nat. Chem.* **2020**. https://doi.org/10.1038/s41557-020-0473-9.

(15) Luo, H.; Liu, Y.; Dimitrov, S. D.; Steier, L.; Guo, S.; Li, X.; Feng, J.; Xie, F.; Fang, Y.; Sapelkin, A.; Wang, X.; Titirici, M.-M. Pt Single-Atoms Supported on Nitrogen-Doped Carbon Dots

for Highly Efficient Photocatalytic Hydrogen Generation. *J. Mater. Chem. A* **2020**, *8* (29), 14690–14696. https://doi.org/10.1039/D0TA04431H.

(16) Zhang, Z.; Zhu, Y.; Asakura, H.; Zhang, B.; Zhang, J.; Zhou, M.; Han, Y.; Tanaka, T.; Wang, A.; Zhang, T.; Yan, N. Thermally Stable Single Atom Pt/m-Al2O3 for Selective Hydrogenation and CO Oxidation. *Nat. Commun.* **2017**, *8* (1), 16100. https://doi.org/10.1038/ncomms16100.

(17) He, T.; Chen, S.; Ni, B.; Gong, Y.; Wu, Z.; Song, L.; Gu, L.; Hu, W.; Wang, X. Zirconium–Porphyrin-Based Metal–Organic Framework Hollow Nanotubes for Immobilization of Noble-Metal Single Atoms. *Angew. Chem. Int. Ed.* **2018**, *57* (13), 3493–3498. https://doi.org/10.1002/anie.201800817.

(18) Wright, W. R. H.; Palkovits, R. Development of Heterogeneous Catalysts for the Conversion of Levulinic Acid to γ-Valerolactone. *ChemSusChem* **2012**, *5* (9), 1657–1667. https://doi.org/10.1002/cssc.201200111.

(19) Dutta, S.; Yu, I. K. M.; Tsang, D. C. W.; Ng, Y. H.; Ok, Y. S.; Sherwood, J.; Clark, J. H. Green Synthesis of Gamma-Valerolactone (GVL) through Hydrogenation of Biomass-Derived Levulinic Acid Using Non-Noble Metal Catalysts: A Critical Review. *Chem. Eng. J.* **2019**, *372*, 992–1006. https://doi.org/10.1016/j.cej.2019.04.199.

(20) Liu, D.; Zhang, L.; Han, W.; Tang, M.; Zhou, L.; Zhang, Y.; Li, X.; Qin, Z.; Yang, H. One-Step Fabrication of Ni-Embedded Hierarchically-Porous Carbon Microspheres for Levulinic Acid Hydrogenation. *Chem. Eng. J.* **2019**, *369*, 386–393. https://doi.org/10.1016/j.cej.2019.03.072.

(21) Hengne, A. M.; Rode, C. V. Cu–ZrO2 Nanocomposite Catalyst for Selective Hydrogenation of Levulinic Acid and Its Ester to γ-Valerolactone. *Green Chem.* **2012**, *14* (4), 1064–1072. https://doi.org/10.1039/C2GC16558A.

(22) Wang, Y.; Mao, J.; Meng, X.; Yu, L.; Deng, D.; Bao, X. Catalysis with Two-Dimensional Materials Confining Single Atoms: Concept, Design, and Applications. *Chem. Rev.* **2019**, *119* (3), 1806–1854. https://doi.org/10.1021/acs.chemrev.8b00501.

(23) Cheng, N.; Zhang, L.; Doyle-Davis, K.; Sun, X. Single-Atom Catalysts: From Design to Application. *Electrochem. Energy Rev.* **2019**, *2* (4), 539–573. https://doi.org/10.1007/s41918-019-00050-6.

(24) Cao, W.; Lin, L.; Qi, H.; He, Q.; Wu, Z.; Wang, A.; Luo, W.; Zhang, T. In-Situ Synthesis of Single-Atom Ir by Utilizing Metal-Organic Frameworks: An Acid-Resistant Catalyst for Hydrogenation of Levulinic Acid to γ-Valerolactone. *J. Catal.* **2019**, *373*, 161–172. https://doi.org/10.1016/j.jcat.2019.03.035.

(25) Zhang, K.; Meng, Q.; Wu, H.; Yuan, T.; Han, S.; Zhai, J.; Zheng, B.; Xu, C.; Wu, W.; He, M.; Han, B. Levulinic Acid Hydrogenation to γ-Valerolactone over Single Ru Atoms on a TiO2@nitrogen Doped Carbon Support. *Green Chem.* **2021**, *23* (4), 1621–1627. https://doi.org/10.1039/D0GC04108D.

# General conclusion & perspectives

The objective of this Ph.D. thesis work was to synthesize the ultra-dispersed metal particles at nanoscale or even smaller size such as single atom state supported on carbon-based materials. Afterwards, the synthesized hybrid materials have been studied to highlight their interaction with hydrogen and tested in selective hydrogenation reactions: hydrogenation of butadiene in gaseous condition and hydrogenation of levulinic acid (LA) in aqueous solution. The main idea is to compare the hydrogen interaction and the catalytic reactivity between metal nanoparticles and single atom catalysts (SACs). In catalysis, the focus is on the SACs as the metal nanoparticles have been already well studied in the literature.

Firstly, three 10 wt.% Pd nanoparticles samples with different average sizes: 6.0, 2.0, and 1.4 nm, and two Pd single atom catalysts (SACs) samples with different metal content: 0.8 and 7.5 wt.%, supported on carbon-based materials were synthesized and characterized. From the PCI curves at room temperature for Pd nanoparticles, the absorption capacity at 1 bar $H_2$ diminishes with the decrease of Pd size. The absorption and desorption show only partial reversibility for Pd nanoparticles at low pressure, while they are completely reversible for Pd bulk, which indicates that hydrogen is trapped inside Pd nanoparticles after the desorption process. The decrease of absorption capacity was confirmed by *in situ* XRD. *In situ* XAS at synchrotron together with TDS experiment confirmed the H trapping inside the lattice of Pd nanoparticles, and a size dependence H trapping effect was found: the smaller the size, the larger the irreversible H amount and the higher the binding energy experienced by H atoms. The DFT and TB simulations suggest that the trapped H is situated at the subsurface of nanoparticles. Moreover, the bond strength for Pd-H becomes weaker as the Pd size decreases and hydrogen atoms in nanoparticles have larger entropy with decreasing the Pd size. During the desorption process, a change of the rate limiting step from surface recombination or $\beta \rightarrow \alpha$ phase transformation in Pd bulk to hydrogen diffusion into $\alpha$ and $\beta$ phases in Pd nanoparticles was demonstrated. On the other side, contrary to Pd nanoparticles, Pd SACs showed very little interaction with hydrogen, as confirmed by PCI and TDS experiments.

Thereafter, 1.0 wt.% Ir single atom catalyst (Ir-SAC) and 3.7 wt.% Ir nanoparticles sample (Ir-NP) were prepared, and a comparative study of Ir-SAC and Ir-NP was carried out to determine their physicochemical properties and the catalytic performance in selective hydrogenation reactions. The Ir single atoms in Ir-SAC and Ir nanoparticles in Ir-NP were

confirmed by HAADF-STEM characterization. The chemical state of Ir atoms in Ir-SAC is different form Ir atoms in Ir-NP. Ir forms stable bond with 4 N (and/or C,O) with an oxidation state of + 3.2 in Ir-SAC, and the XPS binding energies of Ir 4f are 62.5 eV (Ir $4f_{7/2}$) and 65.5 eV (Ir $4f_{5/2}$), which is higher than Ir in Ir-NP and Ir bulk. In hydrogenation of butadiene, Ir single atoms were partially reduced, and the coordination number and oxidation state decreased to around 3 and +2.0 after the pretreatment at 250 °C under hydrogen. Ir-SAC showed 80% conversion at 200 °C with nearly 100% selectivity to butenes, especially with the majority product trans-2-buene which is rarely seen in literature. The reduced Ir single atoms are thought to be the active species in this reaction. In comparison, Ir-NP showed low selectivity to butenes while the conversion exceeded 30% at temperature up to 120 °C. In hydrogenation of LA, Ir-SAC had a moderate conversion of LA to γ-valerolactone: 80% conversion after 24 h reaction time. Ir-SAC showed high stability under air condition up to 400 °C and under hydrogenation of butadiene reaction condition, however the agglomeration of Ir single atoms was observed after the hydrogenation of LA.

Finally, studies of physicochemical properties of single atom catalysts with various transition metals supported on carbon-based materials, and the performances in catalytic reactions of hydrogenation of butadiene and hydrogenation of levulinic acid (LA) were carried out. For the purpose of comparison, metal nanoparticles samples were also synthesized and studied for the catalytic performance in hydrogenation of butadiene. The SACs samples were divided into two categories according to the metal contents: low loading (< 5 wt.%) and high loading (> 5 wt.%). The low metal (Co, Ni, Cu, Mo, Ir, Pd and Pt) loading SACs and high metal (Cu, Pd and Pt) loading SACS samples were proved to be ultra-dispersed on nitrogen-based carbon supported as single atoms or multimers (clusters or rafts), as confirmed by XRD, HAADF-STEM, XPS and XAS characterization. The catalytic tests were performed using the low loading SACs and their corresponding metal nanoparticles. In the hydrogenation of butadiene, Co, Cu and Mo SACs and nanoparticles showed poor conversion of butadiene: < 20%. The Ni, Pd and Pt SACs showed no reactivity, while their corresponding nanoparticles samples had full conversion of butadiene at high temperature with the butane as the majority product. The metal SACs seemed stable under the reaction condition. In hydrogenation of LA, the metal SACs showed mediocre reactivity, except 3.5% Ir SACs which has a full conversion of LA to GVL

after 24h. Co, Ni, Pd, Pt SACs are not reactive for this reaction. The conversions for Cu and Mo samples are 18% and 13%, respectively.

In perspective, for Pd nanoparticles, the nanosize effects, in particular the H trapping at subsurface sites of Pd nanoparticles was observed. Trapped H at the subsurface may play an important role in hydrogenation reactions through a subsurface hydrogen-induced electronic effect leading to the stabilization of metal-H bonds at the surface. Therefore, other studies may be carried out to check if other metal nanoparticles, such as Ir, Rh or Pt which has been frequently used in heterogeneous catalysis, have similar H trapping effect.

Moreover, the hydrogen interaction with Pd SACs were proved to be completely different compared to Pd nanoparticles from PCI and TDS measurements. A more complete systematic study of the hydrogen interaction with Pd SACs, as well as with other metal SACs, including physisorption and chemisorption properties, may be carried out. As confirmed in *operando* XAS, Ir-SAC was partially reduced under hydrogen at high temperature under hydrogen atmosphere. Another XAS experiment may be carried out to check the reversibility of this process, *i.e.*, if the reduced Ir-SAC could be oxidized to the initial chemical state after exposure in an oxidized environment (ex: in air condition). In additional, same *operando* XAS may be realized to observe if other metal single atoms in SACs samples have the similar change of chemical state under hydrogen condition at high temperature.

Finally, in catalysis, the reaction conditions were chosen empirically, no large effort was spent to find the best reaction condition. For example, in hydrogenation of butadiene, the pretreatment temperature was set at 250 °C, other pretreatment temperatures may be tried. In hydrogenation of LA, water was chosen as the solvent, however other solvent may be used, *e.g.*, dioxane and ethanol. Furthermore, the SACs are used frequently in other hydrogenation reactions, such as electrocatalysis and hydrogenation of $CO_2$. Therefore, the metal SACs samples may be tested in other hydrogenation reactions.

## Study of the interaction between hydrogen and ultradispersed metals for heterogeneous catalysis

Heterogeneous catalysis is one of the pillars of the chemical industry as it is involved in a wide range of applications. The heterogeneous reaction occurs usually at the surface of metal catalysts, therefore the downscaling of metal particles to the ultra-small size range, which increases the metal surface area and thus enhances the number of the metallic active sites, has become an important strategy for the design of new and efficient materials. Moreover, nanometric and subnanometric downsizing gives rise to a dramatic change in the electronic properties of metals, which in turn leads to promising catalytic performances.

The purpose of this PhD work is to synthesize ultra-small metal particles at nanoscale or even smaller size such as, single atom state, supported on carbon-based materials, to study their interaction with hydrogen for the purpose of their utilization in selective hydrogenation reactions : hydrogenation of butadiene in gaseous condition and hydrogenation of levulinic acid in aqueous condition. In this work, Pd nanoparticles with different sizes (6.0, 2.0 and 1.4 nm), and various transition metals (Co, Ni, Cu, Mo, Pd, Ir and Pt) single atom catalysts (SACs) were synthesized by liquid impregnation methods. The obtained hybrid materials were characterized by a wide range of laboratory characterization techniques and by synchrotron radiation.

One of the main experimental results proved an interesting H trapping phenomenon in Pd nanoparticles and confirmed by theoretical calculations. H is trapped inside the subsurface interstitial sites of Pd nanoparticles and a size effect is highlighted : the smaller the Pd particle size, the larger the fraction of trapped H and the higher the binding energy experienced by these H atoms.

Another important result related to catalysis demonstrated that, among all the SACs samples, Ir-SAC has the best catalytic performance : high reactivity in hydrogenation of butadiene with nearly 100% selectivity to butenes, in particular with the majority product of trans-2-butene, which is rarely reported in literature. In comparison, Ir nanoparticles show low selectivity to butenes while the conversion is high (> 30%). Ir-SAC has also a relatively good conversion of levulinic acid to γ-valerolactone: 80% conversion in 24 h reaction.

Keywords: heterogeneous catalysis, metal nanoparticles, single atom catalysts, hydrogen

## Etude de l'interaction entre l'hydrogène et des métaux ultra-dispersés pour la catalyse hétérogène

La catalyse hétérogène est l'un des piliers de l'industrie chimique car elle intervient dans un large éventail d'applications. La réaction catalytique se produit généralement à la surface des catalyseurs métalliques, c'est pourquoi la réduction des particules métalliques à une taille ultra-petite, qui augmente la surface du métal et accroît ainsi le nombre de sites actifs, est devenue une stratégie importante pour la conception de nouveaux matériaux efficaces. En outre, la réduction de la taille à l'échelle nanométrique et subnanométrique entraîne un changement radical des propriétés électroniques des métaux, ce qui se traduit par des performances catalytiques prometteuses.

L'objectif de ce travail de thèse est de synthétiser des particules métalliques à taille nanométrique contrôlée allant jusqu'à la dispersion ultime sous forme d'atomes isolés supportés sur des matériaux à base de carbone et d'étudier leur interaction avec l'hydrogène en vue de leur utilisation dans de réactions d'hydrogénation sélective : l'hydrogénation du butadiène en phase gazeuse et l'hydrogénation de l'acide lévulinique en phase liquide. Dans ce travail, des nanoparticules de Pd de différentes tailles (6,0, 2,0 et 1,4 nm) et divers métaux de transition (Co, Ni, Cu, Mo, Pd, Ir et Pt) sous forme d'atomes isolés (single atoms catalysts-SACs, en Anglais) ont été synthétisés par des méthodes d'imprégnation liquide. Les matériaux hybrides obtenus ont été caractérisés par une large palette de techniques de caractérisation de laboratoire et par le rayonement synchrotron.

Un des faits marquants de ce travail est la mise en évidence d'un phénomène de piégeage de l'H dans les nanoparticules de Pd confirmé aussi par des calculs théoriques. L'hydrogène est piégé dans les sites interstitiels de la subsurface des nanoparticules de Pd et un effet de taille est observé : plus la taille des particules de Pd est petite, plus la fraction d'H piégé est grande et plus l'énergie de liaison Pd-H est élevée.

Un autre fait marquant est obtenu en catalyse et démontre que, parmi tous les SACs étudiés, Ir-SAC a la meilleure performance catalytique : haute réactivité dans l'hydrogénation du butadiène avec une sélectivité de presque 100% en butènes, en particulier avec le produit majoritaire étant le trans-2-butène, ce qui est rarement rapporté dans la littérature. En comparaison, les nanoparticules d'Ir montrent une faible sélectivité en butènes alors que la conversion est élevée (> 30%). Ir-SAC présente également une conversion relativement bonne de l'acide lévulinique en γ-valerolactone : 80% de conversion en 24 h de réaction.

Mot clés : catalyse hétérogène, nanoparticules métalliques, catalyseurs des atomes isolées, hydrogène